

# **Review of figures**

## **Papers of Stellar Astrophysics**

**Ian Baeza**

# **Carrol Chapter 7 (Paper 1)**

## **Binary Systems and stellar parameters**

# Carrol Chapter 7 (Paper 1) Binary Systems and stellar parameters

- Optical Double : not binaries just in same line of sight
- Visual Binary: resolved binaries
- Astrometric Binary: use astrometry to determine gravitational interaction
- Eclipsing binary: orbital plane “aligned” with the line of sight, measure due periodic lost of flux
- Spectrum Binary: Two superimposed discernible spectra
- Spectroscopic binary: periodic variations on the spectra can be detected

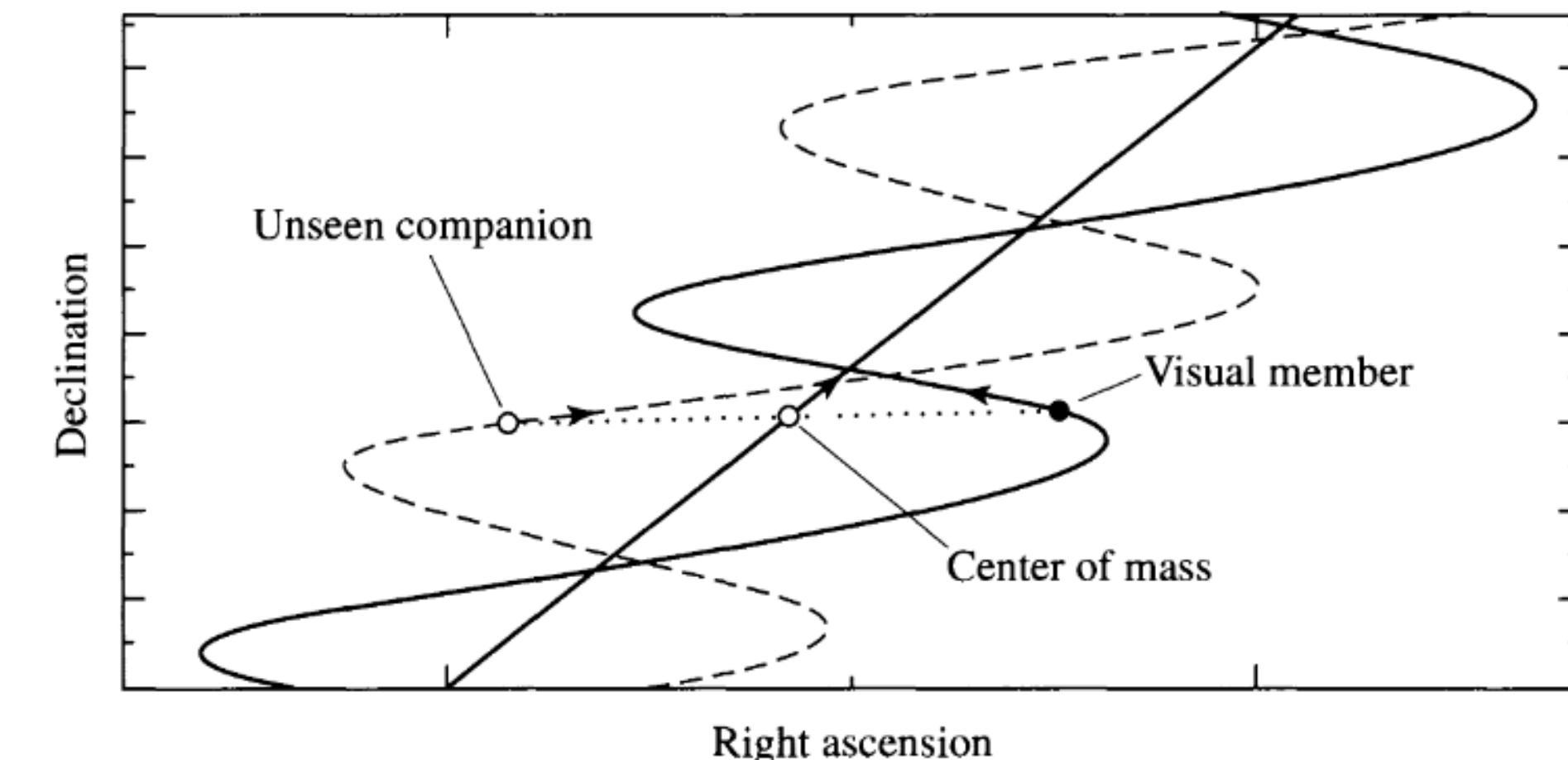


**FIGURE 7.1** An astrometric binary, which contains one visible member. The unseen component is implied by the oscillatory motion of the observable star in the system. The proper motion of the entire system is reflected in the straight-line motion of the center of mass.

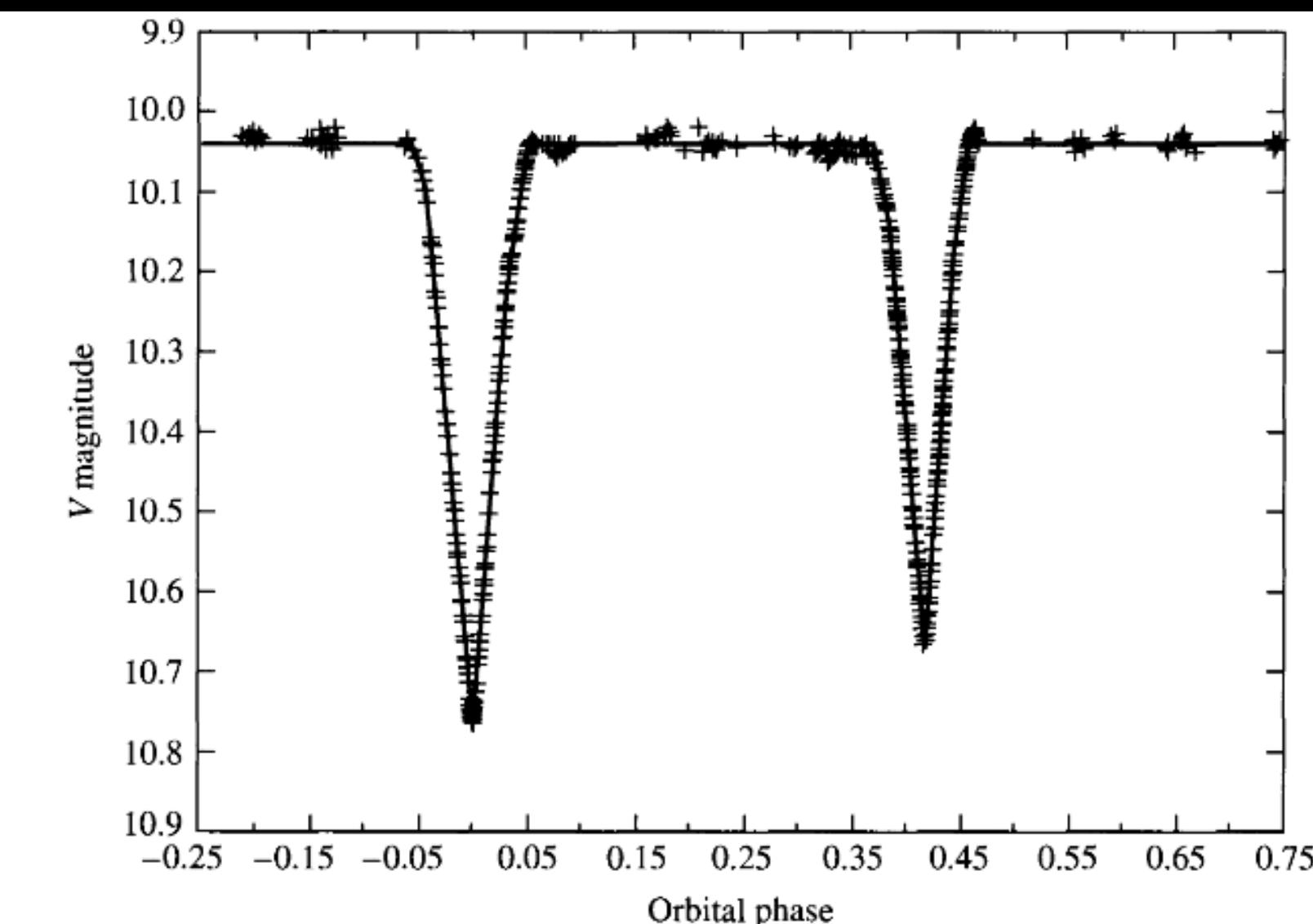


**FIGURE 7.2** The  $V$  magnitude light curve of YY Sagittarii, an eclipsing binary star. The data from many orbital periods have been plotted on this light curve as a function of phase, where the phase is defined to be 0.0 at the primary minimum. This system has an orbital period  $P = 2.6284734$  d, an eccentricity  $e = 0.1573$ , and orbital inclination  $i = 88.89^\circ$  (see Section 7.2). (Figure adopted from Lacy, C. H. S., *Astron. J.*, 105, 637, 1993.)

# Carrol Chapter 7 (Paper 1) Binary Systems and stellar parameters

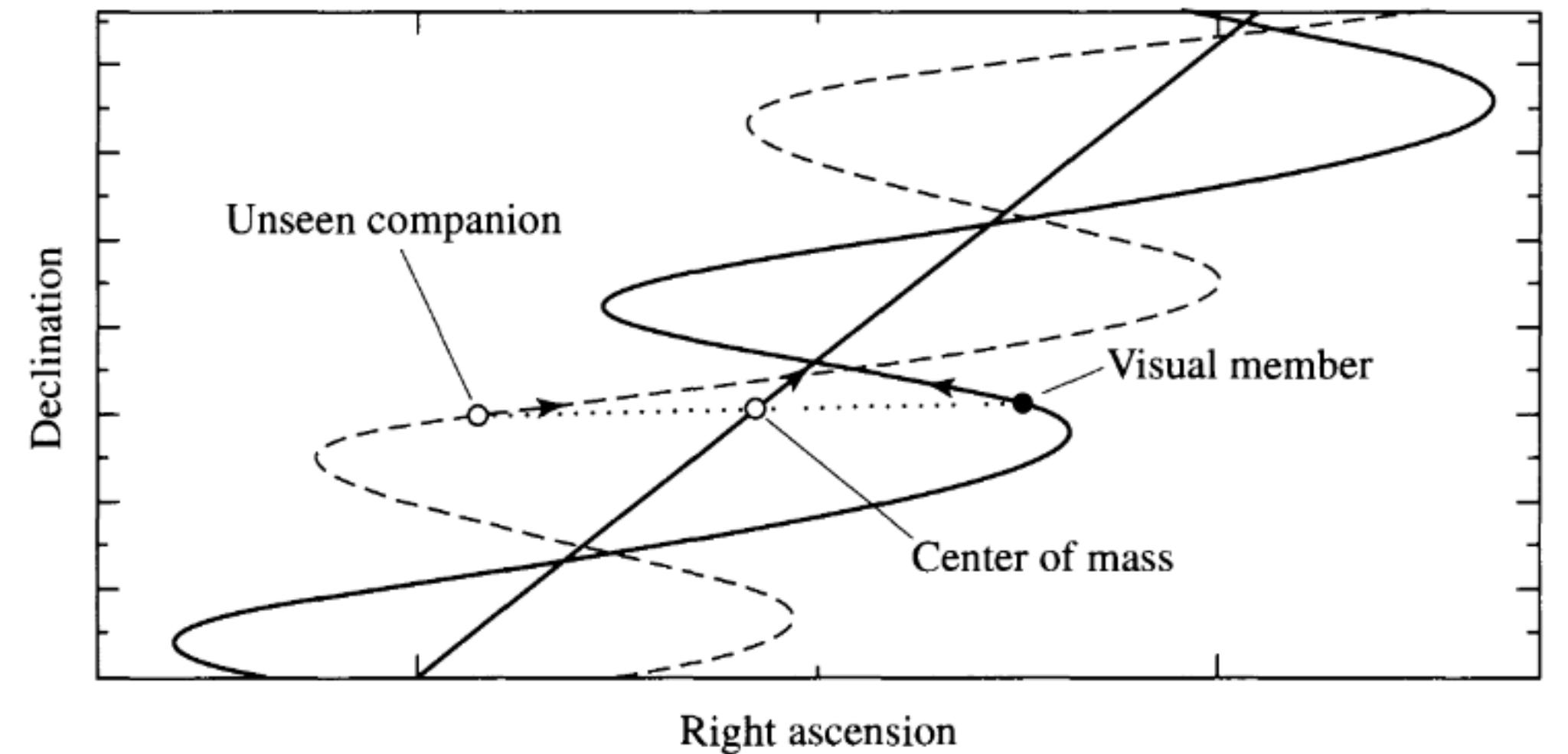


**FIGURE 7.1** An astrometric binary, which contains one visible member. The unseen component is implied by the oscillatory motion of the observable star in the system. The proper motion of the entire system is reflected in the straight-line motion of the center of mass.

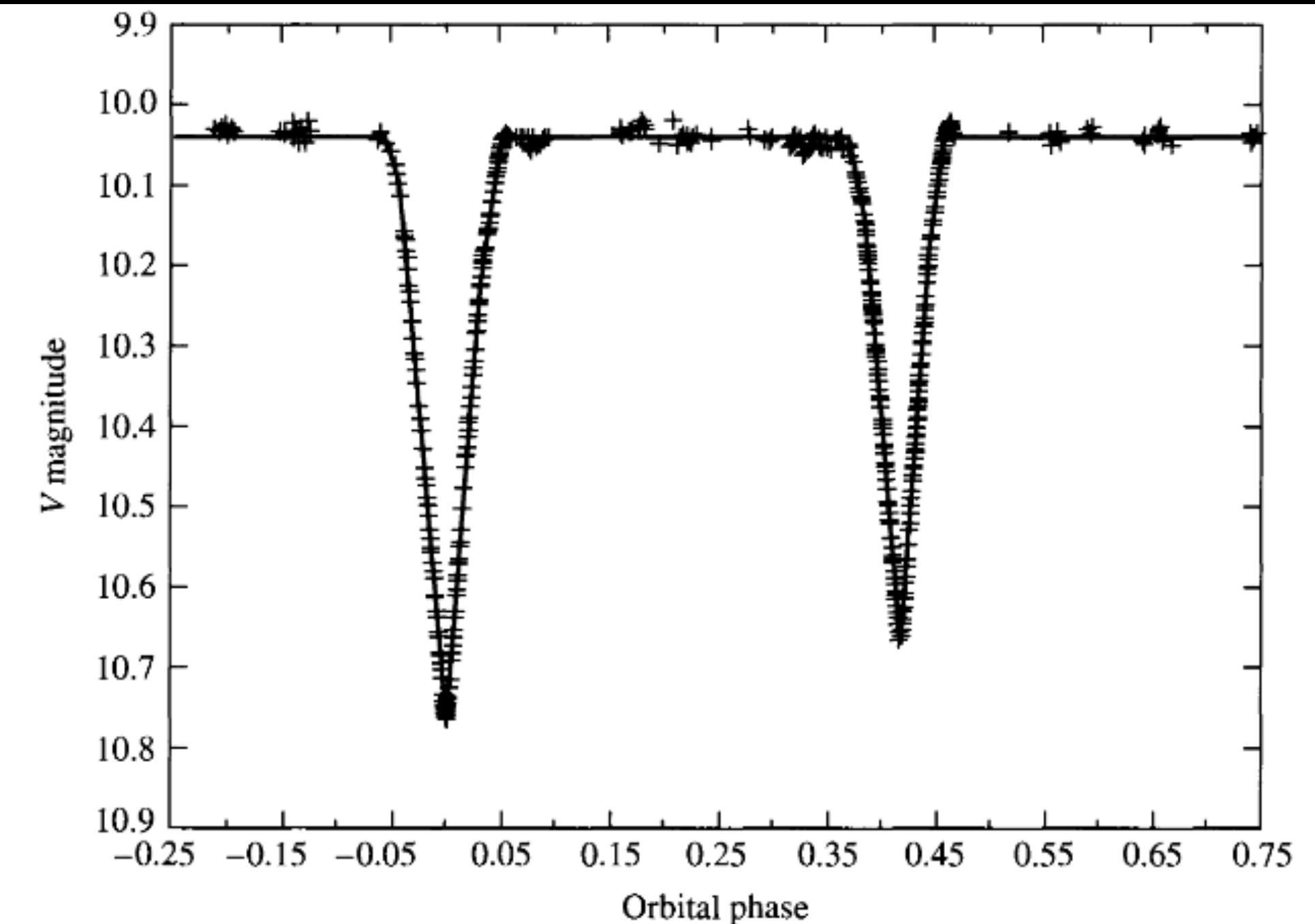


**FIGURE 7.2** The  $V$  magnitude light curve of YY Sagittarii, an eclipsing binary star. The data from many orbital periods have been plotted on this light curve as a function of phase, where the phase is defined to be 0.0 at the primary minimum. This system has an orbital period  $P = 2.6284734$  d, an eccentricity  $e = 0.1573$ , and orbital inclination  $i = 88.89^\circ$  (see Section 7.2). (Figure adopted from Lacy, C. H. S., *Astron. J.*, 105, 637, 1993.)

# Carrol Chapter 7 (Paper 1) Binary Systems and stellar parameters

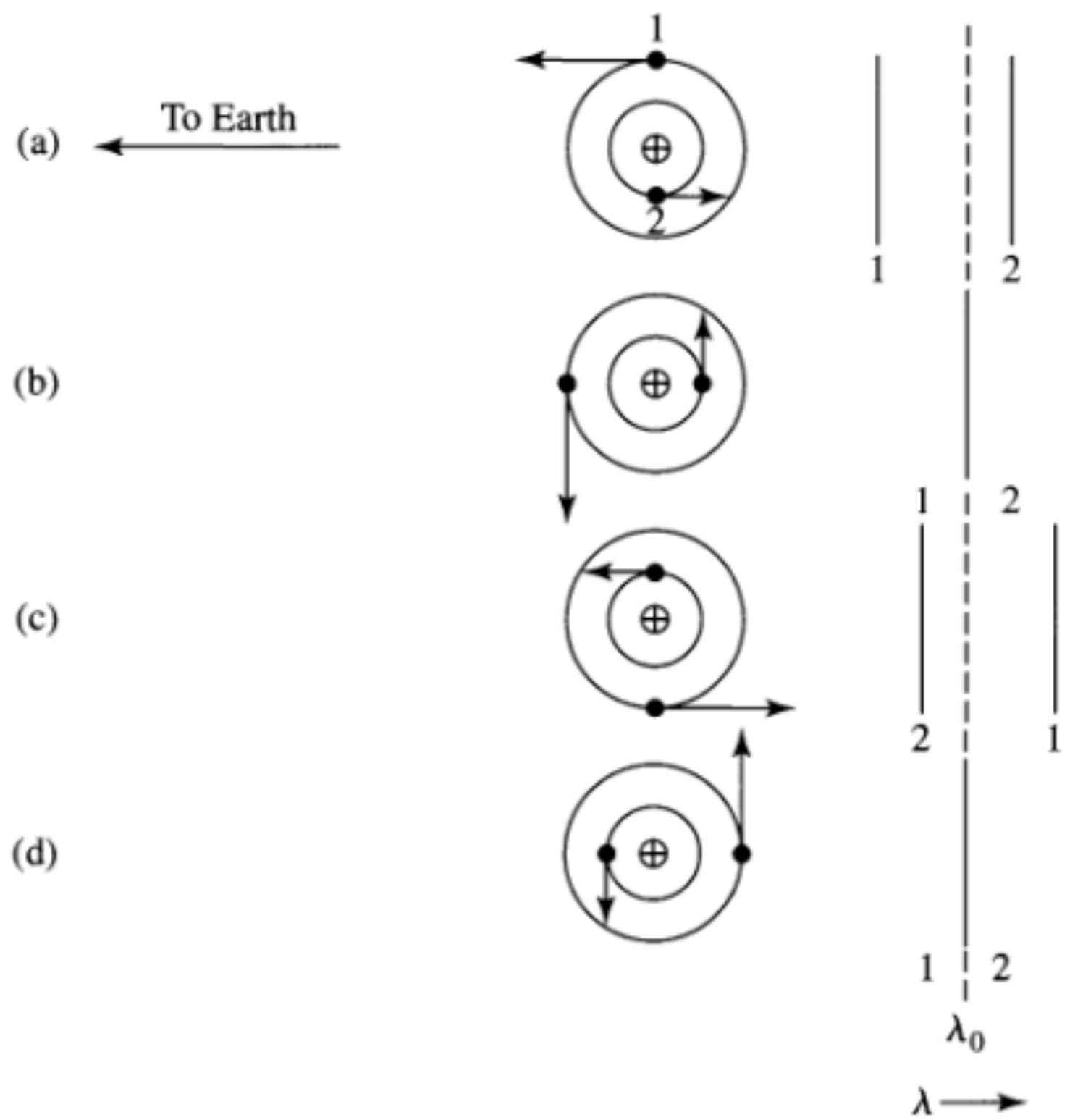


**FIGURE 7.3** The periodic shift in spectral features of a double-line spectroscopic binary. The relative wavelengths of the spectra of Stars 1 and 2 are shown at four different phases during the orbit: (a) Star 1 is moving toward the observer while Star 2 is moving away. (b) Both stars have velocities perpendicular to the line of sight. (c) Star 1 is receding from the observer while Star 2 is approaching. (d) Again both stars have velocities perpendicular to the line of sight.  $\lambda_0$  represents the wavelength of the observed line Doppler-shifted by the velocity of the center of mass of the system.

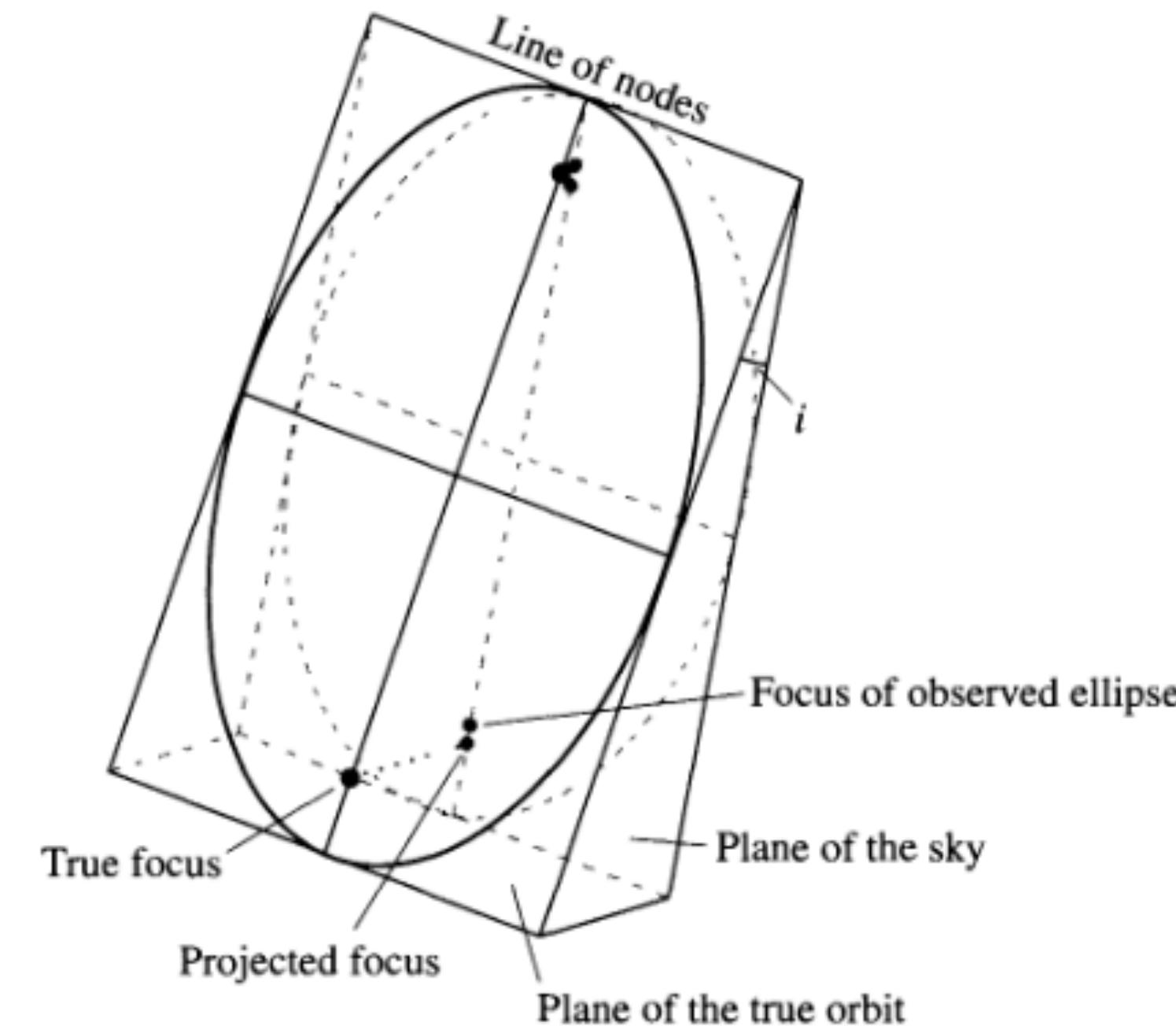
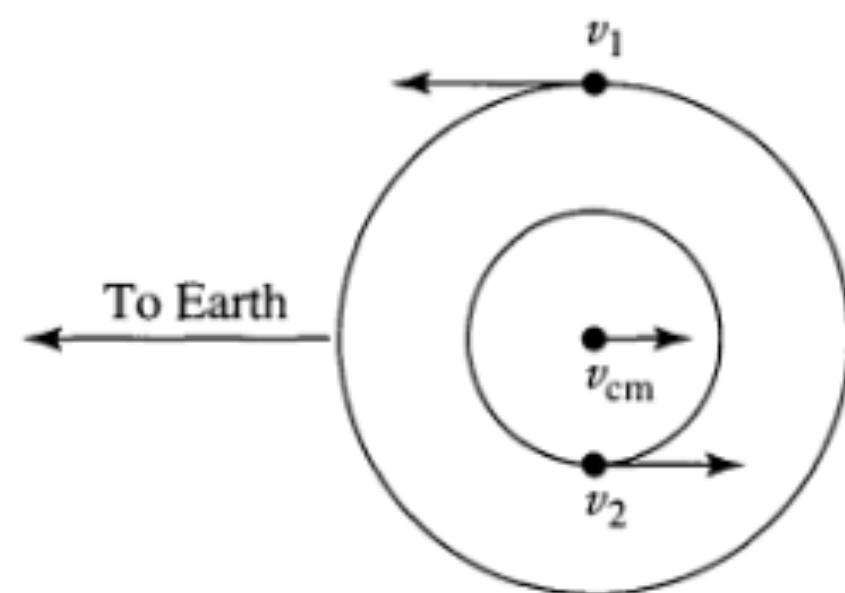


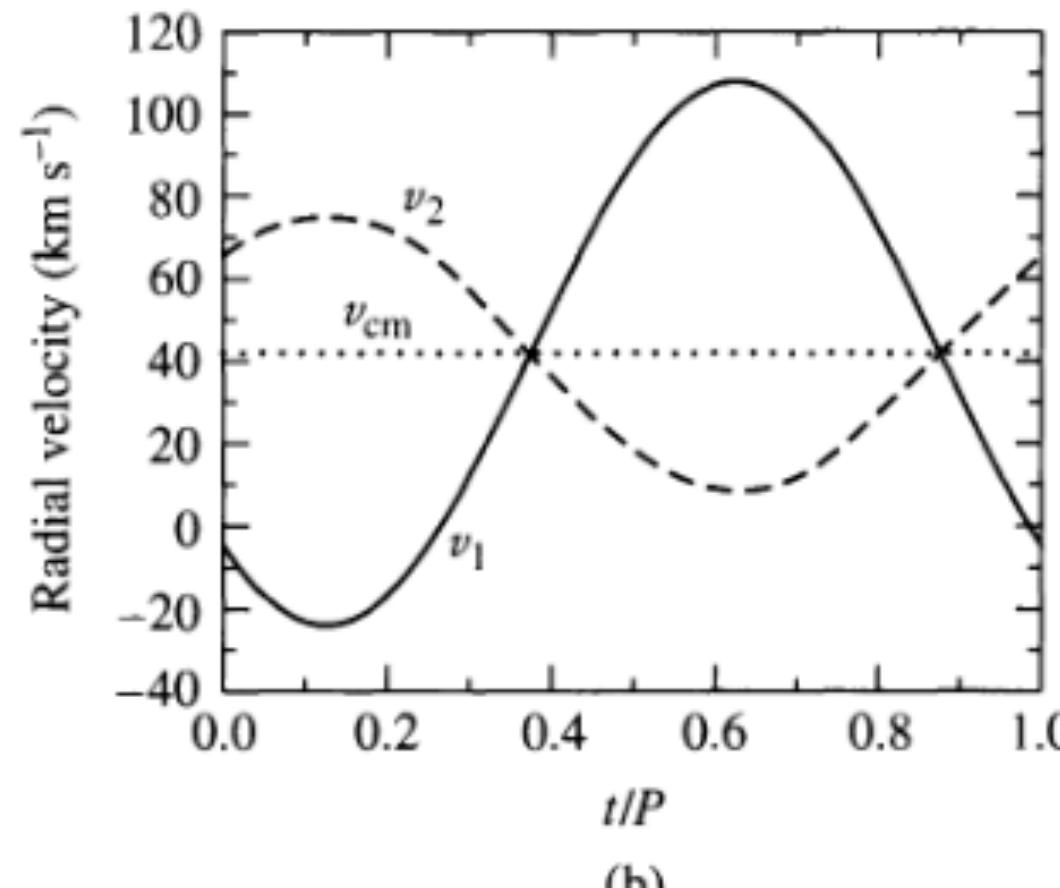
**FIGURE 7.4** An elliptical orbit projected onto the plane of the sky produces an observable elliptical orbit. The foci of the original ellipse do not project onto the foci of the observed ellipse, however.

# Carrol Chapter 7 (Paper 1)

## Binary Systems and stellar parameters

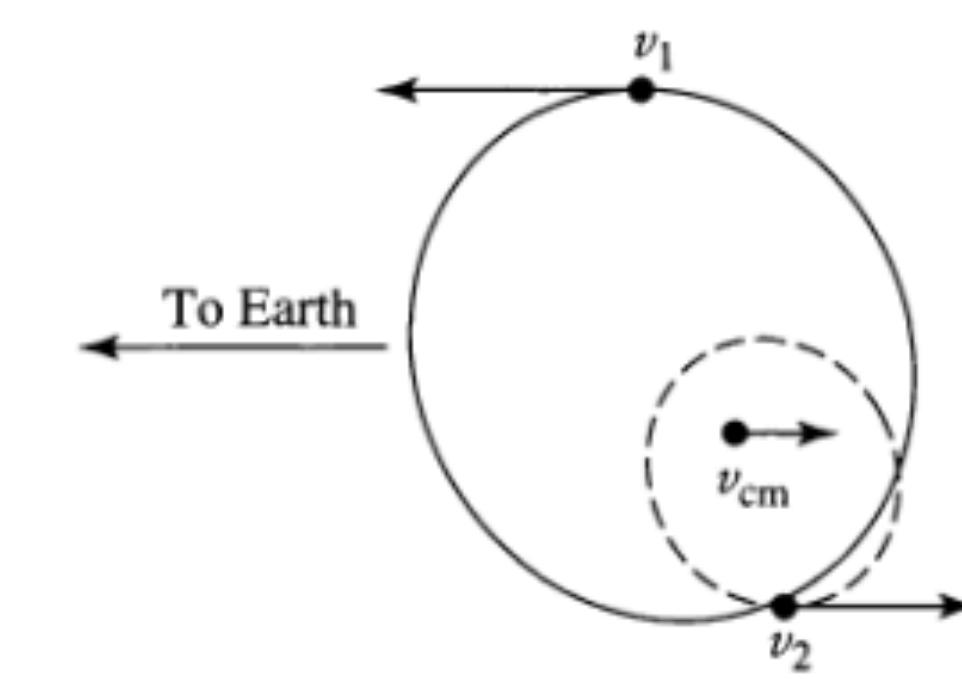


(a)

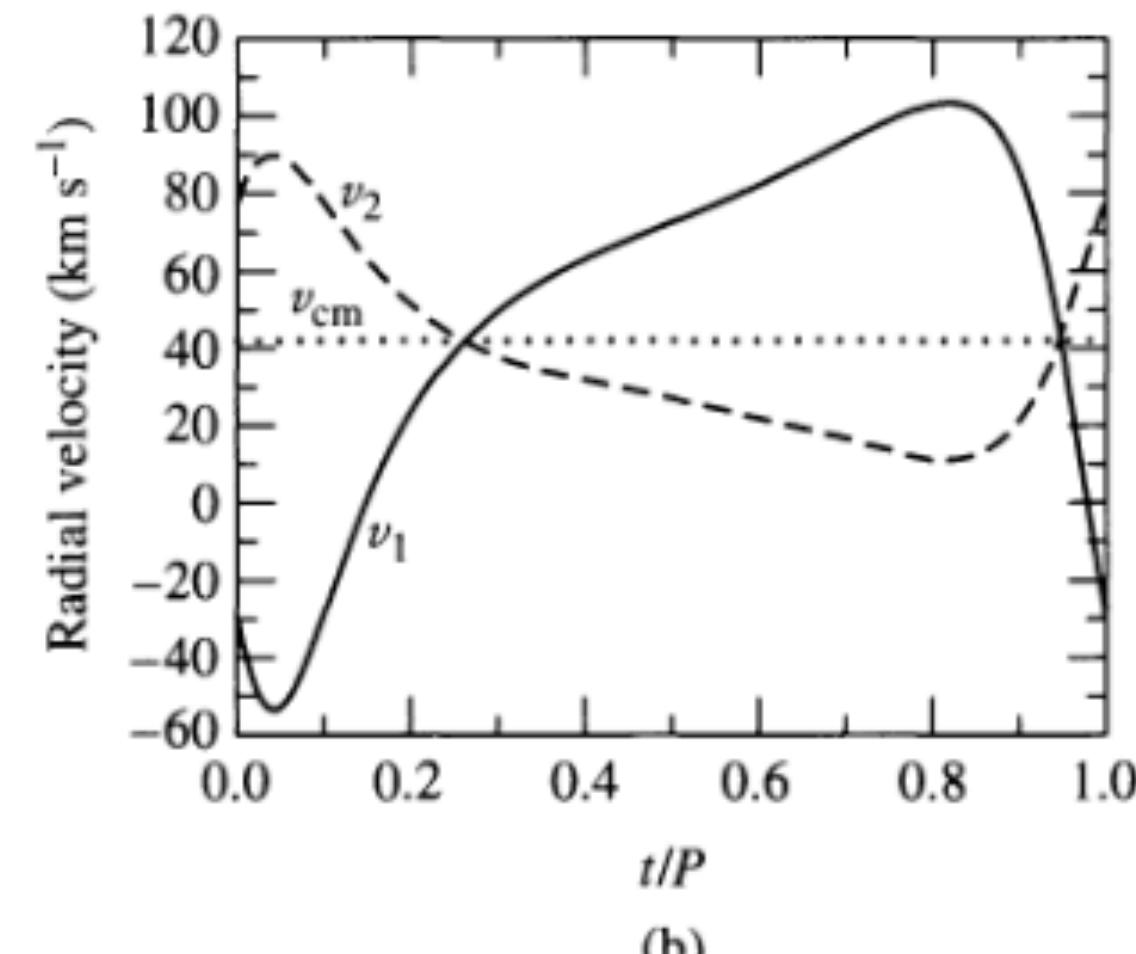


(b)

**FIGURE 7.5** The orbital paths and radial velocities of two stars in circular orbits ( $e = 0$ ). In this example,  $M_1 = 1 M_{\odot}$ ,  $M_2 = 2 M_{\odot}$ , the orbital period is  $P = 30$  d, and the radial velocity of the center of mass is  $v_{\text{cm}} = 42 \text{ km s}^{-1}$ .  $v_1$ ,  $v_2$ , and  $v_{\text{cm}}$  are the velocities of Star 1, Star 2, and the center of mass, respectively. (a) The plane of the circular orbits lies along the line of sight of the observer. (b) The observed radial velocity curves.



(a)



(b)

**FIGURE 7.6** The orbital paths and radial velocities of two stars in elliptical orbits ( $e = 0.4$ ). As in Fig. 7.5,  $M_1 = 1 M_{\odot}$ ,  $M_2 = 2 M_{\odot}$ , the orbital period is  $P = 30$  d, and the radial velocity of the center of mass is  $v_{\text{cm}} = 42 \text{ km s}^{-1}$ . In addition, the orientation of periastron is  $45^\circ$ .  $v_1$ ,  $v_2$ , and  $v_{\text{cm}}$  are the velocities of Star 1, Star 2, and the center of mass, respectively. (a) The plane of the orbits lies along the line of sight of the observer. (b) The observed radial velocity curves.

# Carroll Chapter 7 (Paper 1) Binary Systems and stellar parameters

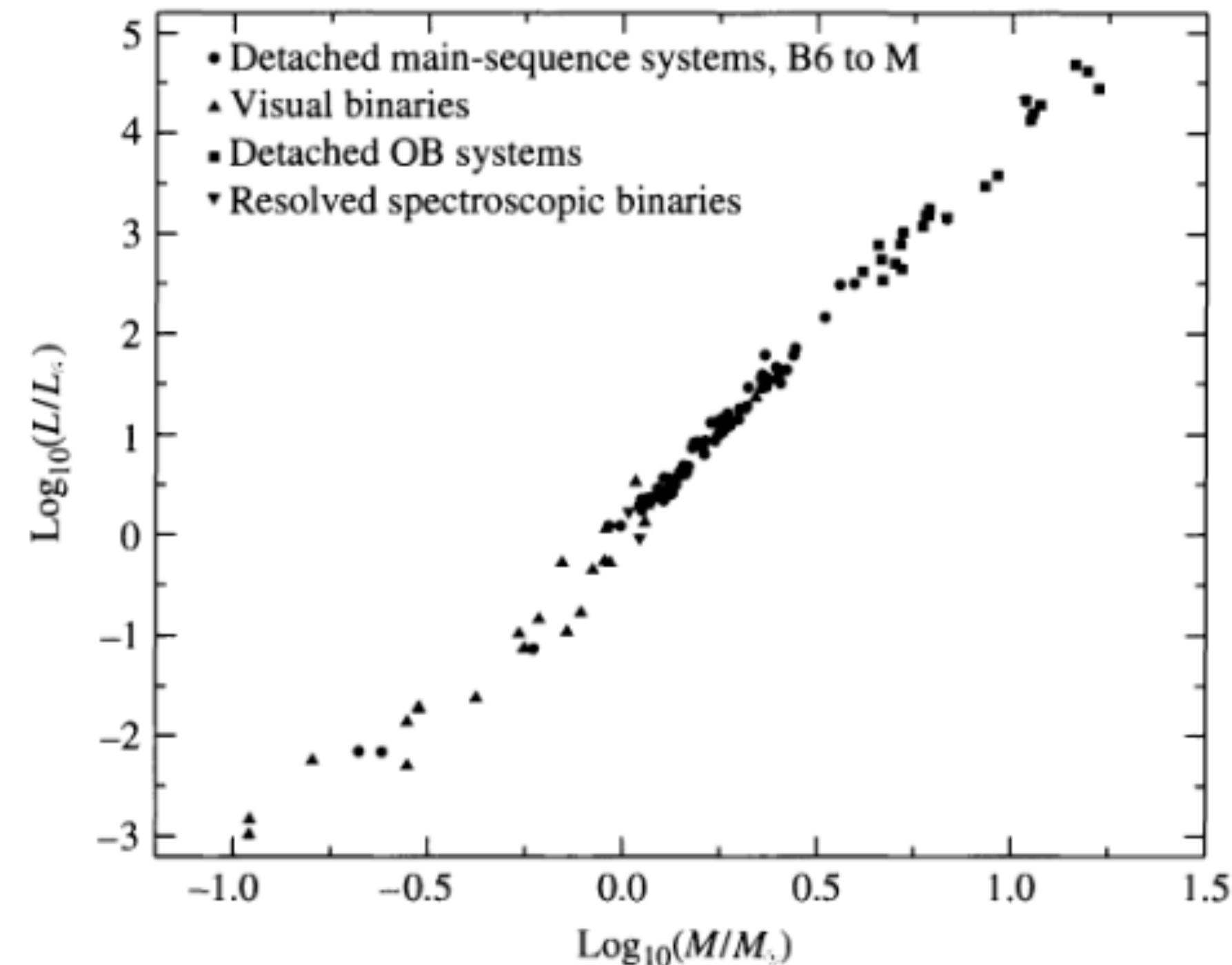


**FIGURE 7.7** The mass–luminosity relation. (Data from Popper, *Annu. Rev. Astron. Astrophys.*, 18, 115, 1980.)

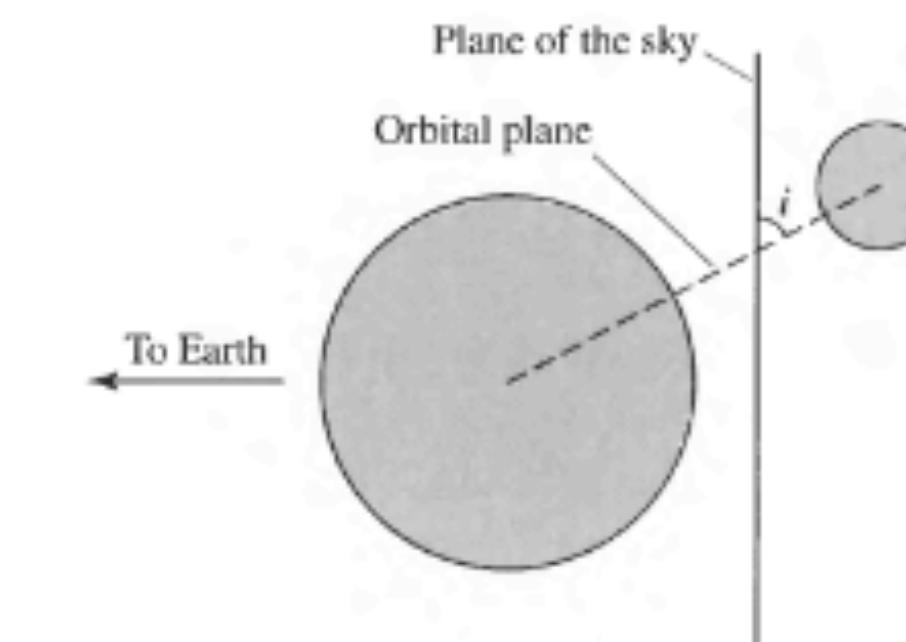


**FIGURE 7.8** The geometry of an eclipsing, spectroscopic binary requires that the angle of inclination  $i$  be close to  $90^\circ$ .

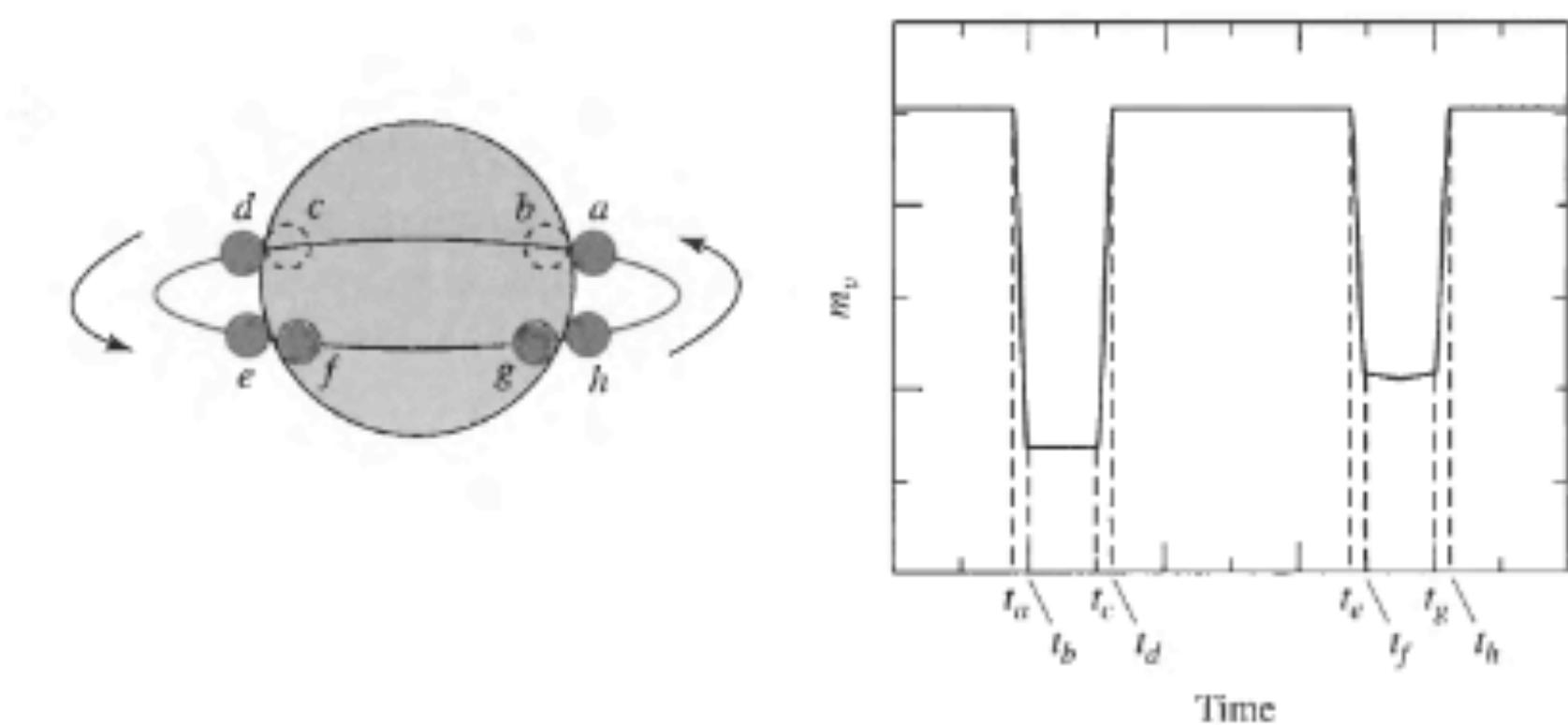


**FIGURE 7.9** The light curve of an eclipsing binary for which  $i = 90^\circ$ . The times indicated on the light curve correspond to the positions of the smaller star relative to its larger companion. It is assumed in this example that the smaller star is hotter than the larger one.

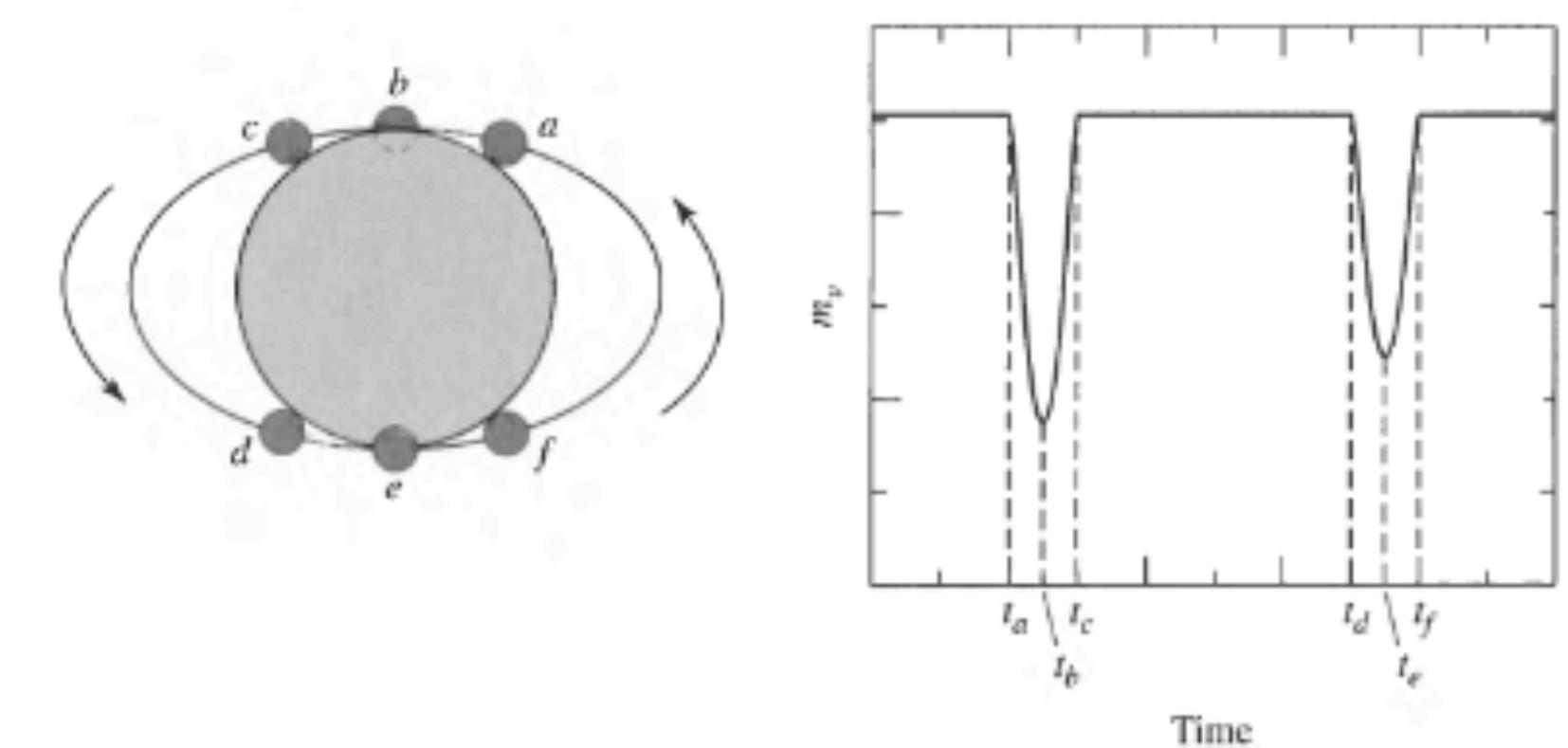


**FIGURE 7.10** The light curve of a partially eclipsing binary. It is assumed in this example that the smaller star is hotter than its companion.

# Carrol Chapter 7 (Paper 1) Binary Systems and stellar parameters

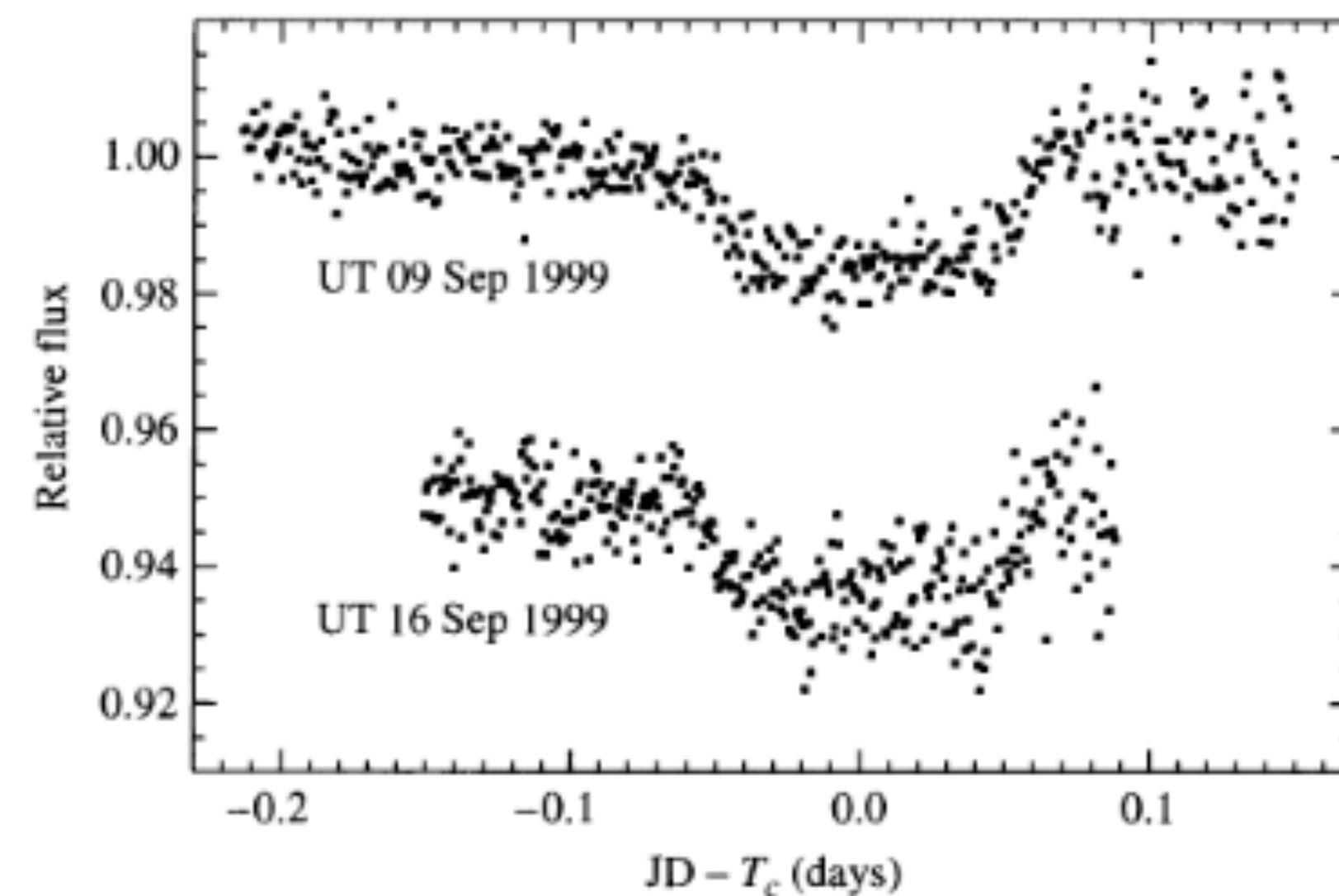


**FIGURE 7.12** The photometric detection of two transits of an extrasolar planet across the disk of HD 2094589 in September 1999. The September 16 transit was artificially offset by  $-0.05$  relative to the transit of September 9 in order to avoid overlap of the data.  $T_c$  designates the midpoint of the transit, and JD represents the Julian Date (time) of the particular measurement. (Figure adapted from Charbonneau, Brown, Latham, and Mayor, *Ap. J.*, 529, L45, 2000.)

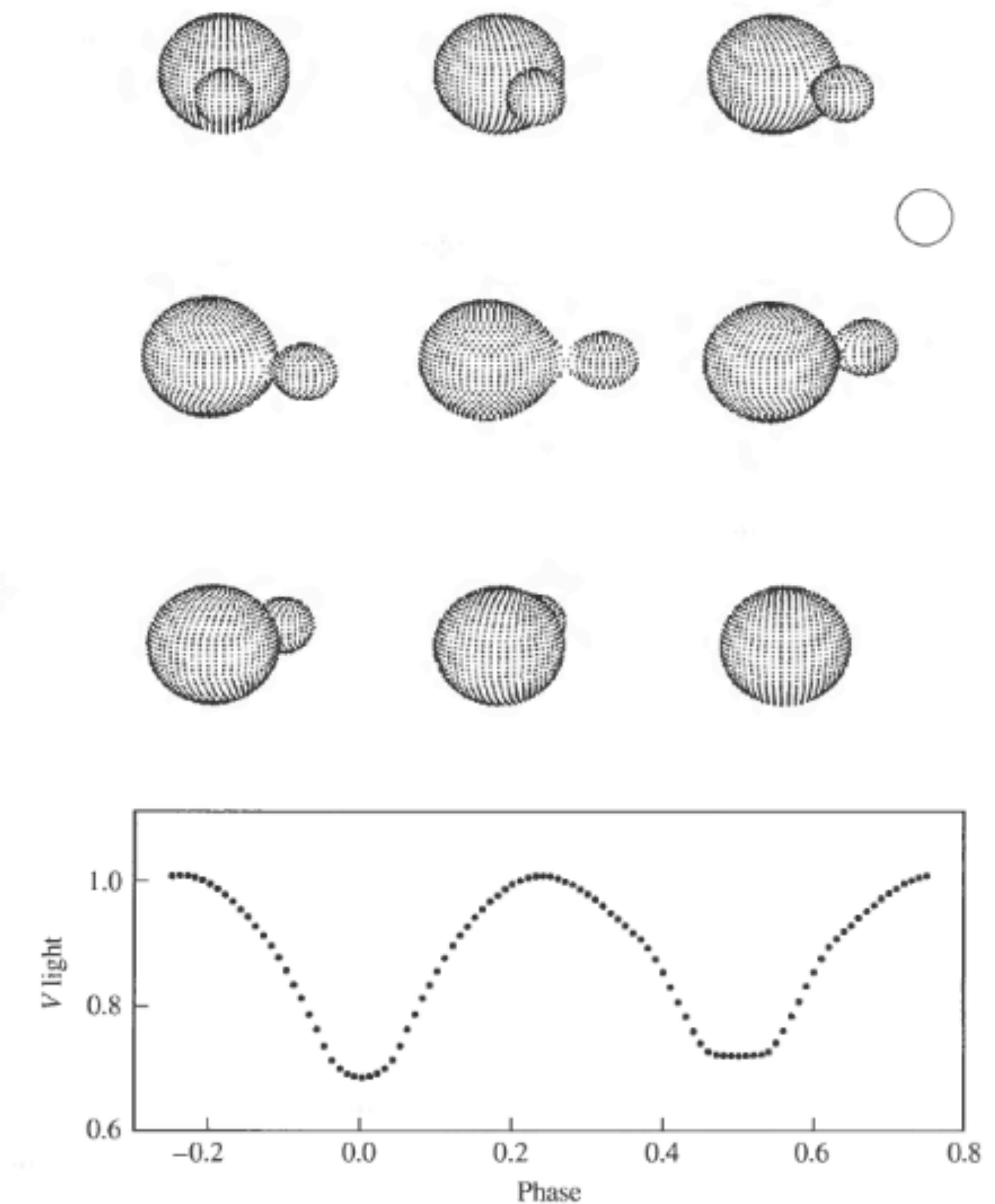


**FIGURE 7.11** A synthetic light curve of RR Centauri, an eclipsing binary star system for which the two components are in close contact. The open circle represents the size of the Sun. The orbital and physical characteristics of the RR Cen system are  $P = 0.6057$  d,  $e = 0.0$ ,  $M_1 = 1.8 M_{\odot}$ ,  $M_2 = 0.37 M_{\odot}$ . The spectral classification of the primary is F0V (see Section 8.1 for a discussion of stellar spectral classifications). (Figure adapted from R. E. Wilson, *Publ. Astron. Soc. Pac.*, 106, 921, 1994; ©Astronomical Society of the Pacific.)

# Eclipsing binaries in the All Sky survey catalogue (Paper 2)

# Eclipsing binaries in the All Sky survey catalogue (Paper 2)

B. Paczyński et. al. 2006

- All Sky Automated Survey (ASAS)
- EC: Eclipsing Contact Binary
- ED: Eclipsing detached Binary
- ESD: Eclipsing semidetached Binary
- W UMa-type binary: stars with both Roche lobes filled (common envelope)

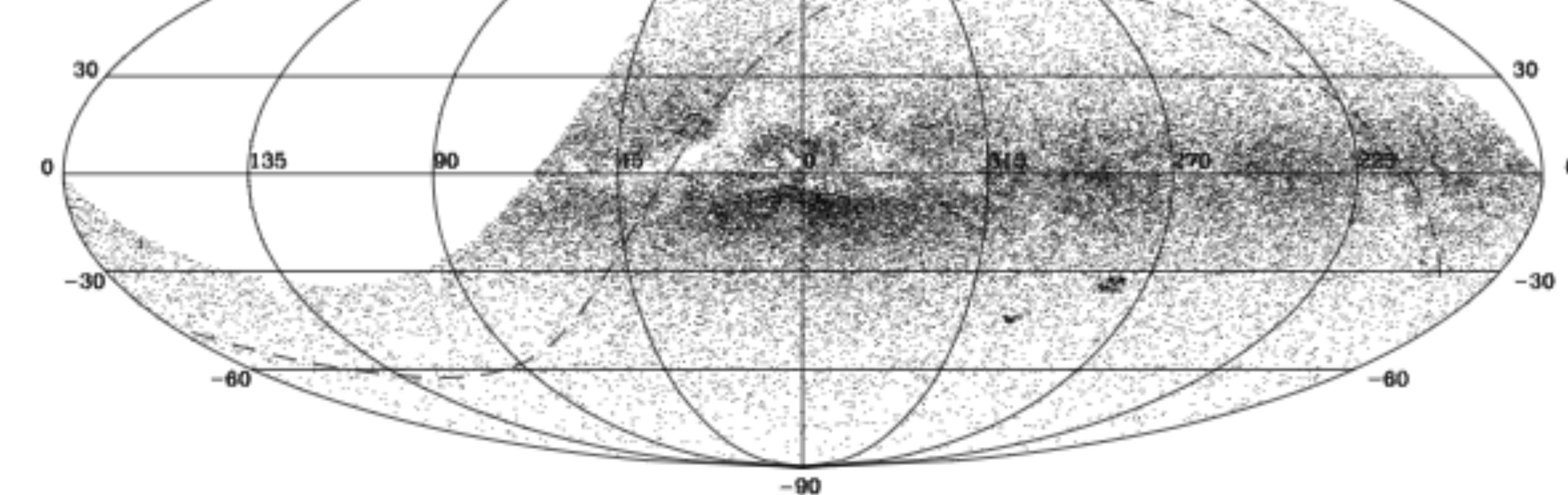


Figure 1. The distribution of the 50 099 ASAS variables in the sky in the Galactic coordinates. The Milky Way is clearly seen, as well as the patches of interstellar extinction. The celestial equator is shown with a dashed line. The distribution is limited to declination  $< +28^\circ$ .

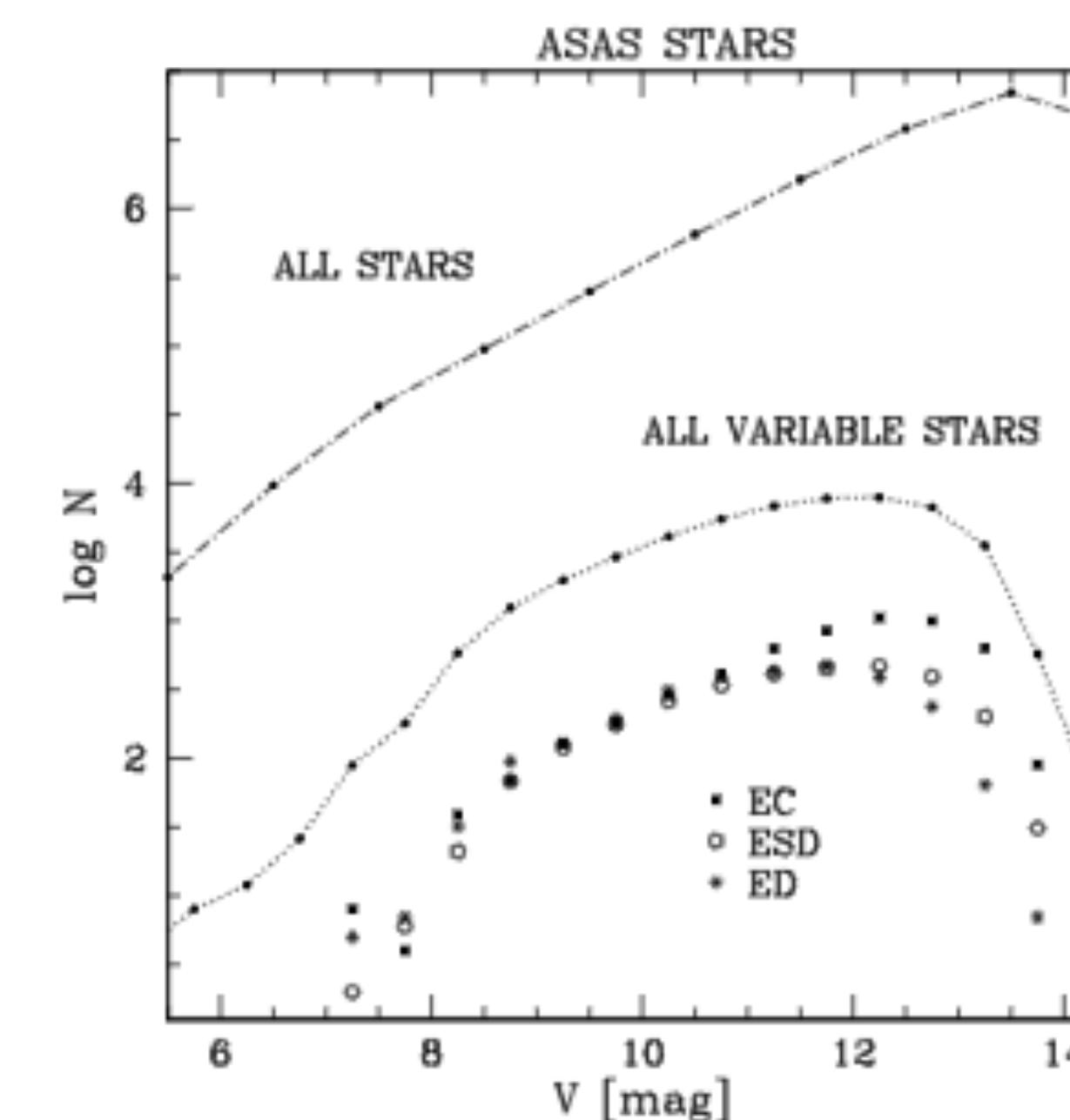


Figure 2. The distribution of the ASAS stars as a function of V-band magnitude. The total number of stars is about 17 000 000. The total number of variable stars is 50 099. The total number of eclipsing binaries is 5384 for contact systems (EC), 2949 for semi-detached systems (ESD), and 2743 for detached systems (ED). Note, that the efficiency of discovering variable stars declines for  $V > 12$ , because the detection limit is approached, and for  $V < 8$ , because of saturation effects.

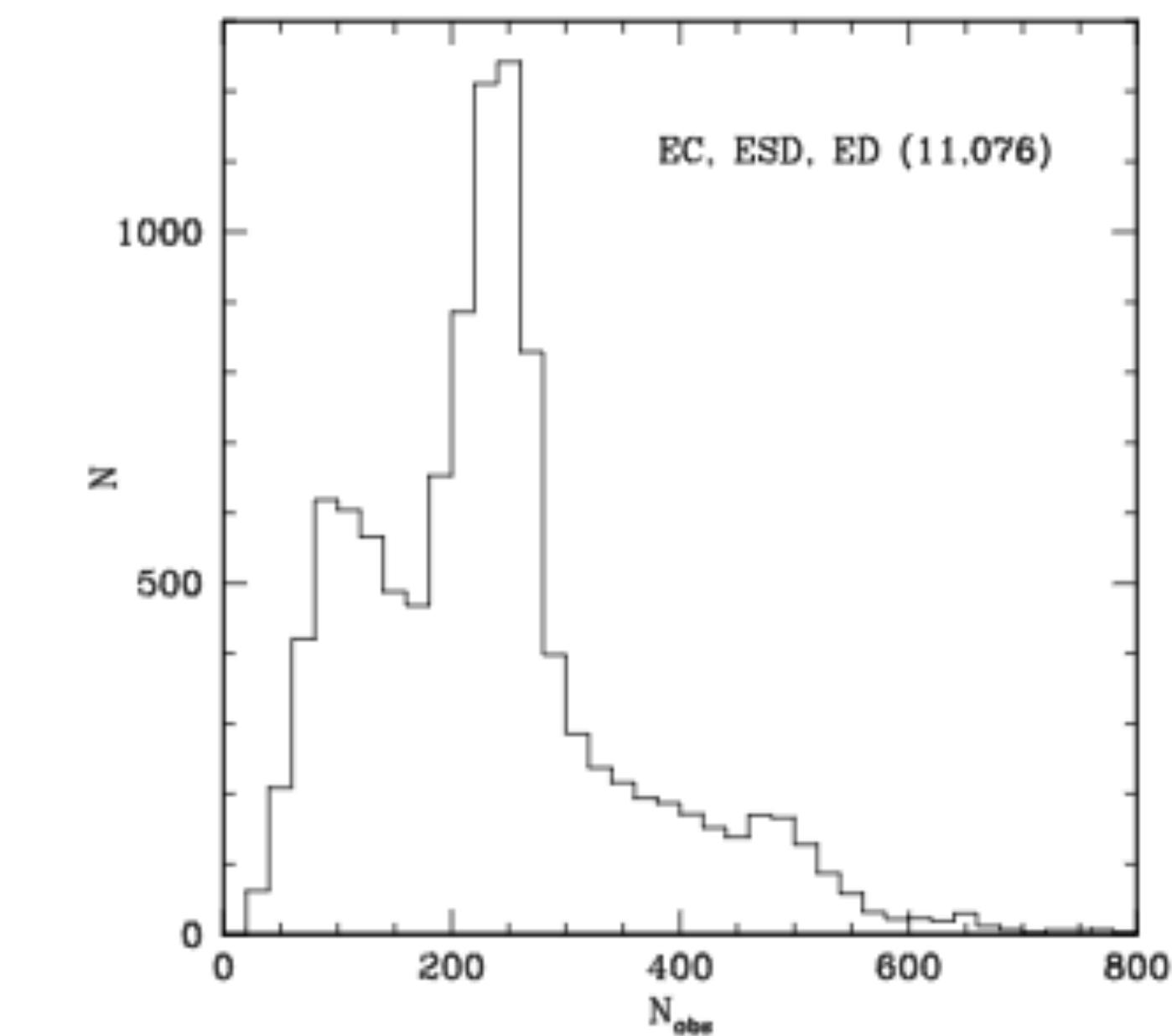


Figure 3. The histogram of the number of photometric measurements obtained during 5 yr of the ASAS life. A small subset of data extends back to 8 yr.

# Eclipsing binaries in the All Sky survey catalogue (Paper 2)

B. Paczyński et. al. 2006

- A2-A4 plane: is a plane of Fourier parameters that are able to tell information about the shape of the curve

(simetry of curves and flatness of the wings around the major peak)

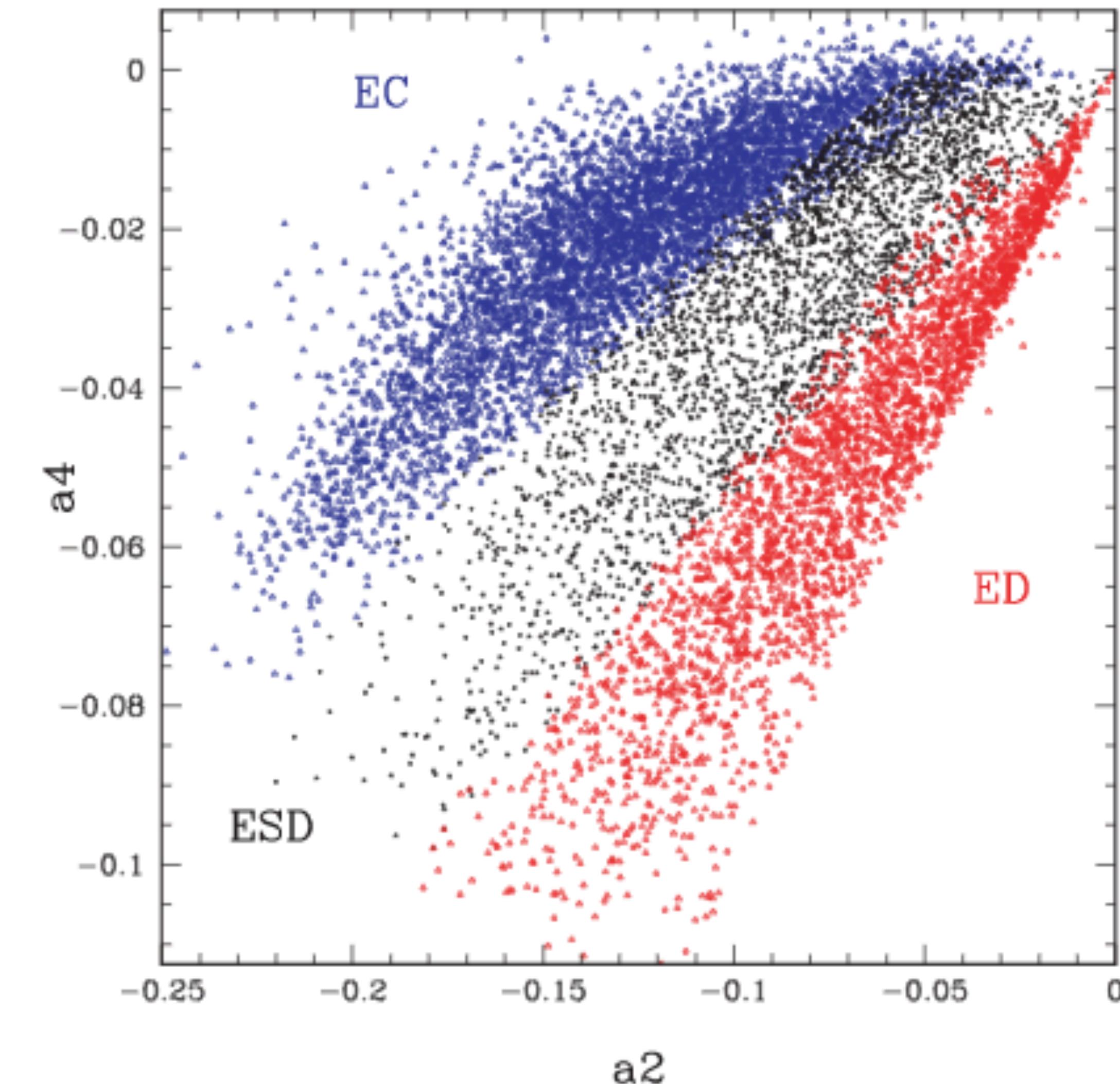


**Figure 4.** Classification of eclipsing binaries in the Fourier coefficients plane  $a_2 - a_4$ . The three symbols refer to contact (EC), semi-detached (ESD), and detached (ED) binaries, following Pojmański (2002). Note: when the amplitude of variability is very small, the classification is very uncertain, as in the upper right-hand corner.

# Eclipsing binaries in the All Sky survey catalogue(Paper 2)

B. Paczyński et. al. 2006

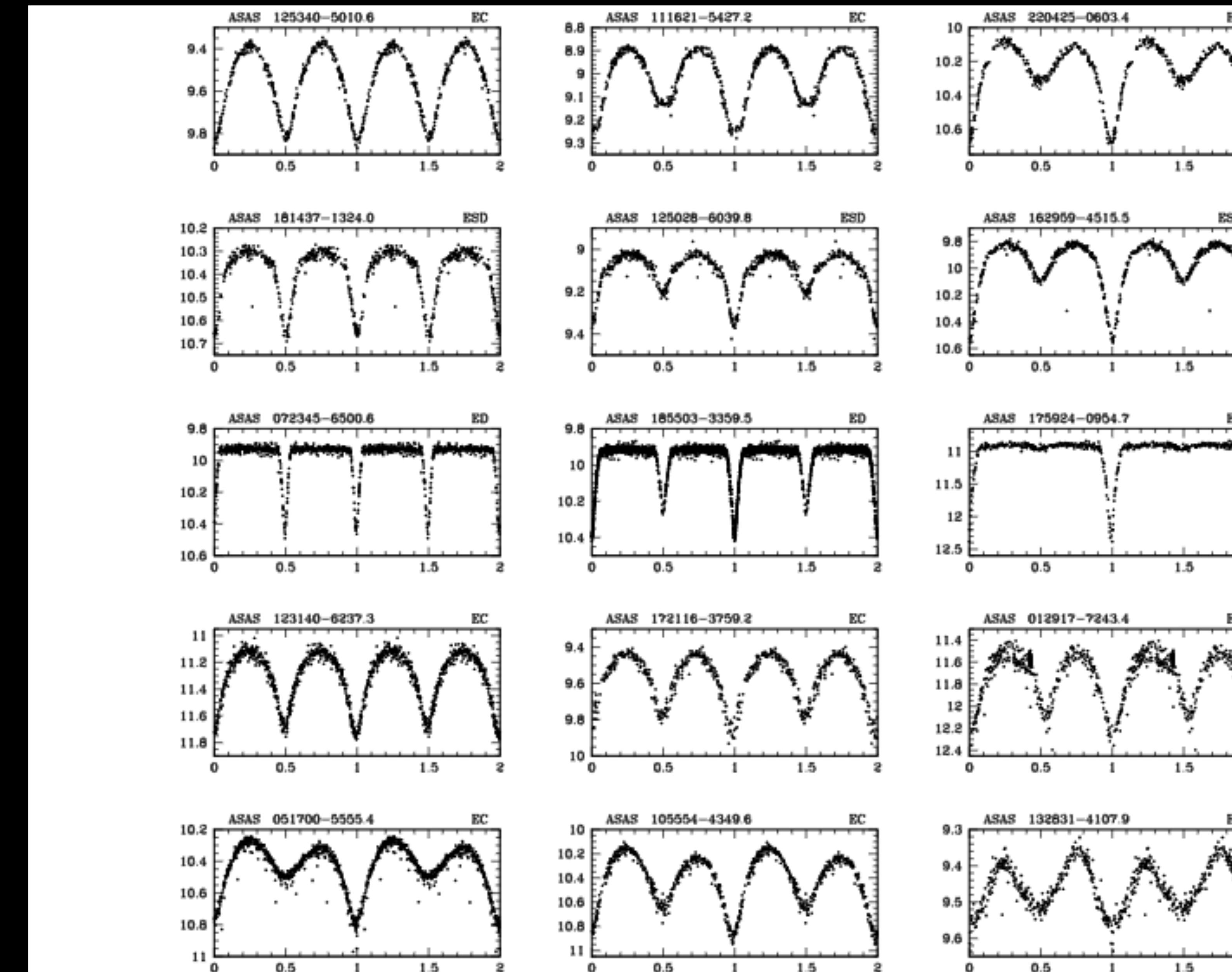


**Figure 5.** Examples of light curves of nine contact (EC), three semi-detached (ESD) and three detached binaries (ED) are shown. All these are the ASAS discoveries, even though all of them are very bright. Note, a distinct difference in the light curve shapes between contact and semi-detached binaries. The first three rows are sorted by minimum depth difference, the fourth row presents contact binaries with long and exceptionally long periods, and the fifth with the distinct maximum height difference. See Table 1 for details.

# Eclipsing binaries in the All Sky Survey catalogue(Paper 2)

B. Paczyński et. al. 2006

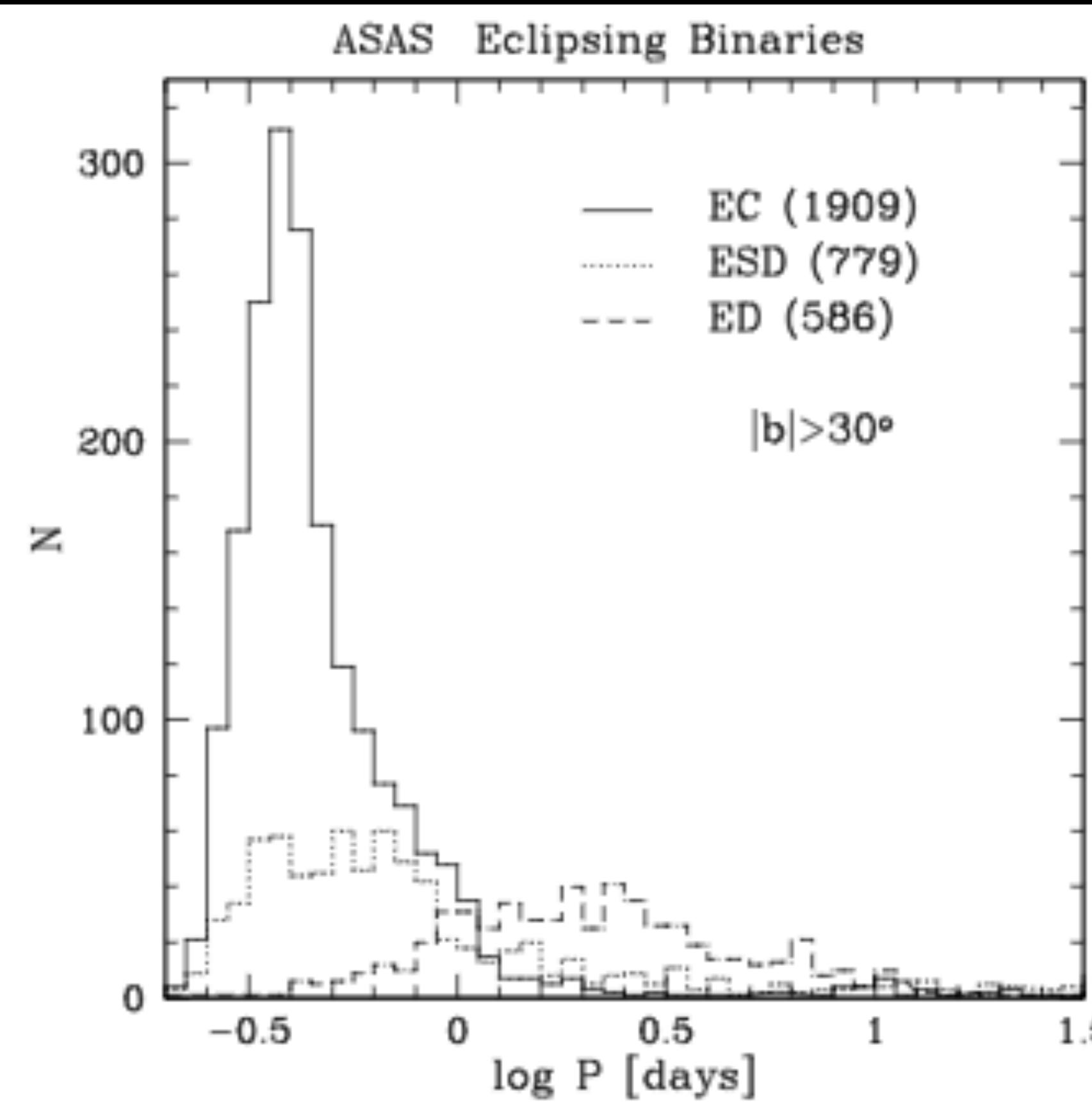


**Figure 6.** The distribution of periods of the ASAS contact binaries (EC) at high Galactic latitude  $|b| > 30^\circ$  is plotted. The distribution peaks near 0.37 d, it has a sharp cut-off at 0.2 d, and a tail extending far beyond 1 d. Also shown is the distribution of orbital periods of semi-detached (ESD) and detached (ED) binaries. Contact binaries outnumber other binaries for binary periods shorter than 1 d.

$$D_p = -2[1.2a_2 - 2a_2^2 + (a_1 + a_3)] \quad (\text{mag}), \quad (1)$$

$$D_s = -2[1.2a_2 - 2a_2^2 - (a_1 + a_3)] \quad (\text{mag}), \quad (2)$$

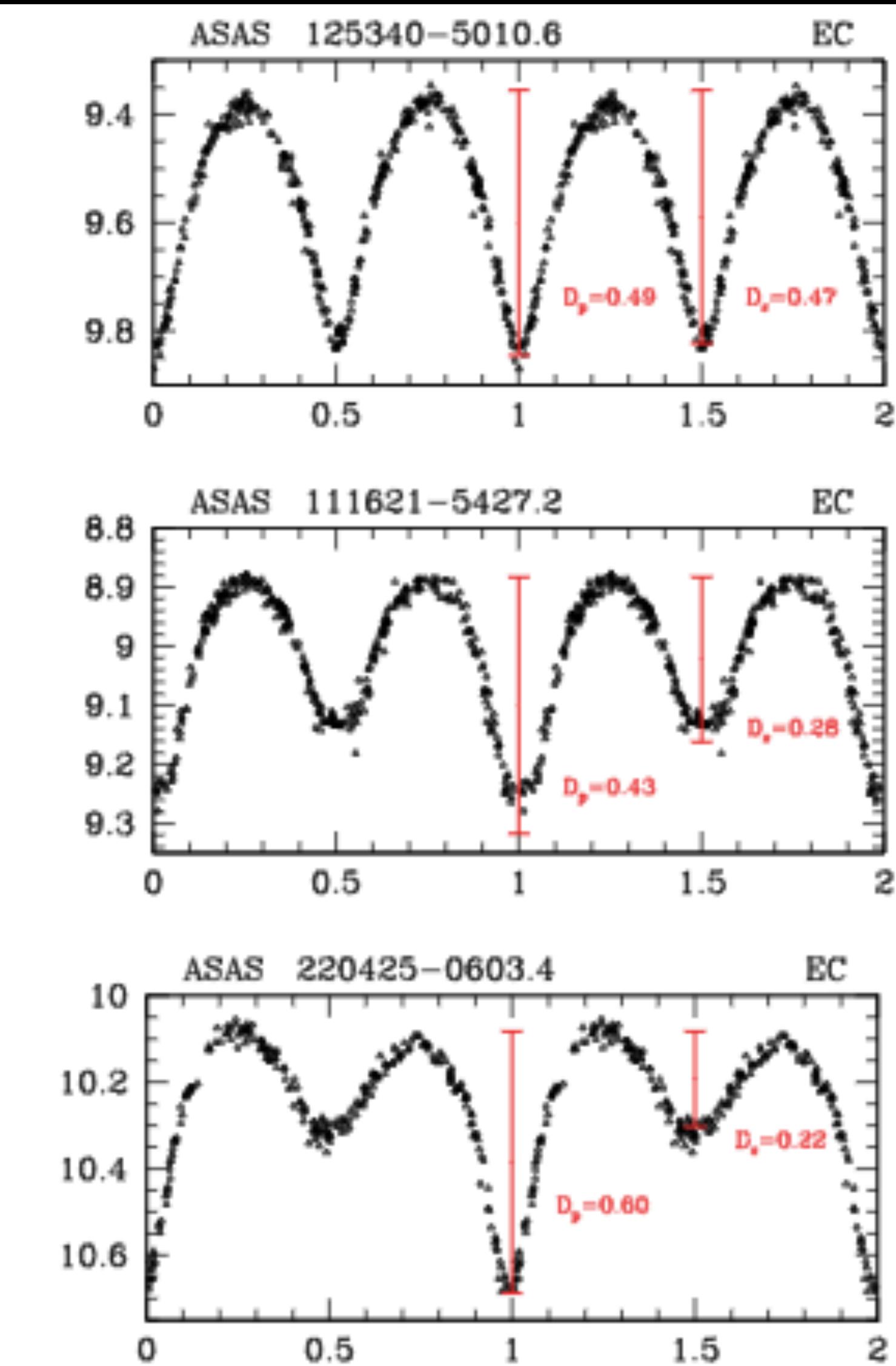


**Figure 7.** The first row of EC stars from Fig. 5 is shown. Vertical lines represent depth of a primary ( $D_p$ ) and a secondary ( $D_s$ ) eclipse calculated with equations (1) and (2), respectively. Flat bottom eclipses may result in a significant error, which is somewhat reduced in the  $D_s/D_p$  ratio.

# Eclipsing binaries in the All Sky survey catalogue B. Paczyński et al. 2006 (Paper 2)

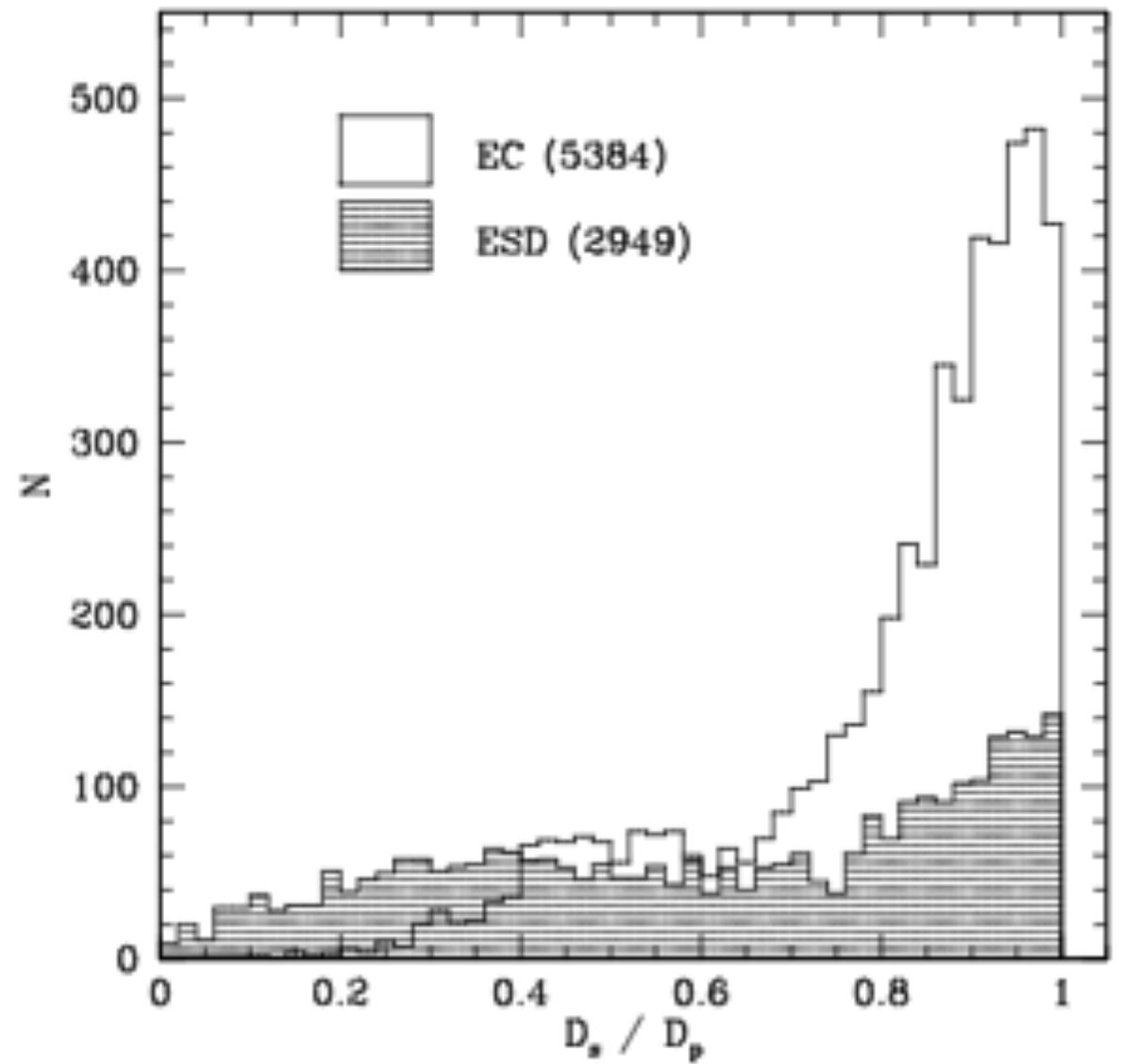


**Figure 9.** The ratio of the eclipse depths, integrated over binary periods, is shown for contact (EC) and semi-detached (ESD) systems. Stars in a thermal contact have the eclipse depth ratio close to 1. Note, the step in the histogram at  $D_s/D_p \approx 0.7$ . The same feature is also apparent in Fig. 8 at  $\log P \approx -0.4$ .

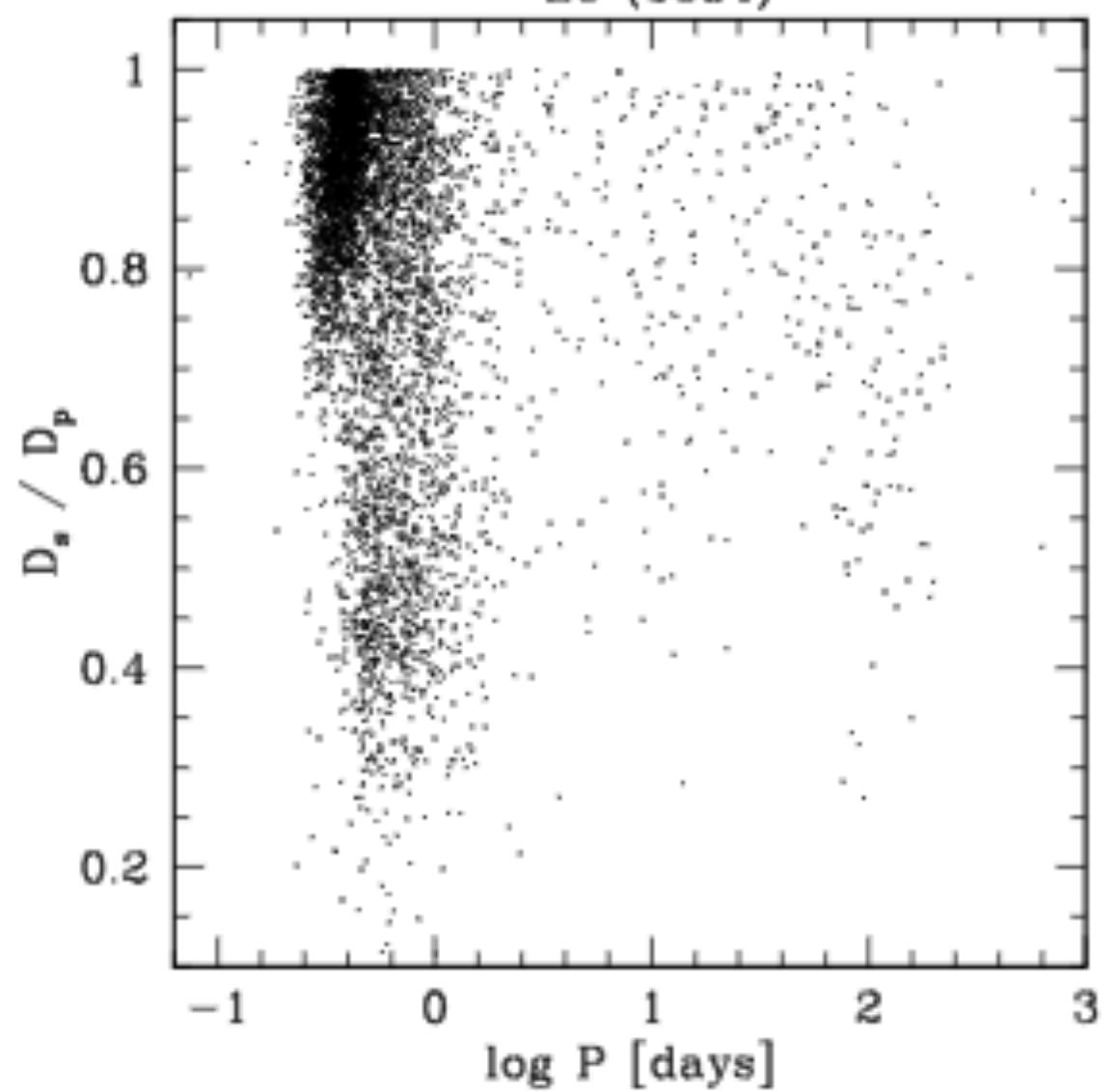


**Figure 8.** The ratio of eclipse depth is shown for contact binaries as a function of their period. Stars in thermal contact have the eclipse depth ratio close to 1.

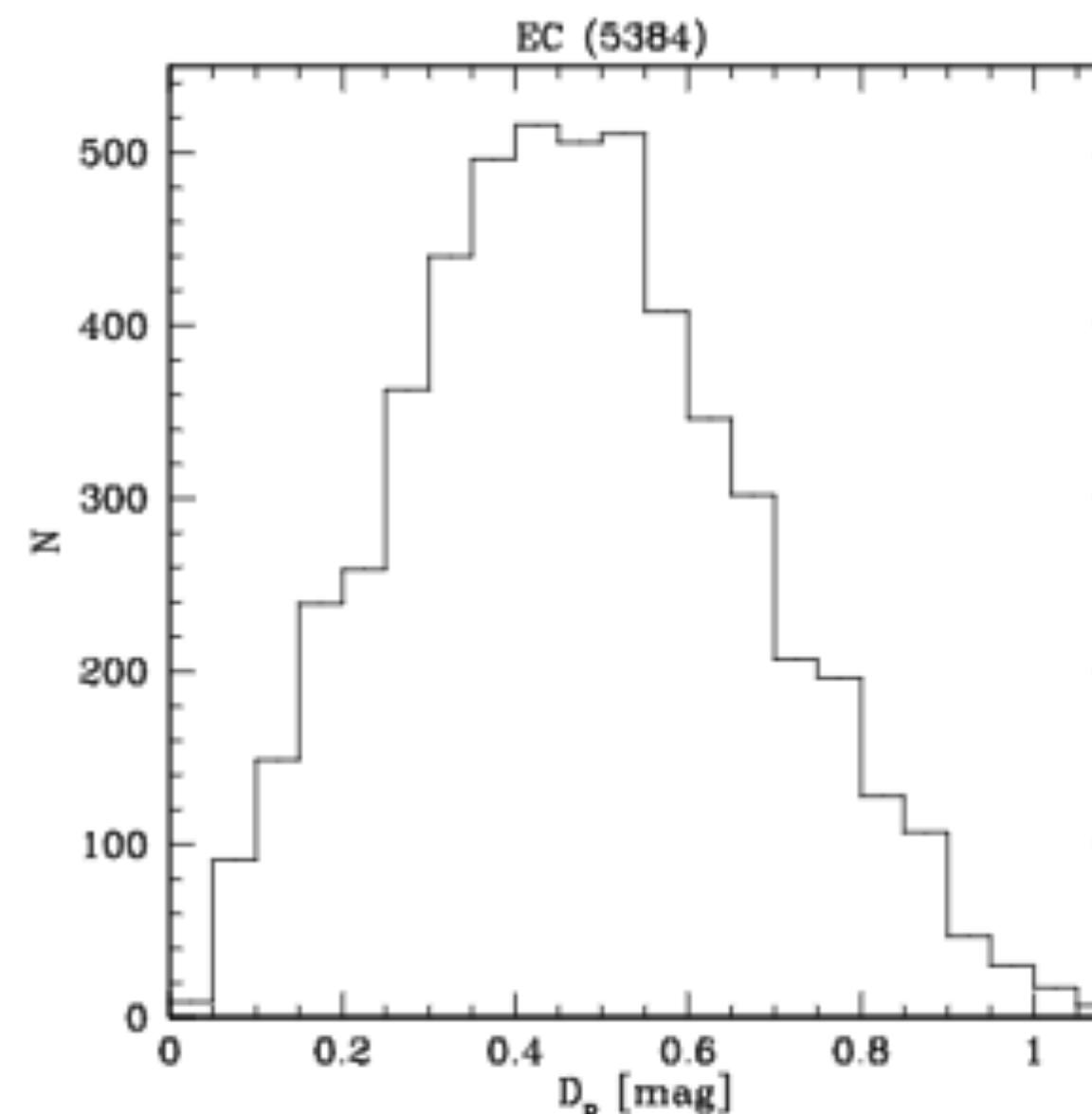


**Figure 11.** The distribution of the primary eclipse depth integrated over all periods.

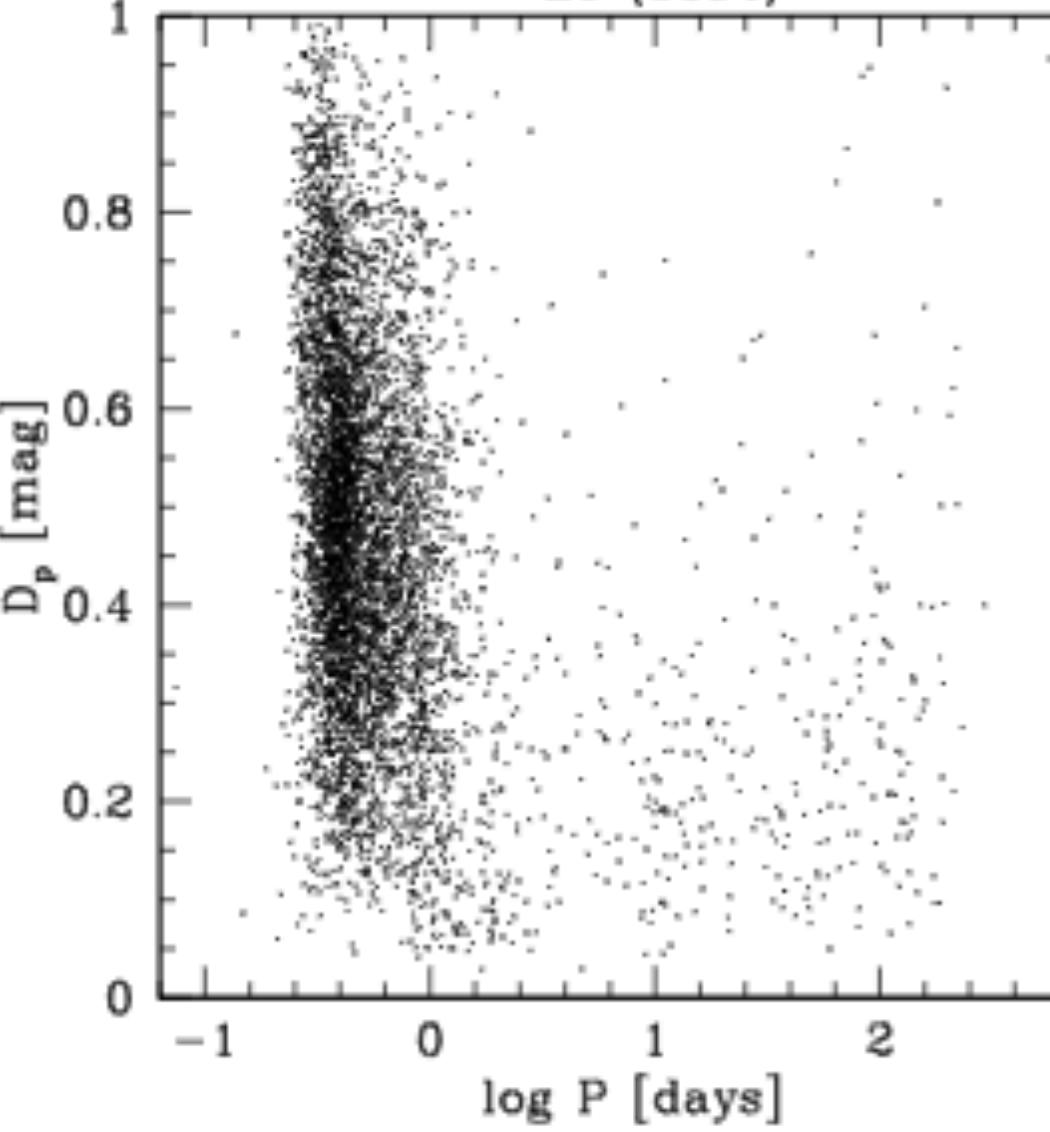


**Figure 10.** The distribution of the primary eclipse depth as a function of orbital period for contact binaries.  $D_p$  is the fraction of light obscured in the primary eclipse.

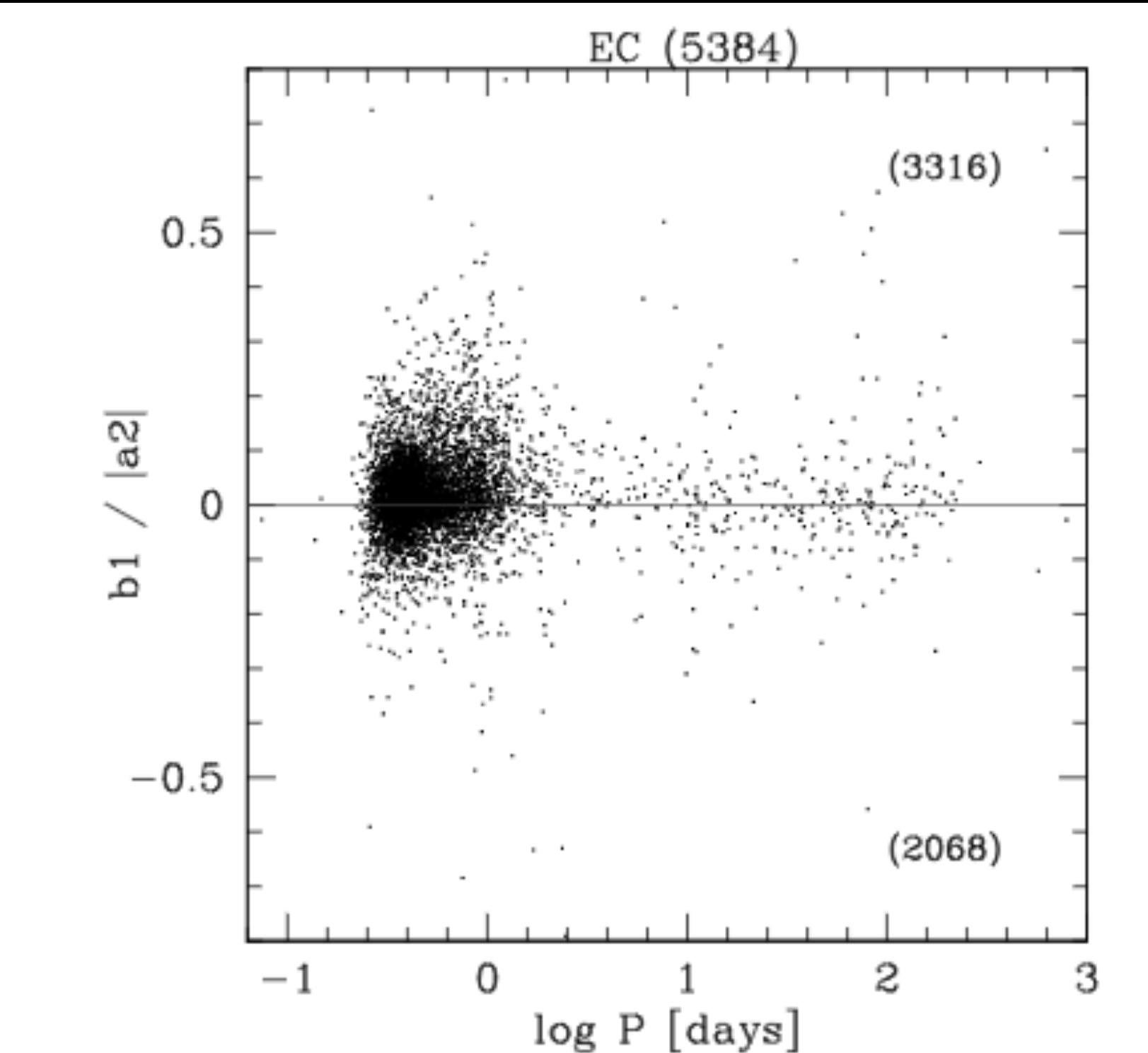


**Figure 12.** The distribution of light curve asymmetry of contact binaries is shown – this is known as the O'Connell (1951) effect. Most stars have their light maxima of approximately equal height, but there is an asymmetry in the distribution: the maxima that follow the primary minimum are on average higher than the maxima preceding the primary eclipse. The O'Connell effect is likely a consequence of the gas streams in these binaries.

O'Connell effect: The out-of-eclipse brightness maxima of some binary stars are unequally high.

# **Evolutionary Processes in Close Binary Systems(Paper 3)**

# Evolutionary Processes in Close Binary Systems(Paper 3)

B. Paczyński 1971

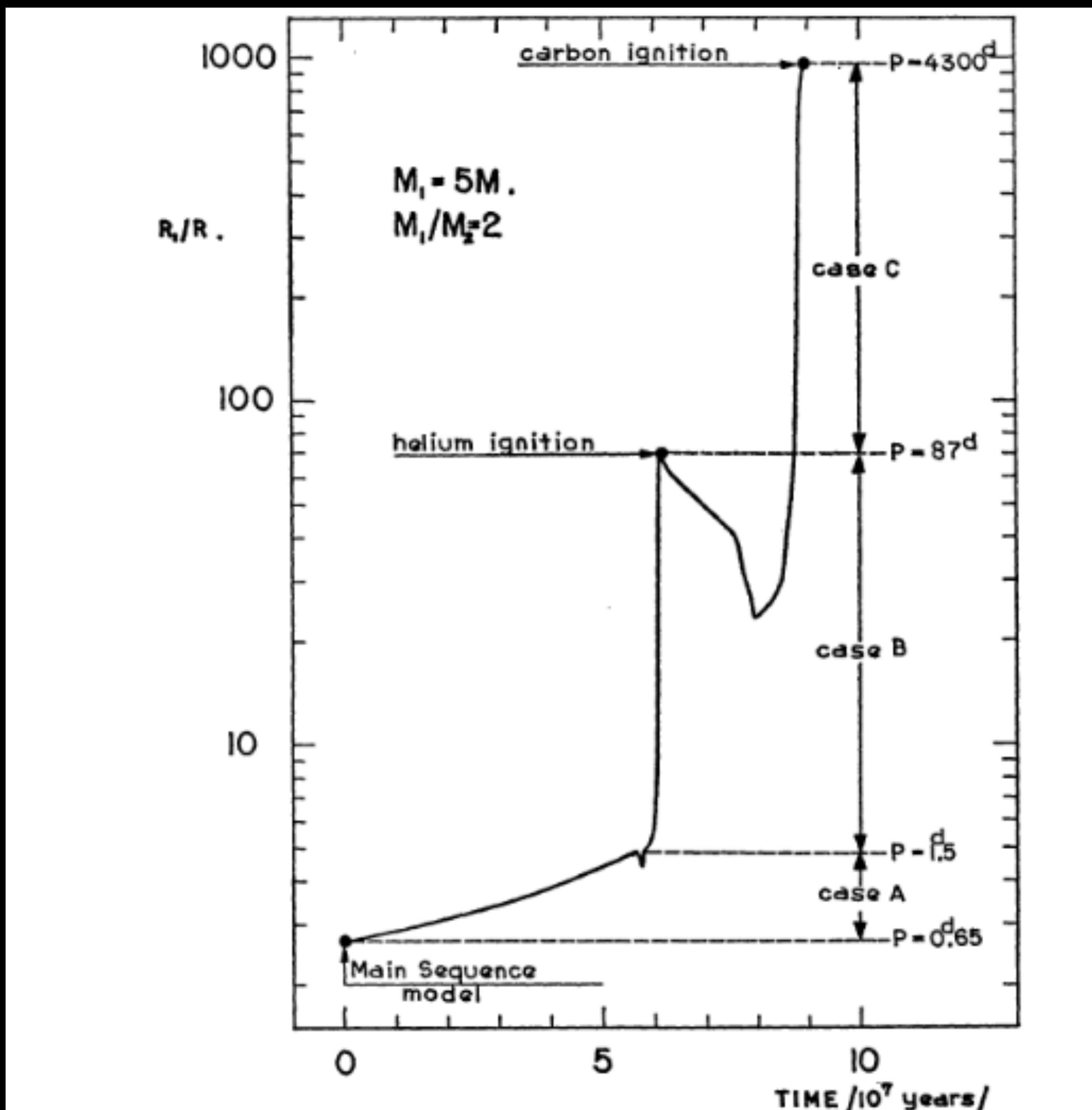


FIGURE 1. The time variation of the radius of a  $5 M_\odot$  star. The ranges of orbital periods corresponding to the evolution with mass exchange in cases A, B, and C are indicated. A mass ratio of  $M_1/M_2=2$  is adopted.

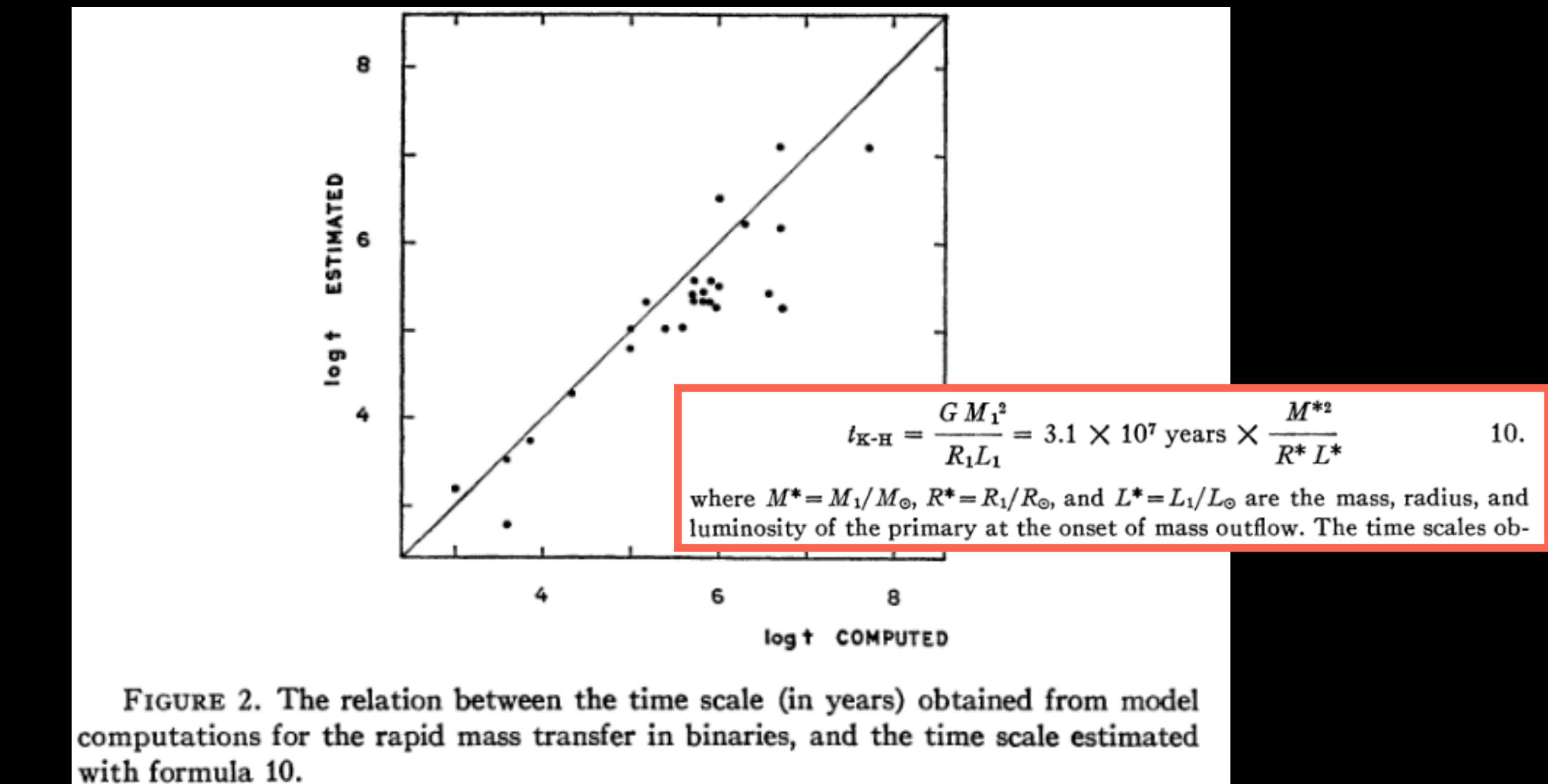


FIGURE 2. The relation between the time scale (in years) obtained from model computations for the rapid mass transfer in binaries, and the time scale estimated with formula 10.

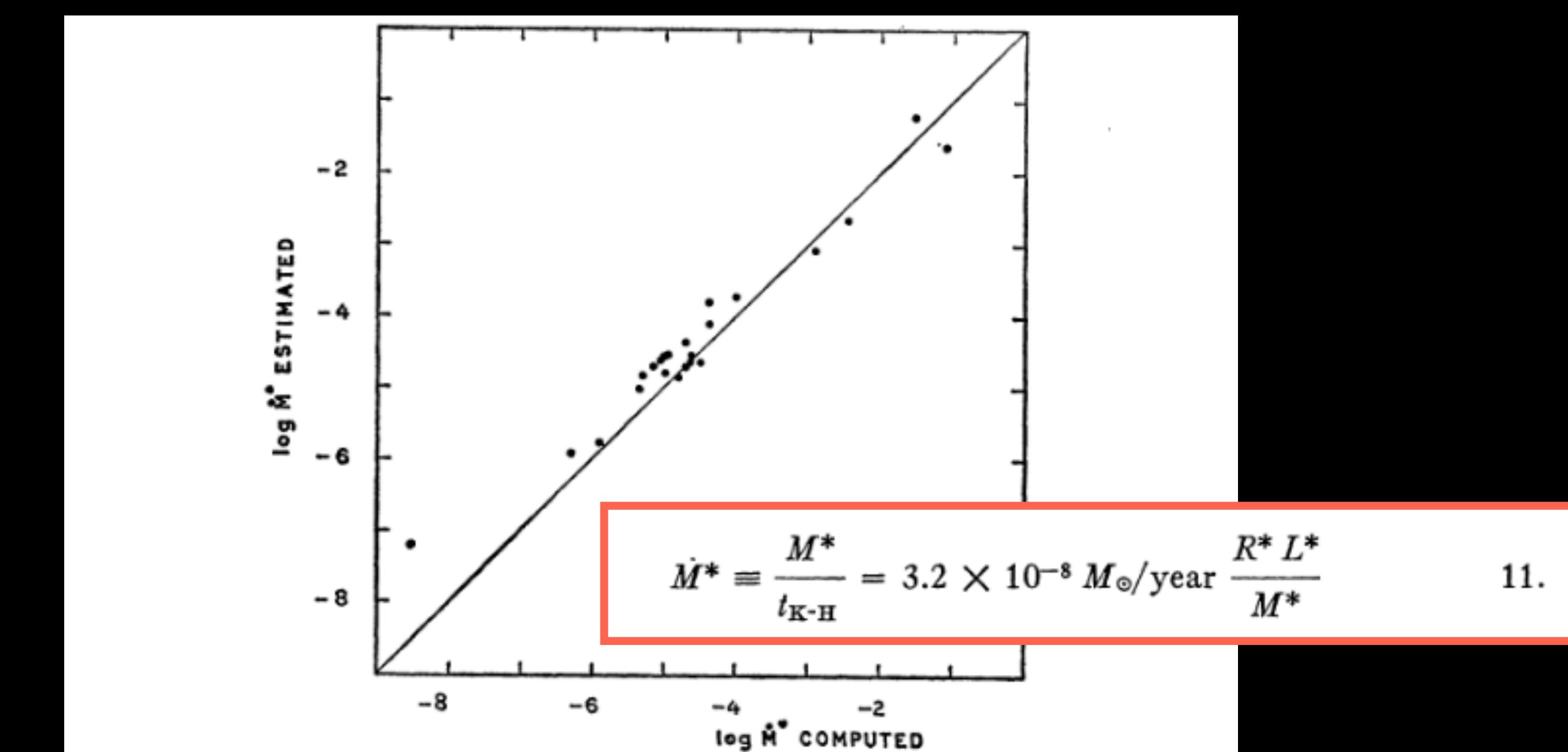


FIGURE 3. The relation between the highest rate of mass transfer (in solar masses per year) obtained from model computations of the rapid mass exchange in binaries, and the rate estimated with formula 11.

# Evolutionary Processes in Close Binary Systems(Paper 3)

B. Paczyński 1971

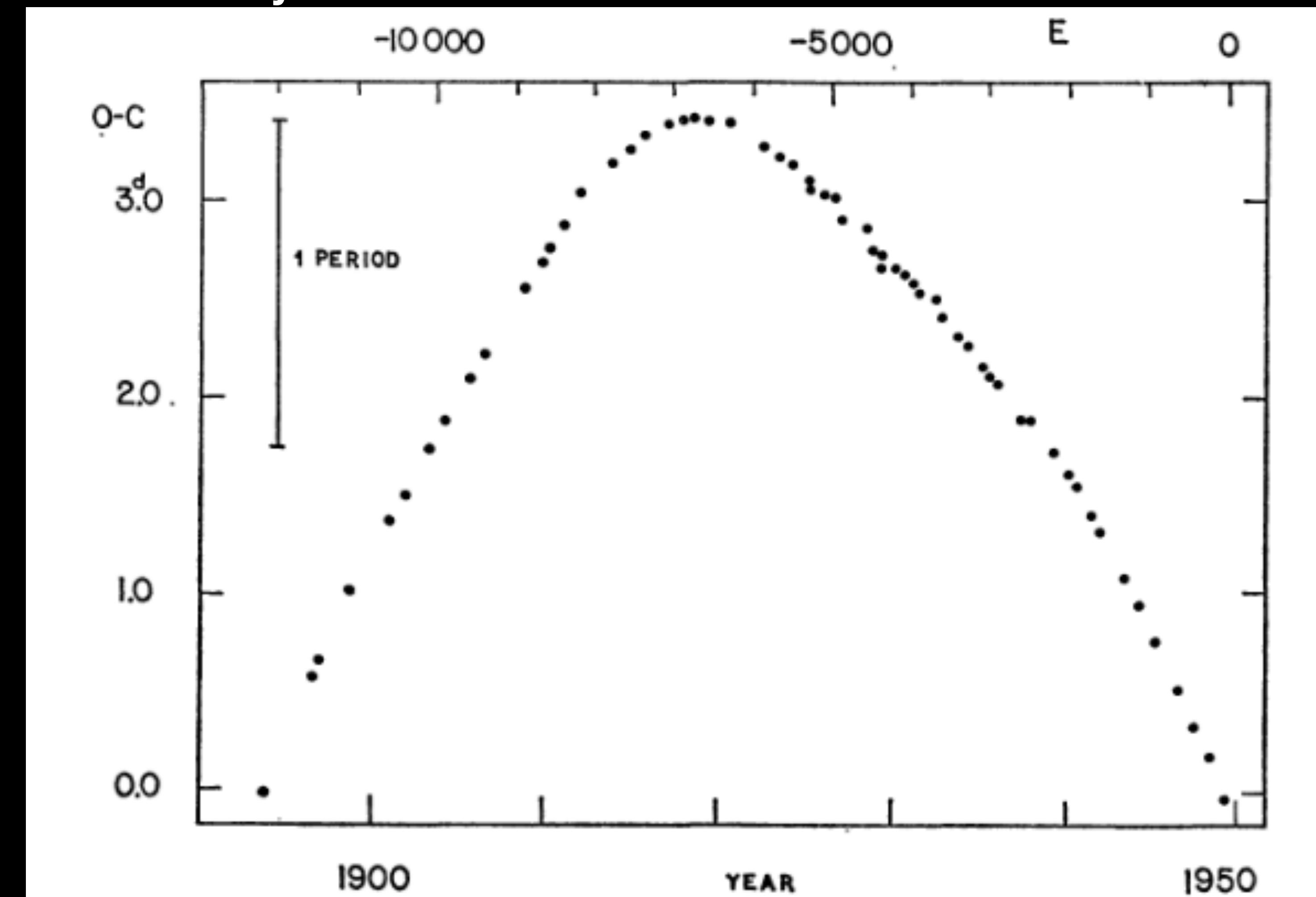
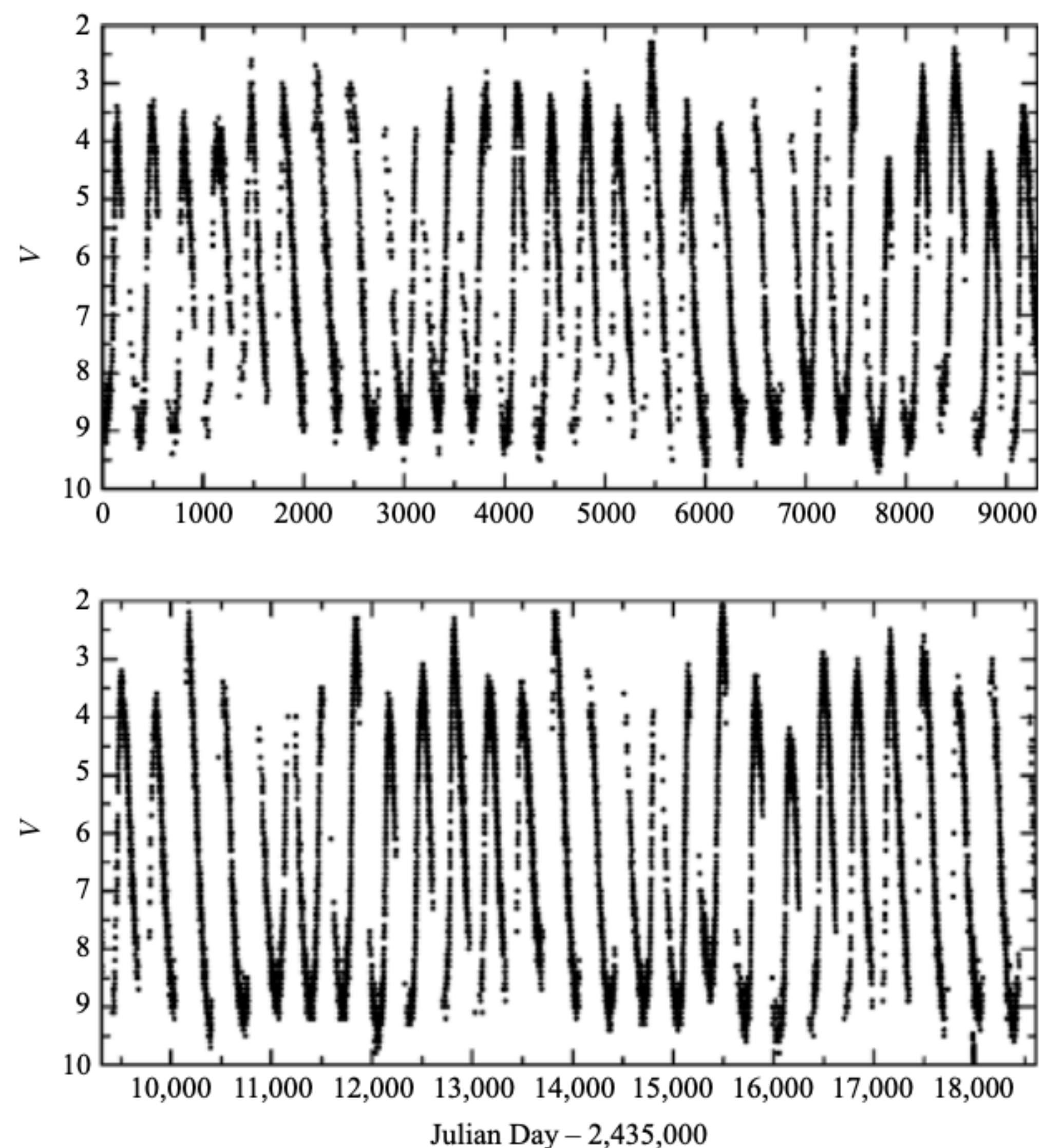


FIGURE 4. Observed minus calculated moments of eclipses versus time for the binary SV Centauri. The observed moments were taken from the compilation by Wood & Forbes (1963), while the formula Primary Minimum =  $JD\ 24\ 33053.217 + 1.6604206 \times E$  was used to calculate those moments. This diagram implies a time scale of period changes of  $P/\dot{P} = 10^6$  years, and indicates the possibility of rapid mass transfer in this binary.

# **Chapter 14 Carroll (Radial Pulsation Paper 4)**

## Chapter 14 Carroll (Radial Pulsation Paper 4)



**FIGURE 14.1** The light curve of Mira from September 14, 1954 (JD 2,435,000) through September 2005. Recall that magnitudes dimmer than 6 are undetectable to the unaided eye. (We acknowledge with thanks the variable-star observations from the AAVSO International Database contributed by observers worldwide.)

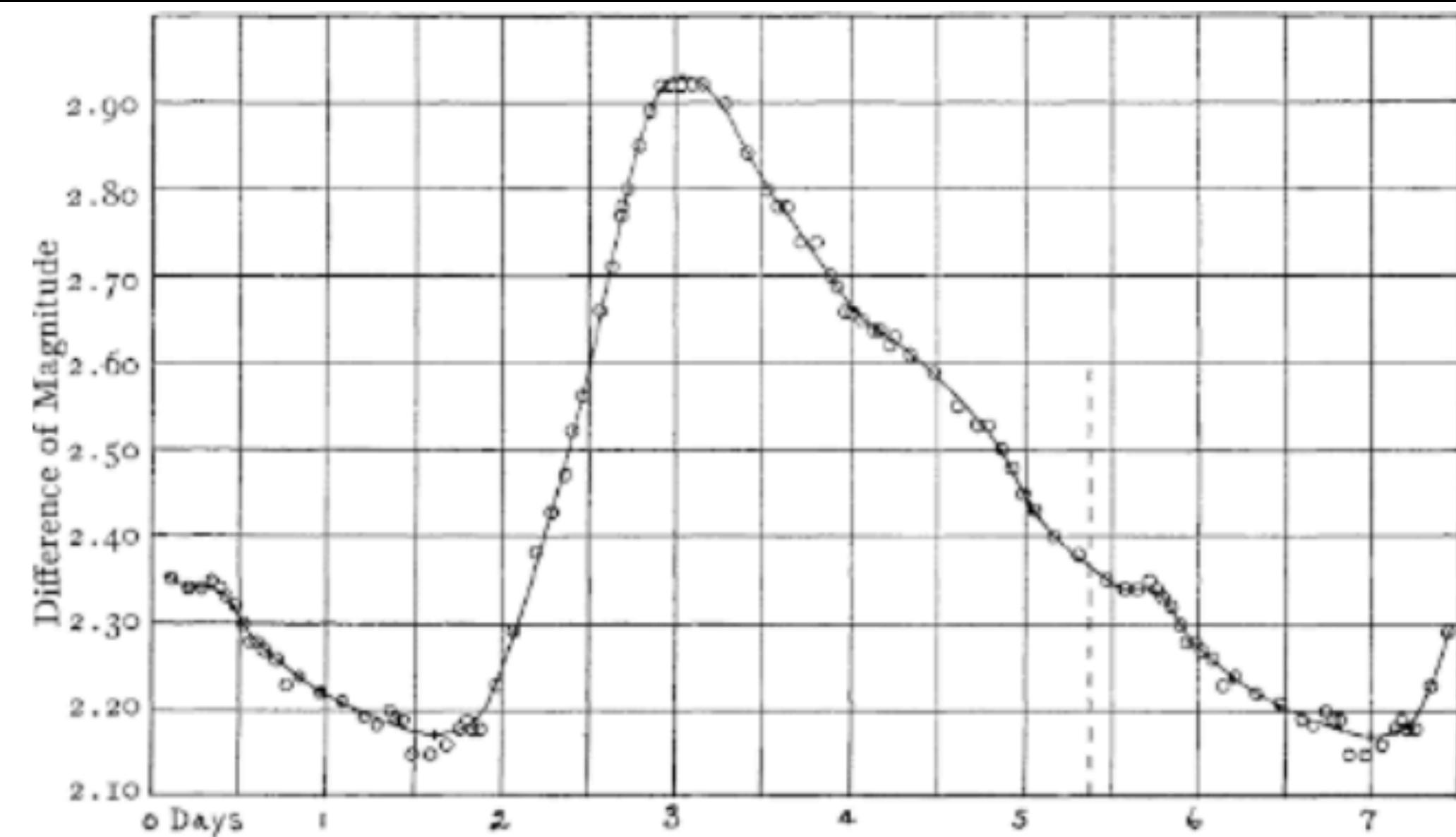


**FIGURE 14.2** The light curve of  $\delta$  Cephei. Its pulsation period is 5.37 days. (Figure from Stebbins, Joel, *Ap. J.*, 27, 188, 1908.)

# Chapter 14 Carroll (Radial Pulsation Paper 4)

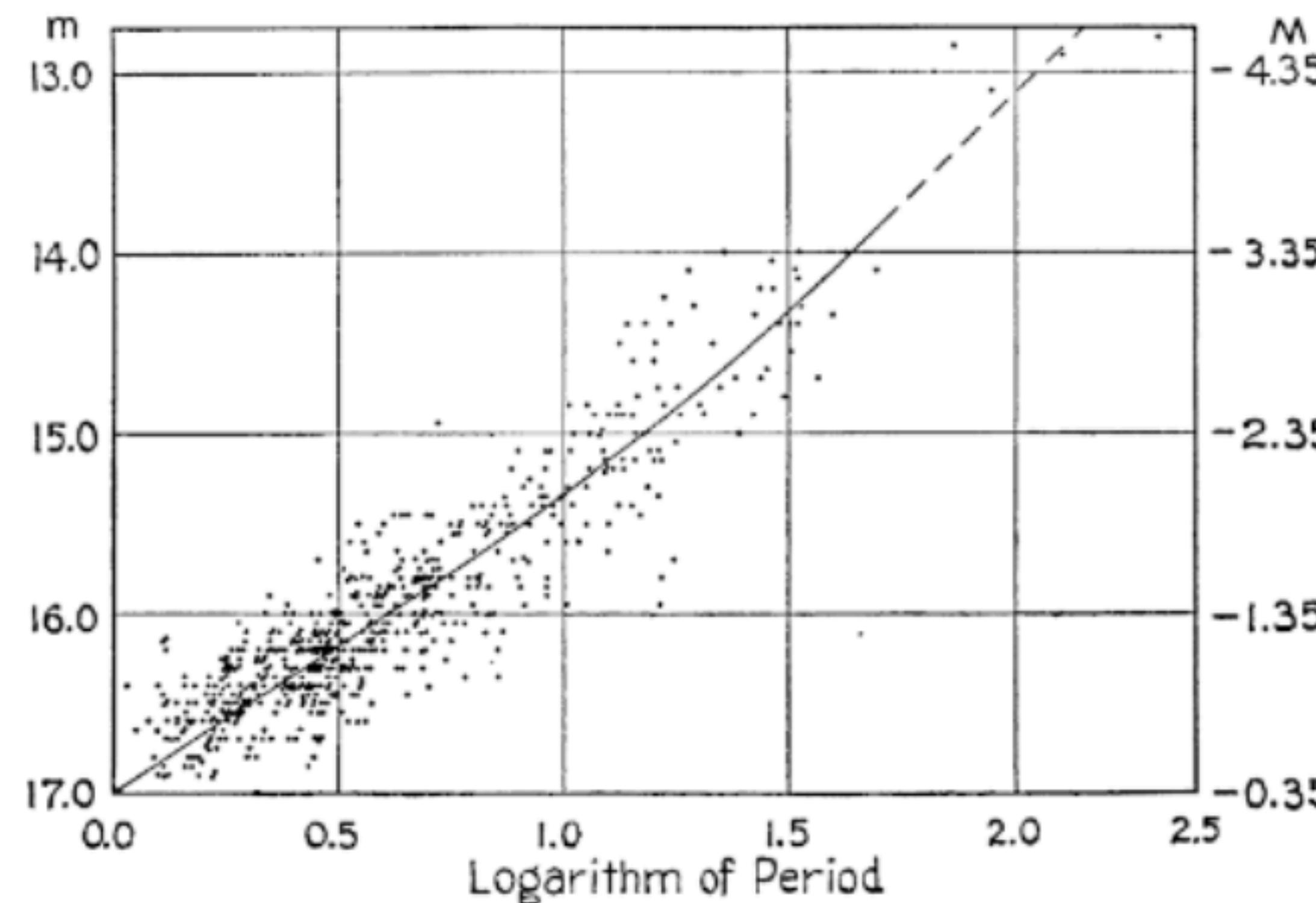


**FIGURE 14.4** Classical Cepheids in the Small Magellanic Cloud, with the period in units of days.  
(Figure from Shapley, *Galaxies*, Harvard University Press, Cambridge, MA, 1961.)

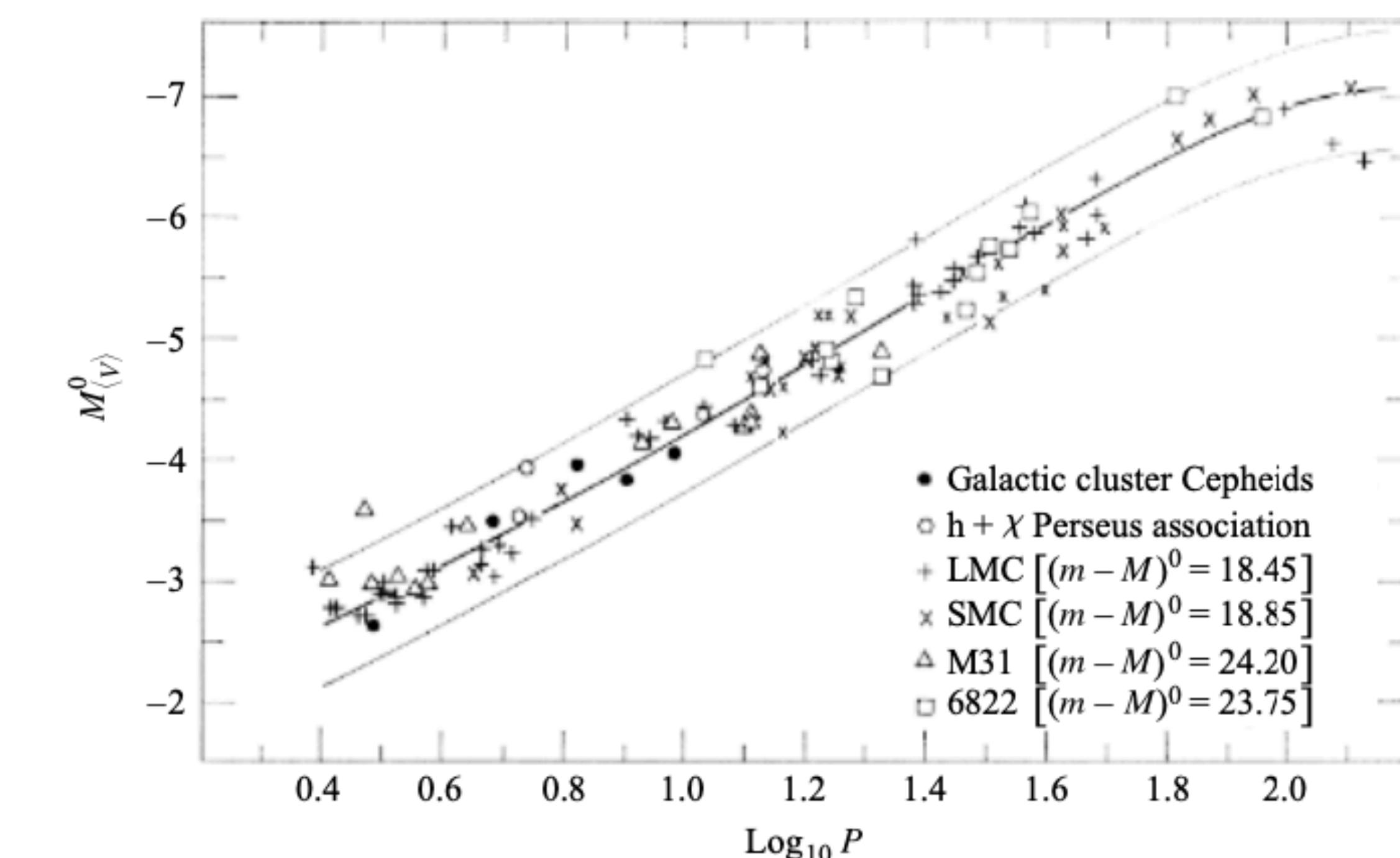


**FIGURE 14.5** The period-luminosity relation for classical Cepheids. (Figure adapted from Sandage and Tamman, *Ap. J.*, 151, 531, 1968.)

# Chapter 14 Carroll (Radial Pulsation Paper 4)

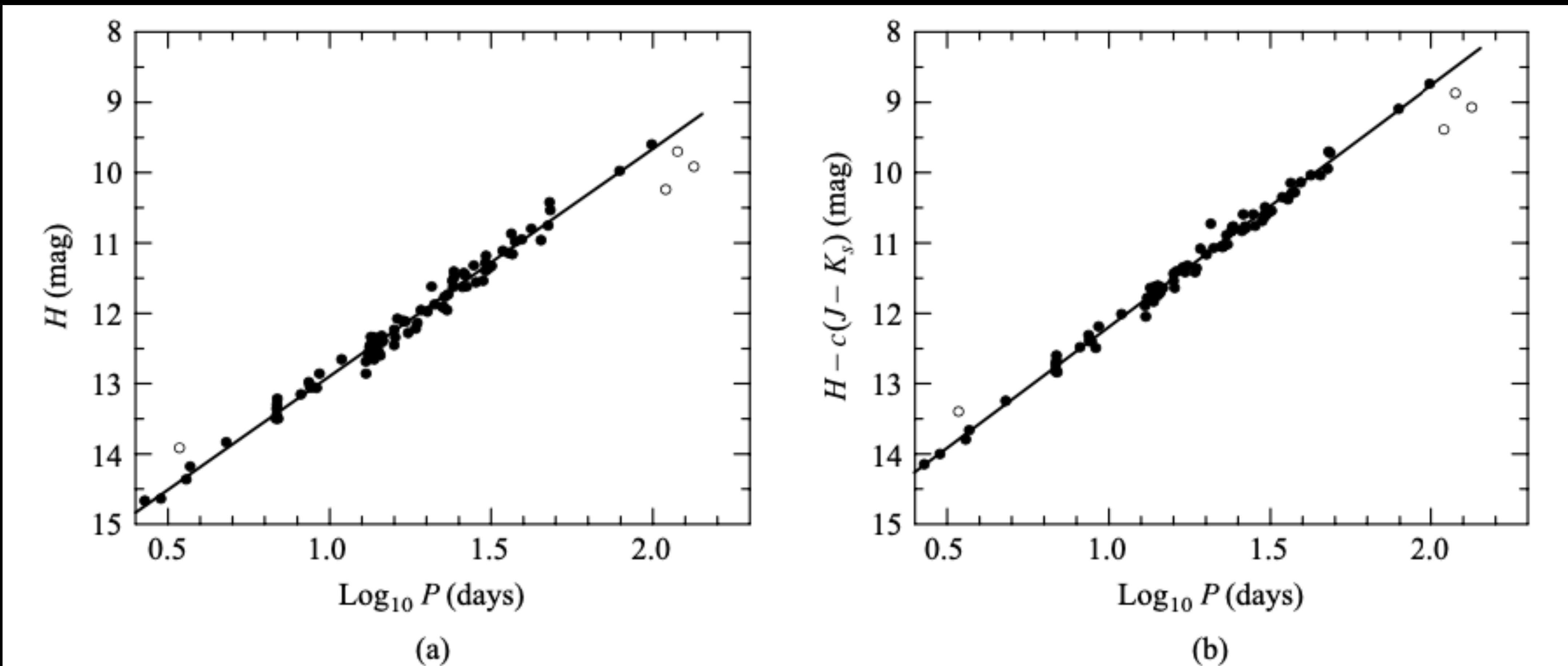


**FIGURE 14.6** (a) The infrared period–luminosity relation for 92 Cepheids in the Large Magellanic Cloud. The infrared  $H$  band was used for the observations. The open circles represent four Cepheids that were excluded from the least-squares linear fit. (b) The period–luminosity–color relation for the same Cepheids. (Data from Persson, S. E., et al., *Astron. J.*, 128, 2239, 2004.)

## Chapter 14 Carroll (Radial Pulsation Paper 4)

Type	Range of Periods	Population Type	Radial or Nonradial
Long-Period Variables	100–700 days	I,II	R
Classical Cepheids	1–50 days	I	R
W Virginis stars	2–45 days	II	R
RR Lyrae stars	1.5–24 hours	II	R
$\delta$ Scuti stars	1–3 hours	I	R,NR
$\beta$ Cephei stars	3–7 hours	I	R,NR
ZZ Ceti stars	100–1000 seconds	I	NR

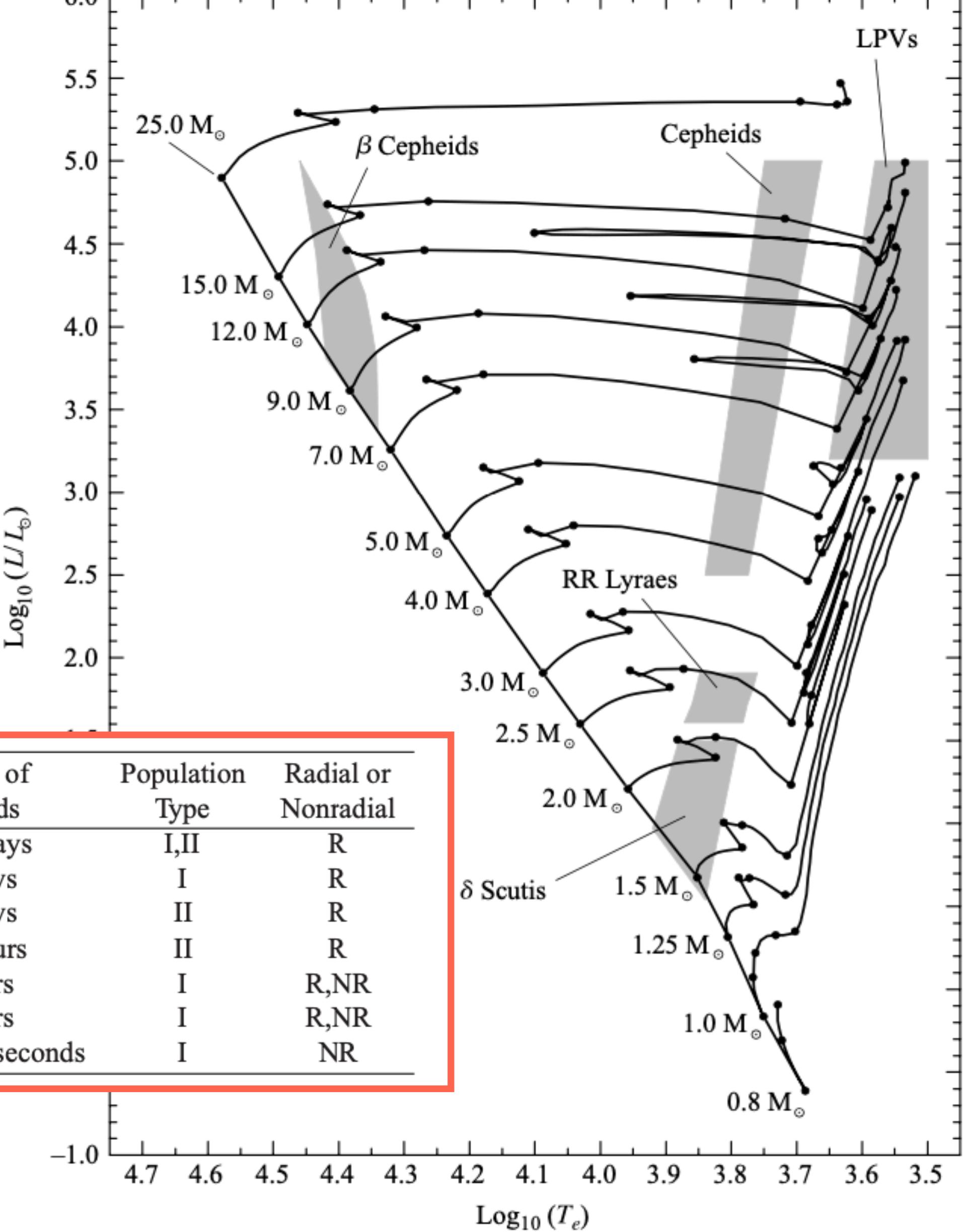


**FIGURE 14.8** Pulsating stars on the H–R diagram. (Data for the evolutionary tracks from Schaller, et al., *Astron. Astrophys. Suppl.*, 96, 269, 1992.)

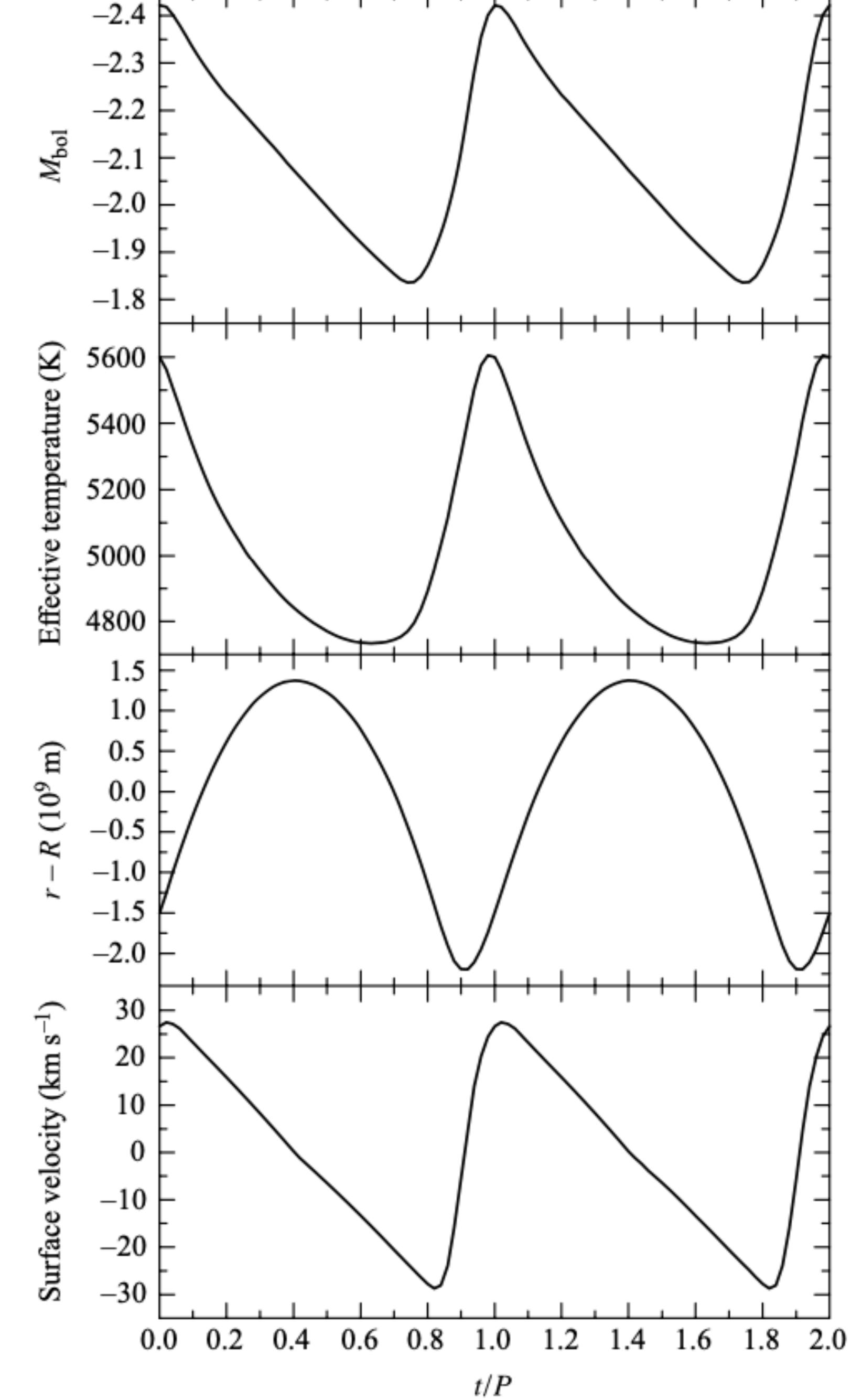


**FIGURE 14.7** Observed pulsation properties of  $\delta$  Cephei, a typical classical Cepheid. Schwarzschild, *Harvard College Observatory Circular* 431, 1938.)

# Chapter 14 Carroll (Radial Pulsation Paper 4)

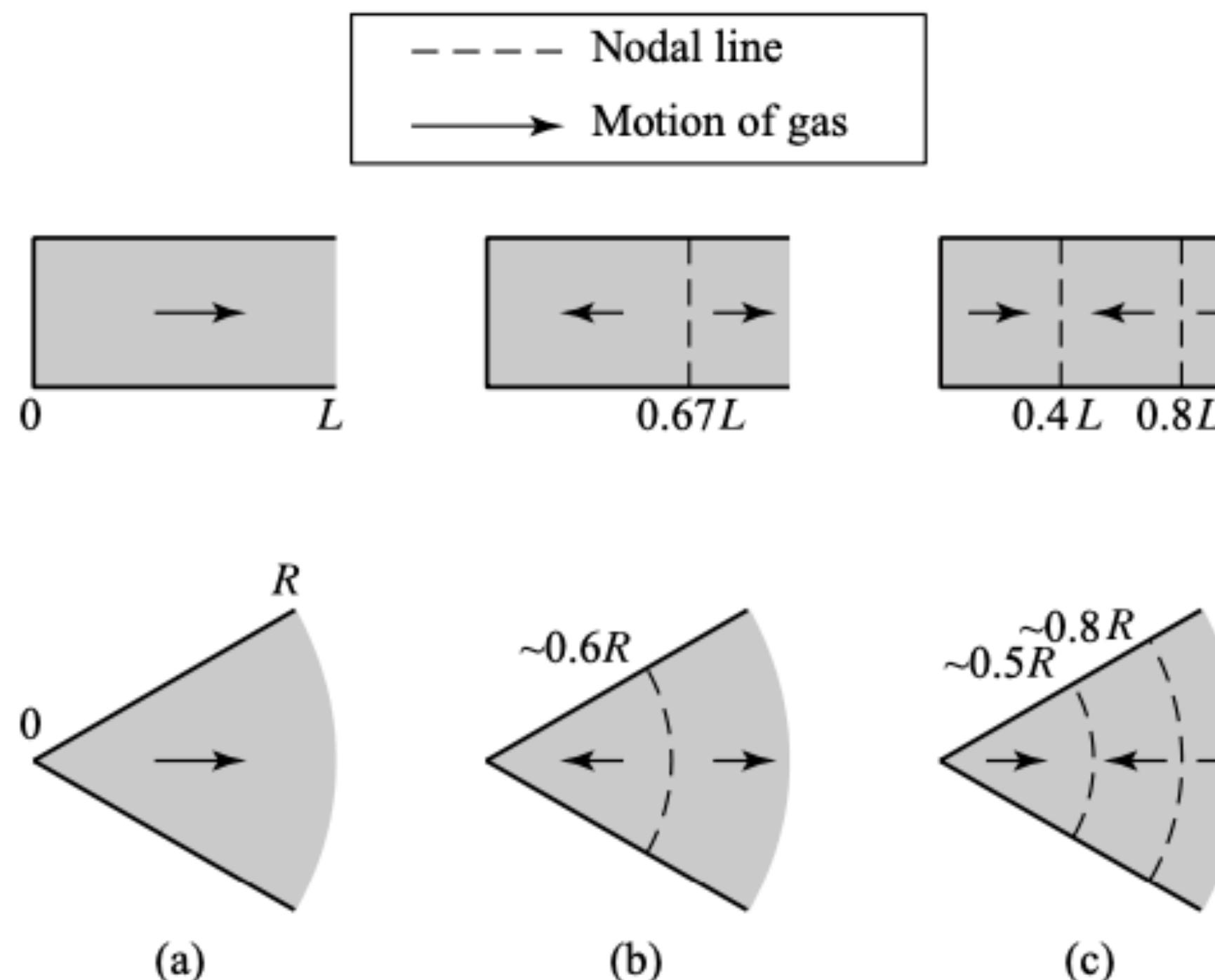


**FIGURE 14.9** Standing sound waves in an organ pipe and in a star for (a) the fundamental mode, (b) the first overtone, and (c) the second overtone.

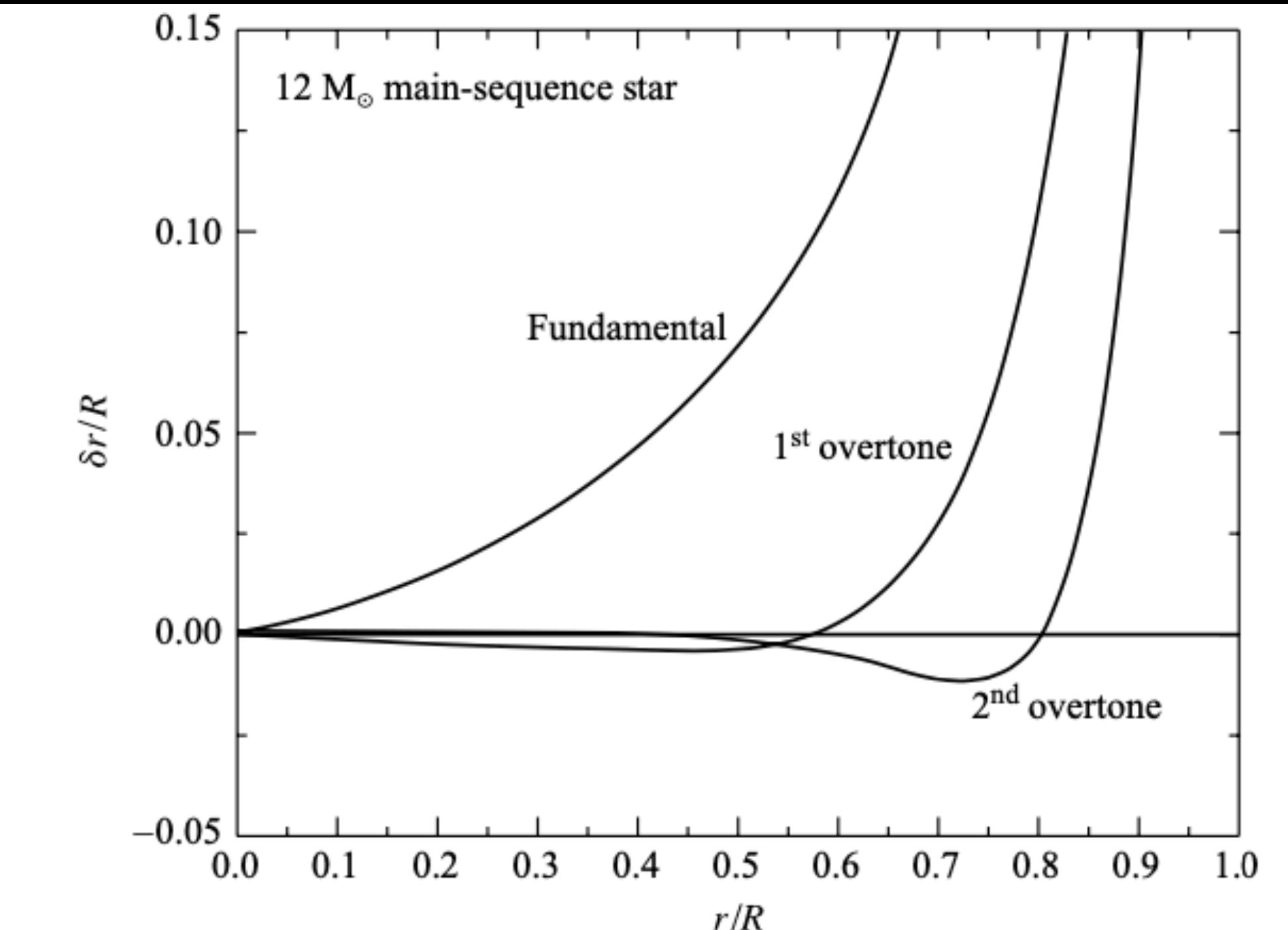


**FIGURE 14.10** Radial modes for a pulsating star. The waveform for each mode has been arbitrarily scaled so that  $\delta r/R = 1$  at the surface of the star. Actually, the maximum surface ratio of  $\delta r/R$  is approximately 0.05 to 0.10 for a classical Cepheid.

# Chapter 14 Carroll (Radial Pulsation Paper 4)

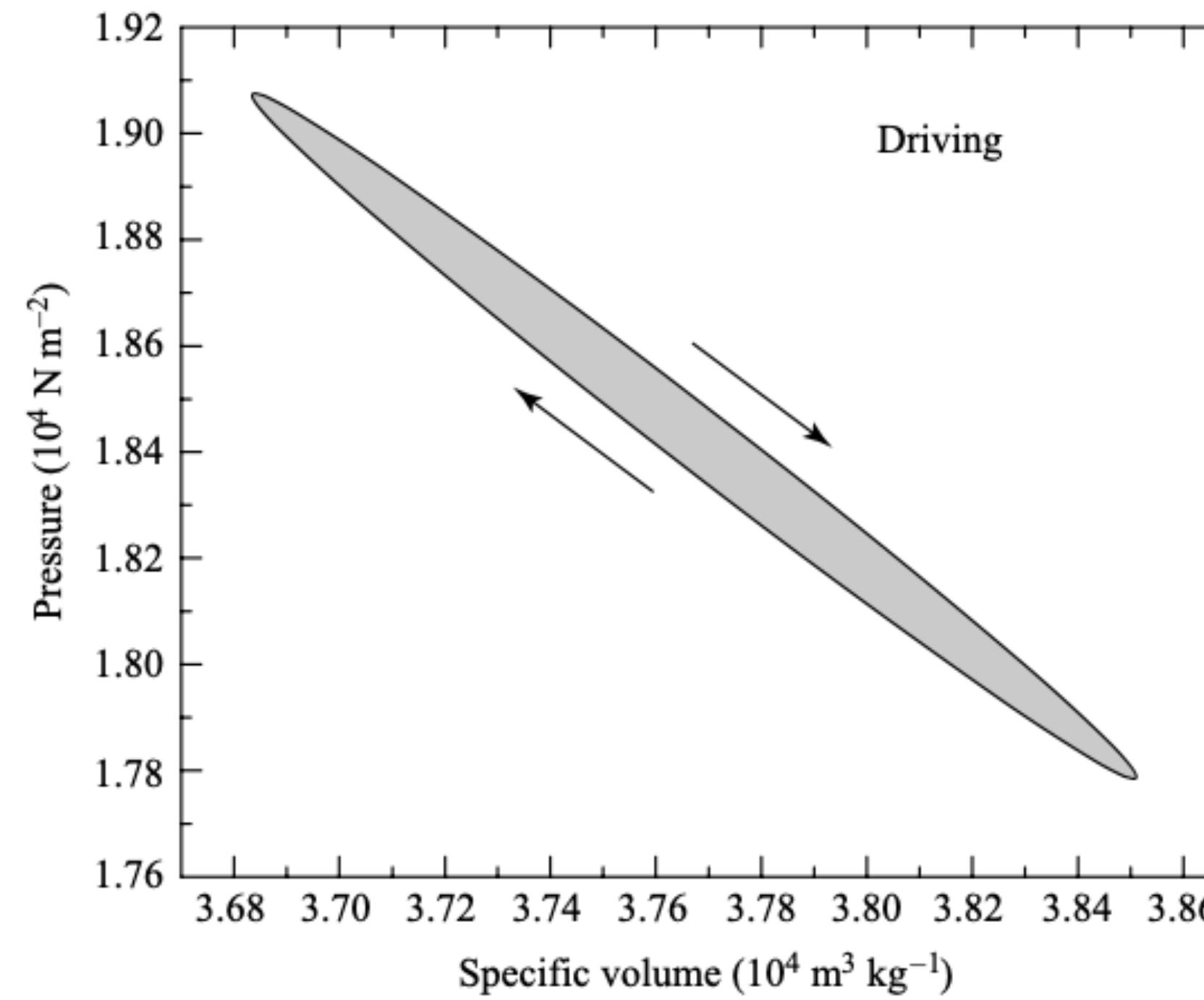


**FIGURE 14.11**  $P$ - $V$  diagram for a driving layer of an RR Lyrae star model. You may recall the analogous use of  $P$ - $V$  diagrams in discussing heat engines in introductory physics courses. A clockwise path in a  $P$ - $V$  diagram corresponds with net driving.

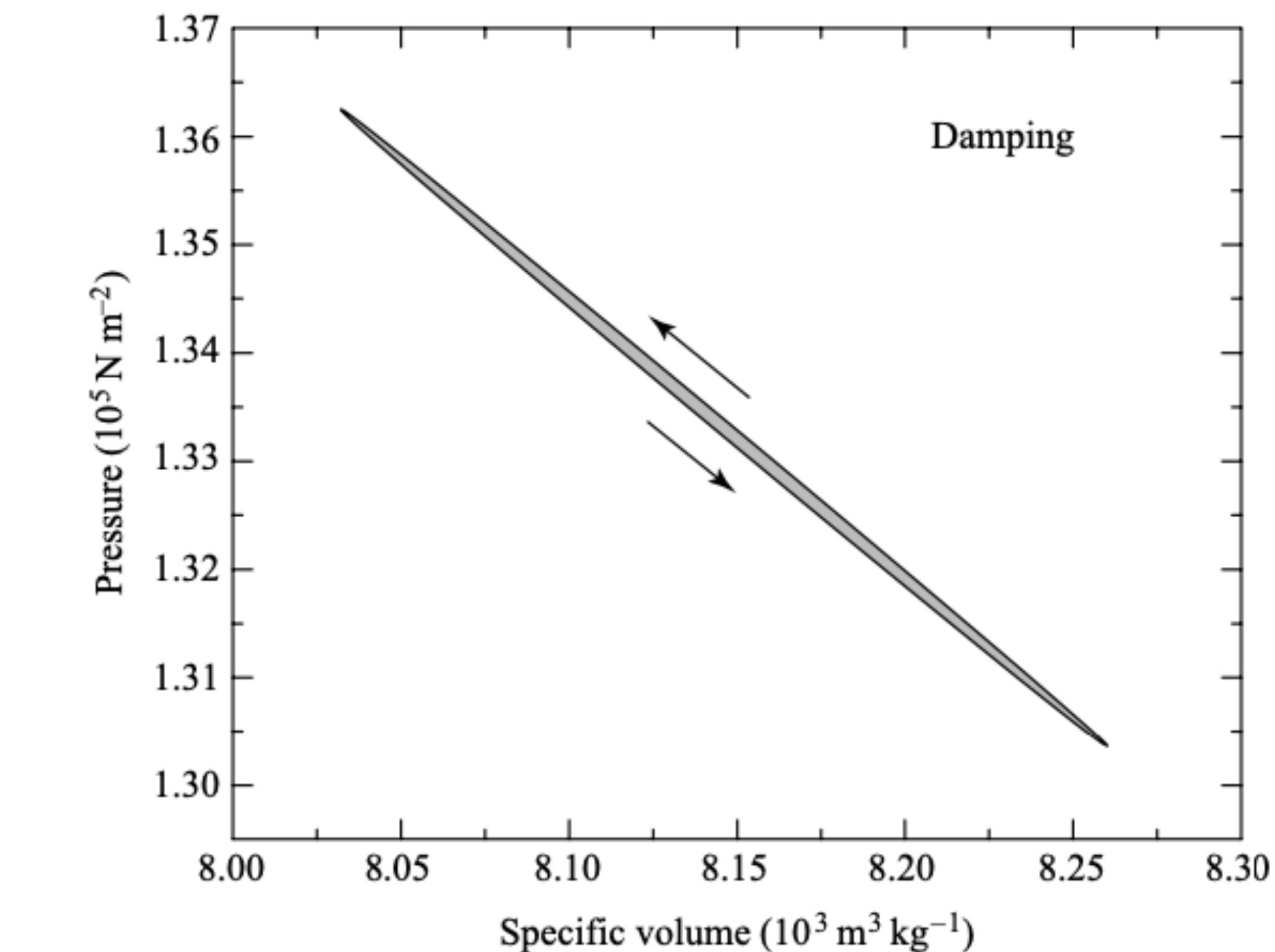


**FIGURE 14.12**  $P$ - $V$  diagram for a damping layer of an RR Lyrae star model. A counterclockwise path in a  $P$ - $V$  diagram corresponds to net damping.

# Chapter 14 Carroll (Radial Pulsation Paper 4)

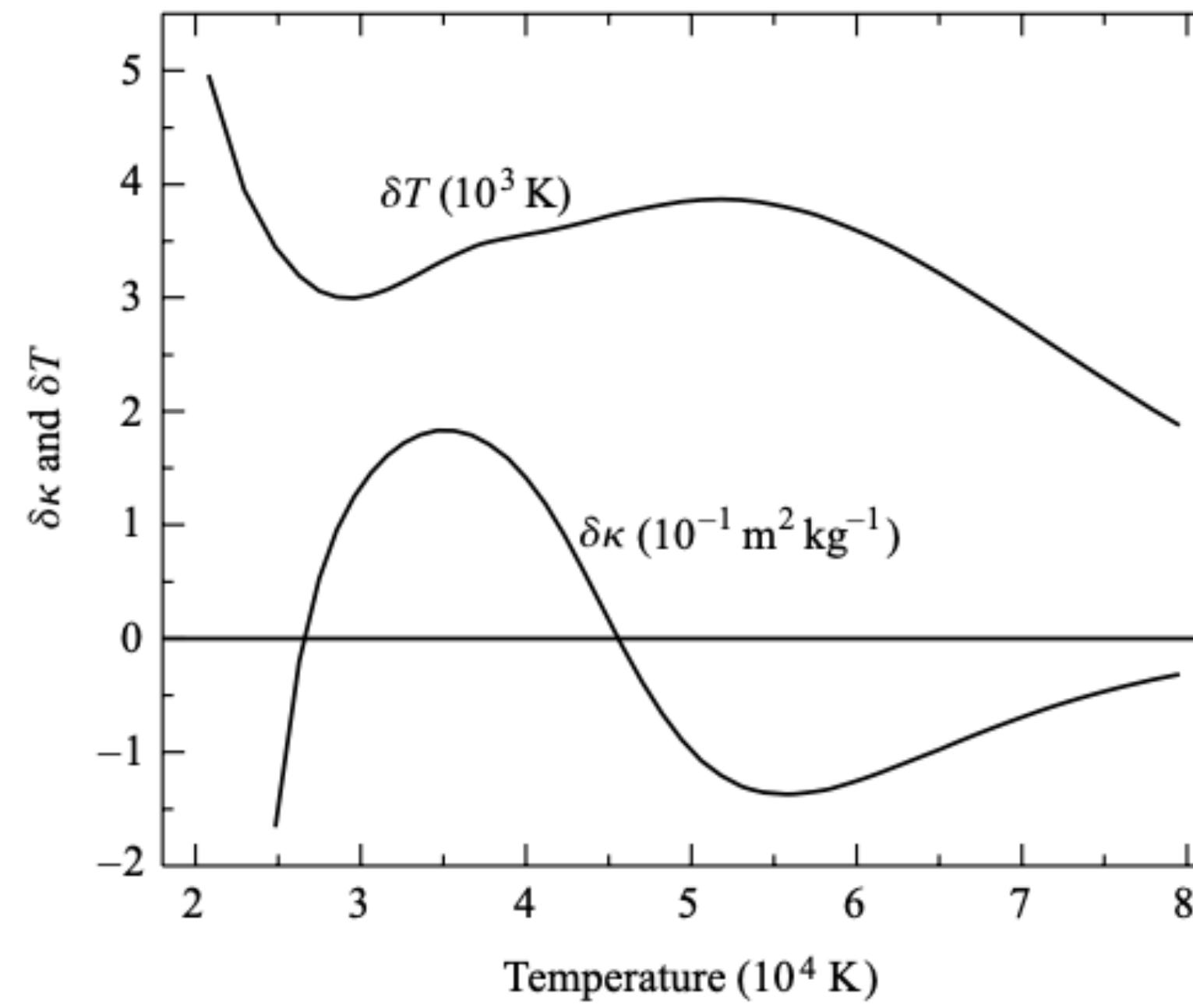


**FIGURE 14.13** Variations in the temperature and opacity throughout an RR Lyrae star model at the time of maximum compression. In the He II partial ionization zone ( $T \approx 40,000$  K),  $\delta\kappa > 0$  and  $\delta T$  is reduced. These are the  $\kappa$ - and  $\gamma$ -mechanisms that drive the star's oscillations.

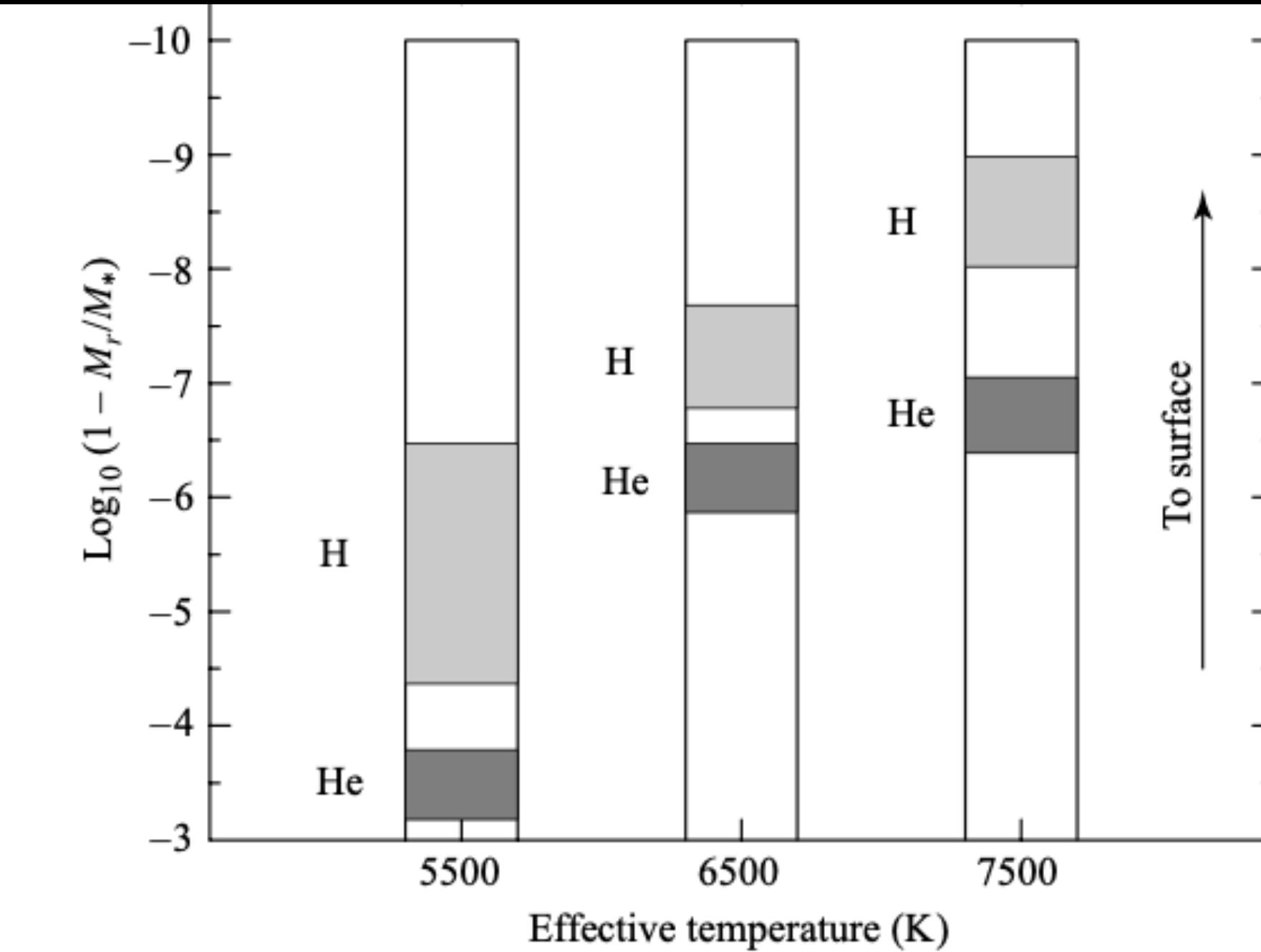


**FIGURE 14.14** Hydrogen and helium ionization zones in stars of different temperatures. For each point in the star, the vertical axis displays the logarithm of the fraction of the star's mass that lies above that point.

# **Chapter 14 Carroll (Non Radial Pulsation Paper 6)**

## Chapter 14 Carroll (Non Radial Pulsation Paper 6)

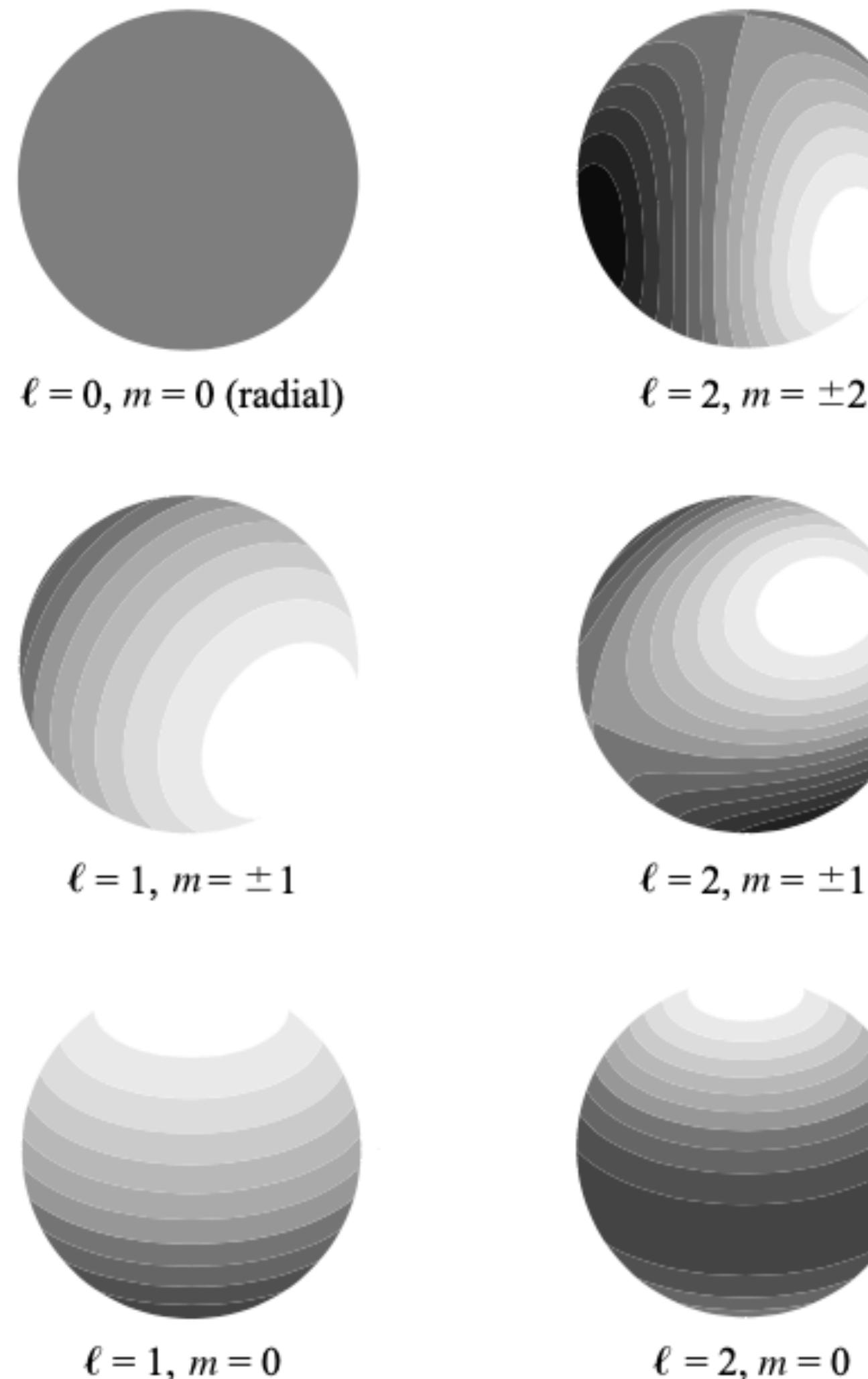


**FIGURE 14.16** Nonradial pulsation patterns. The modes of pulsation are represented by the real parts of the spherical harmonic functions,  $Y_\ell^m(\theta, \phi)$ .

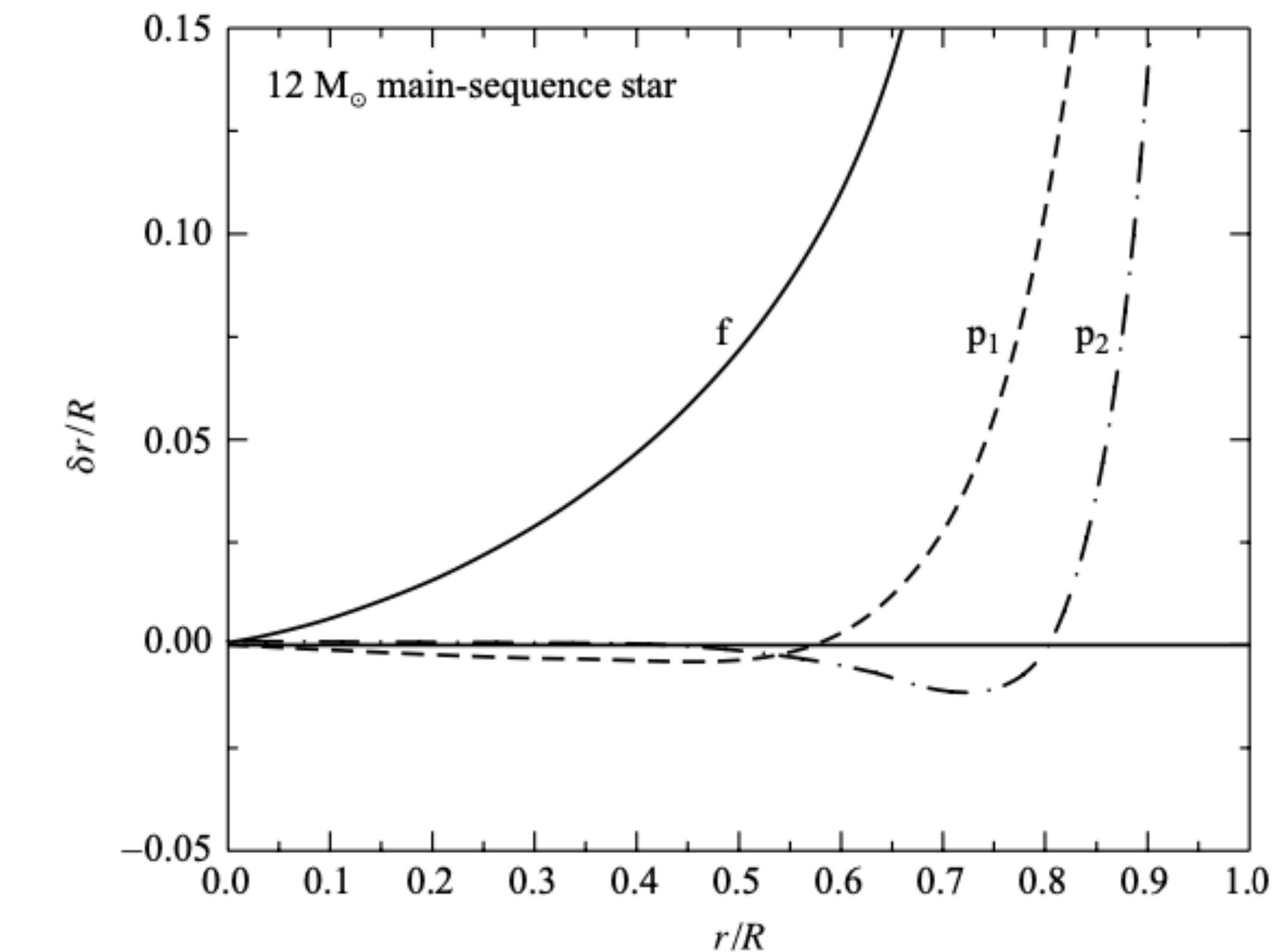
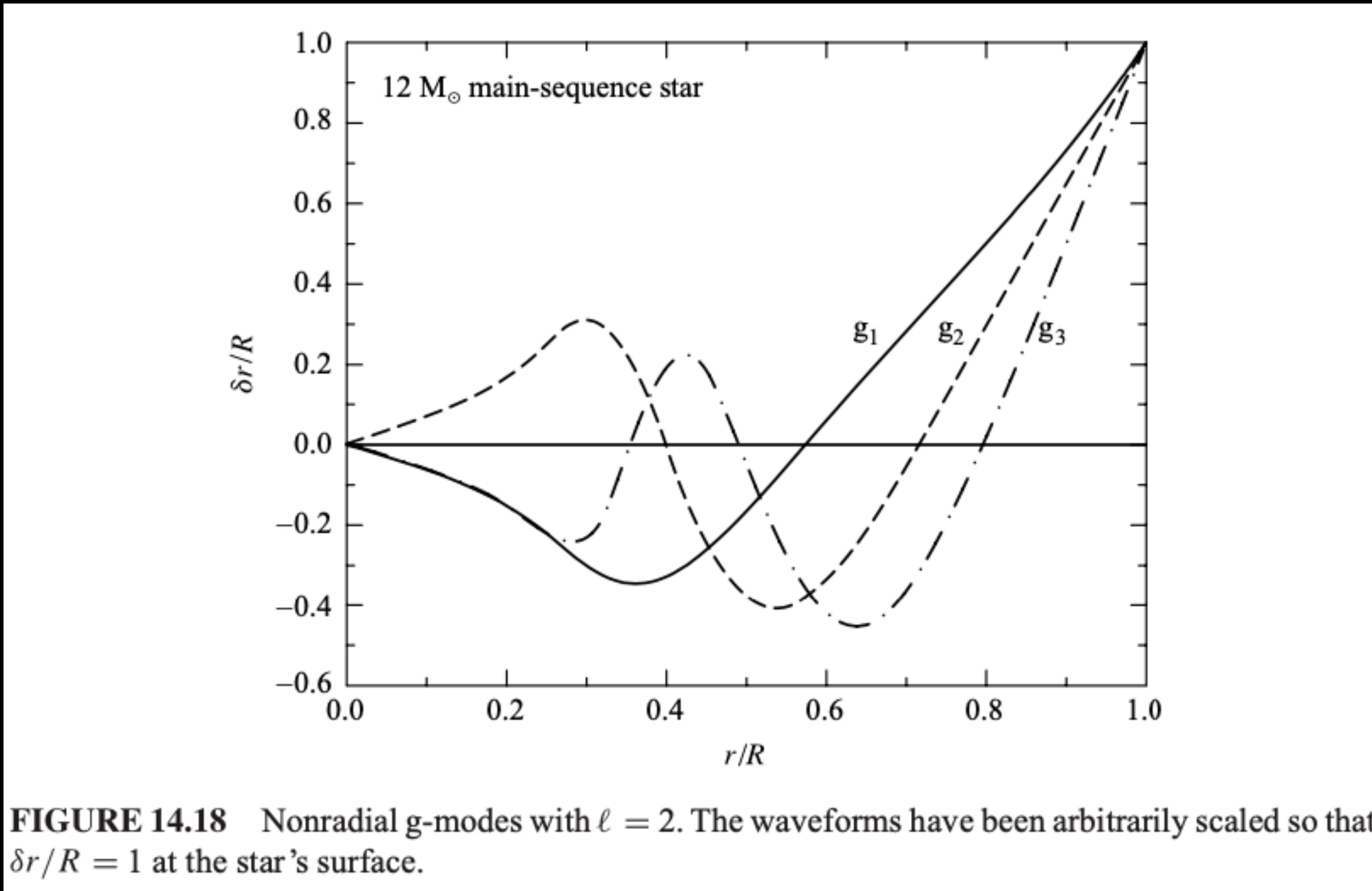


**FIGURE 14.17** Nonradial p-modes with  $\ell = 2$ . The waveforms have been arbitrarily scaled so that  $\delta r/R = 1$  at the star's surface. The f-mode is also shown.

Chapter 14 Carroll  
(Non Radial Pulsation Paper 6)



## Chapter 14 Carroll (Non Radial Pulsation Paper 6)

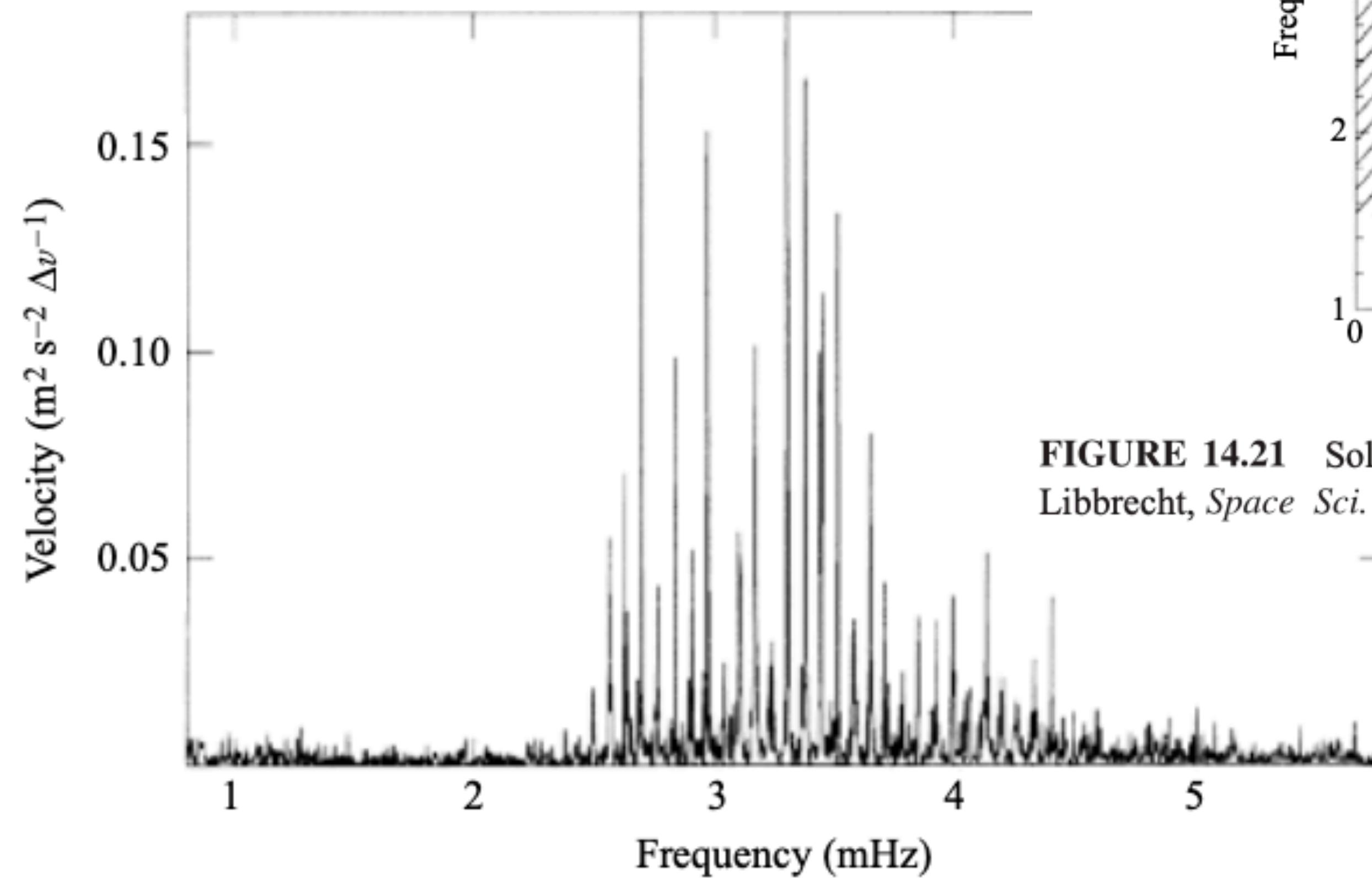


**FIGURE 14.20** Relative power of solar p-modes; a period of five minutes corresponds to a frequency of 3.33 mHz. (Figure adapted from Grec, Fossat, and Pomerantz, *Nature*, 288, 541, 1980.)

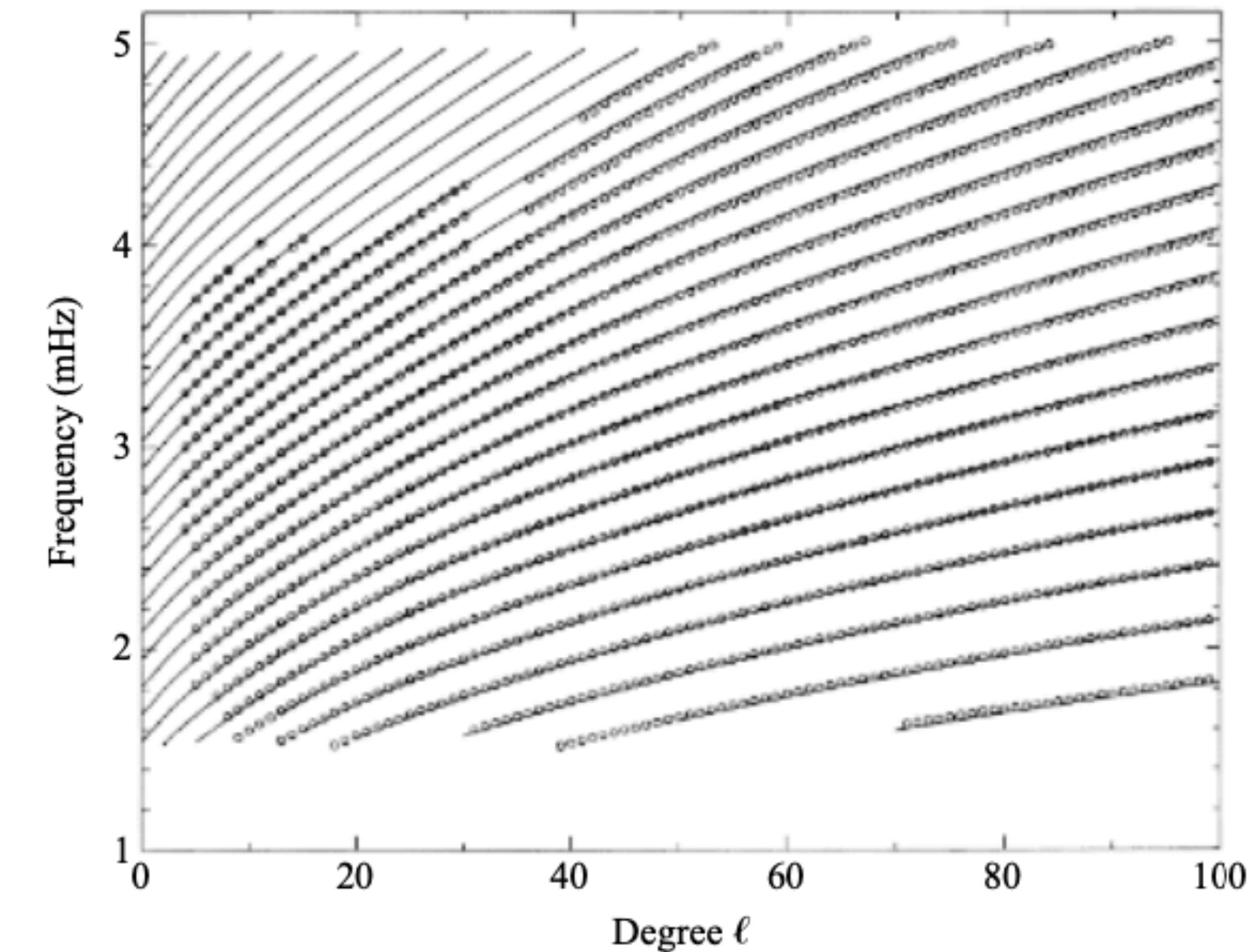


**FIGURE 14.21** Solar p-modes: observations (circles) and theory (lines). (Figure adapted from Libbrecht, *Space Sci. Rev.* 47, 275, 1988.)

# Theoretical Models for Classical Cepheids

## II. Period-Luminosity, Period-Color and Period-Luminosity-Color Relations (Paper 5)

# Theoretical Models for Classical Cepheids

Giuseppe Bono (Paper 5)

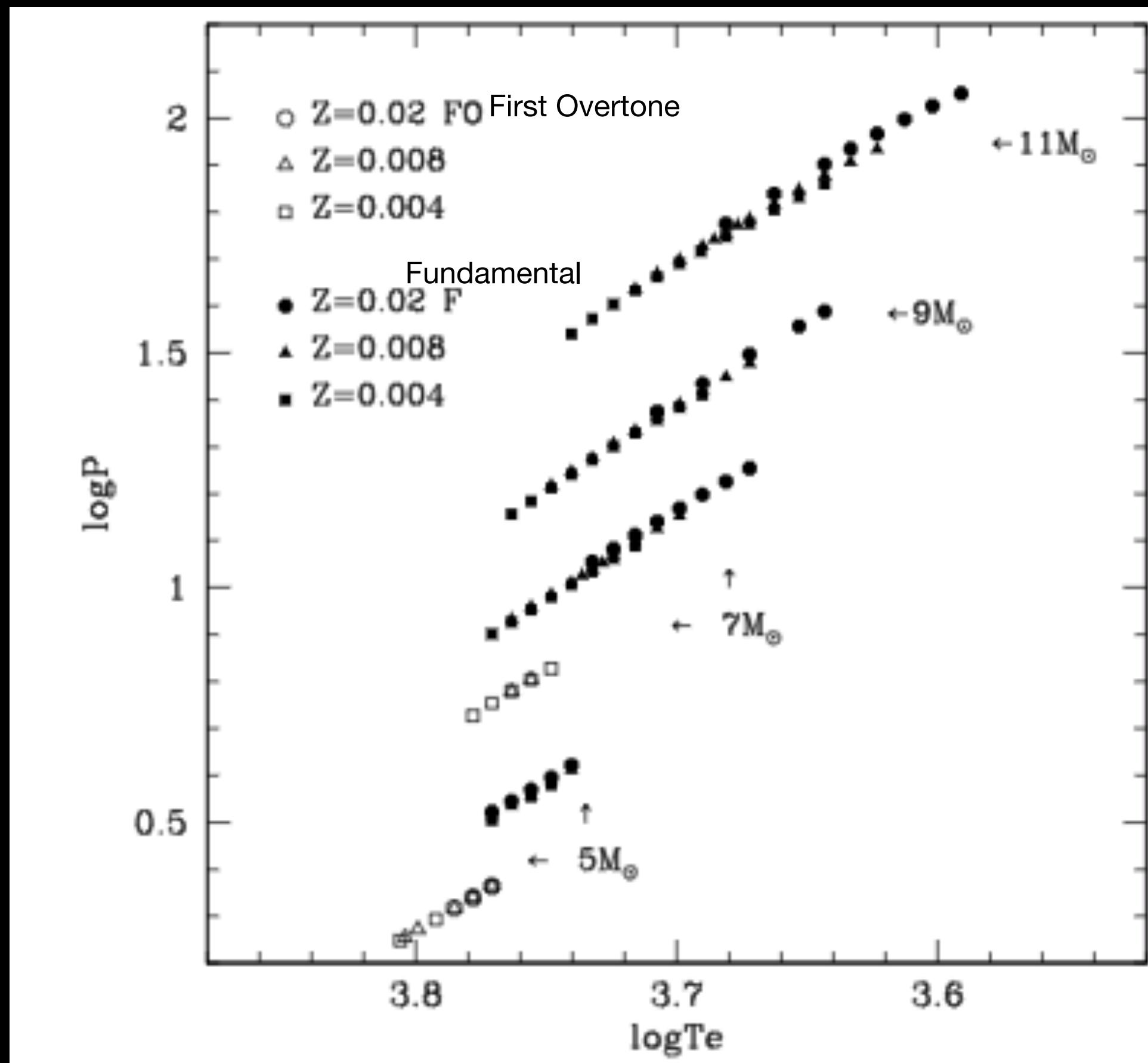


FIG. 1.—Distribution in the  $\log T_e$ - $\log P$  plane of fundamental (F) and first-overtone (FO) pulsators with different masses and chemical compositions. For each given mass and chemical composition the luminosity level has been fixed according to a canonical mass-luminosity relation (see text).

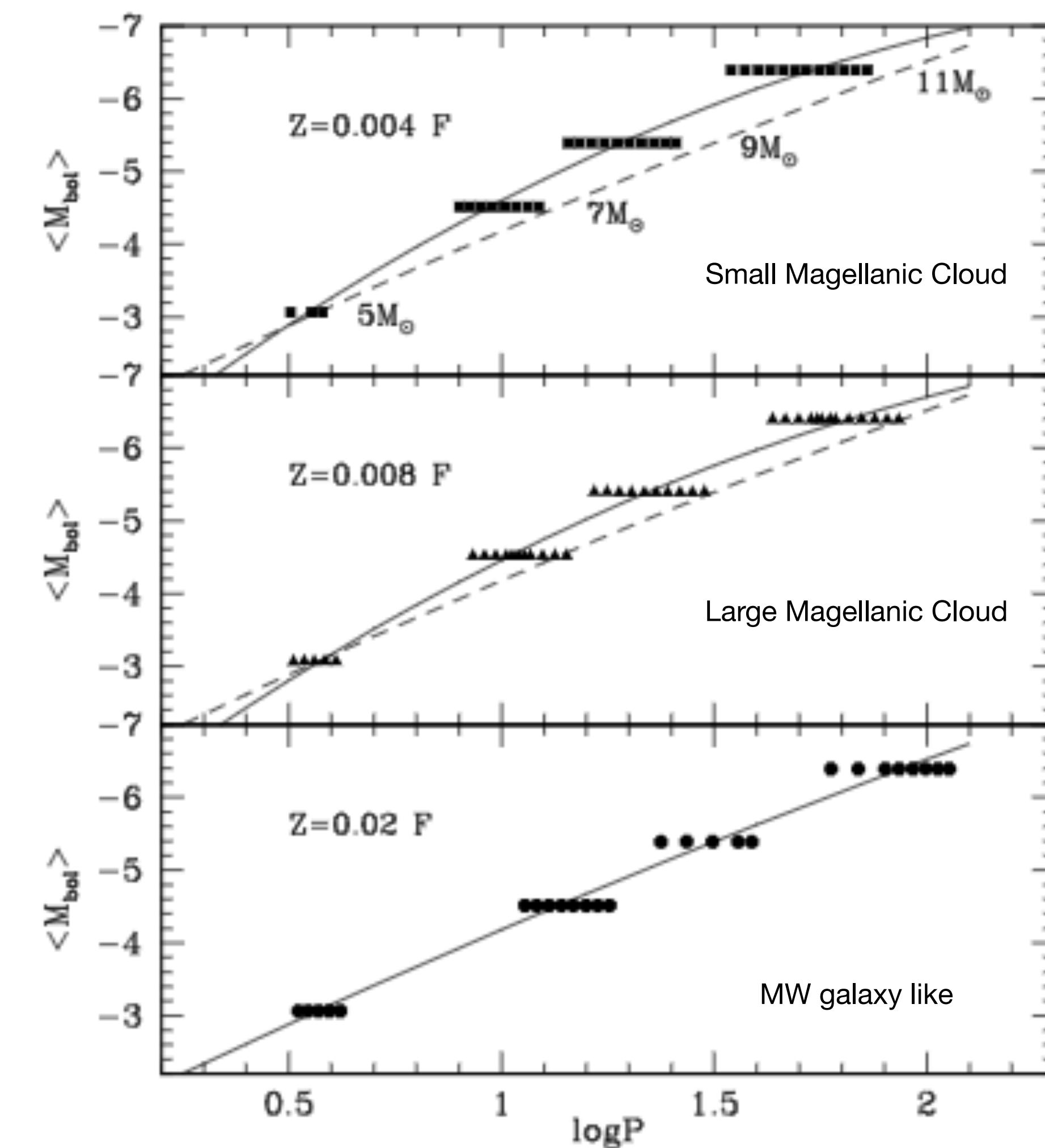


FIG. 2.—Location in the  $\log P$ - $\langle M_{\text{bol}} \rangle$  plane of fundamental pulsators. In each panel the solid line refers to the quadratic least-squares fit of theoretical models at the labeled metallicity, whereas the dashed line, in the upper two panels, shows the solar metallicity relation.

# Theoretical Models for Classical Cepheids

Giuseppe Bono (Paper 5)

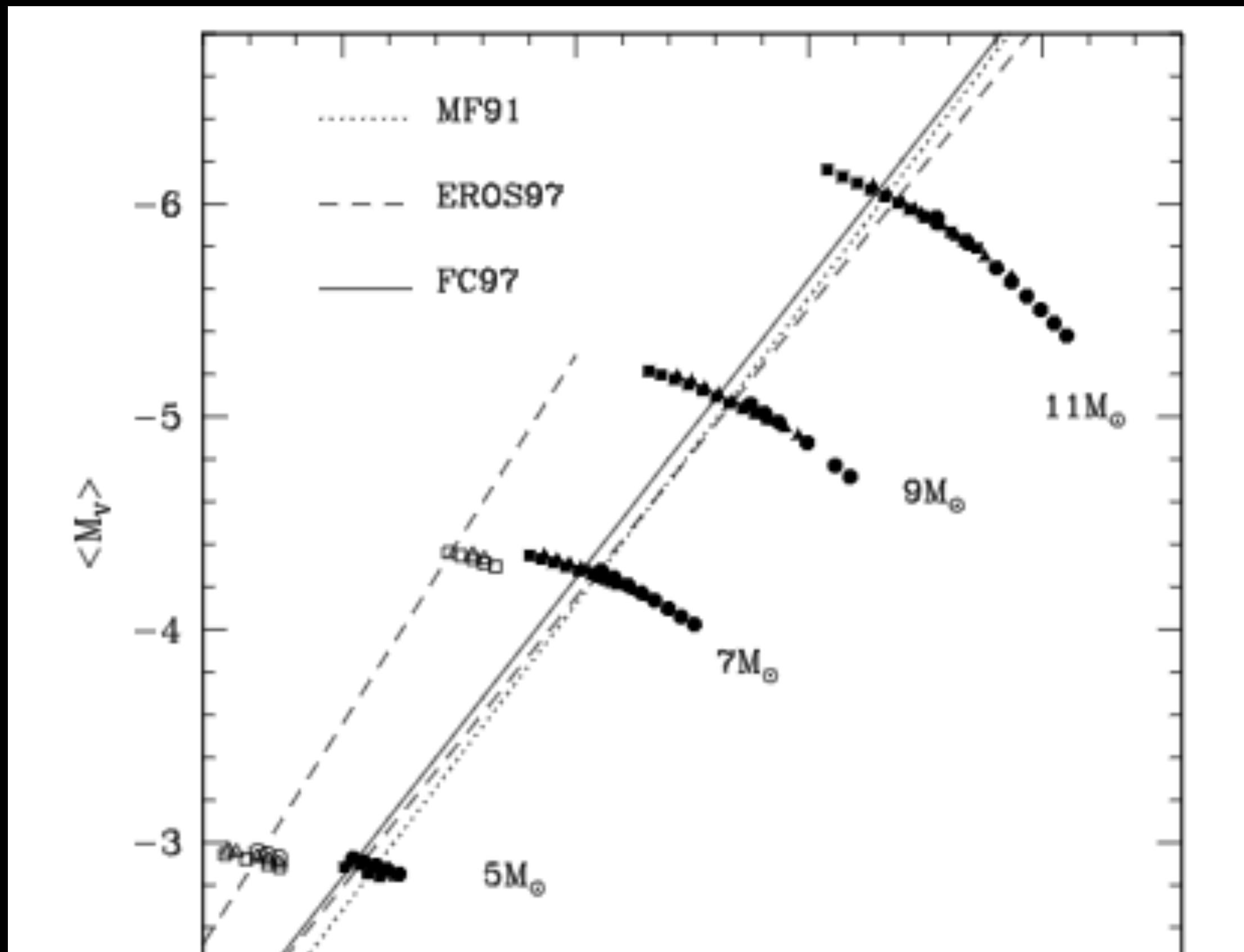


FIG. 3.—Location in the  $\log P-\langle M_V \rangle$  plane of fundamental and first-overtone pulsators with different masses and chemical compositions, in comparison with current empirical  $PL_V$  relations (see text). Symbols as in Fig. 1.

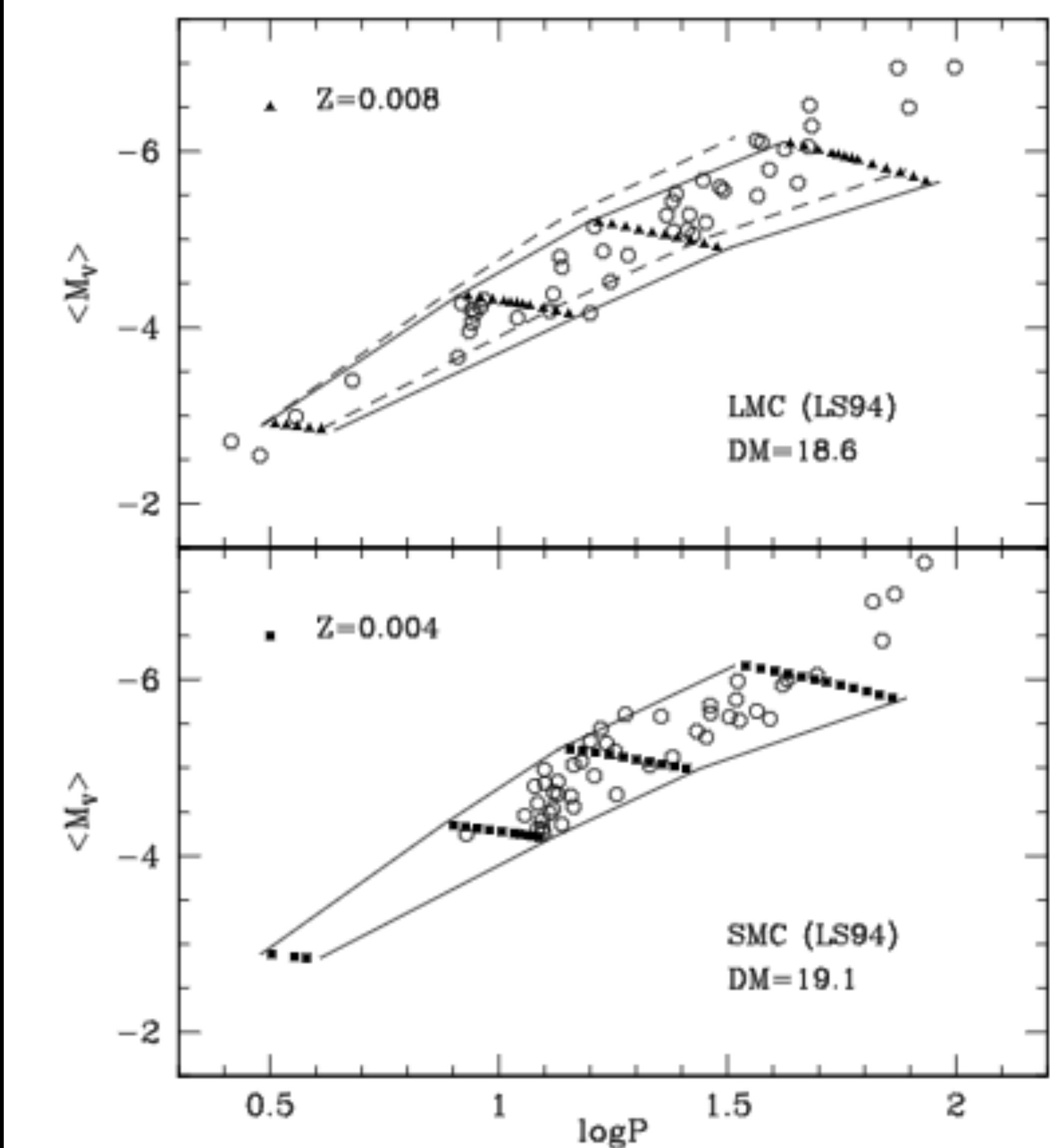


FIG. 4.—Bottom: Comparison in the  $\log P-\langle M_V \rangle$  plane of fundamental pulsators with  $Y = 0.25$ ,  $Z = 0.004$  (filled squares) and SMC Cepheids (open circles: data by LS94) by adopting a distance modulus  $DM_{SMC} = 19.1$ . The solid lines show the predicted blue and red edges of the instability strip with  $Z = 0.004$ . Top: Same as in bottom, but for models with  $Y = 0.25$ ,  $Z = 0.008$  (filled triangles) and LMC Cepheids with  $DM_{LMC} = 18.6$ . In this case the solid lines show the predicted blue and red edges of the instability strip with  $Z = 0.008$ , whereas the dashed lines refer to  $Z = 0.004$ .

# Theoretical Models for Classical Cepheids

Giuseppe Bono (Paper 5)

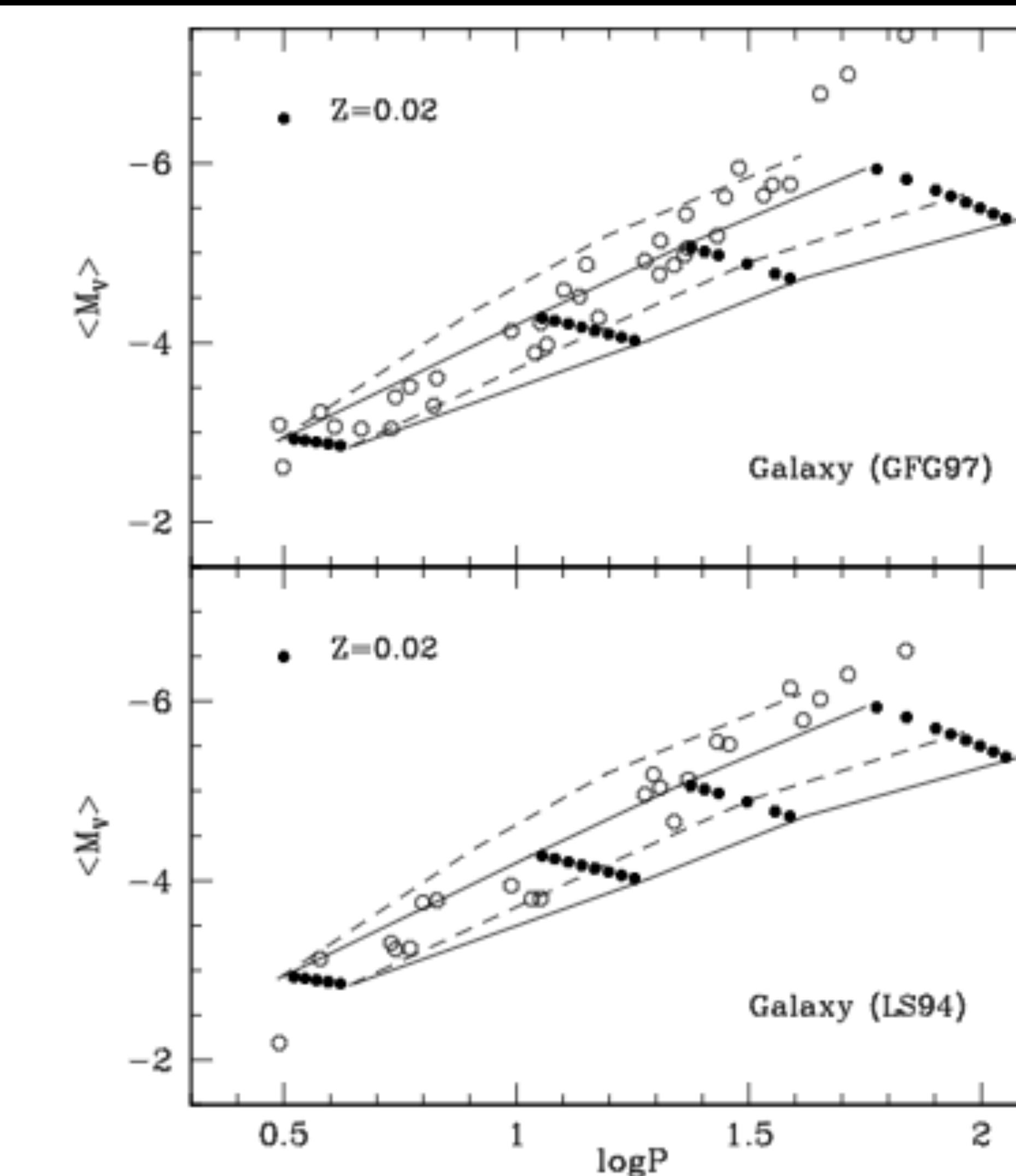


FIG. 5.—Comparison in the  $\log P$ - $\langle M_V \rangle$  plane of fundamental pulsators with  $Y = 0.28$ ,  $Z = 0.02$  (filled circles) and Galactic Cepheids (open circles; data by LS94 and GFG97). The solid lines show the predicted blue and red edges of the instability strip with  $Z = 0.02$ , whereas the dashed lines refer to  $Z = 0.008$ .

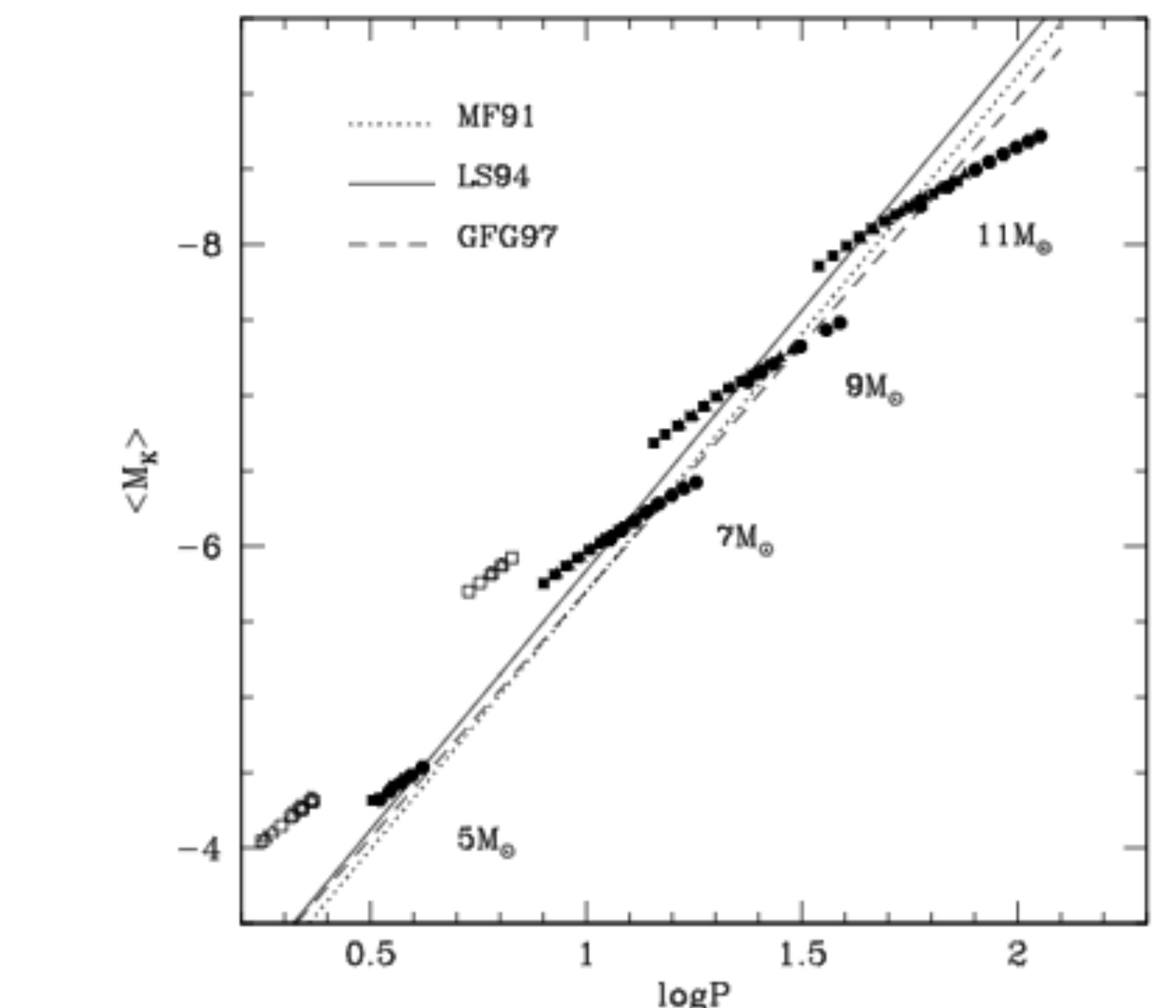


FIG. 6.—Same as in Fig. 3, but for infrared magnitudes

# Theoretical Models for Classical Cepheids

Giuseppe Bono (Paper 5)

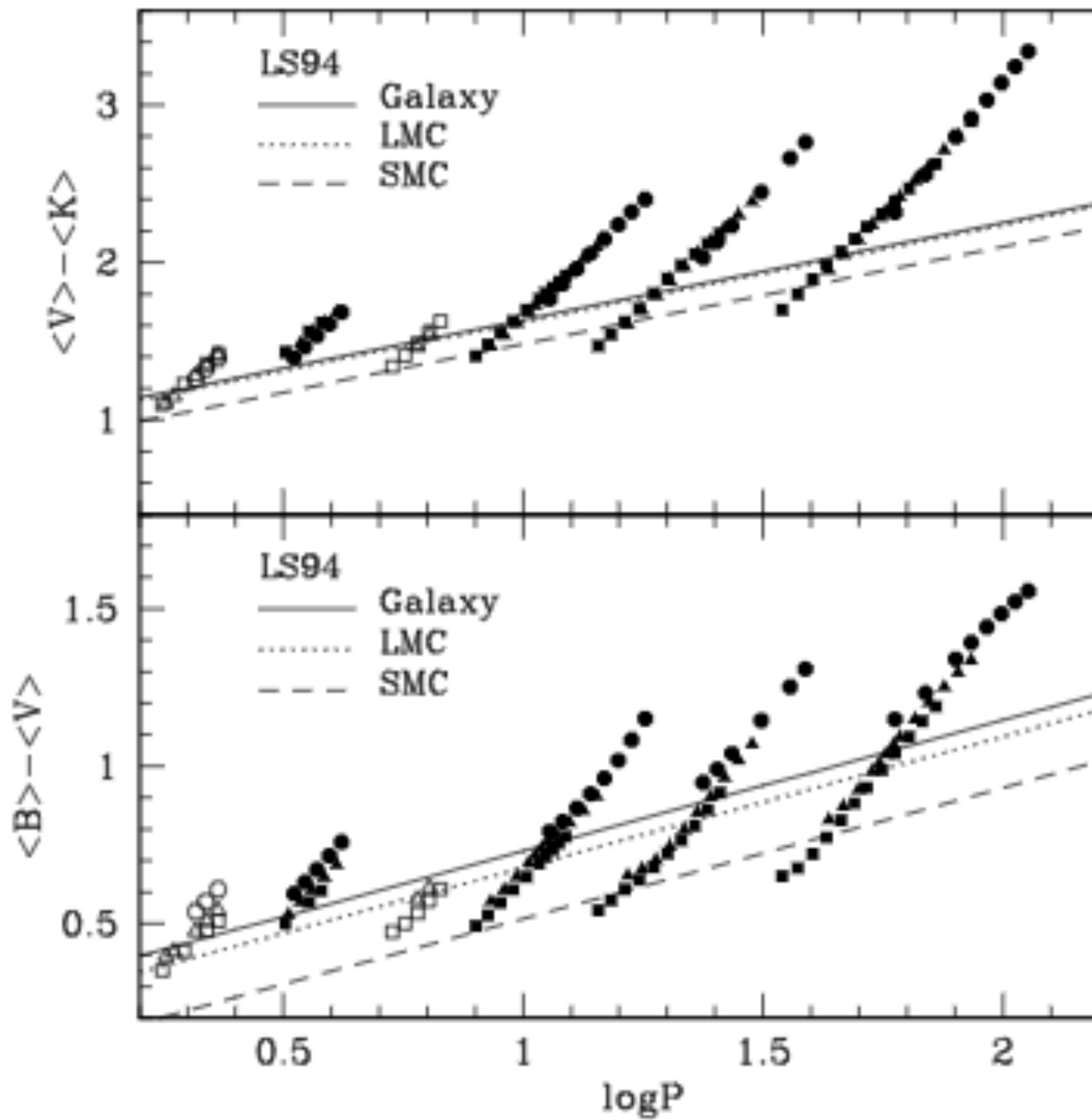


FIG. 10.—Comparison between theoretical models and empirical  $\log P$ –( $B$ – $V$ ) (bottom) and  $\log P$ –( $V$ – $K$ ) (top) relations from LS94. The symbols are as in Fig. 1.

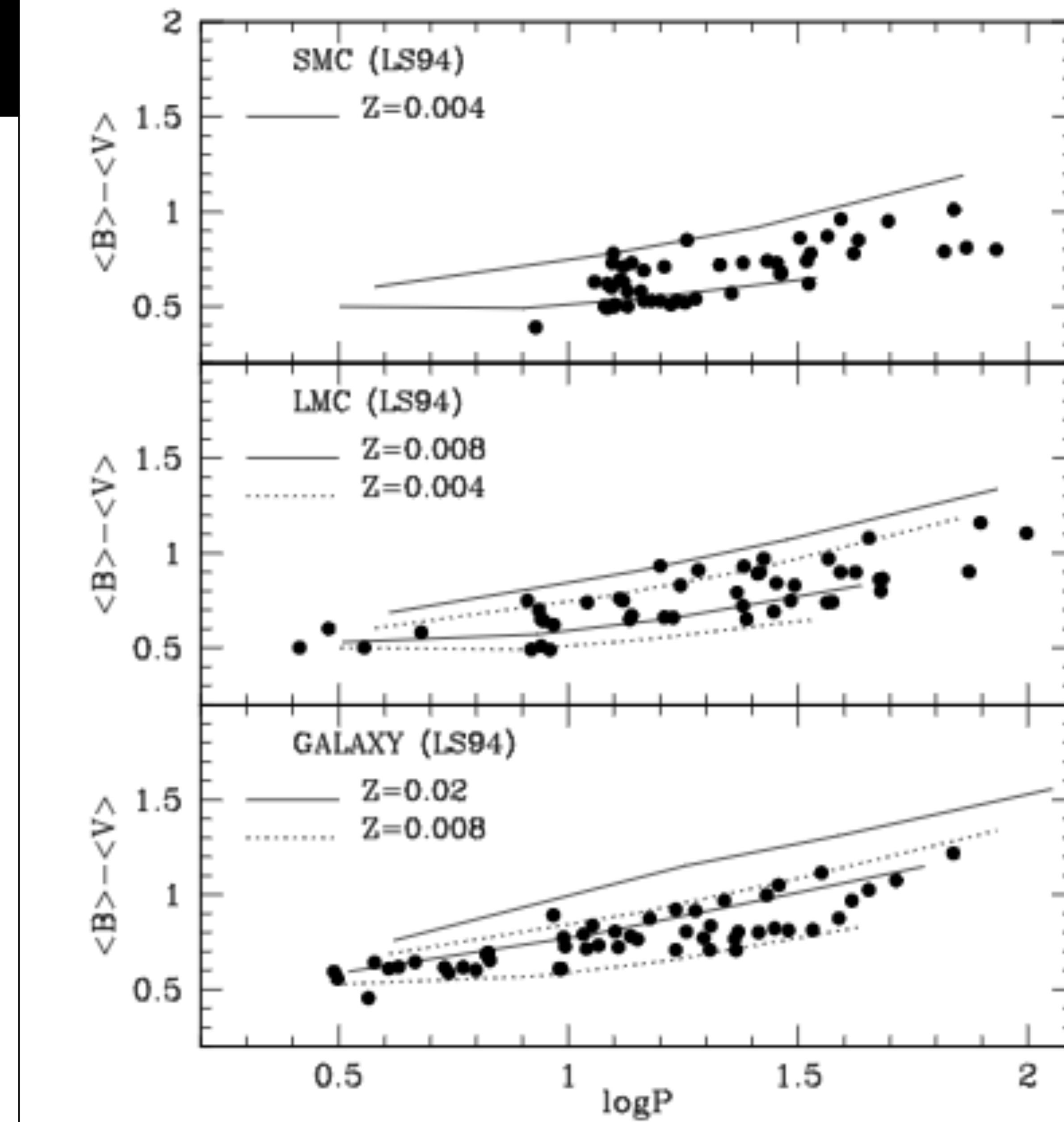


FIG. 11.—Comparison between LS94 data for Galactic and Magellanic Cepheids in the  $\log P$ –( $B$ – $V$ ) plane and the predicted edges of the instability strip at the three labeled metallicities.

$$\langle M_V \rangle = \alpha + \beta \log P + \gamma(\langle B \rangle - \langle V \rangle)$$

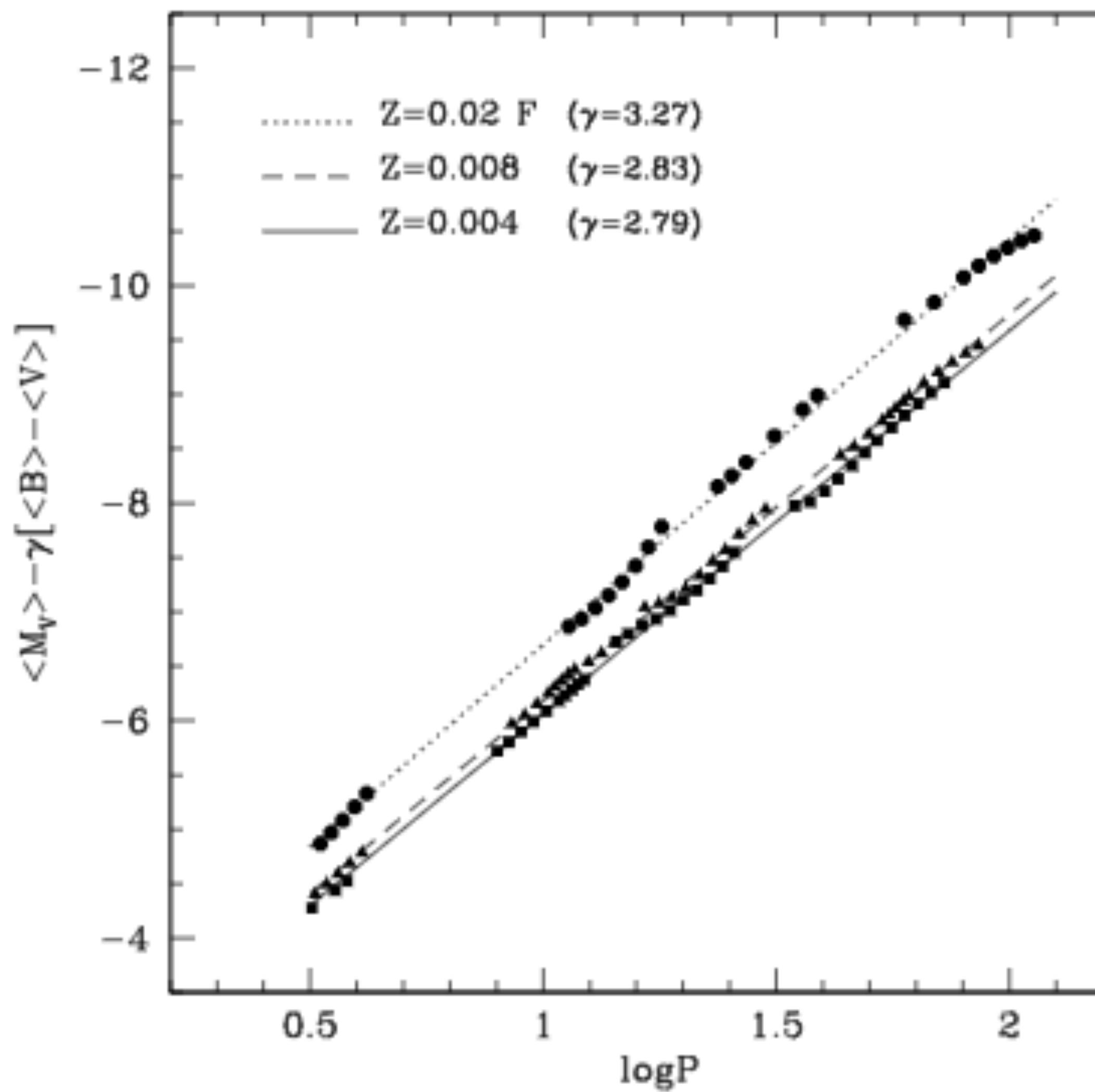


FIG. 16.—Predicted (projected onto a plane) optical PLC relations for fundamental pulsators with different chemical compositions (see Table 1). The symbols are as in Fig. 1.

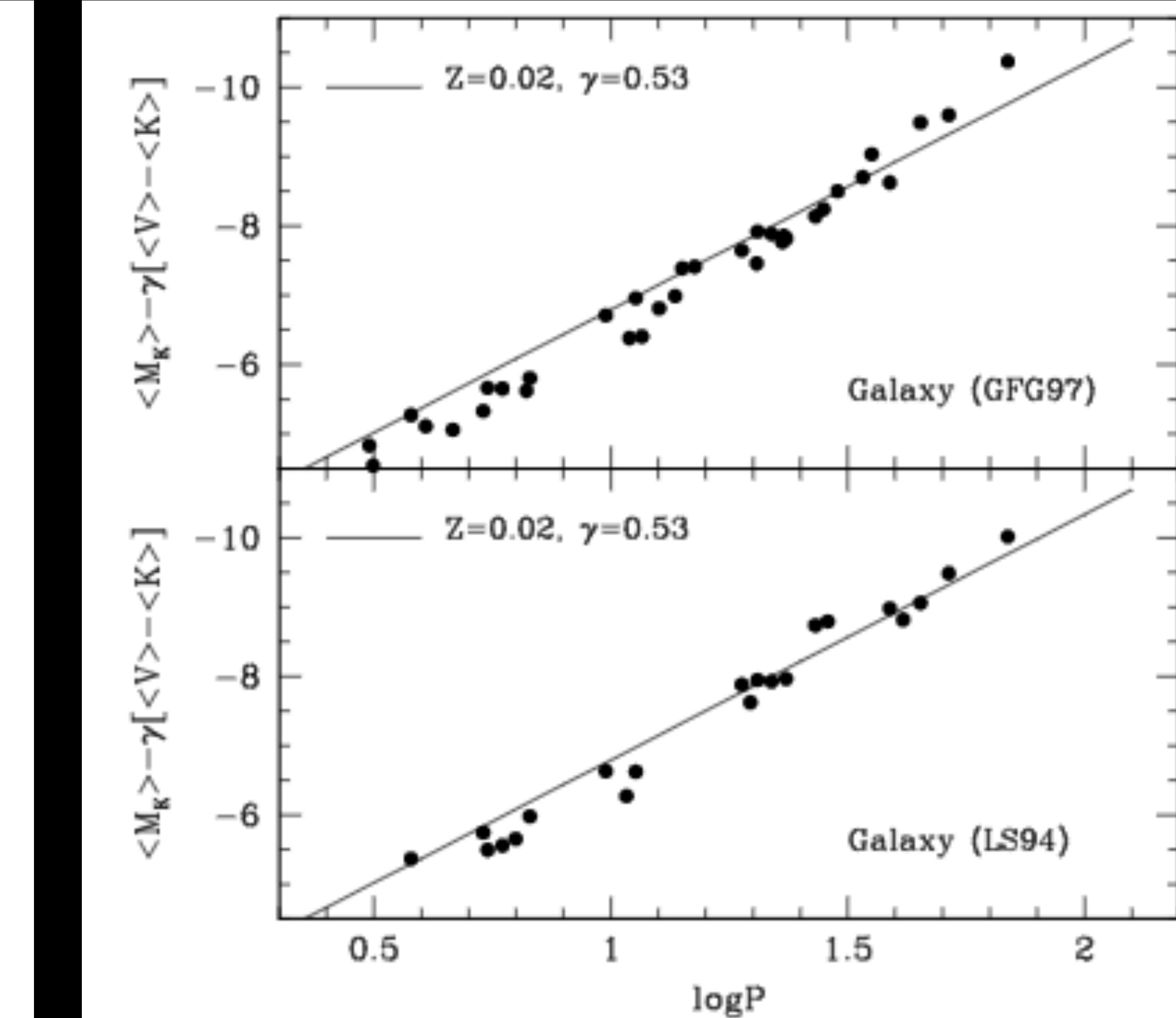


FIG. 20.—The theoretical projected infrared PLC relation for  $Z = 0.02$  (solid line) compared with the location of Galactic Cepheids (filled points: data by LS94 and GFG97).

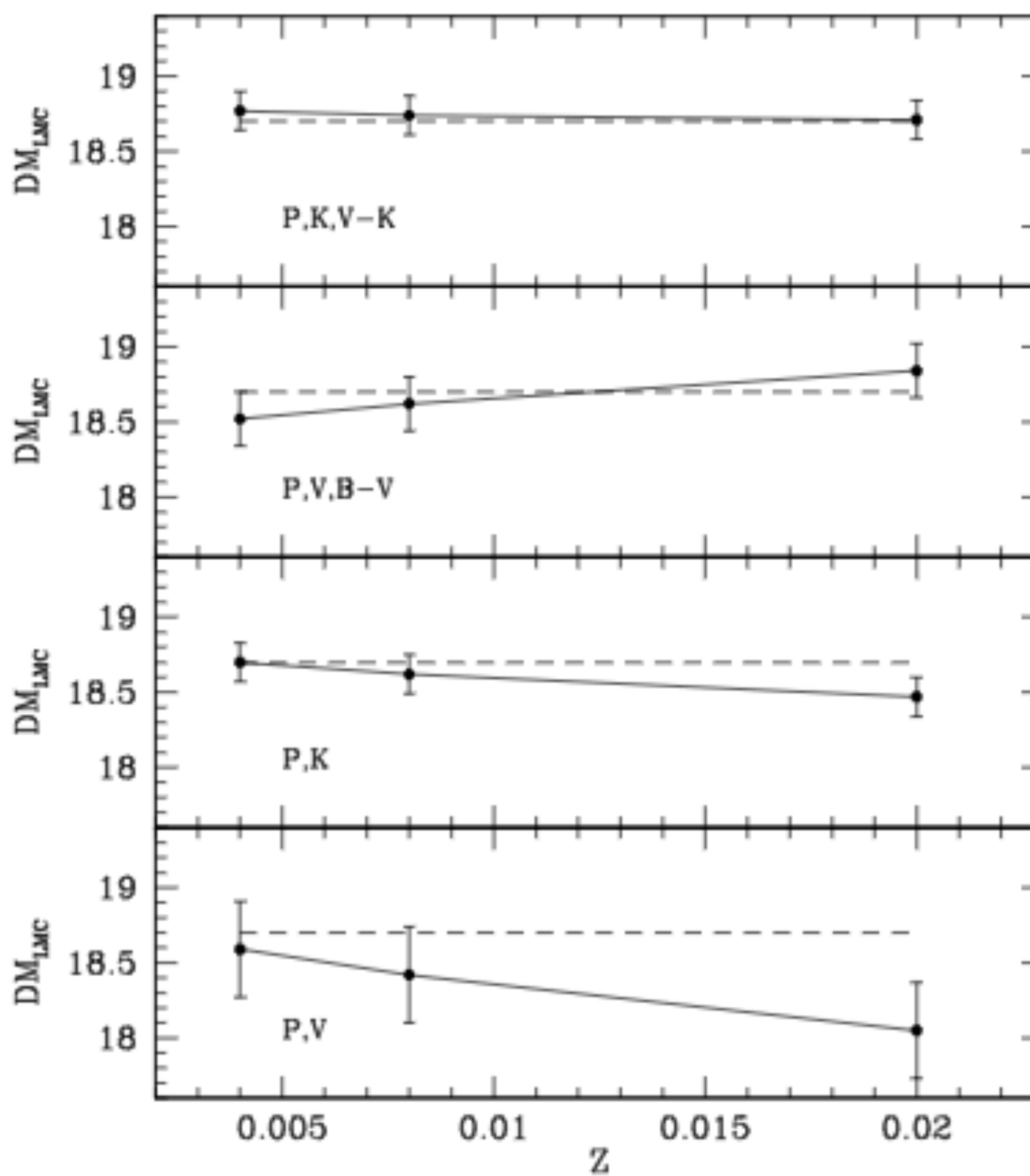


FIG. 21.—Individual distance modulus of LMC Cepheids (*filled points*), with the related error bar, as obtained from LS94 data and predicted PL and PLC relations with different metallicities. The dashed line is a reference distance modulus of 18.7 mag.

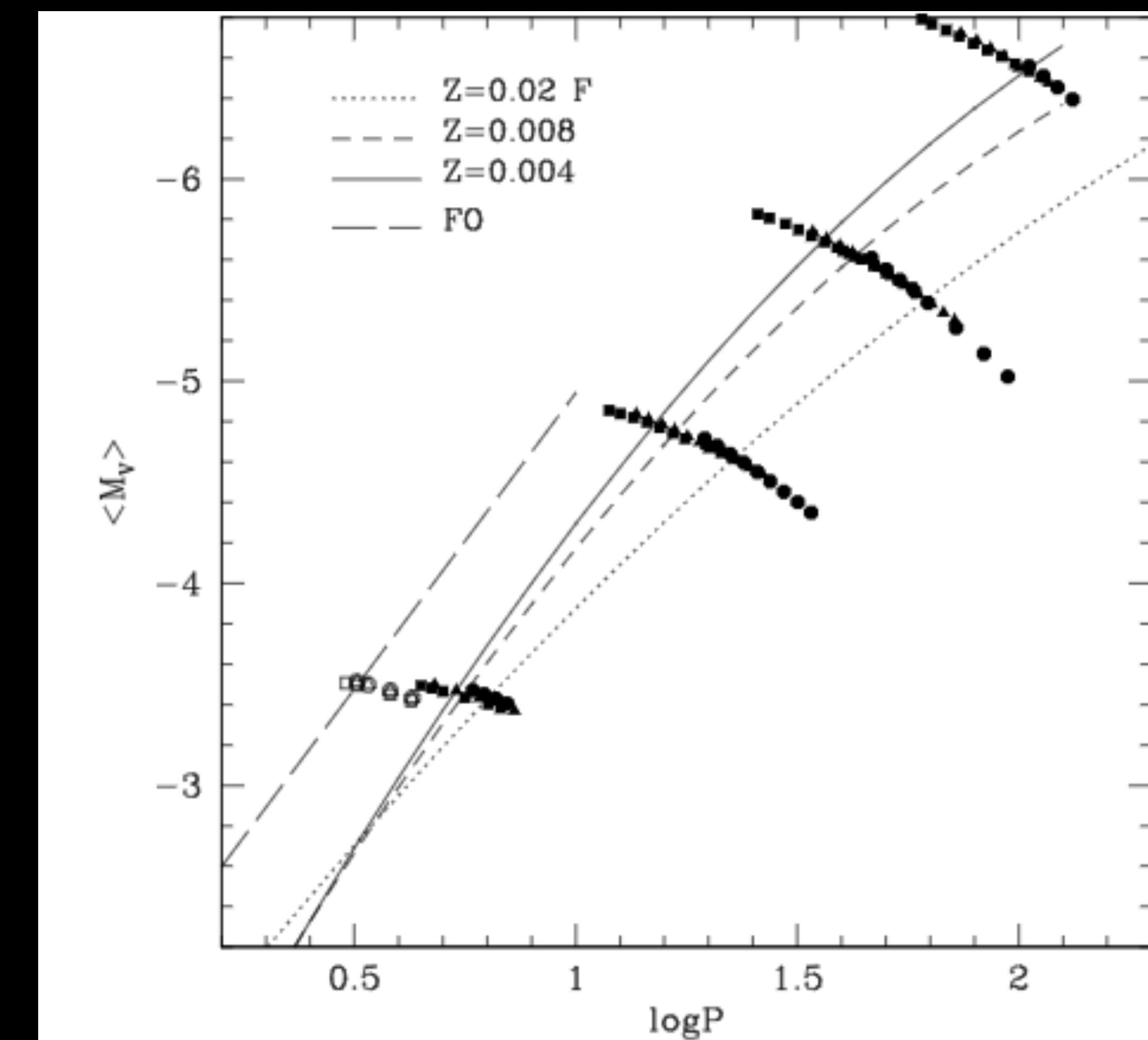
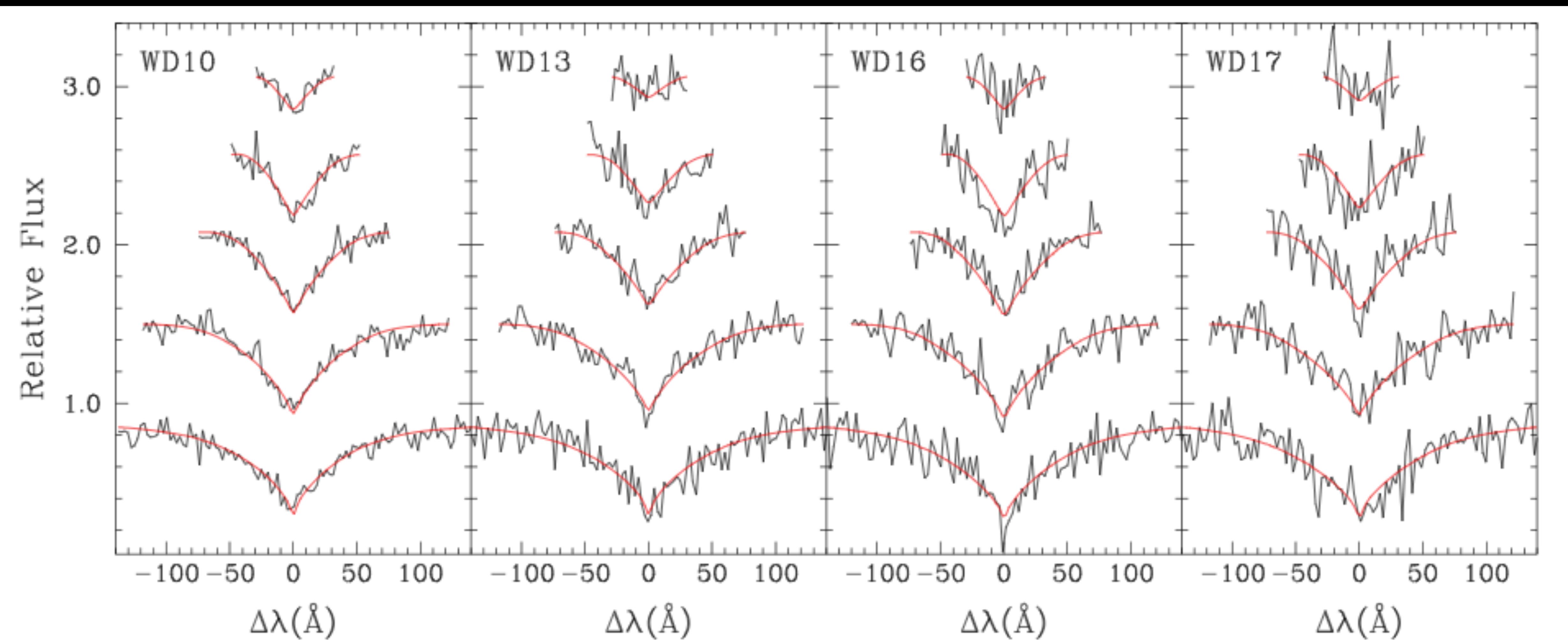


FIG. 22.—Comparison in the  $\log P - \langle M_V \rangle$  plane between sequences of nonlinear, convective models constructed by adopting the same values of the stellar mass and chemical compositions but different assumptions concerning the mass-luminosity relation. Open and filled symbols show the location of first-overtone and fundamental models whose luminosity has been fixed according to a noncanonical (mild overshooting) ML relation. The lines of different style show the analytical  $PL_{\langle M_V \rangle}$  relations derived by adopting the sequences of models whose luminosity has been fixed according to a canonical (no overshooting) ML relation. See text for further details.

# **The White Dwarf Initial-Final Mass Relation for progenitor Stars from 0.85 to 7.5 M sun (Paper 7)**

# The White Dwarf Initial Final Mass relation

Jeffrey D. Cummings



**Figure 1.** Balmer line fits for the co-added spectra of the four re-observed white dwarfs consistent with membership in NGC 2099, which are binned for display purposes. H $\beta$ , H $\gamma$ , H $\delta$ , H $\epsilon$ , and H8 are shown from bottom to top.

# The White Dwarf Initial Final Mass relation

Jeffrey D. Cummings

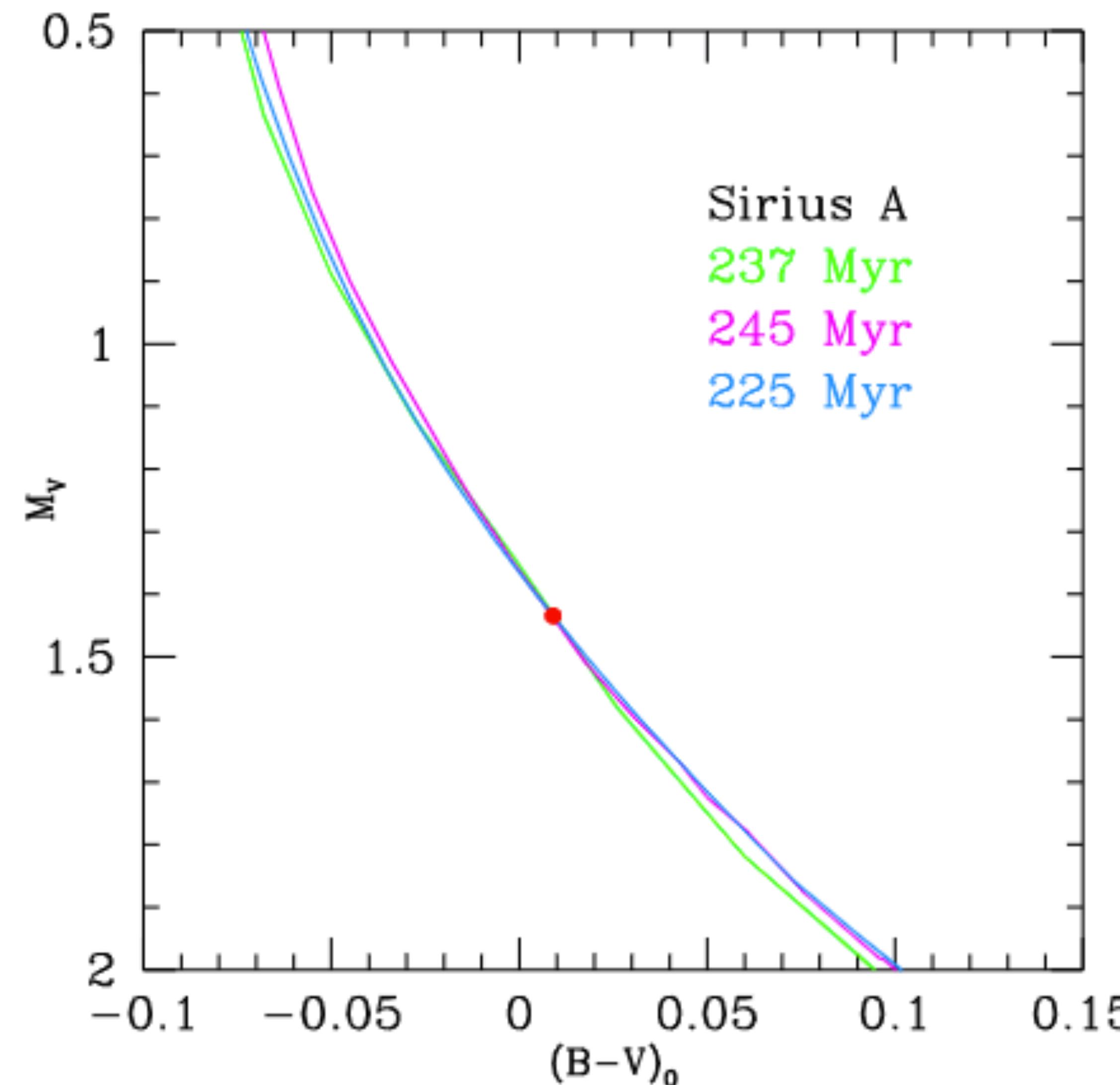


**Figure 2.** Color-magnitude diagram analysis of Sirius A using the  $\text{Y}^2$  (green), PARSEC (magenta), and MIST (blue) isochrones. The measured ages are given.

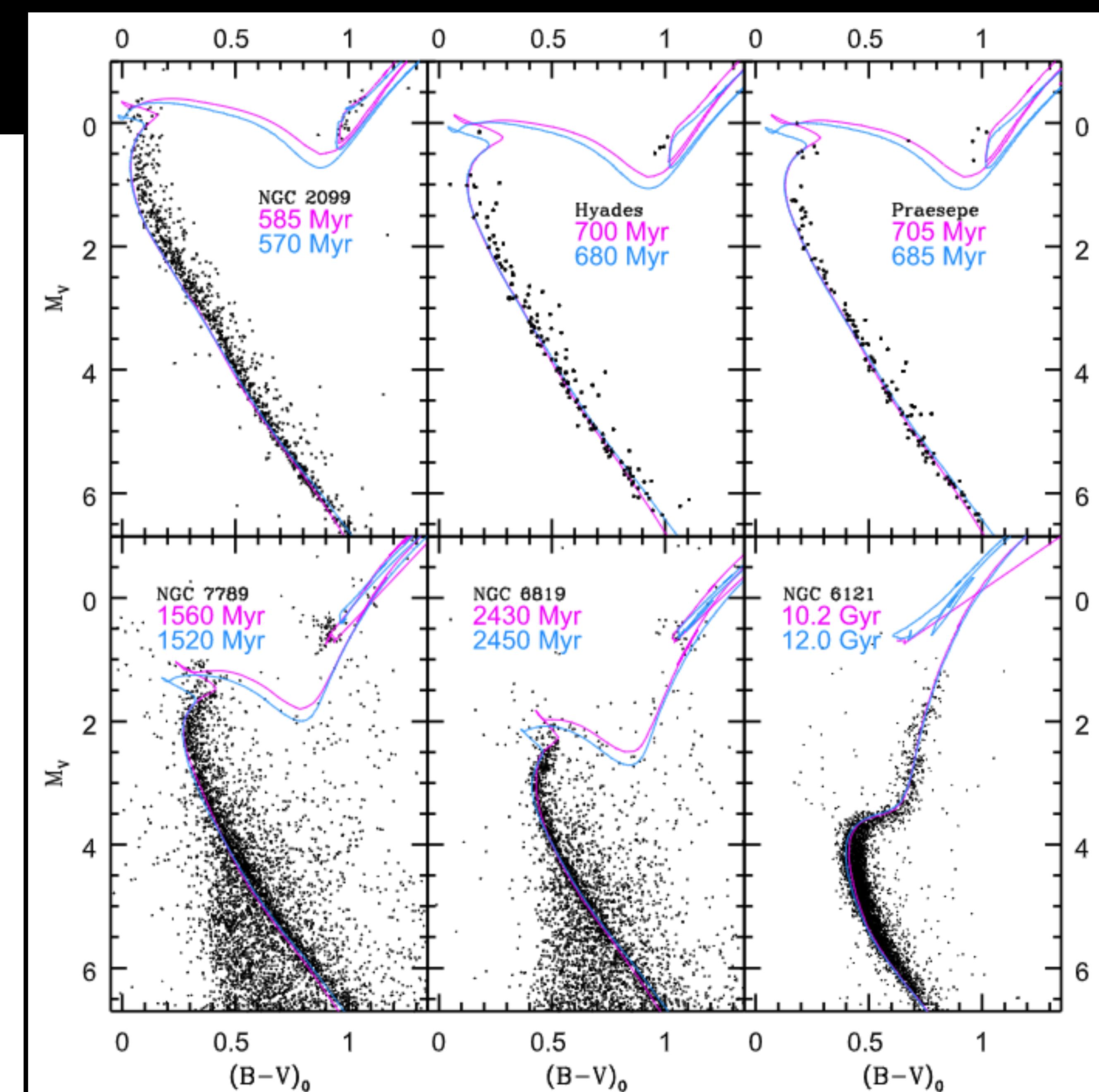


**Figure 3.** Color-magnitude analysis of the six older star clusters. The PARSEC isochrone ages are shown in magenta and the non-rotating MIST isochrone ages are shown in blue. See Table 2 for the photometric sources and the cluster parameters.

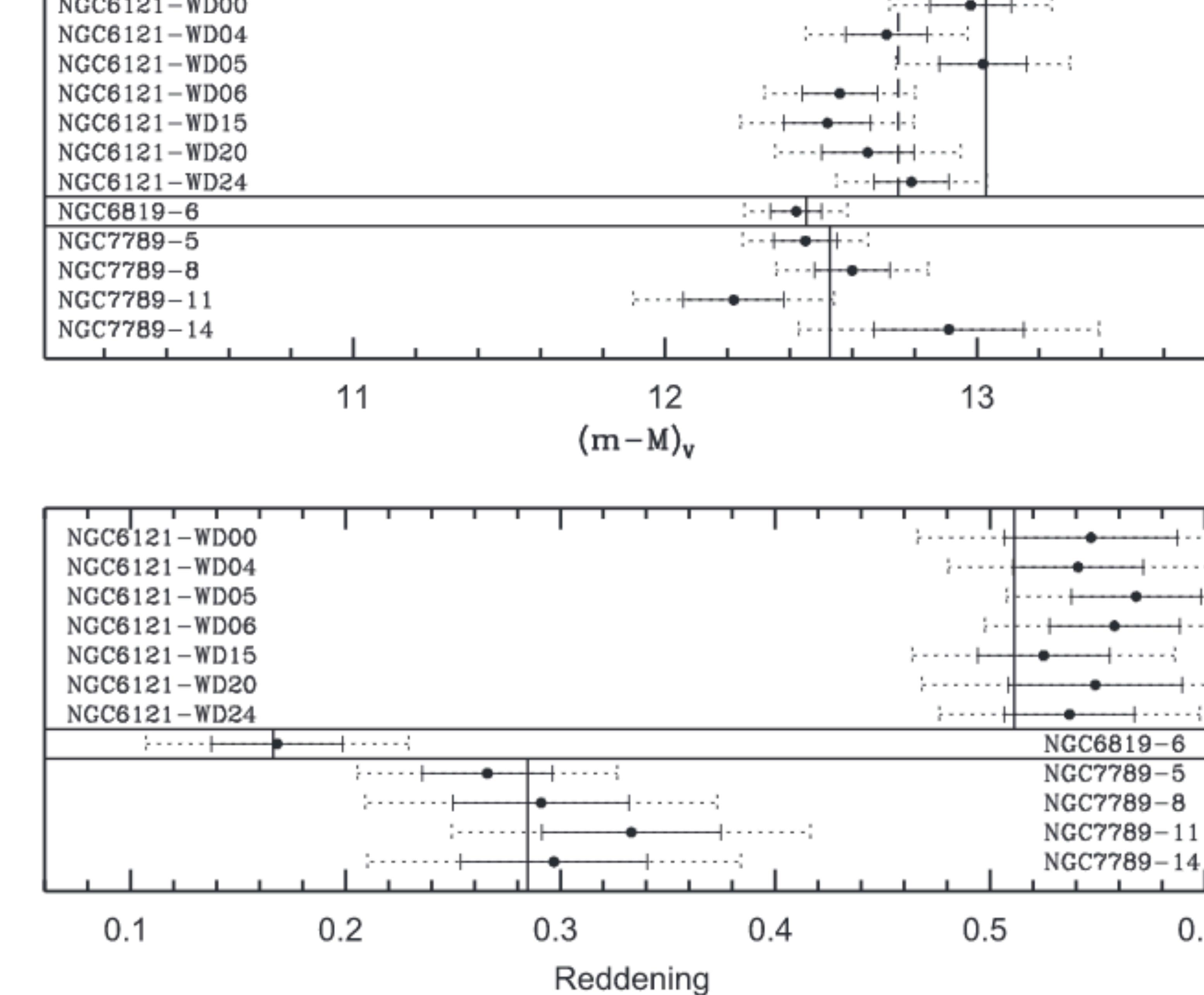


**Figure 4.** Upper panel: comparison of apparent distance modulus  $(m - M)_V$  of each white dwarf vs. the cluster's photometric distance modulus in Figure 3 (shown as solid vertical lines). For NGC 6121, however, systematic issues in the photometry results in a clear systematic offset of the photometric distance modulus and the mean distance modulus of the white dwarf members shown as a dashed vertical line. The solid error bars represent the  $\sigma$  errors and the dashed error bars on  $2\sigma$  errors. Lower panel: comparison of apparent reddening  $E(V - I)$  for NGC 6121 and apparent  $E(B - V)$  for NGC 6819 and NGC 7789. White dwarfs within  $2\sigma$  of both the cluster distance modulus and reddening are adopted as single-star members.

# The White Dwarf Initial Final Mass

## Jeffrey D. Cummings

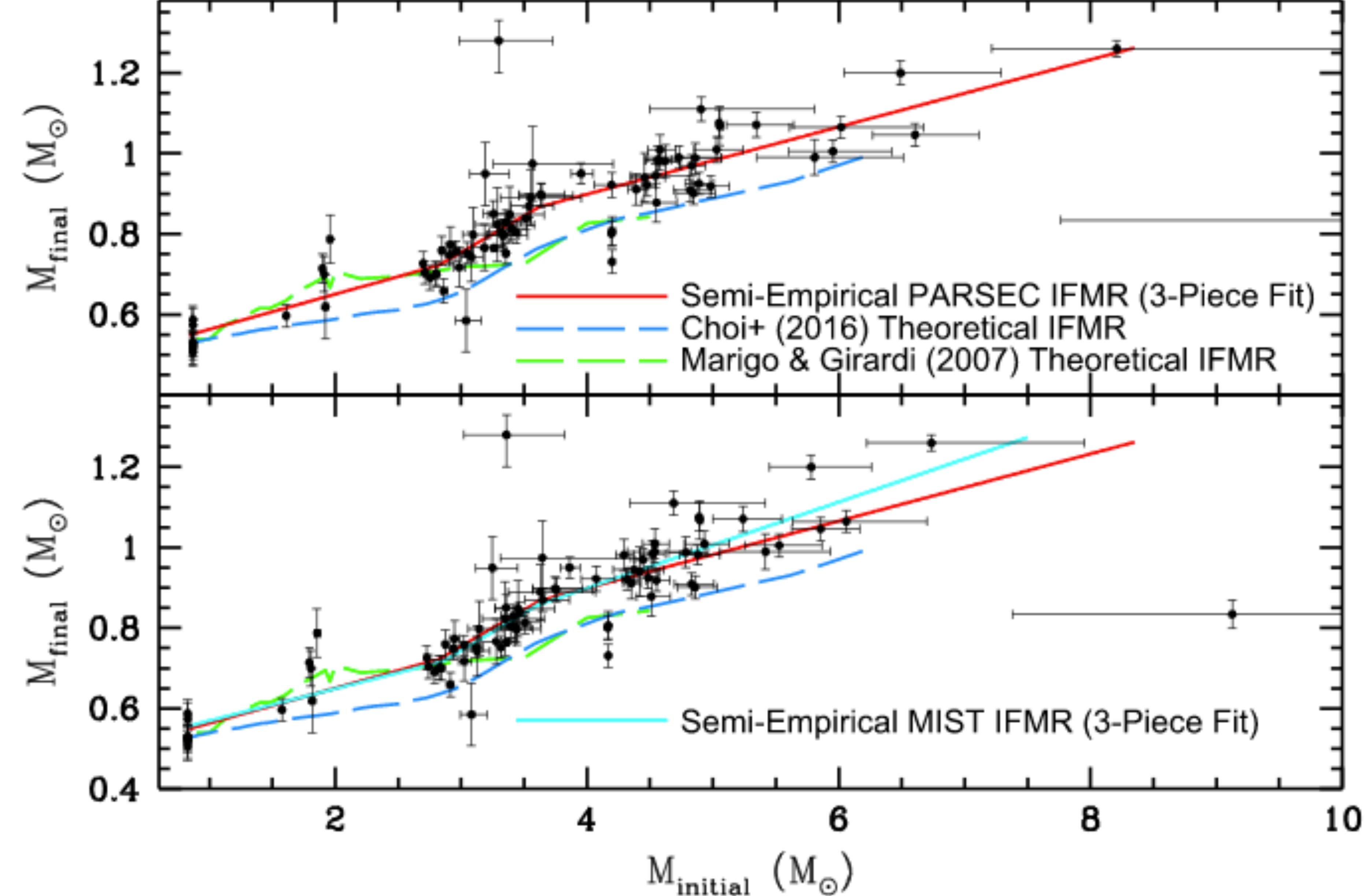


**Figure 5.** Upper panel: PARSEC-based IFMR data in black. The semi-empirical trend is in three pieces and is shown in red. The data are also compared to the theoretical IFMR from Choi et al. (2016) for non-rotating stars in dashed blue. The observed data show a remarkably consistent shape, but at intermediate and higher masses there is a systematic offset with the observed white dwarfs having masses  $\sim 0.1 M_{\odot}$  higher than theory predicts. Lower panel: comparable MIST-based IFMR data in black. A similar three-piece fit to this semi-empirical data is shown in cyan, with the same three-piece relation from the upper panel shown in red for comparison. These relations are consistent at lower and intermediate masses, but at high masses they begin to diverge with increasing mass. This also increases the systematic difference between the MIST-based IFMR and model at the highest masses.

# The White Dwarf Initial Final Mass relation

## Jeffrey D. Cummings

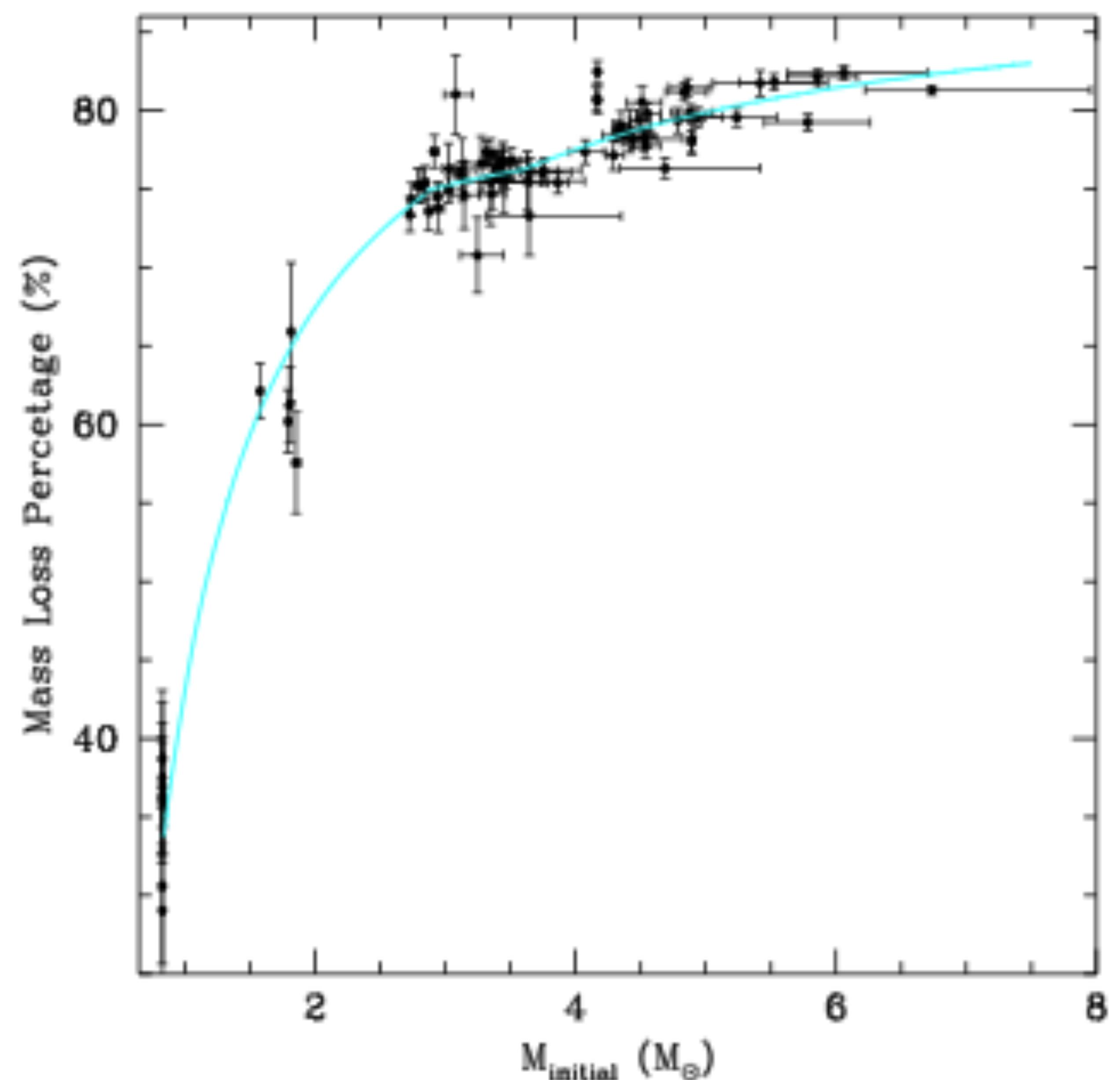


**Figure 6.** From the MIST-based IFMR we plot the total mass loss that occurs throughout a star's lifetime as a percentage of its  $M_{\text{initial}}$ . This mass loss ranges from 33% at  $M_{\text{initial}}$  of  $0.83 M_{\odot}$  to 83% at  $M_{\text{initial}}$  of 7.5. The trend in cyan is a direct conversion of the relation shown in cyan in the lower panel of Figure 5.

# **Evidence for terrestrial Planetary System Remnants at White Dwarfs**

**(Paper 8)**

# Evidence for terrestrial Planetary System Remnants at White Dwarfs

J. Farihi

- DBZ/ DZ:  
(D) Degenerate stars,  
(B) warm enough to exhibit helium lines,  
(Z) for metallic features
- If metals dominates over features of Hydrogen we suspect that came from external polluter

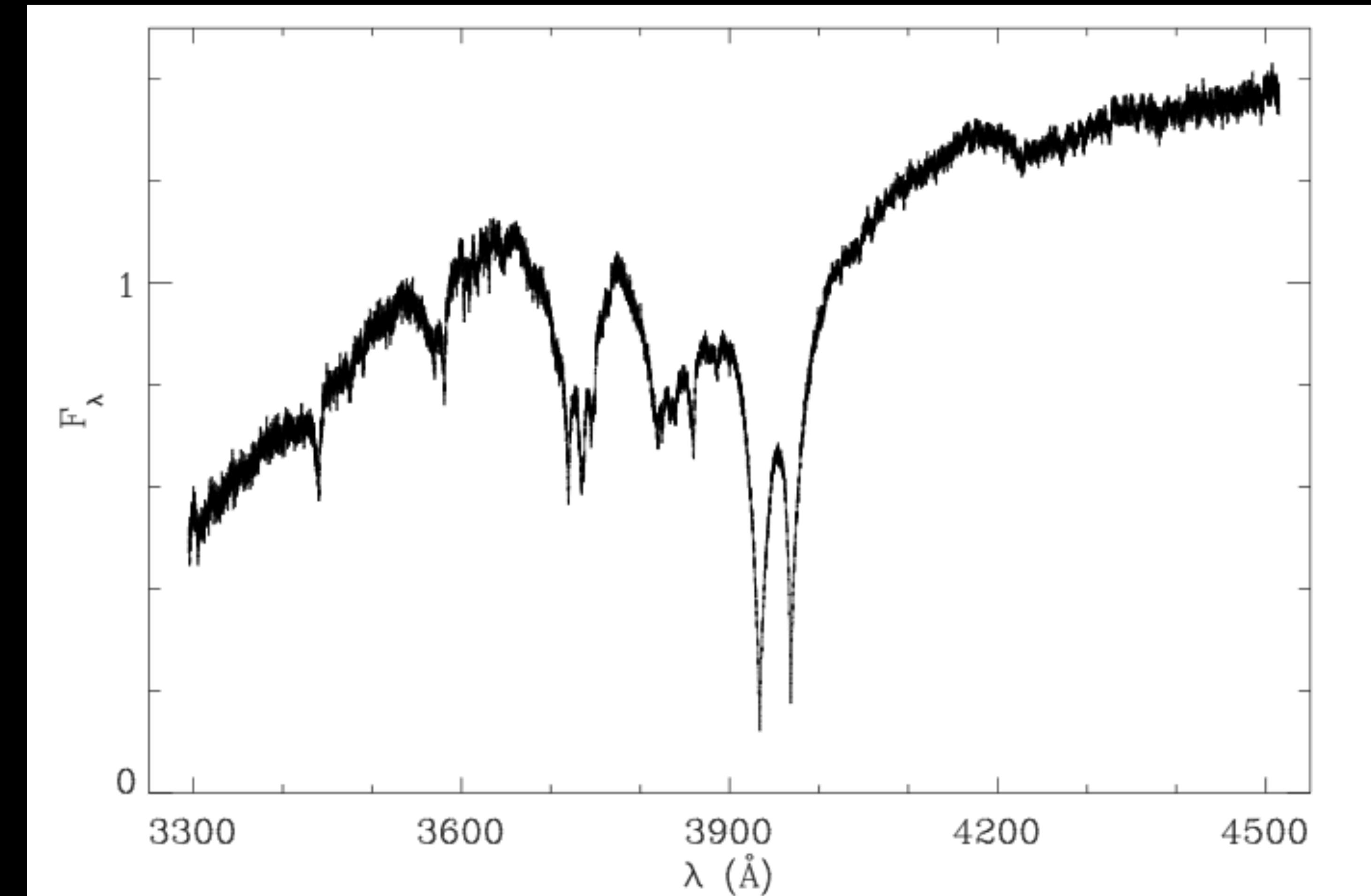


**FIGURE 1.** vMa 2 was the third white dwarf to be discovered (van Maanen 1919), and is the prototype of the DZ spectral class. This  $R \approx 20000$  VLT UVES spectrum (which extends to 6700 $\text{\AA}$ ) reveals only metallic lines of iron, calcium, and magnesium; the pollution is refractory-rich yet hydrogen deficient. From the SPY project (Napiwotzki et al. 2003).

# Evidence for terrestrial Planetary System Remnants at White Dwarfs

J. Farihi

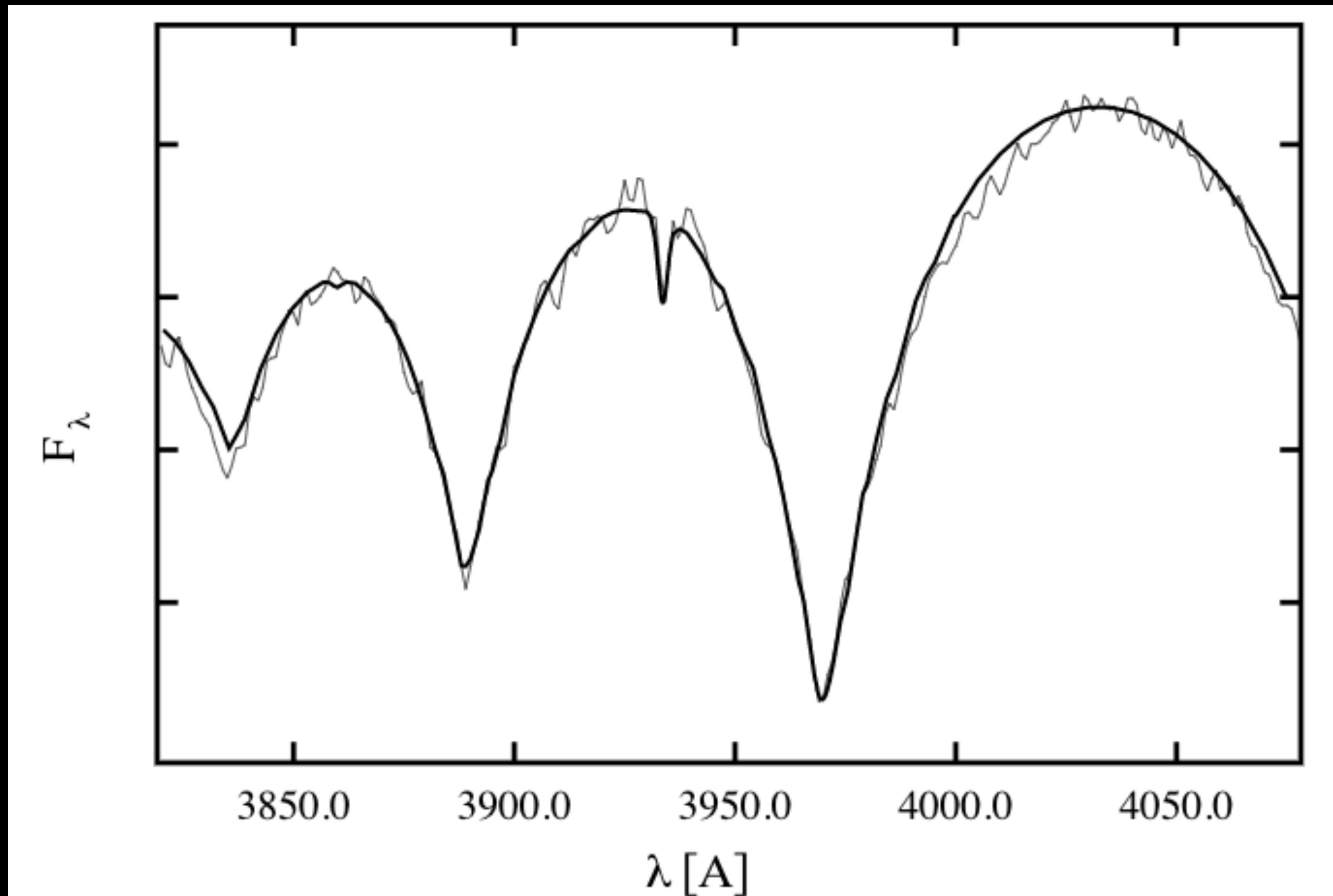


**FIGURE 2.** The detection of the Ca II K-line in the optical spectrum of G29-38. Note the much stronger line seen in vMa 2 represents an abundance 1500 times lower than determined for G29-38. Line strength is a strong function of atmospheric composition (i.e. hydrogen or helium) and stellar effective temperature. From Koester et al. (1997).

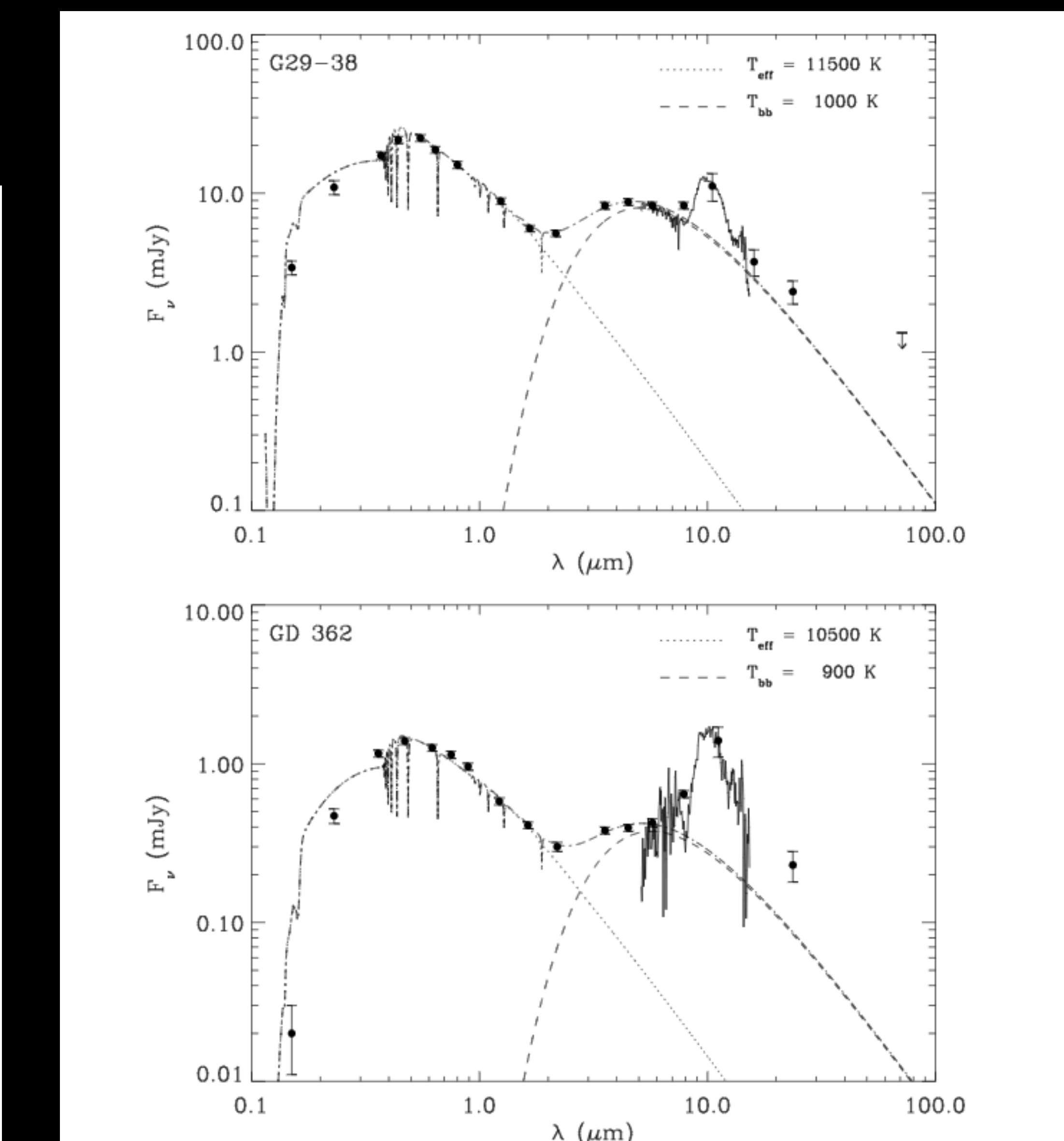


**FIGURE 3.** The broad SEDs of G29-38 and GD 362. The data points with error bars show short wavelength and *Spitzer* photometry fitted by 1) stellar atmosphere models drawn as dotted lines, and 2) thermal blackbody models shown as dashed lines. Also shown are their *Spitzer* infrared spectra revealing strong silicate emission from olivine particles (Jura et al. 2007b; Reach et al. 2005).

# Evidence for terrestrial Planetary System Remnants at White Dwarfs

J. Farihi

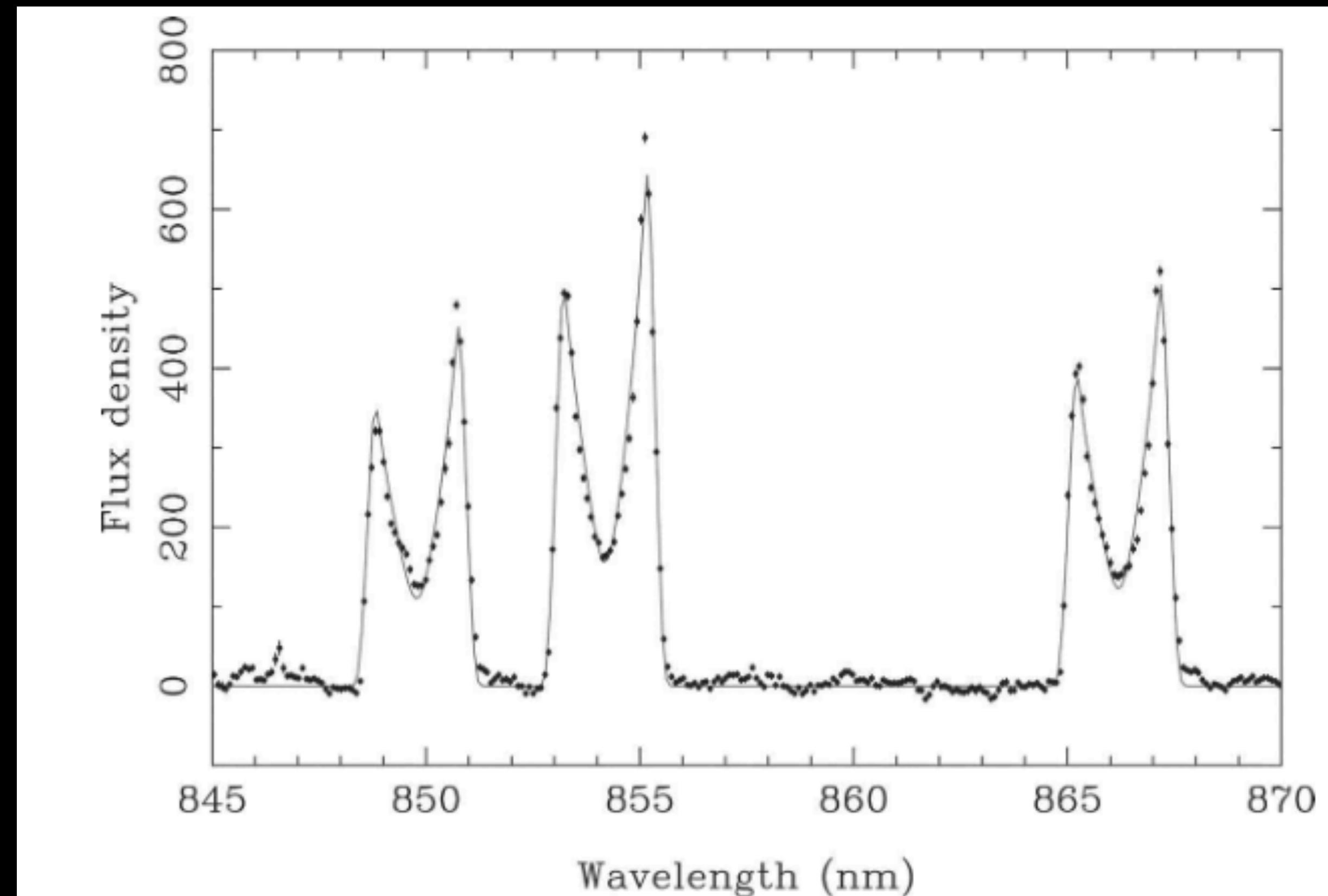


**FIGURE 4.** Calcium emission in the optical spectrum of SDSS 1228. The width of the emission lines indicates Keplerian rotation at  $\pm 630 \text{ km s}^{-1}$ . Emission lines from iron are also seen in this star, but not from hydrogen or helium. From Gänsicke et al. (2006).

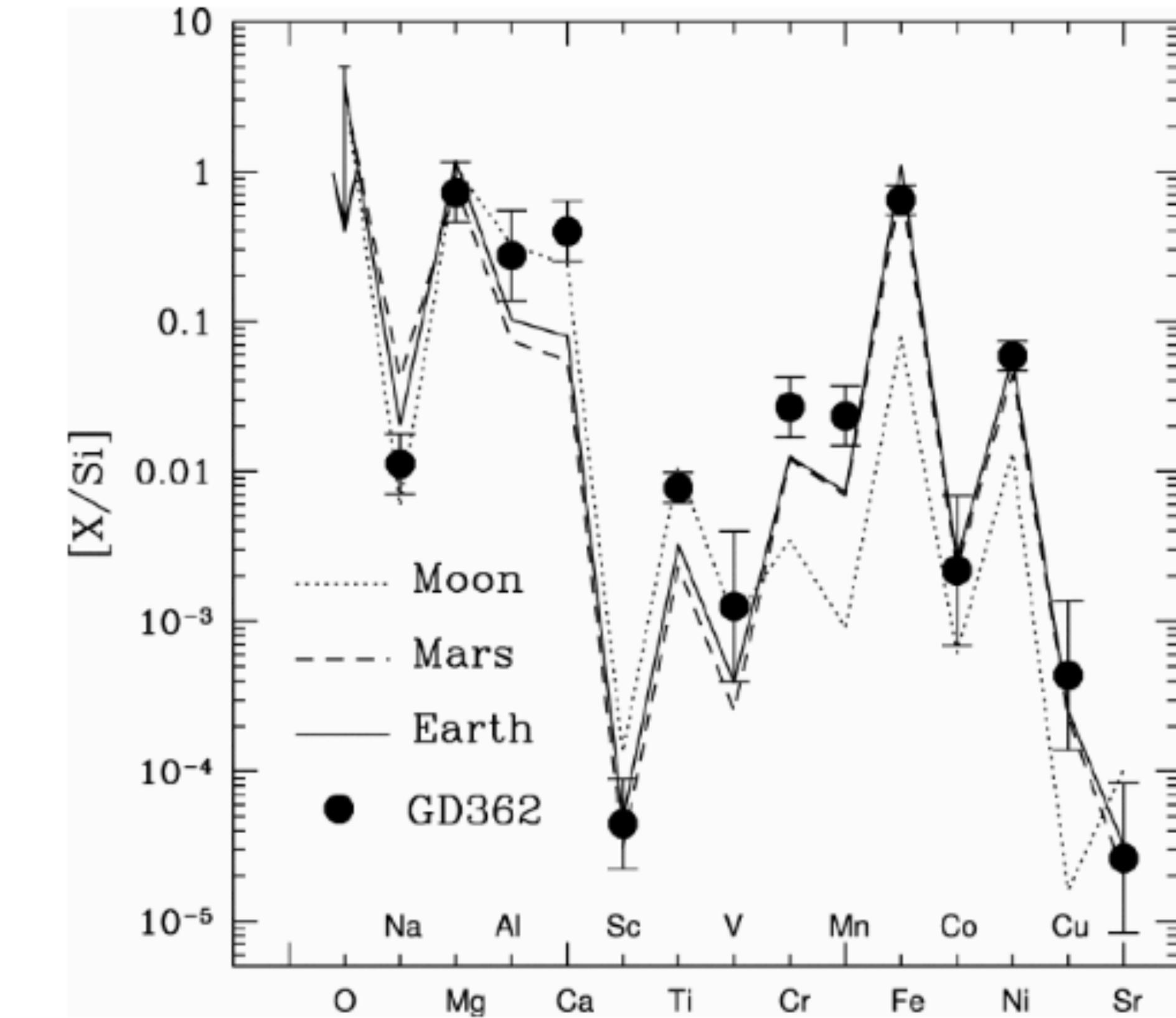


**FIGURE 5.** Fifteen elements heavier than helium in the highly contaminated photosphere of GD 362 reveal a pattern that is similar to a combination of Earth and Moon compositions. From Zuckerman et al. (2007).

# Evidence for terrestrial Planetary System Remnants at White Dwarfs

J. Farihi

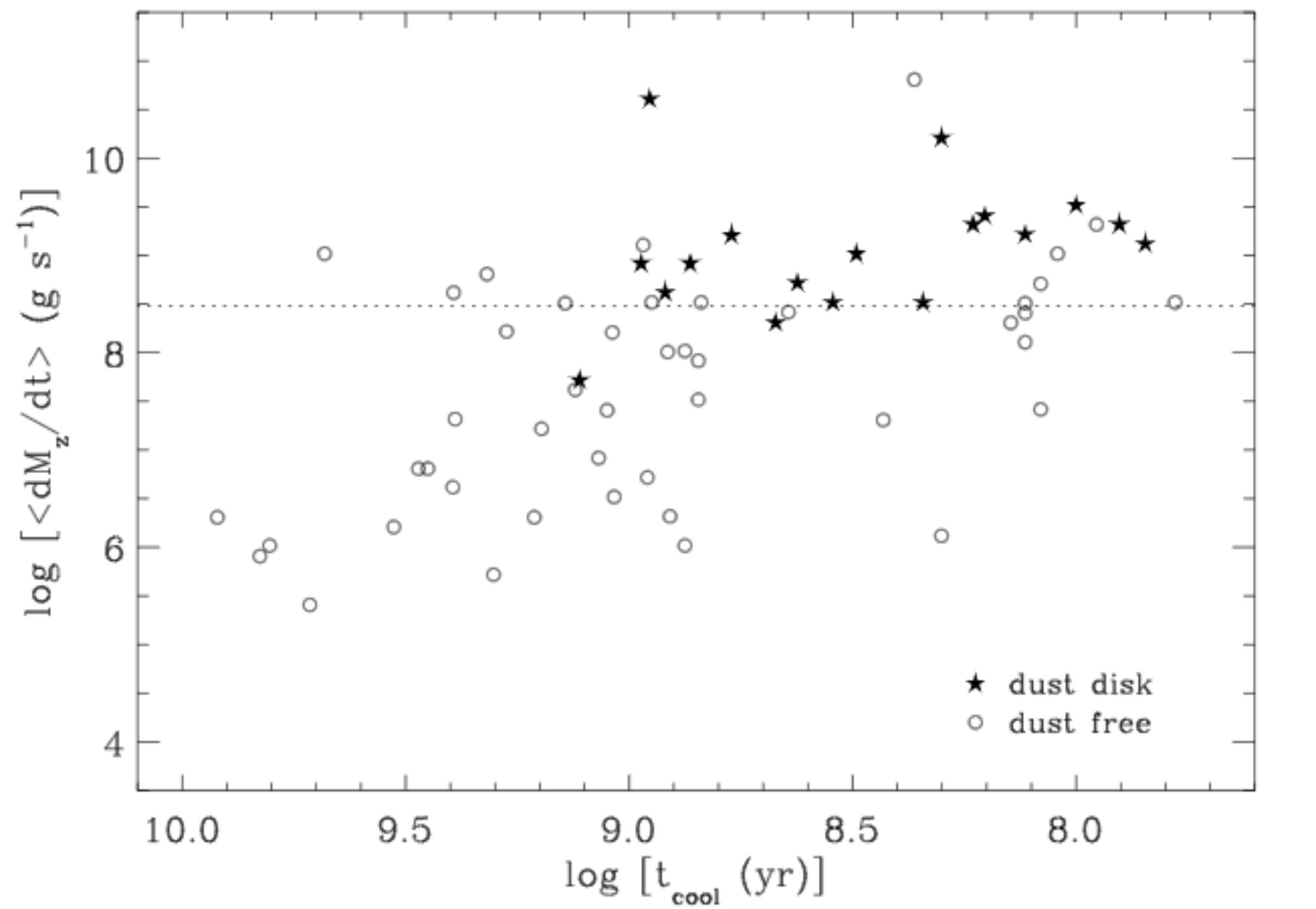


**FIGURE 6.** Dust disk frequency among all 61 metal-rich white dwarfs observed by *Spitzer* IRAC. Plotted on are the time-averaged metal accretion rate and cooling age for each star. The dotted line corresponds to  $3 \times 10^8 \text{ g s}^{-1}$ . G166-58 is the only star with a disk that is located significantly below this accretion rate benchmark, and with a cooling age beyond 1 Gyr (Farihi et al. 2008b). Adapted from Farihi et al. (2010c).

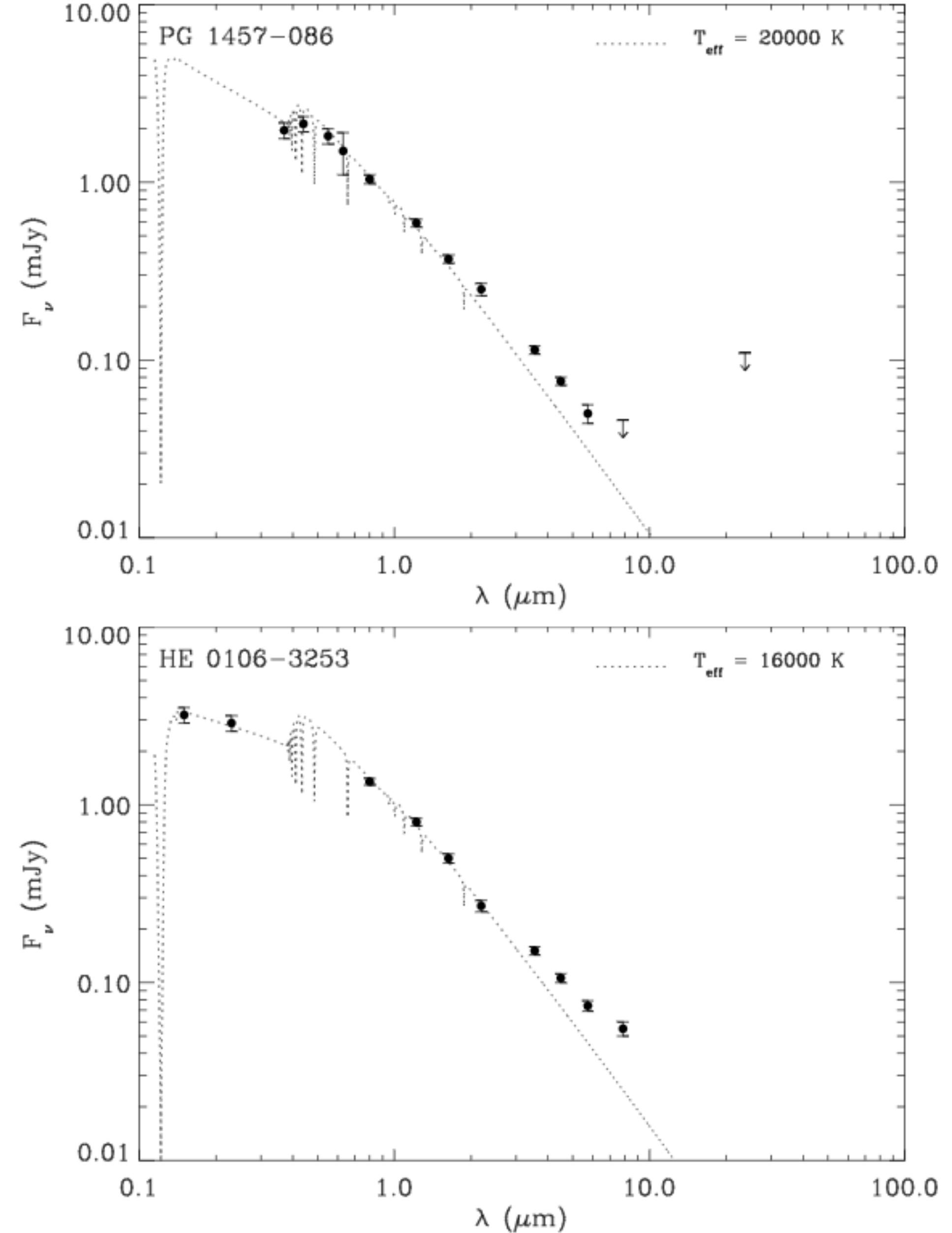


**FIGURE 7.** The two most subtle infrared excesses detected from narrow, circumstellar dust rings (Farihi et al. 2010c, 2009). Without supporting short wavelength data, the infrared photometry would have been difficult to interpret as an excess with confidence.

# Evidence for terrestrial Planetary System Remnants at White Dwarfs

J. Farihi

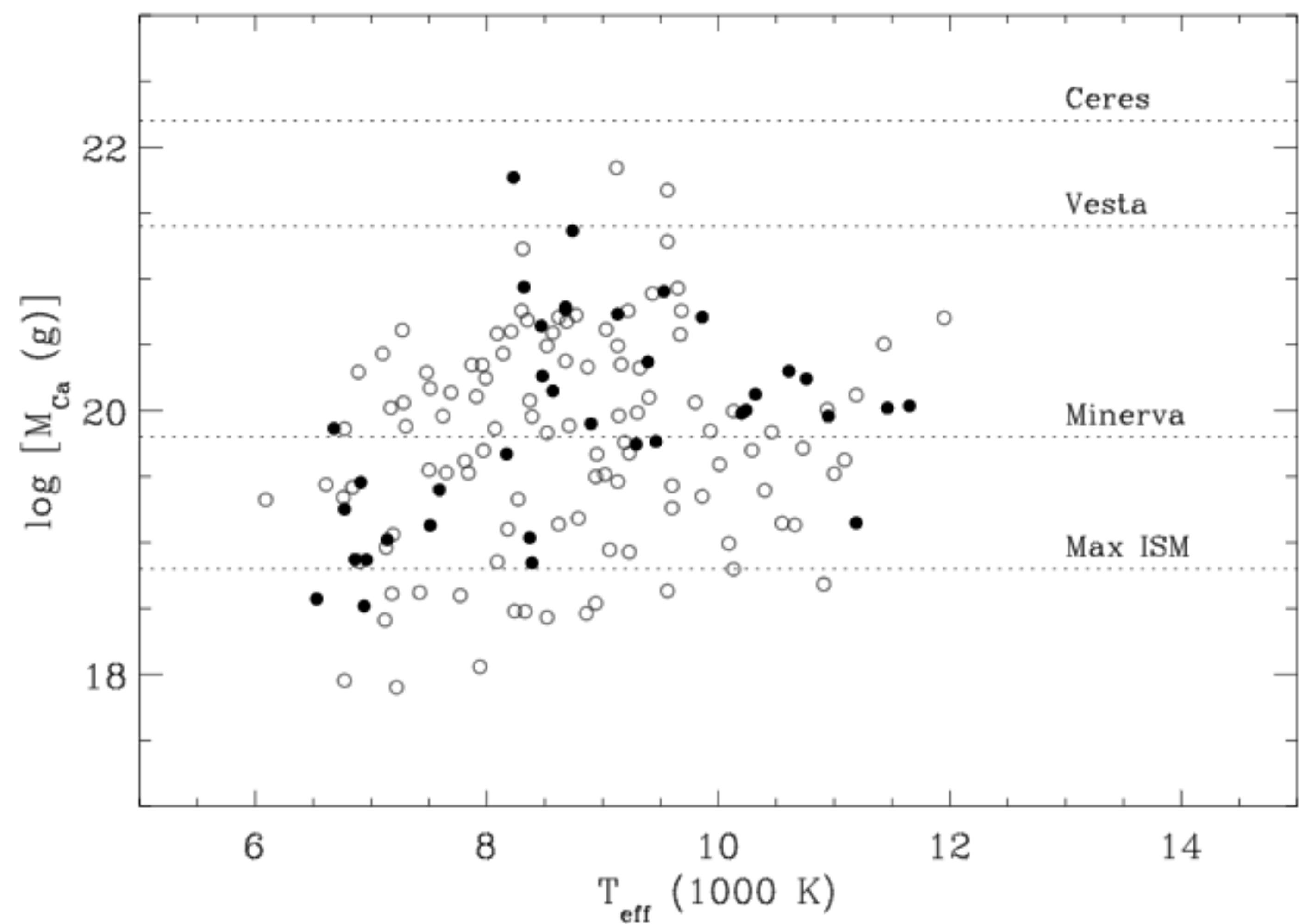


**FIGURE 8.** Calcium masses in the convective envelopes of 146 DBZ stars from the SDSS. The open and filled circles represent stars with and without trace hydrogen, respectively. The top three dotted lines mark the mass of calcium contained in the two largest Solar System asteroids Ceres and Vesta, and the 150 km diameter asteroid Minerva, assuming calcium is 1.6% by mass as in the bulk Earth (Allègre et al. 1995). The dotted line at the bottom is the maximum mass of calcium that can be accreted over  $10^6 \text{ yr}$  by a cool white dwarf moving at a velocity of  $50 \text{ km s}^{-1}$  through an interstellar cloud with a density of  $1000 \text{ cm}^{-3}$ . Adapted from Farihi et al. (2010a).

**Dinamic atmospheres and winds of cool  
luminous giants**

**(Paper 9)**

# Dinamic atmospheres and winds of cool luminous giants

S. Hofner

- The paper ask if the molecule that they are studying is able to drive winds or not

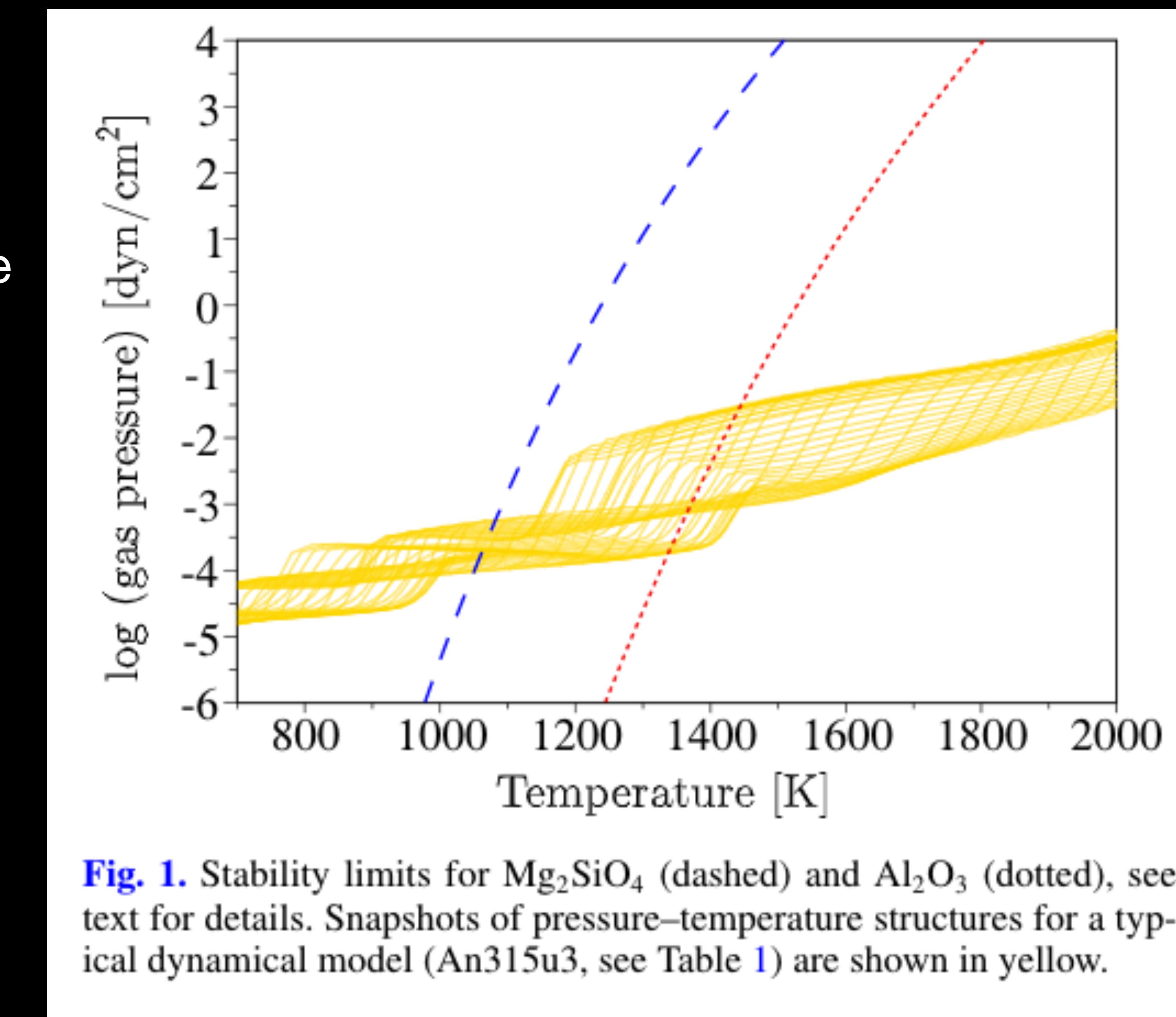


**Fig. 1.** Stability limits for  $\text{Mg}_2\text{SiO}_4$  (dashed) and  $\text{Al}_2\text{O}_3$  (dotted), see text for details. Snapshots of pressure–temperature structures for a typical dynamical model (An315u3, see Table 1) are shown in yellow.

# Dinamic atmospheres and winds of cool luminous giants

S. Hofner

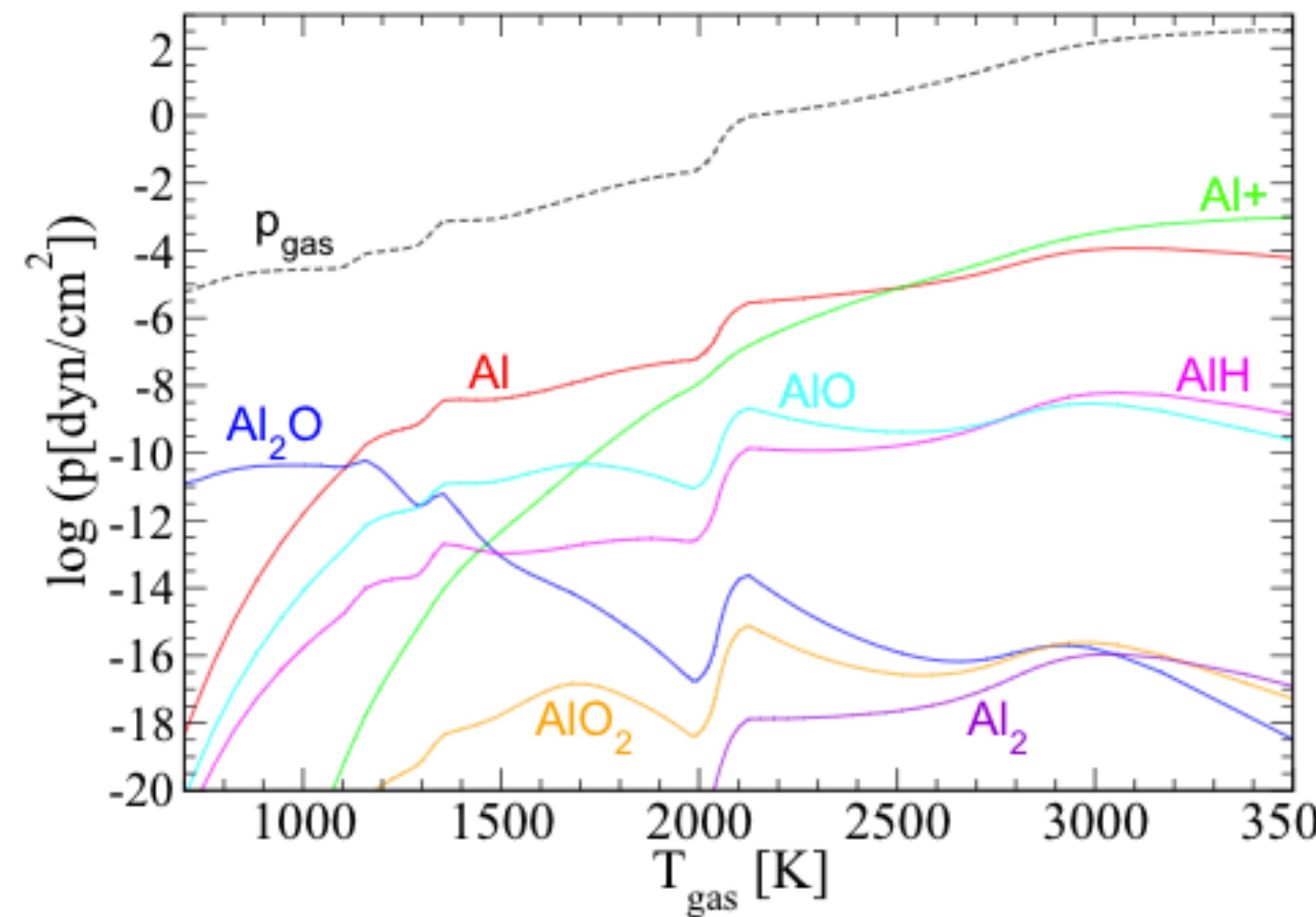


**Fig. 2.** Partial pressures of Al-bearing atomic and molecular species versus gas temperature for a snapshot taken from a typical model (An315u3, see Table 1). The values are computed assuming chemical equilibrium in the gas phase.

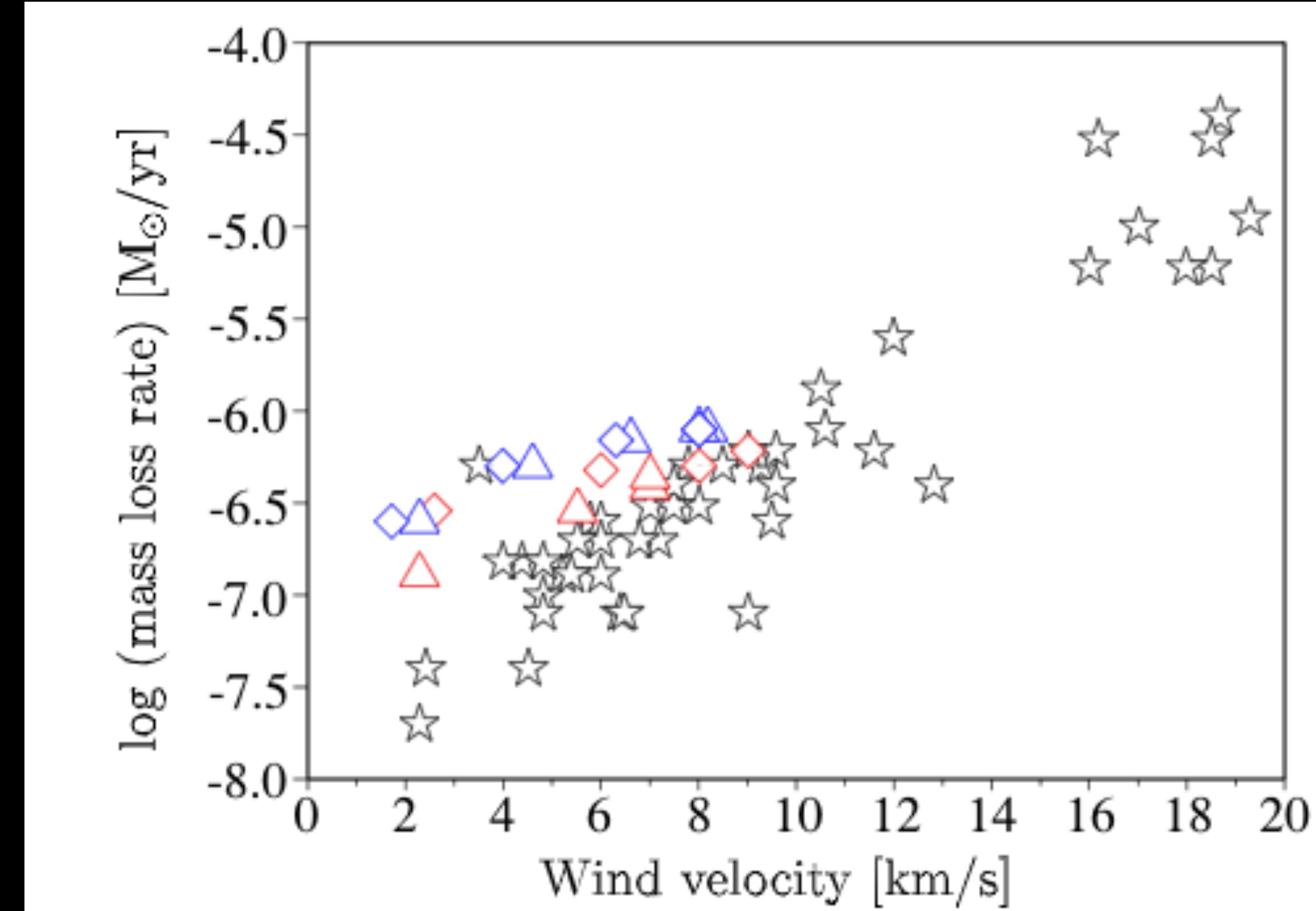
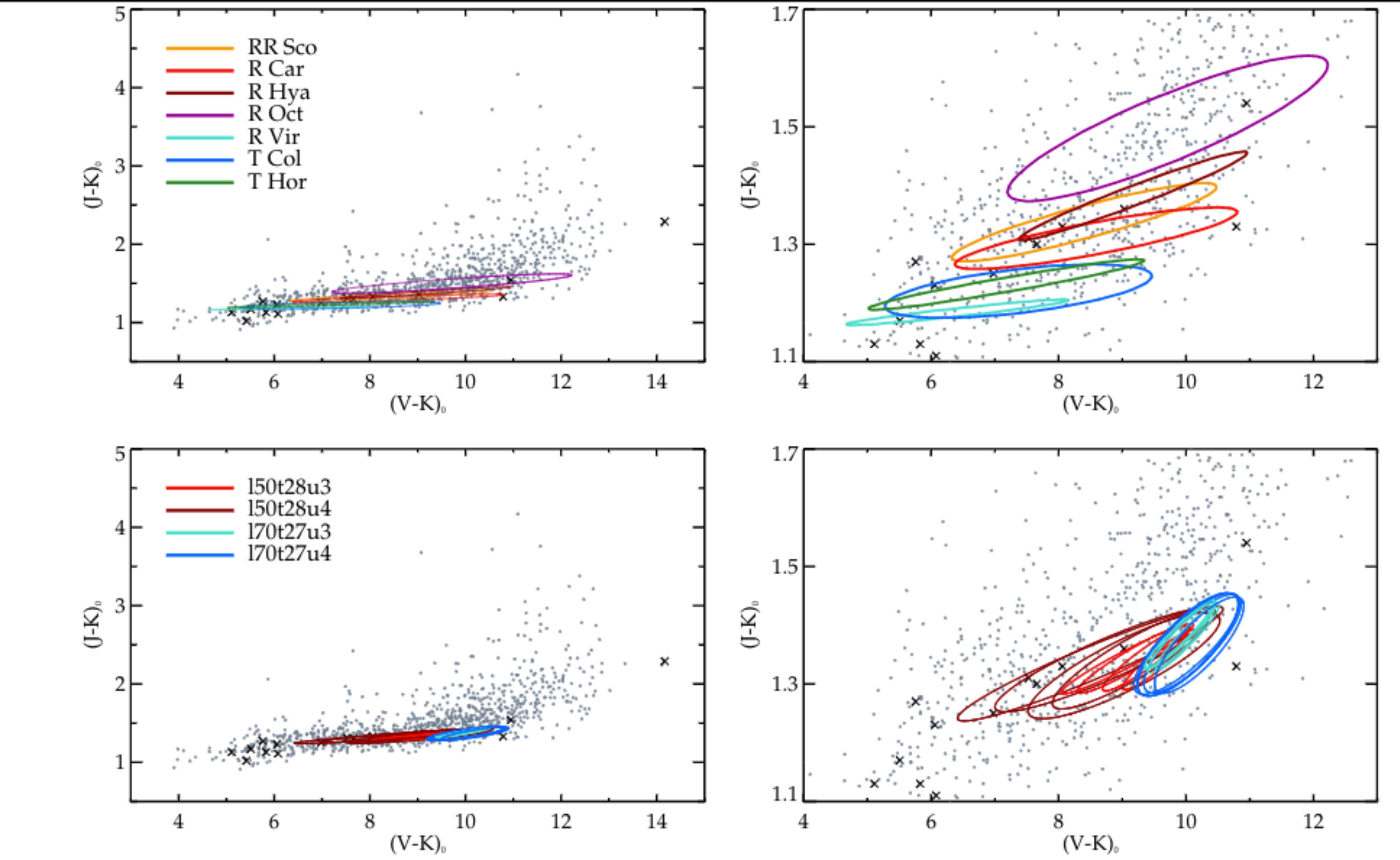


**Fig. 3.** Mass loss rate versus wind velocity for M-type AGB stars: black symbols (stars) mark observations by Olofsson et al. (2002) and González Delgado et al. (2003), red symbols models of series A and blue symbols models of series B (triangles and squares indicate pulsation amplitudes of 3 and 4 km s<sup>-1</sup>, respectively; see Table 1 for details). We note that the stellar parameters of the models were chosen to produce weak to moderate winds, as such environments seem to be favorable for Al<sub>2</sub>O<sub>3</sub> formation.

# Dinamic atmospheres and winds of cool luminous giants

S. Hofner



# Dinamic atmospheres and winds of cool luminous giants

S. Hofner

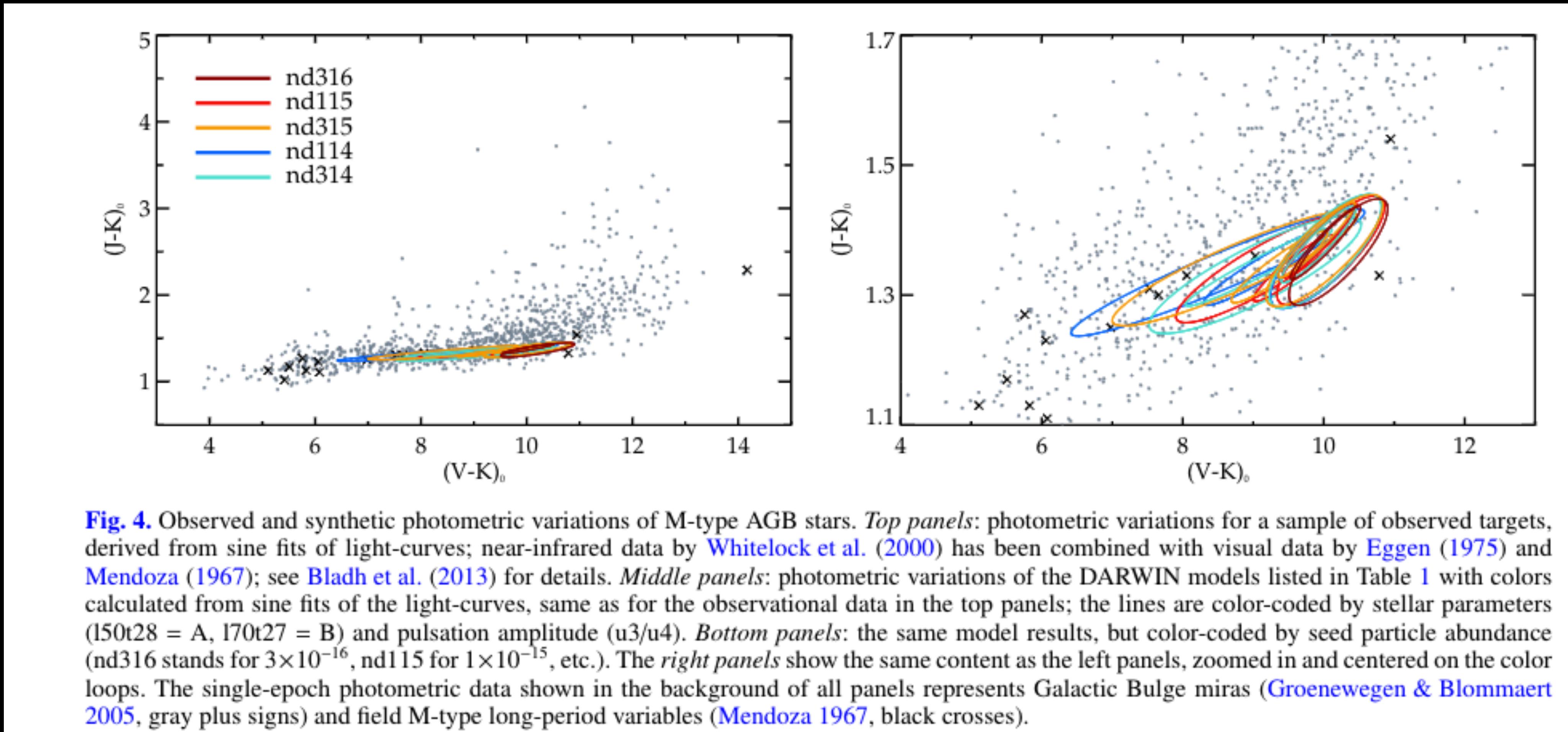


**Fig. 4.** Observed and synthetic photometric variations of M-type AGB stars. *Top panels*: photometric variations for a sample of observed targets, derived from sine fits of light-curves; near-infrared data by [Whitelock et al. \(2000\)](#) has been combined with visual data by [Eggen \(1975\)](#) and [Mendoza \(1967\)](#); see [Bladh et al. \(2013\)](#) for details. *Middle panels*: photometric variations of the DARWIN models listed in Table 1 with colors calculated from sine fits of the light-curves, same as for the observational data in the top panels; the lines are color-coded by stellar parameters ( $l50t28 = A$ ,  $l70t27 = B$ ) and pulsation amplitude ( $u3/u4$ ). *Bottom panels*: the same model results, but color-coded by seed particle abundance (nd316 stands for  $3 \times 10^{-16}$ , nd115 for  $1 \times 10^{-15}$ , etc.). The *right panels* show the same content as the left panels, zoomed in and centered on the color loops. The single-epoch photometric data shown in the background of all panels represents Galactic Bulge miras ([Groenewegen & Blommaert 2005](#), gray plus signs) and field M-type long-period variables ([Mendoza 1967](#), black crosses).

# Dinamic atmospheres and winds of cool luminous giants

S. Hofner

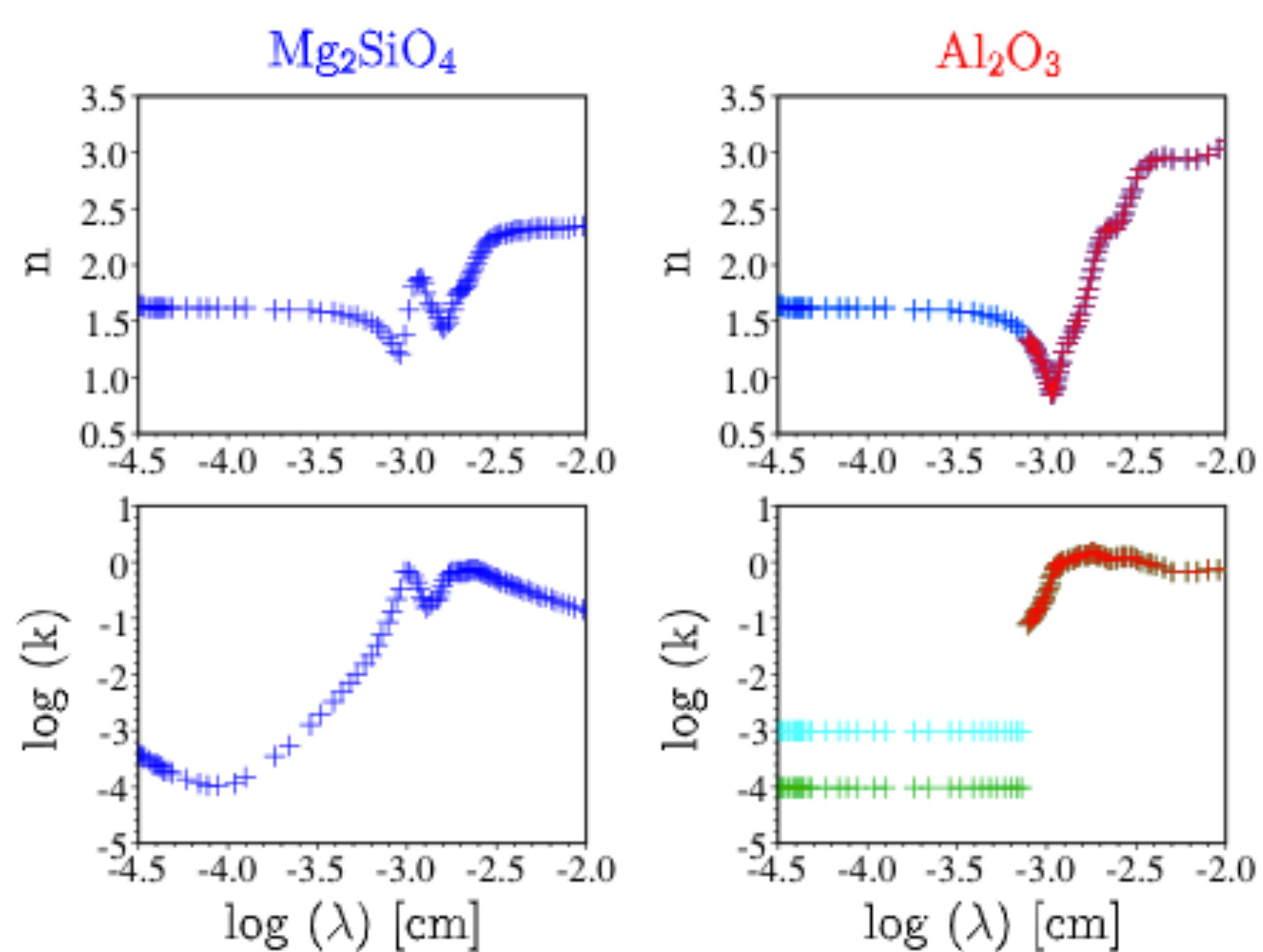


**Fig. 5.** Refractive index data. *Left panels:*  $\text{Mg}_2\text{SiO}_4$  (Jäger et al. 2003). *Right panels:*  $\text{Al}_2\text{O}_3$  (high- $k$  and low- $k$  data sets, see Sect. 3.2.1).

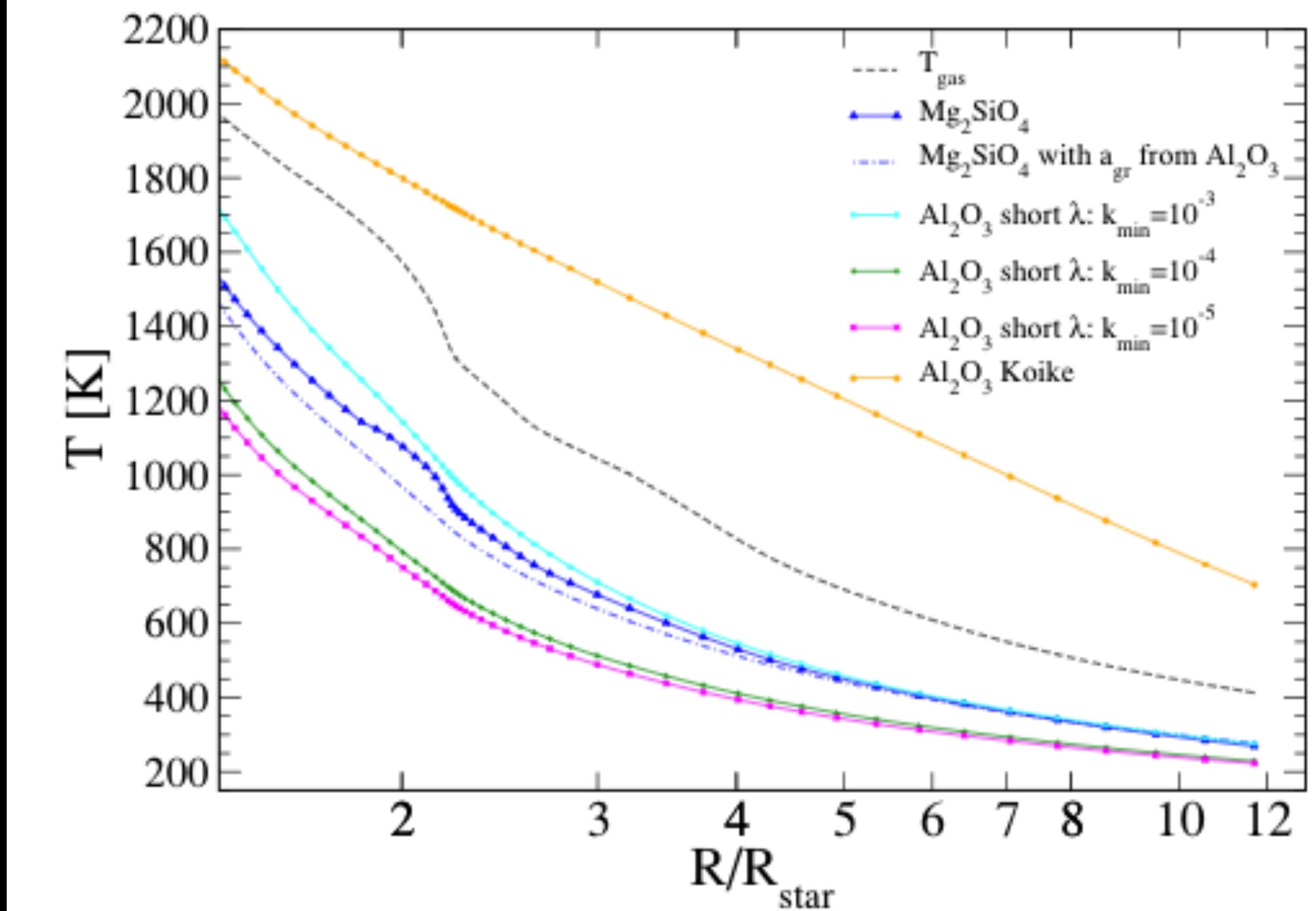


**Fig. 6.** Radiative equilibrium temperature of dust grains as a function of distance from the star in a typical model (An315u3). The different curves correspond to different sets of optical properties (see legend and text in Sects. 3.2.1 and 3.2.3).

# Dinamic atmospheres and winds of cool luminous giants

S. Hofner

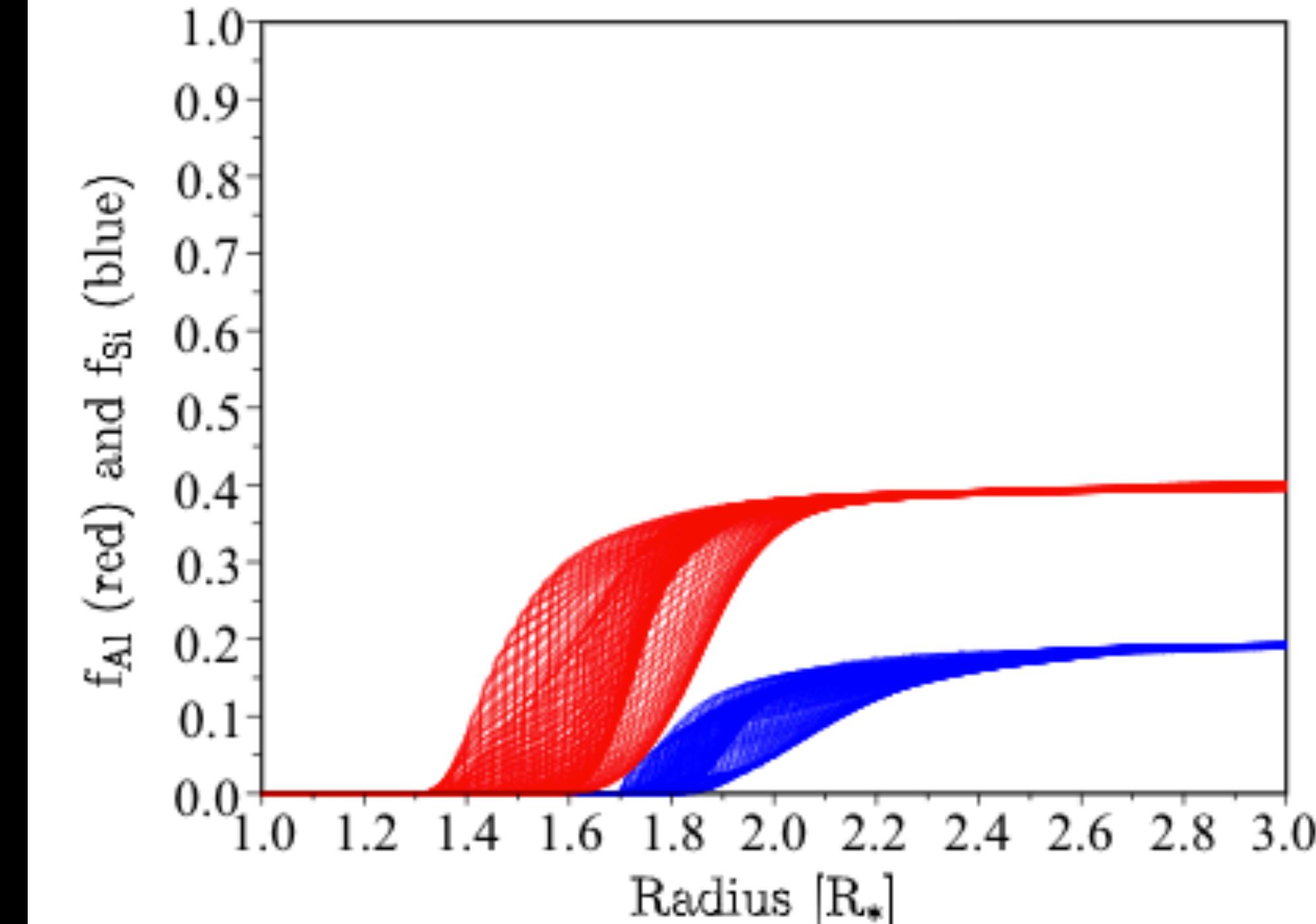
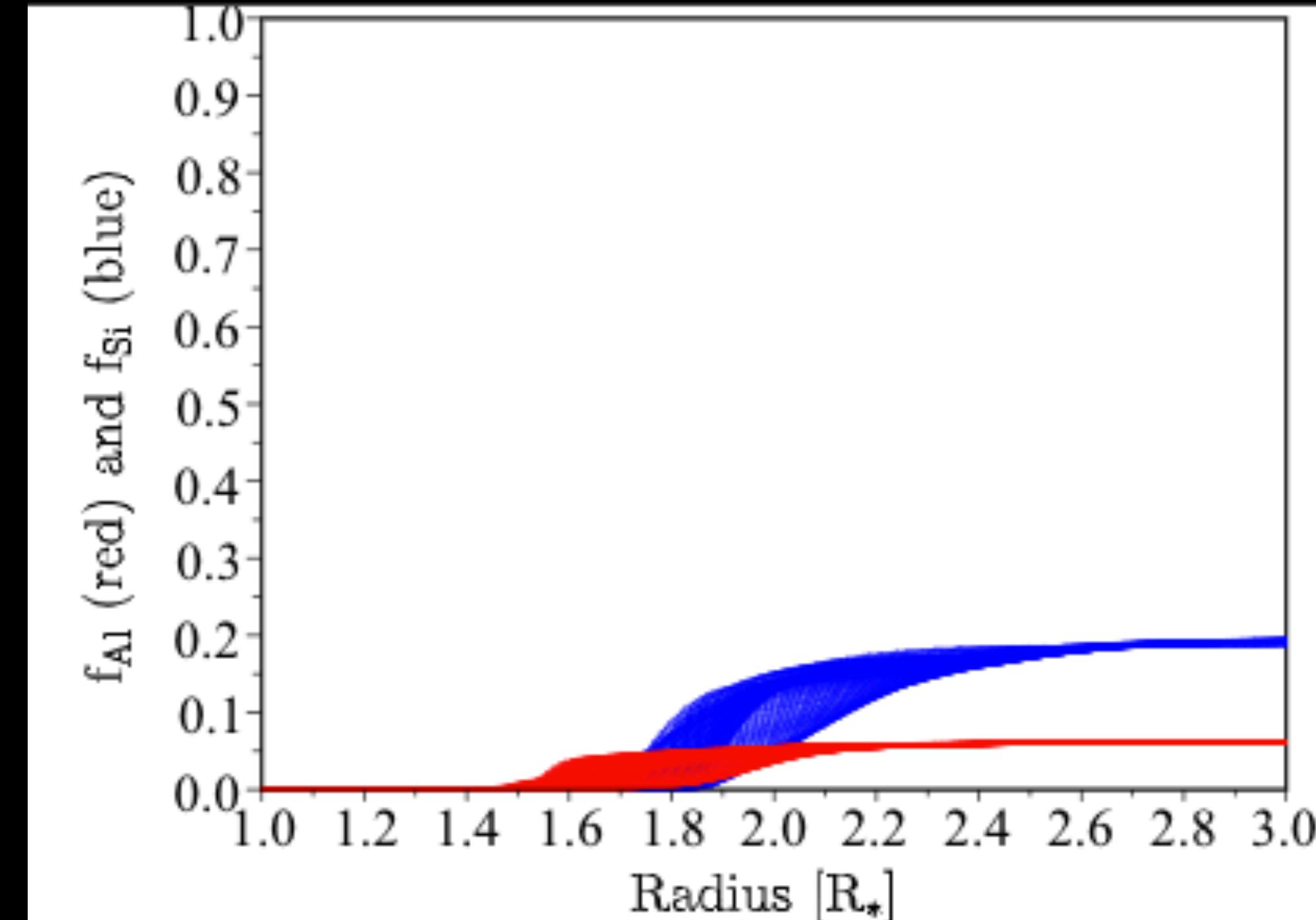
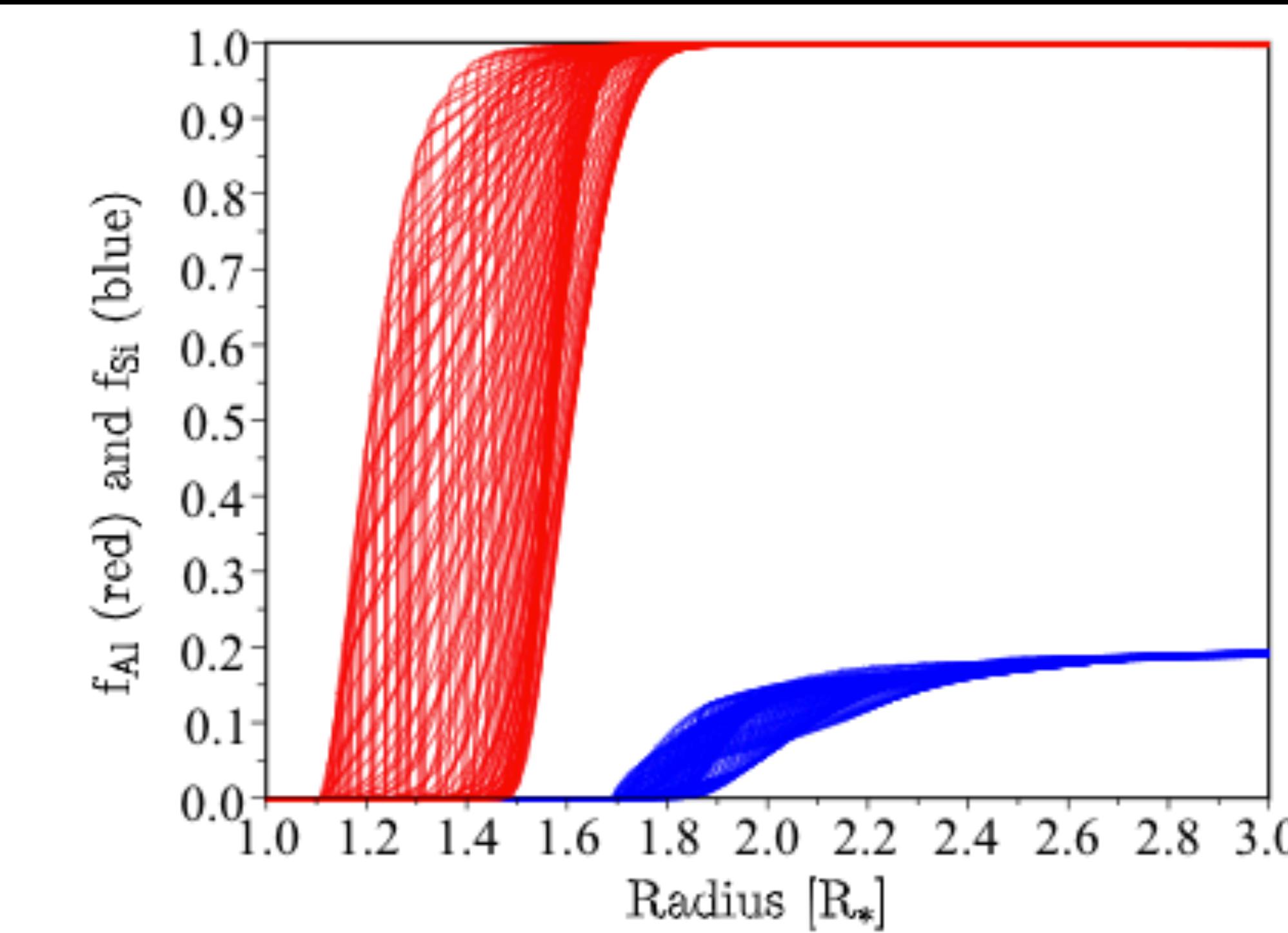


**Fig. 7.** The time-dependent radial distribution of  $\text{Al}_2\text{O}_3$  and silicate dust (expressed as condensation fractions of Al and Si, respectively) in model An315u3, zoomed in on the inner edge of the circumstellar dust shell (snapshots of 100 pulsation phases). The blue area (showing a similar shape in all panels) corresponds to Fe-free silicates ( $\text{Mg}_2\text{SiO}_4$ ). The red curves (covering different areas in the 3 panels) represent  $\text{Al}_2\text{O}_3$  (treated here as passive, separate grains) for different grain temperatures, resulting from the high- $k$  optical data set (*top*), the low- $k$  data (*bottom*), and the assumption of  $\text{Al}_2\text{O}_3$  grain temperatures being equal to those of  $\text{Mg}_2\text{SiO}_4$  grains of comparable sizes (*middle*).

# Dinamic atmospheres and winds of cool luminous giants

S. Hofner

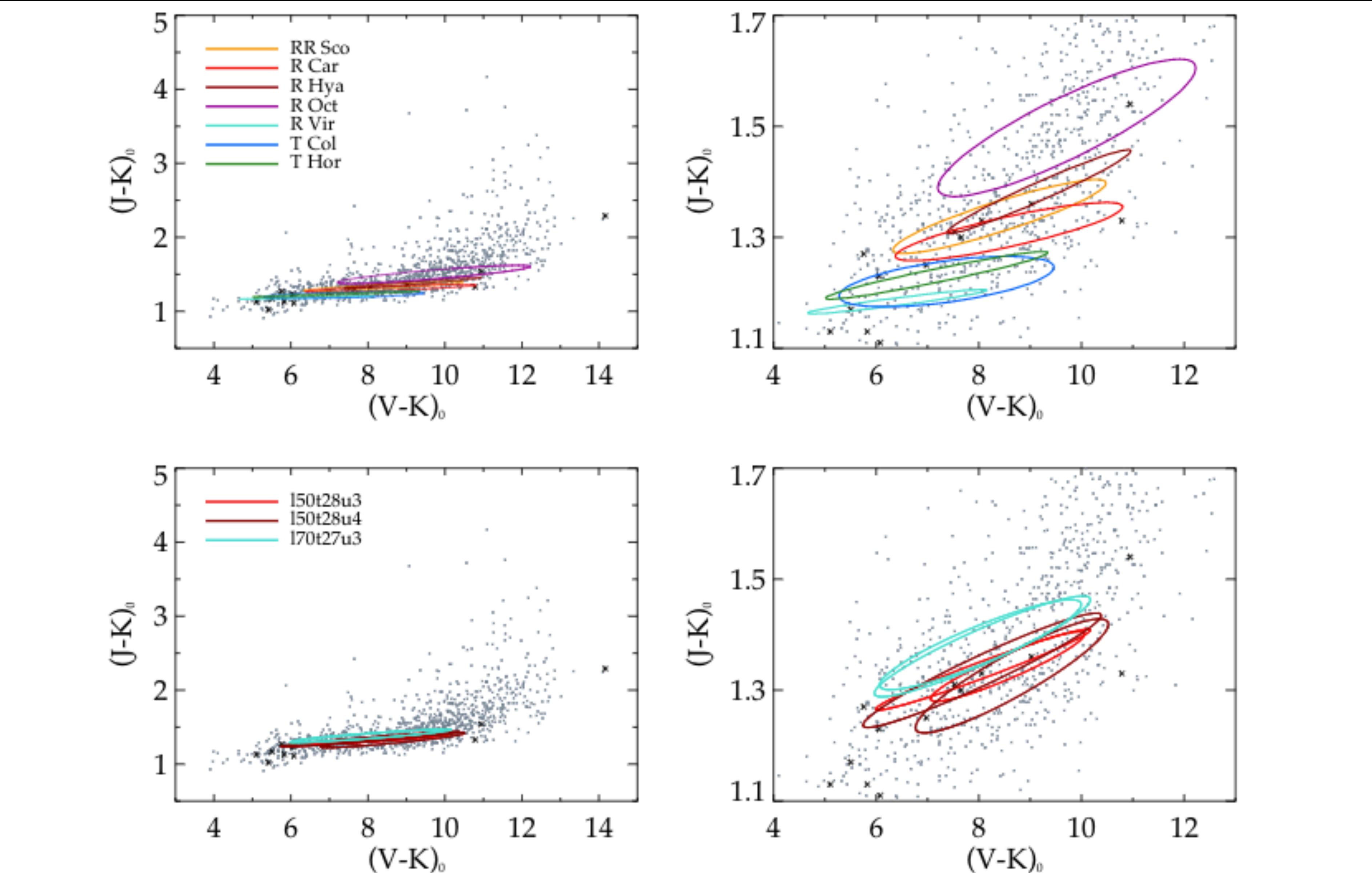


**Fig. 8.** Observed and synthetic photometric variations of M-type AGB stars. *Upper panels:* photometric variations for a sample of observed targets, derived from sine fits of light-curves (see Fig. 4 and related text for details). *Lower panels:* photometric variations for the core-mantle grain models listed in Table 4 with colors calculated from sine fits of the light-curves, same as for the observational data in the top panels; the lines are color-coded by stellar parameters and pulsation amplitude.

# Dinamic atmospheres and winds of cool luminous giants

S. Hofner

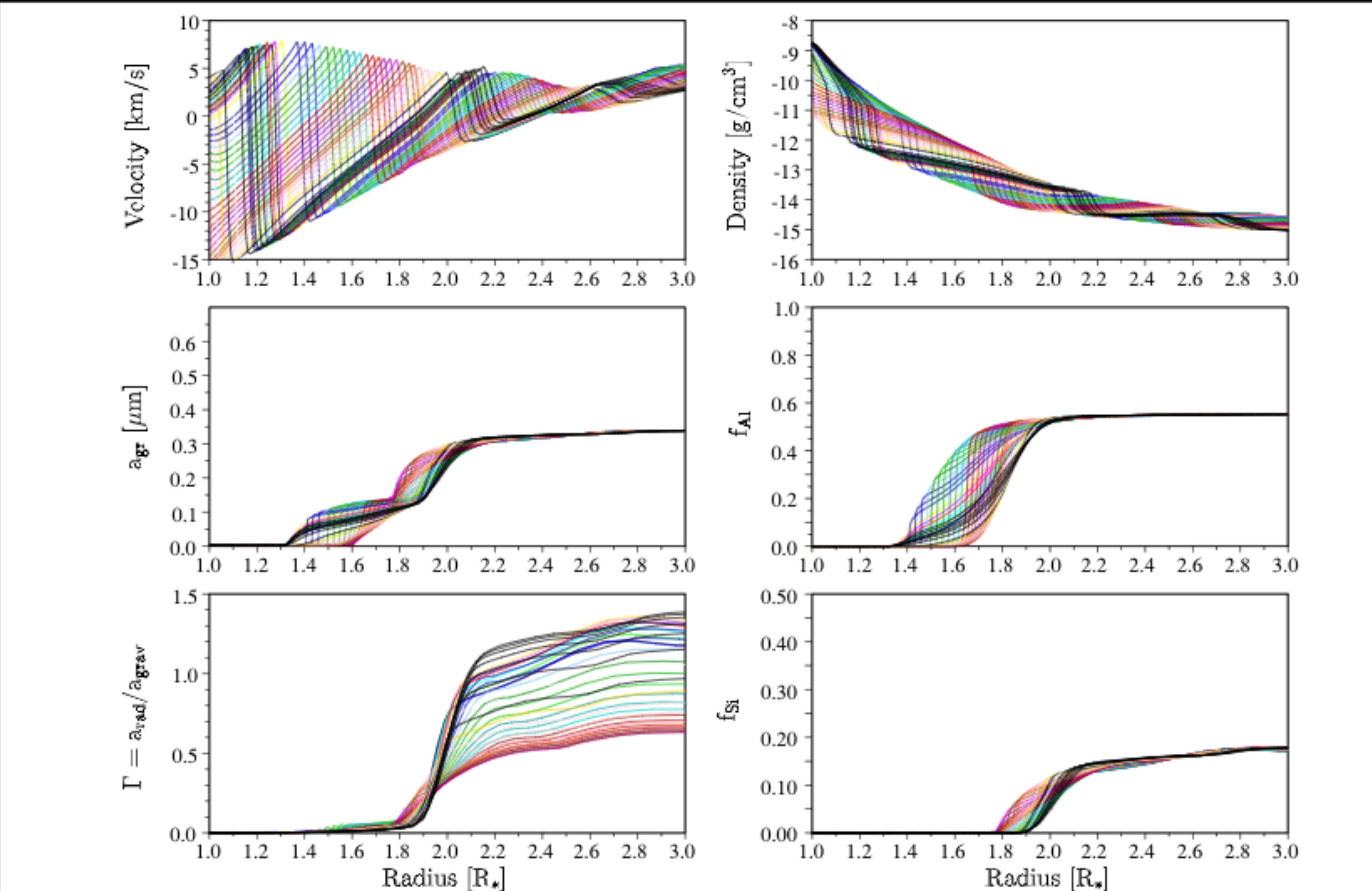


**Fig. 9.** The time-dependent radial structure of model An315u3cmg, zoomed in on the dust formation region (snapshots of 40 pulsation phases). *Left, top to bottom:* velocity, the radius of the composite grains and the ratio of radiative to gravitational acceleration; *Right, top to bottom:* gas density, Al condensation fraction, Si condensation fraction.

# **V1309 Scorpii: merger of a contact binary**

## **(Paper 10)**

# V1309 Scorpii: merger of a contact binary

R. Tylenda (Paper 10)

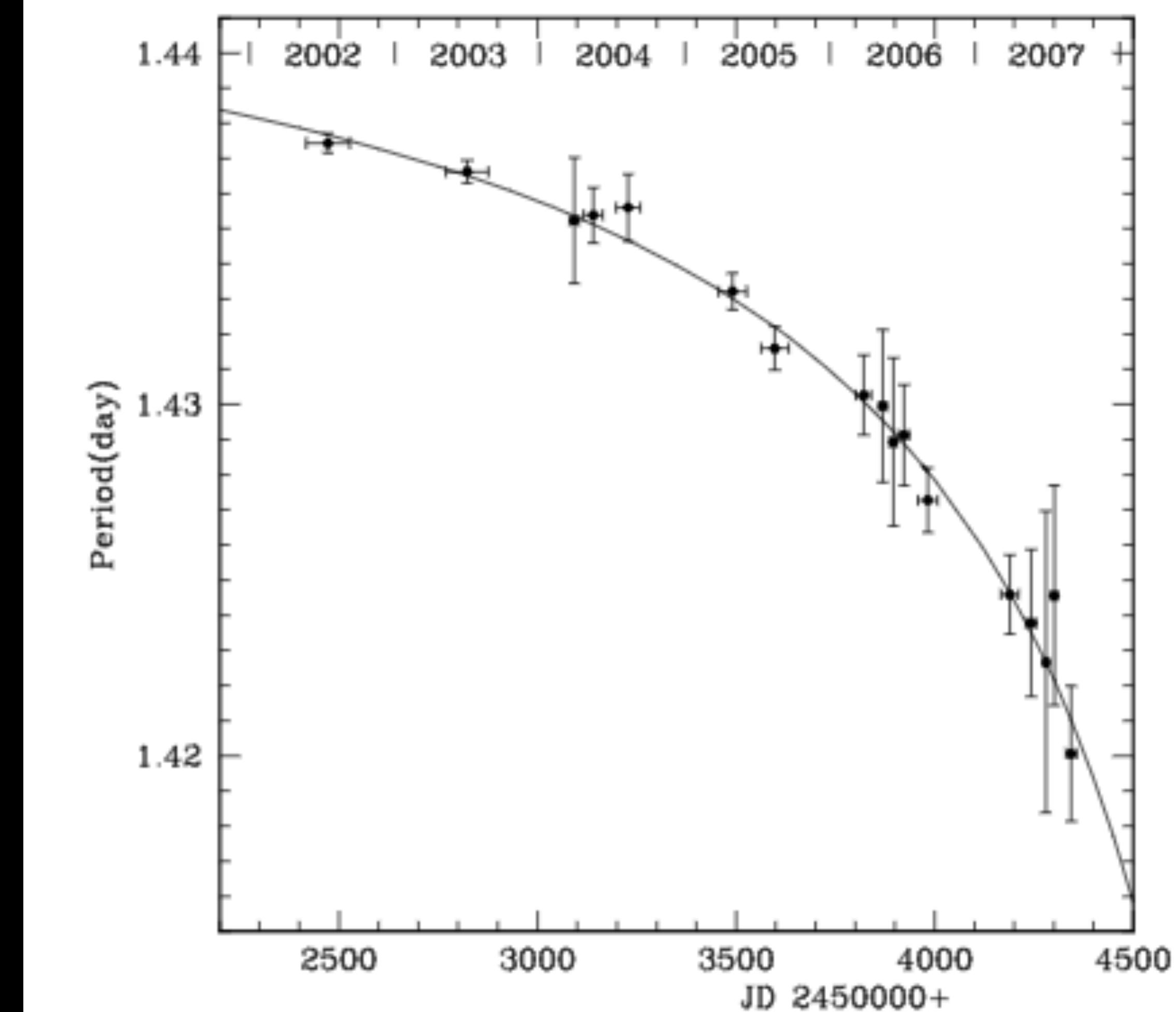
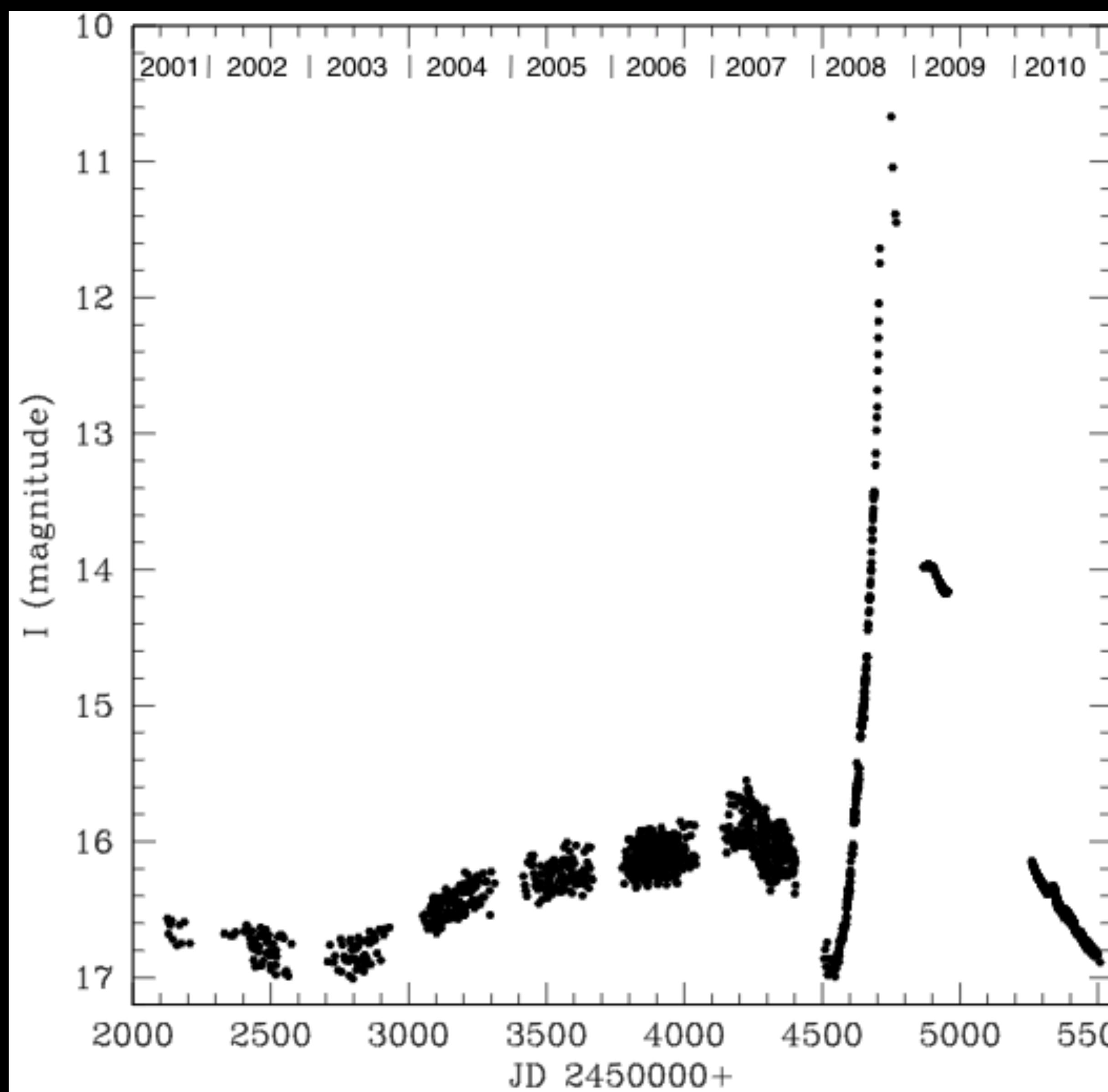


**Fig. 2.** Evolution of the period of the photometric variations of the V1309 Sco progenitor. The line shows a least-squares fit of an exponential formula to the data (see text and Eq. (1)).

**Fig. 1.** Light curve of V1309 Sco from the OGLE-III and OGLE-IV projects:  $I$  magnitude versus time of observations in Julian Dates. Time in years is marked on top of the figure. At maximum the object attained  $I \approx 6.8$ .

- V838 Mon type: is a spectroscopy binary

# V1309 Scorpii: merger of a contact binary

R. Tylenda (Paper 10)

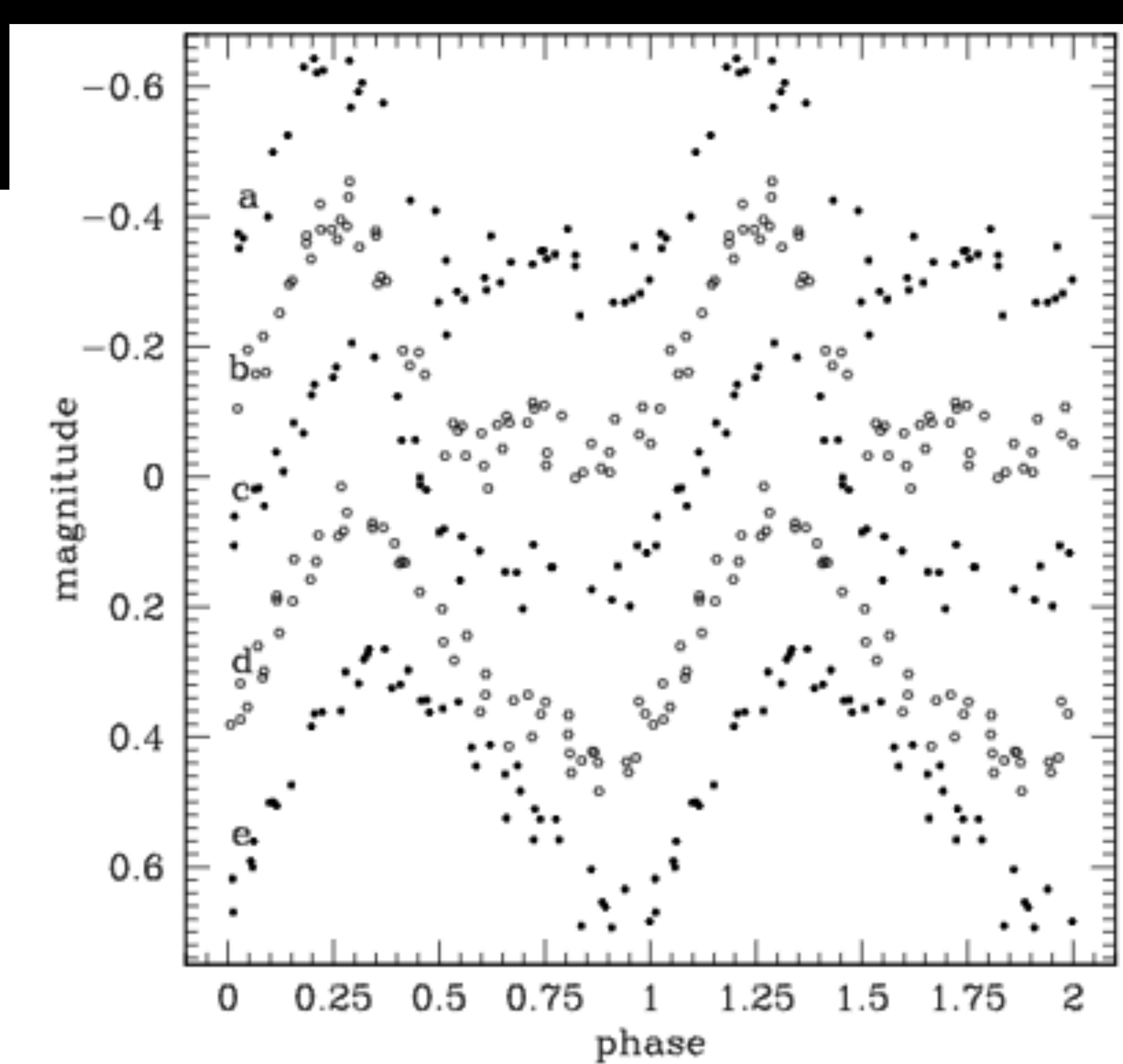
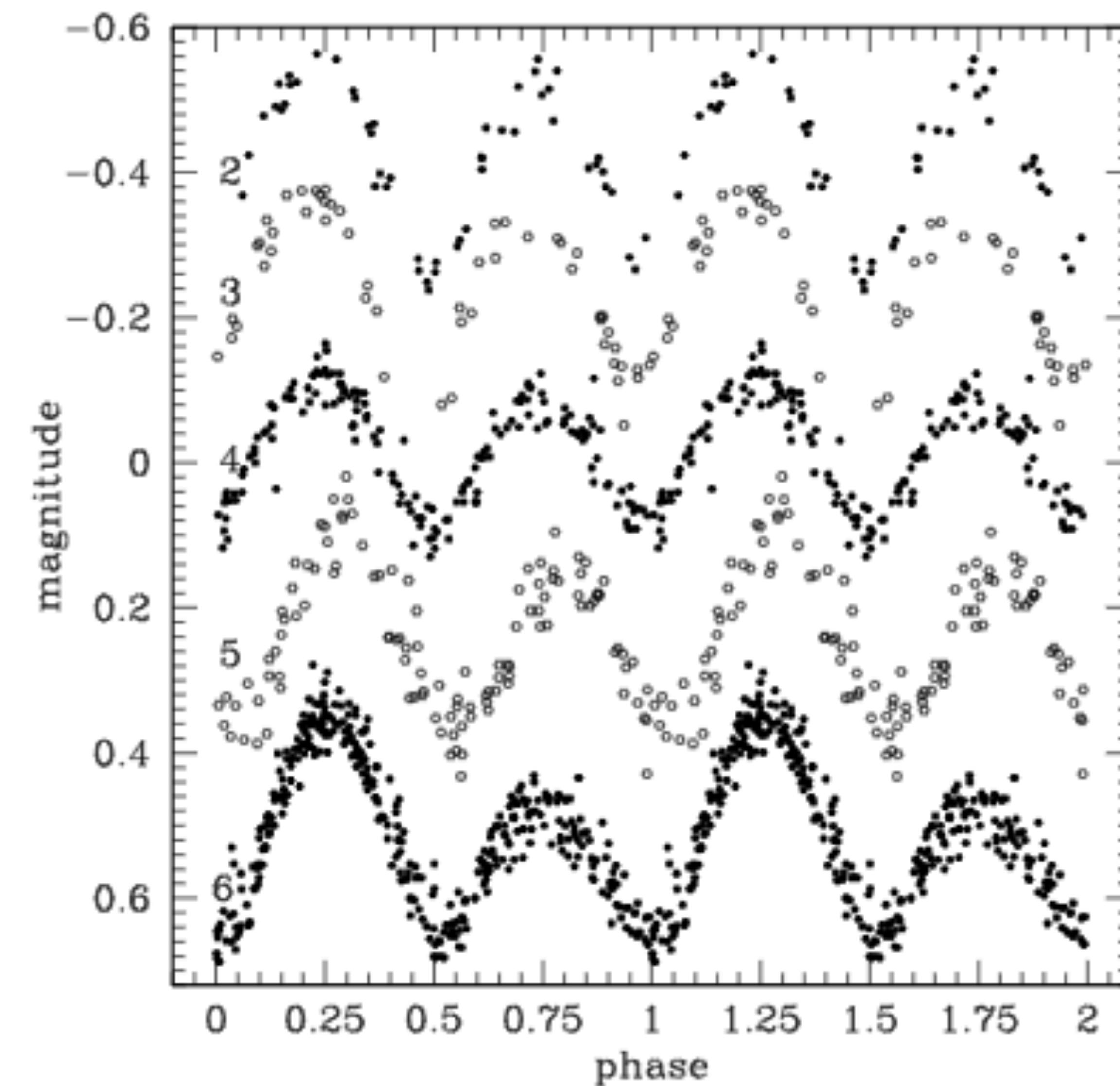


**Fig. 3.** Light curves obtained from folding the data with the period described by Eq. (1). *Upper part:* seasons 2002–2006. *Lower part:* season 2007 devived into five subsamples (time goes from a to e). The zero point of the magnitude (ordinate) scale is arbitrary.

# V1309 Scorpii: merger of a contact binary

R. Tylenda (Paper 10)

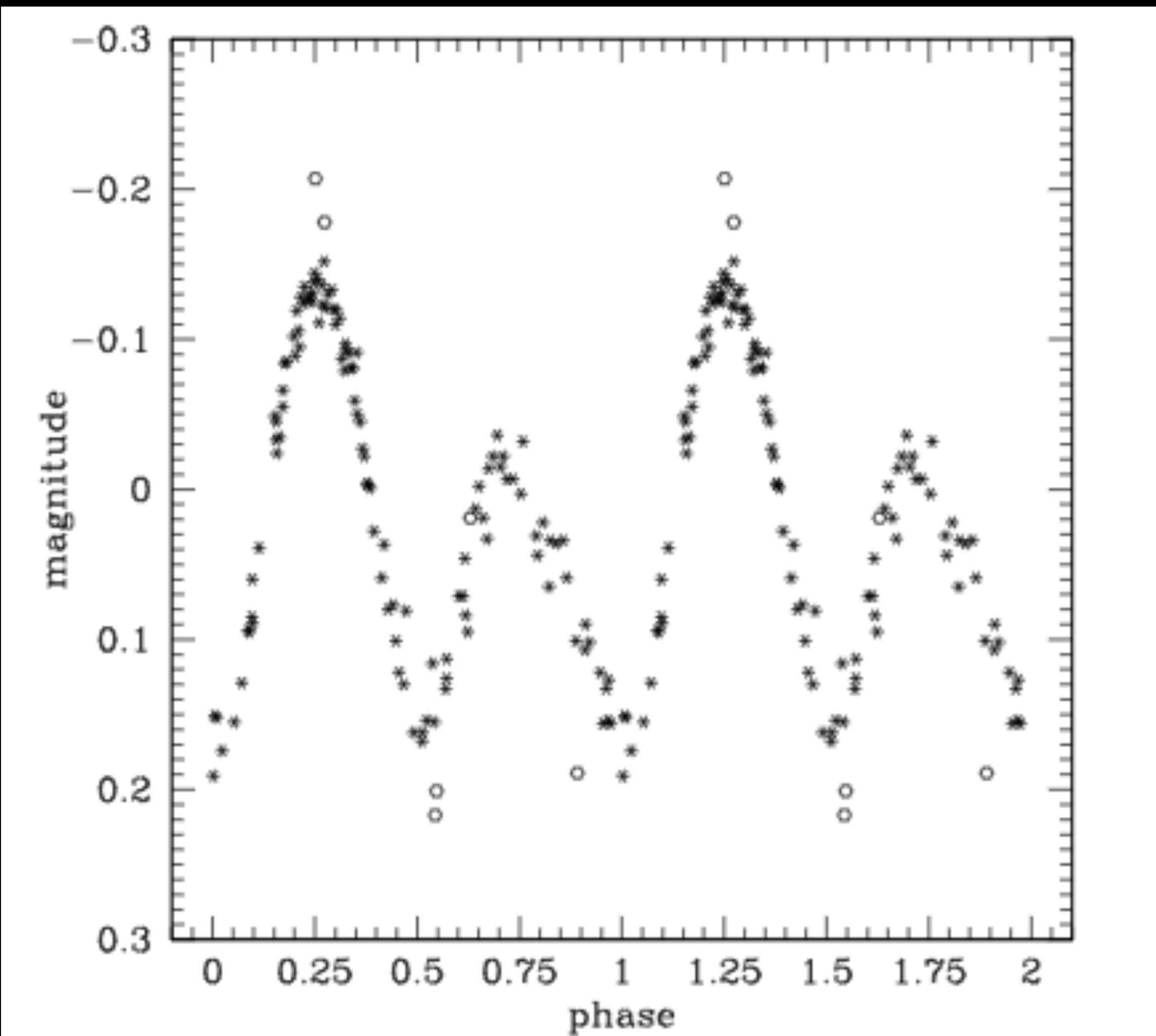


**Fig. 4.**  $V$  (open points) and  $I$  (asterisks) measurements obtained in JD 2453 880–2453 910 (season 2006) and folded with the period described by Eq. (1). The zero point of the magnitude (ordinate) scale is arbitrary.

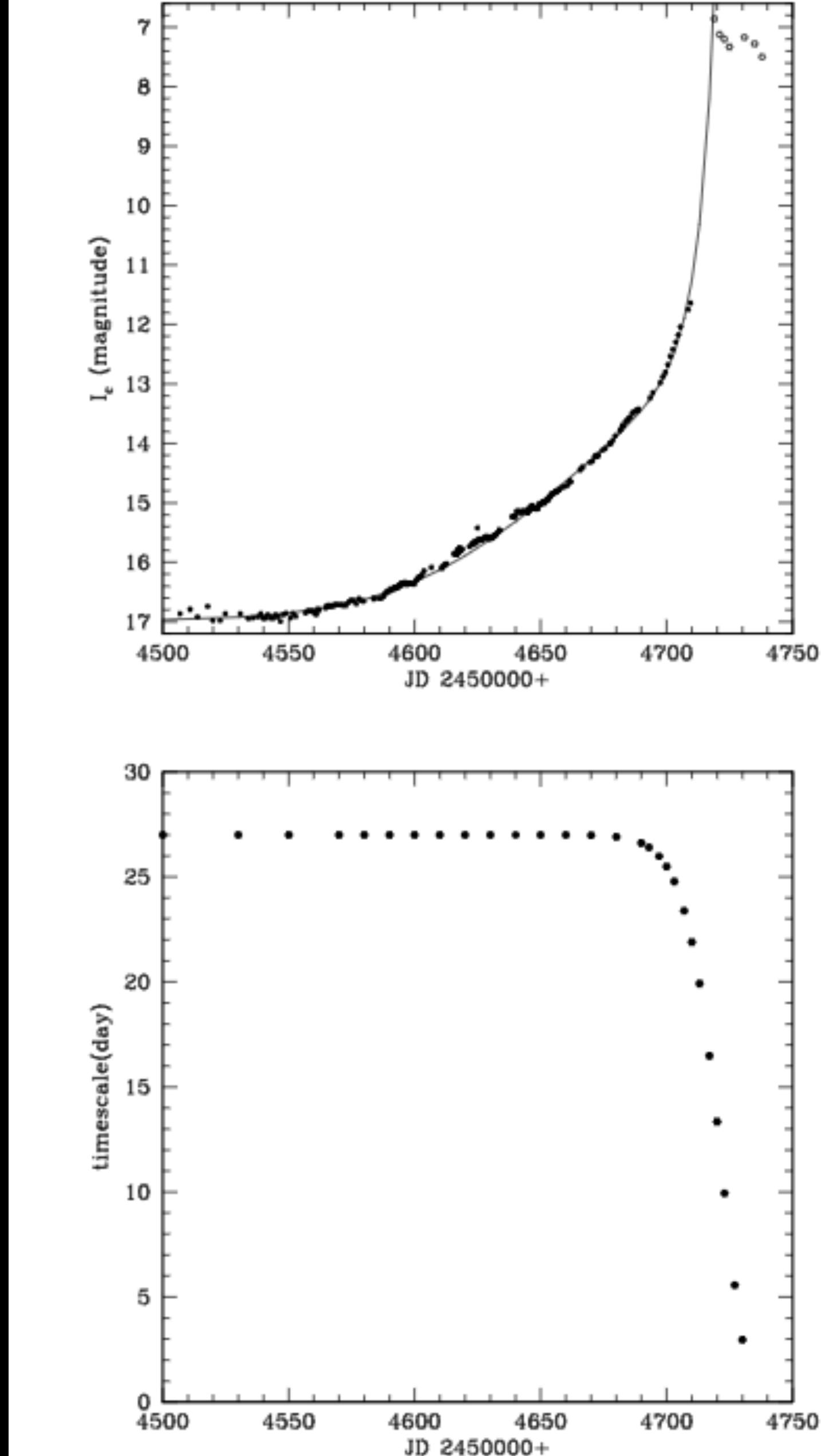


**Fig. 5.**  $I$  light curve of V1309 Sco during its rise to maximum in 2008 (*upper part*). Full points: data from OGLE III, open points: data from AAVSO. The line shows a fit of an exponential formula (Eq. (2)). The time scale used in the formula is plotted in the lower part of the figure.

# V1309 Scorpii: merger of a contact binary

R. Tylenda (Paper 10)

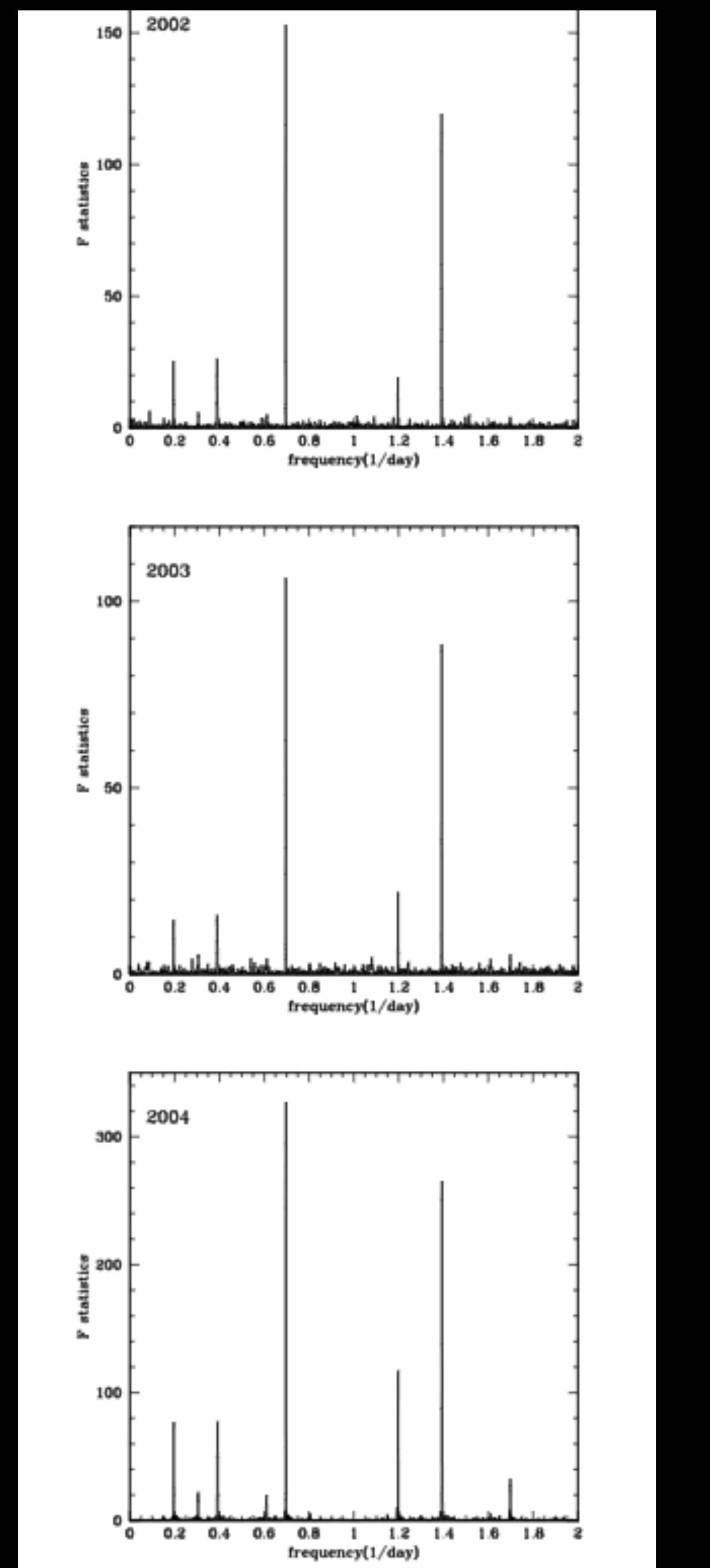


**Fig.A.1.** Periodograms from the observations of the progenitor of V1309 Sco in 2002–2004.

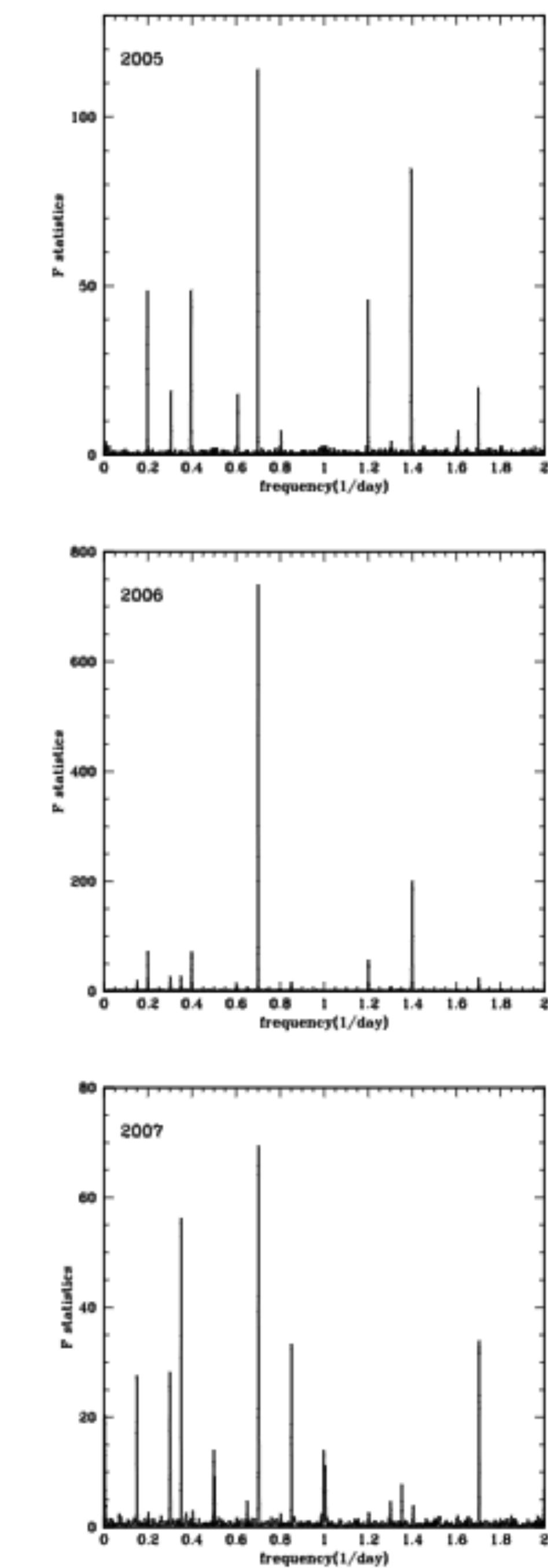


**Fig.A.2.** Periodograms from the observations of the progenitor of V1309 Sco in 2005–2007.

**Resolving the extended atmosphere and their inner  
wind of Mira (o Ceti) with long ALMA baselines**

**(Paper 11)**

# Resolving the extended atmosphere and their inner wind of Mira

K.T. Wong (Paper 11)

- V: vibrational state
- J: rotational transition

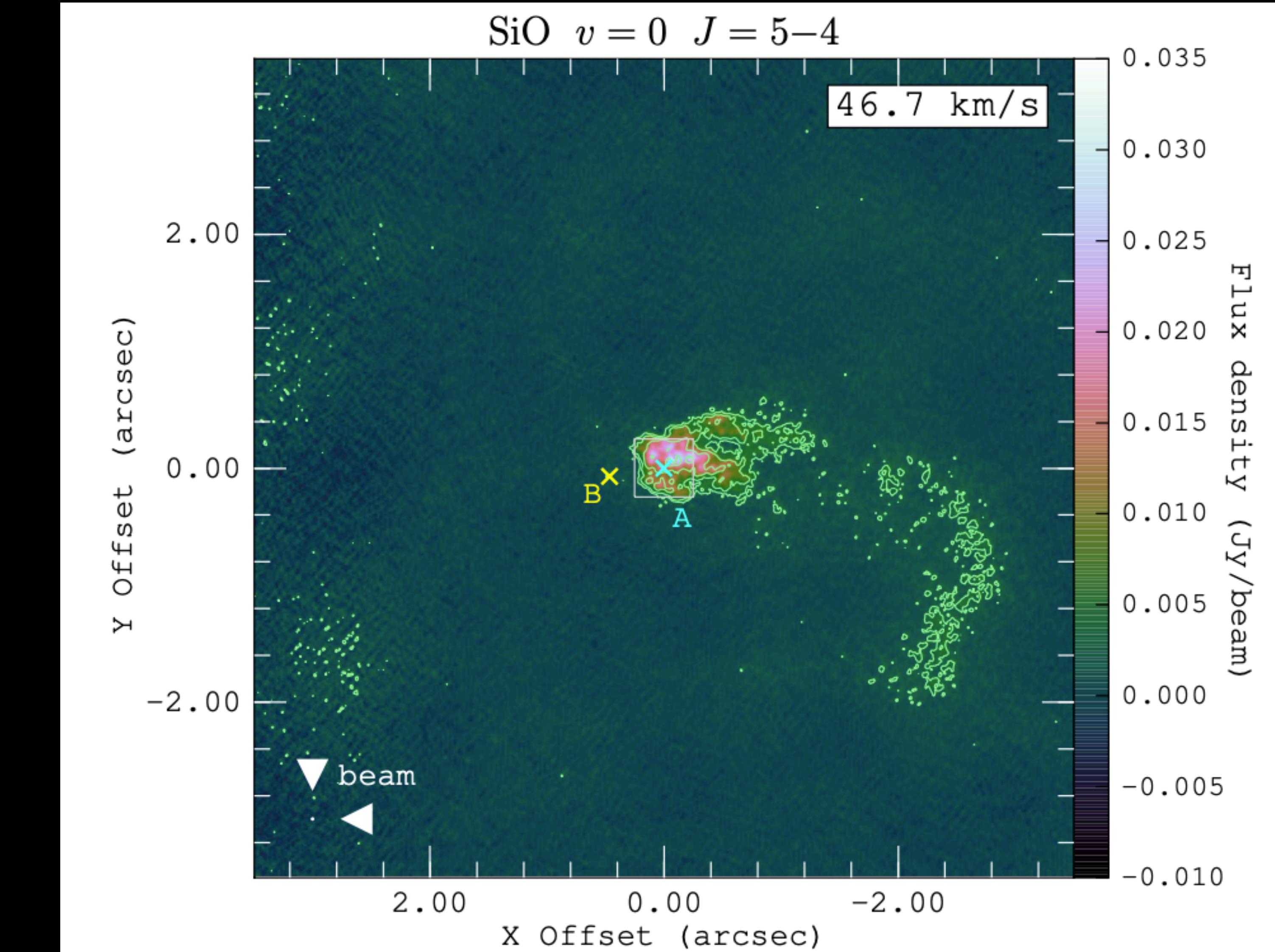
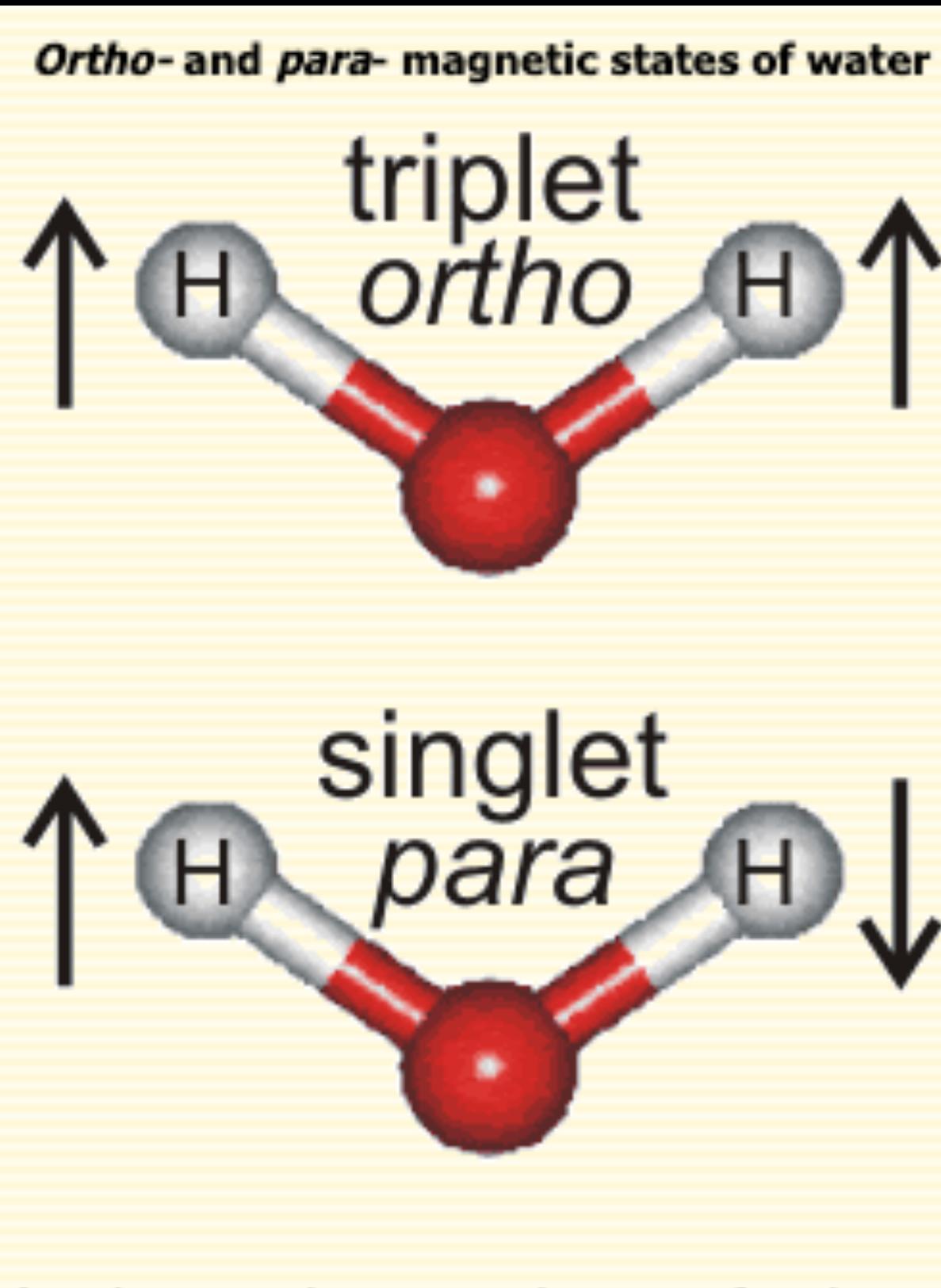
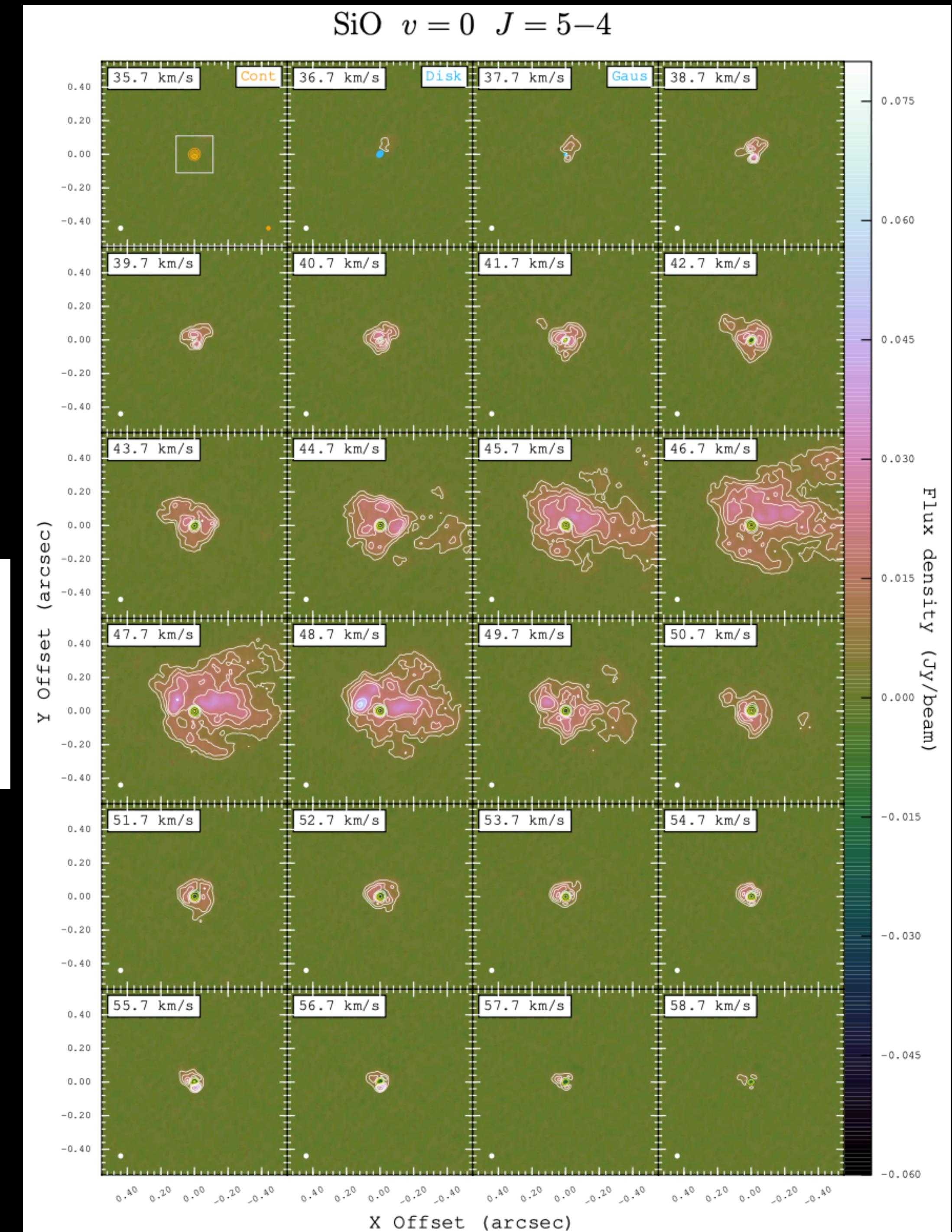


**Fig. 1.** Map of SiO  $v = 0$   $J = 5-4$  (with the continuum) at the channel of the systemic velocity ( $46.7 \text{ km s}^{-1}$ ) with a channel width of  $1.0 \text{ km s}^{-1}$ . The positions of Mira A ( $\alpha$  Ceti; cyan cross) and Mira B (VZ Ceti; yellow cross) are indicated in the image. The horizontal and vertical axes are the relative offsets (arcsec) in the directions of right ascension (X) and declination (Y), respectively, with respect to the continuum centre of Mira A. The white box centred at the fitted position of Mira A indicates the  $0''.50 \times 0''.50$  region as shown in Fig. 7, within which we extract the SiO and H<sub>2</sub>O line spectra from an array of positions. The horizontal and vertical axes are the relative offsets (arcsec) with respect to the Mira A in right ascension and declination, respectively. The light green contours represent 4, 8, 16, and  $32\sigma$  of the SiO emission from the gas near Mira A, where the map rms noise is  $\sigma = 0.80 \text{ mJy beam}^{-1}$ . The circular restoring beam of  $0''.032$  FWHM for the SiO image is indicated in white in the bottom left corner.

# Resolving the extended atmosphere and their inner wind of Mira

K.T. Wong (Paper 11)

**Fig. 2.** Channel maps of post-imaging continuum-subtracted SiO  $v = 0 J = 5-4$  from LSR velocity  $35.7 \text{ km s}^{-1}$  to  $58.7 \text{ km s}^{-1}$ , with a channel width of  $1.0 \text{ km s}^{-1}$ . The systemic velocity is  $46.7 \text{ km s}^{-1}$ . The horizontal and vertical axes indicate the relative offsets (arcsec) in the directions of right ascension ( $X$ ) and declination ( $Y$ ), respectively, with respect to the fitted absolute position of Mira A. The white contours represent  $6, 12, 18, 24, 48$ , and  $72\sigma$  and yellow contours represent  $-60, -36$ , and  $-6\sigma$ , where  $\sigma = 0.80 \text{ mJy beam}^{-1}$  is the map rms noise. The circular restoring beam of  $0''.032$  FWHM for the SiO image is indicated in white in the bottom left corner of each panel. In the *first panel of the top row*, orange contours at  $0.1, 0.3, 0.5, 0.7$ , and  $0.9$  times the peak flux density ( $73.4 \text{ mJy beam}^{-1}$ ) of the 229 GHz continuum emission are also drawn and the corresponding restoring beam of  $0''.028$  FWHM is indicated in orange in the bottom right corner. The white box centred at Mira A indicates the  $0''.22 \times 0''.22$  region of the zoomed maps of SiO  $v = 0$  (Fig. 3),  $v = 2$  (Fig. 5), and H<sub>2</sub>O  $v_2 = 1$  (Fig. 6). In the *second and third panels of the top row*, the sizes of the uniform disk and Gaussian models, respectively, in our continuum analysis are drawn in blue.



# Resolving the extended atmosphere and their inner wind of Mira

K.T. Wong (Paper 11)

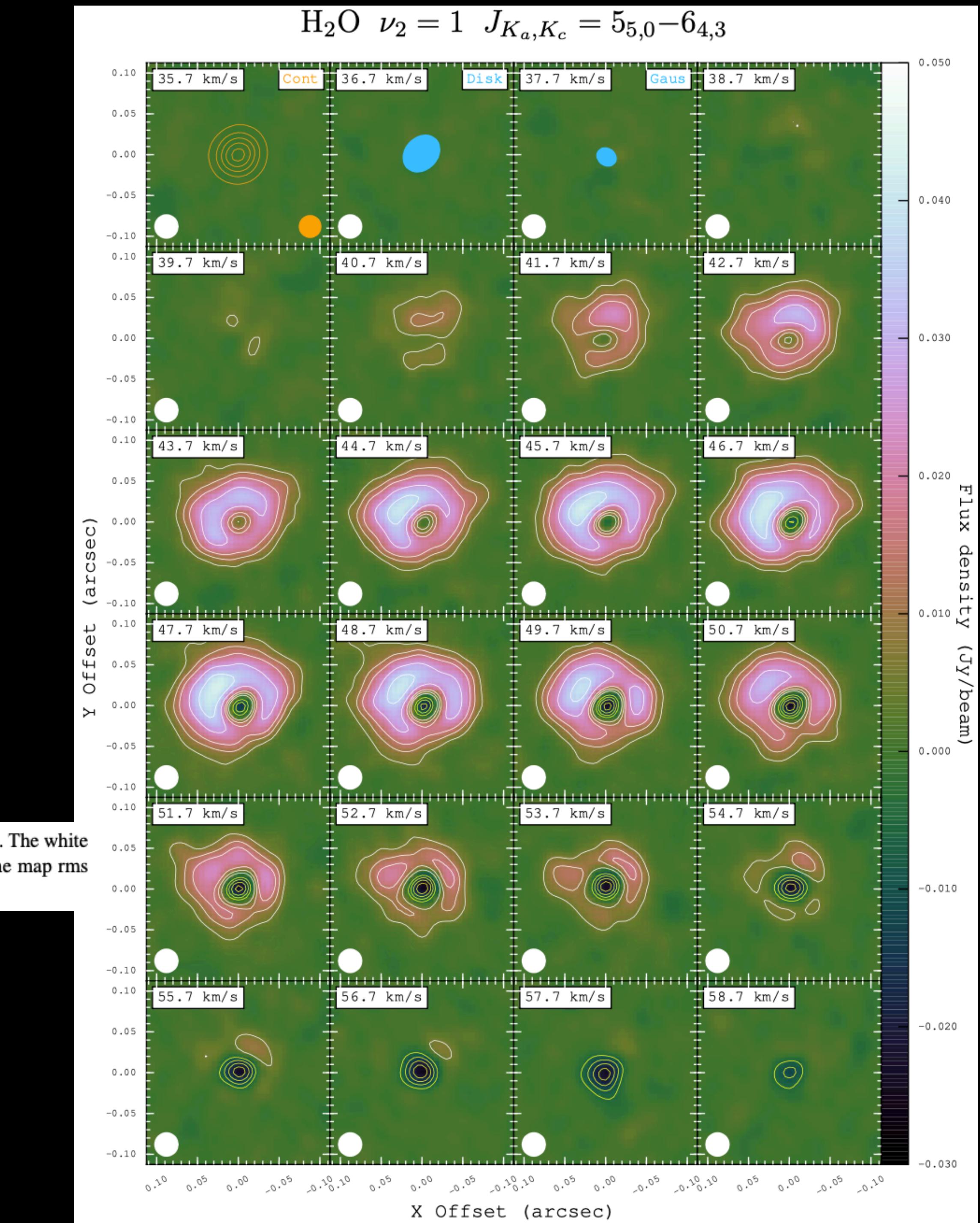


**Fig. 6.** Same as Fig. 2 for the zoomed ( $0''.22 \times 0''.22$ ) channel maps of post-imaging continuum-subtracted  $\text{H}_2\text{O } \nu_2 = 1 J_{K_a,K_c} = 5_{5,0}-6_{4,3}$ . The white contours represent 6, 12, 18, 30, and 42 $\sigma$  and yellow contours represent -24, -18, -12, and -6 $\sigma$ , where  $\sigma = 0.85 \text{ mJy beam}^{-1}$  is the map rms noise. The circular restoring beam of  $0''.030$  FWHM for the  $\text{H}_2\text{O}$  images is indicated in white in the bottom left corner of each panel.

# Resolving the extended atmosphere and their inner wind of Mira

K.T. Wong (Paper 11)

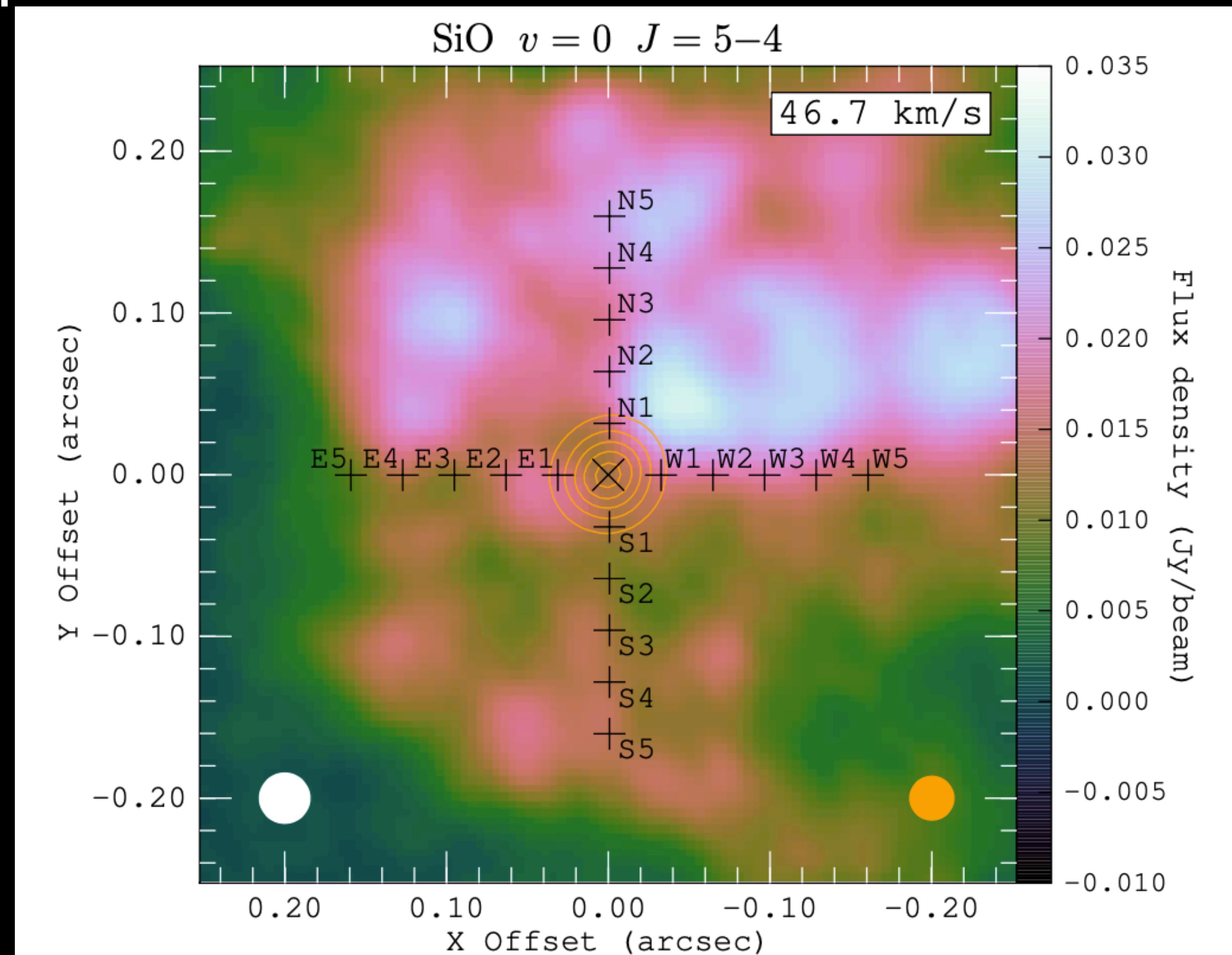


**Fig. 7.** Map of SiO  $v = 0$ ,  $J = 5-4$  (with the continuum) at the channel of the systemic velocity ( $46.7 \text{ km s}^{-1}$ ) with a channel width of  $1 \text{ km s}^{-1}$ . The centre of Mira's continuum is indicated by a black cross. Orange contours represent 10%, 30%, 50%, 70%, and 90% of the peak continuum flux ( $73.4 \text{ mJy beam}^{-1}$ ). The black plus signs (+) indicate the positions at which SiO and H<sub>2</sub>O spectra are sampled and modelled in Sect. 4. The sampling positions are separated by 32 mas along each arm of this array of points. The circular restoring beam of 0'032 FWHM for the SiO image is indicated in white at the bottom left and that of 0'028 FWHM for the 229 GHz continuum contours is indicated in orange at the bottom right.

# Resolving the extended atmosphere and their inner wind of Mira

K.T. Wong (Paper 11)

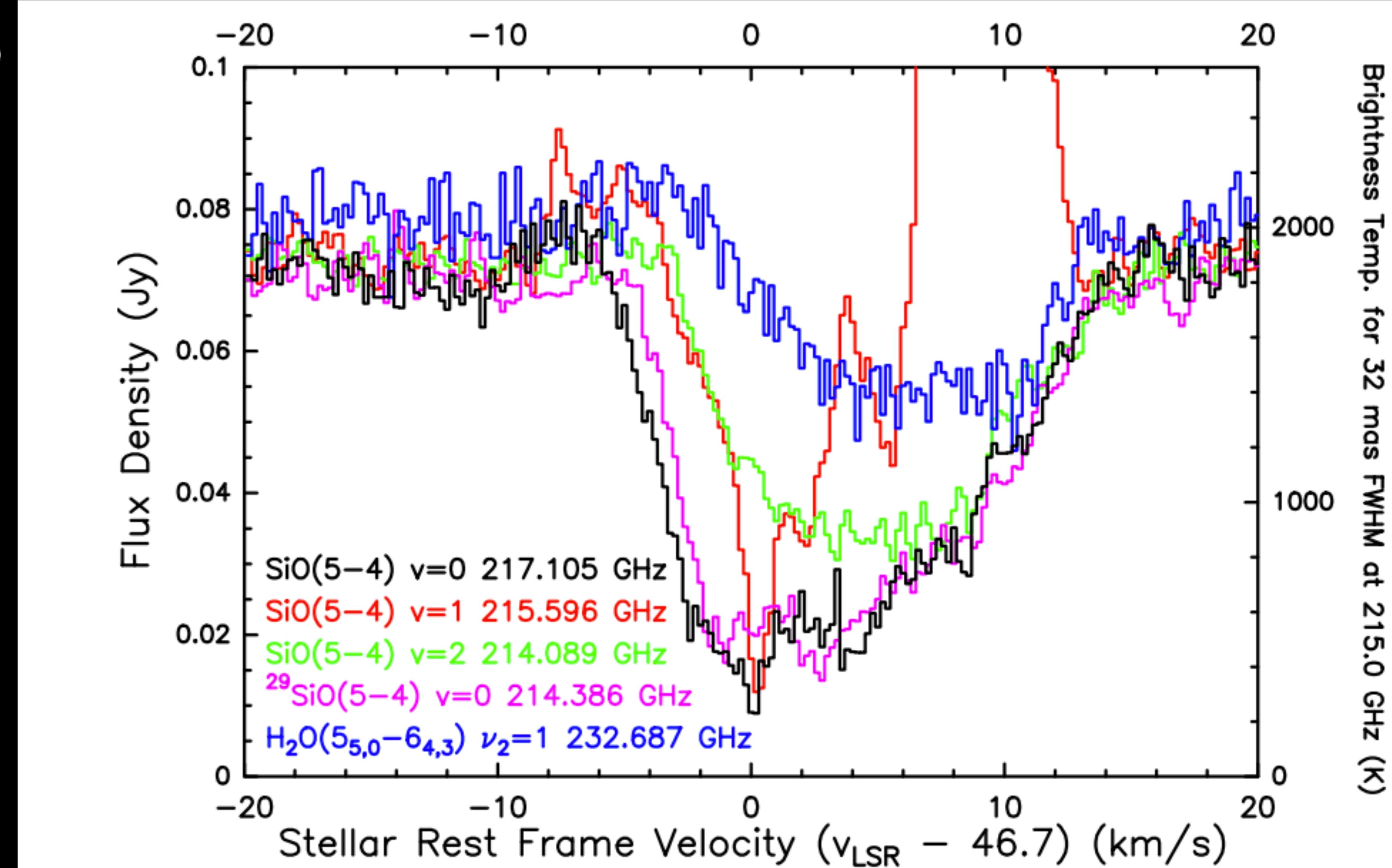
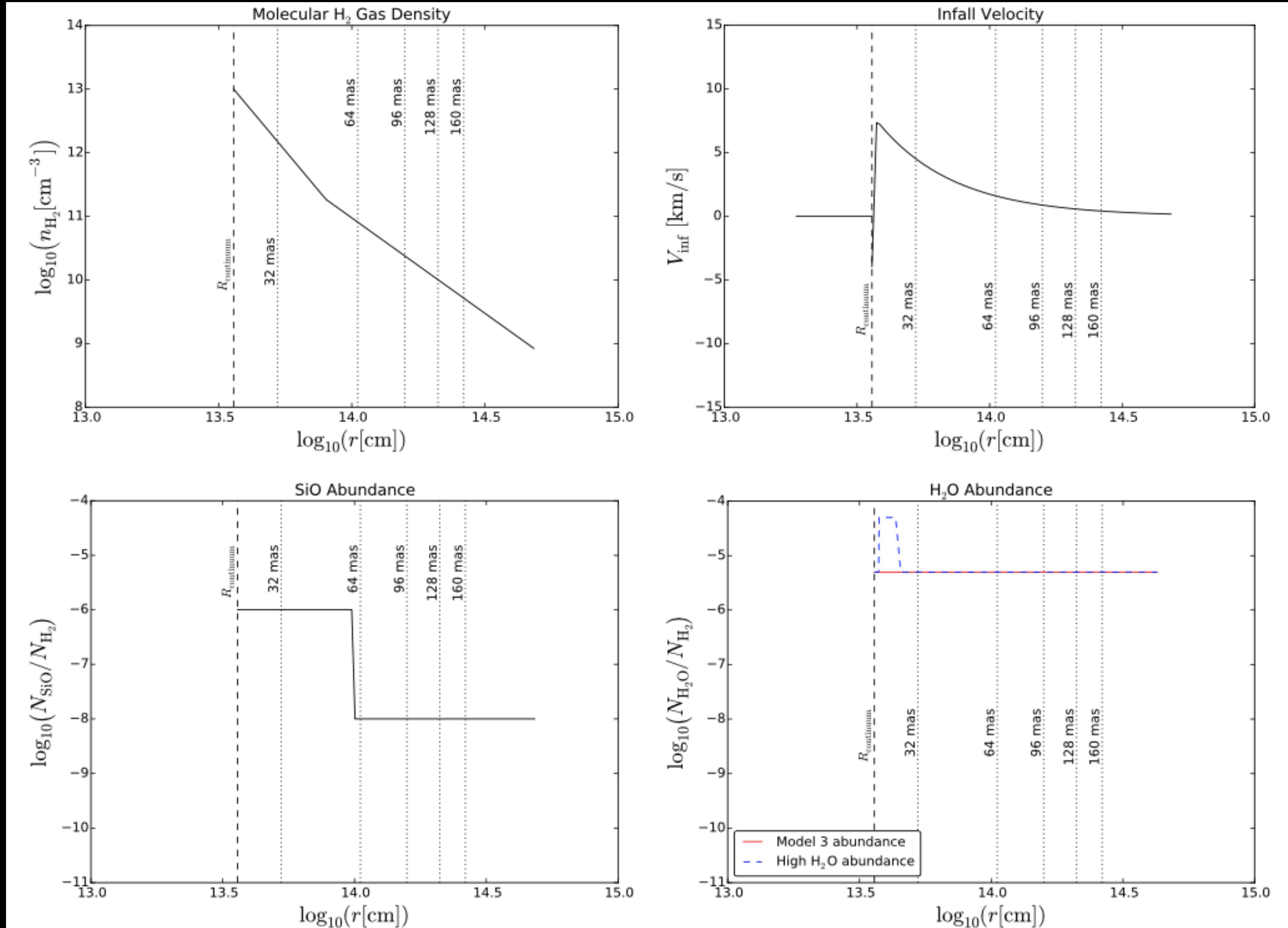


**Fig. 8.** Spectral lines in ALMA Band 6 extracted from the line of sight towards the centre of Mira's continuum. The SiO  $\nu = 1$   $J = 5-4$  transition (in red) shows intense maser emission around  $+10 \text{ km s}^{-1}$ , with the peak flux density of 1.73 Jy at  $+8.8 \text{ km s}^{-1}$ . The maser spectrum above 0.10 Jy is not shown in this figure.

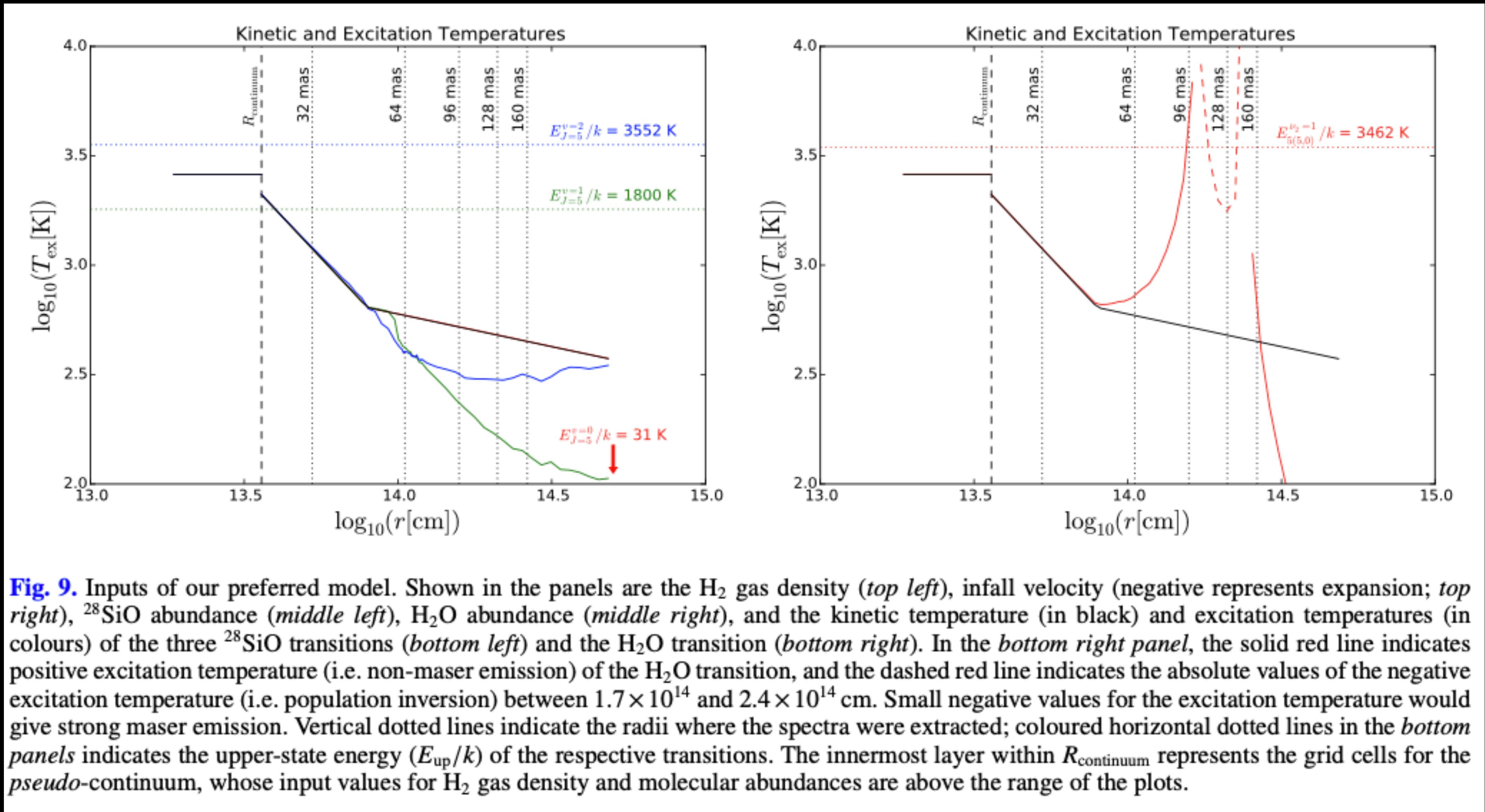
# Resolving the extended atmosphere and their inner wind of Mira

K.T. Wong (Paper 11)



# Resolving the extended atmosphere and their inner wind of Mira

K.T. Wong (Paper 11)



# Resolving the extended atmosphere and their inner wind of Mira

K.T. Wong (Paper 11)

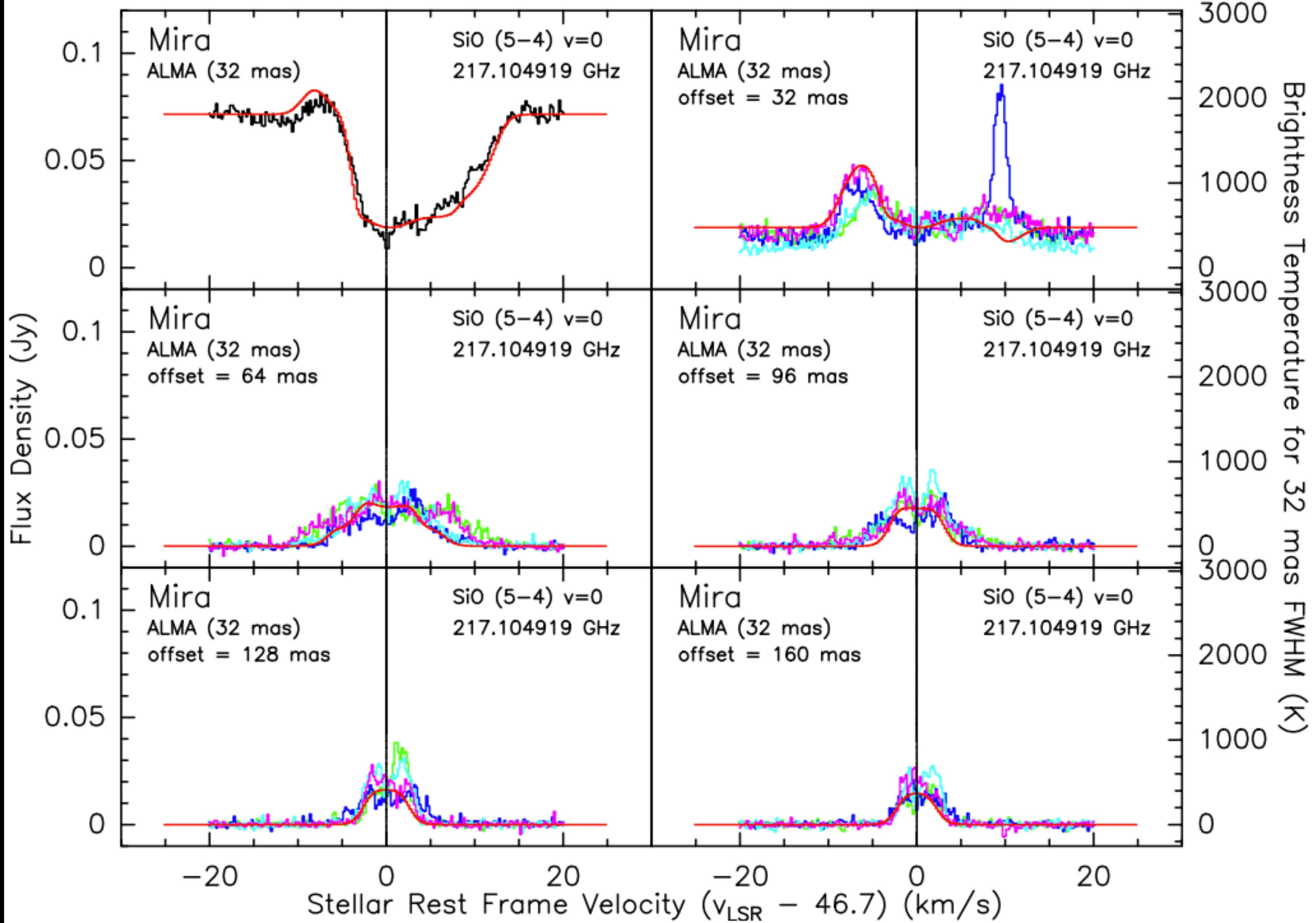


**Fig. 10.** Preferred model: spectra of SiO  $v = 0$   $J = 5-4$  at various positions. The black histogram is the observed spectrum at the centre of continuum, green, blue, cyan, and magenta histograms are the observed spectra along the eastern, southern, western, and northern legs, respectively, at various offset radial distances as indicated in each panel. The red curves are the modelled spectra predicted by RATRAN. Our model does not produce the population inversion (i.e. negative excitation temperature) required for maser emission in this SiO transition, so we do not expect our modelled spectra to show any maser emission, as seen in the upper right panel (see text for the discussion of the spike).

# Resolving the extended atmosphere and their inner wind of Mira

K.T. Wong (Paper 11)

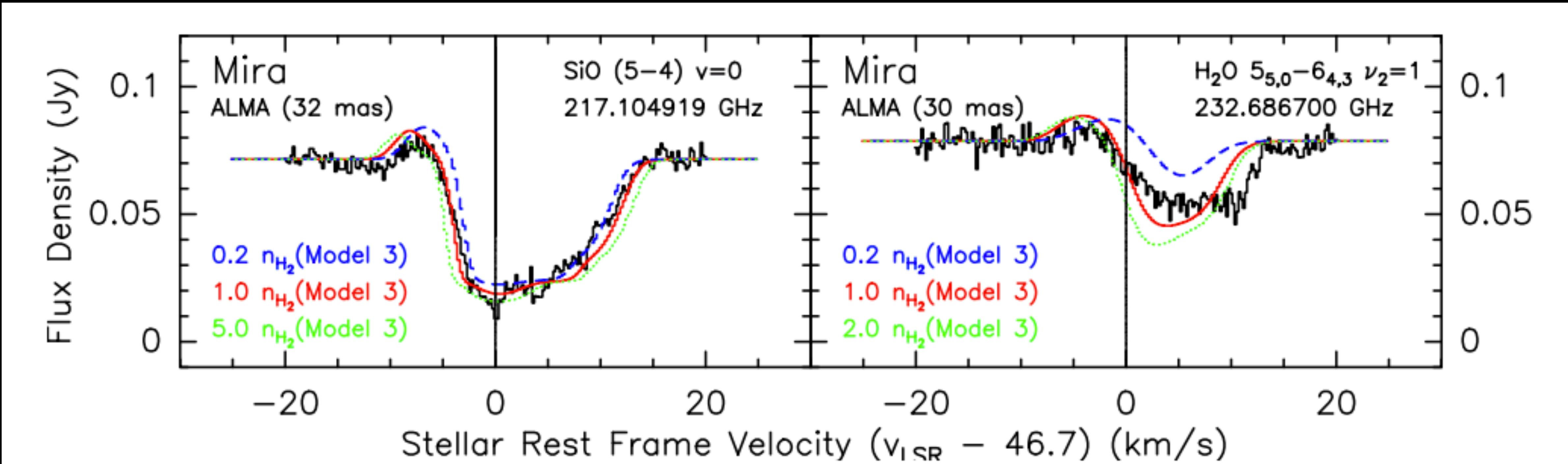


**Fig. 13.** Spectra of SiO  $v = 0$   $J = 5-4$  (left) and H<sub>2</sub>O  $\nu_2 = 1$   $J_{K_a,K_c} = 5_{5,0}-6_{4,3}$  (right) extracted from the centre of the continuum. The black histogram is the observed spectrum and the red curves are the modelled spectra from our preferred model, Model 3. The blue dashed curves are the spectra obtained by reducing the input H<sub>2</sub> gas density by a factor of 5; and the green dotted curves are the spectra obtained by increasing the input gas density by a factor of 5 for the modelling of SiO, and a factor of 2 for H<sub>2</sub>O.

# Resolving the extended atmosphere and their inner wind of Mira

## K.T. Wong (Paper 11)

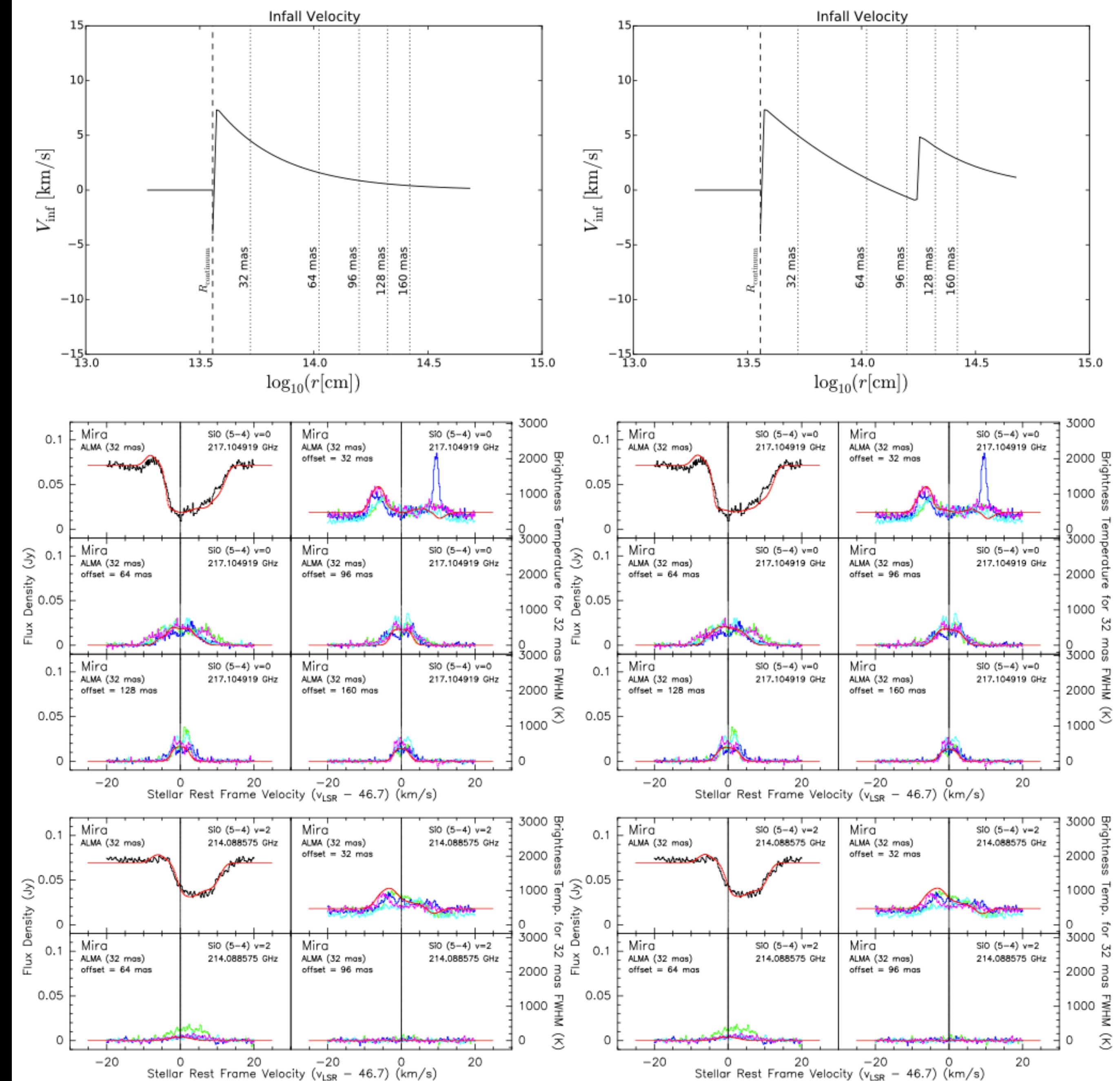


**Fig. 18.** Input radial velocity profile (top row) and modelled SiO (middle and bottom rows) spectra of two nearly identical models, except that for the model on the left there is only one large-scale velocity variation close to the radio continuum, while for the model on the right there is an additional strong velocity variation near  $1.8 \times 10^{14} \text{ cm} = 109 \text{ mas} \sim 5 R_{\star}$ .

# Resolving the extended atmosphere and their inner wind of Mira

K.T. Wong (Paper 11)

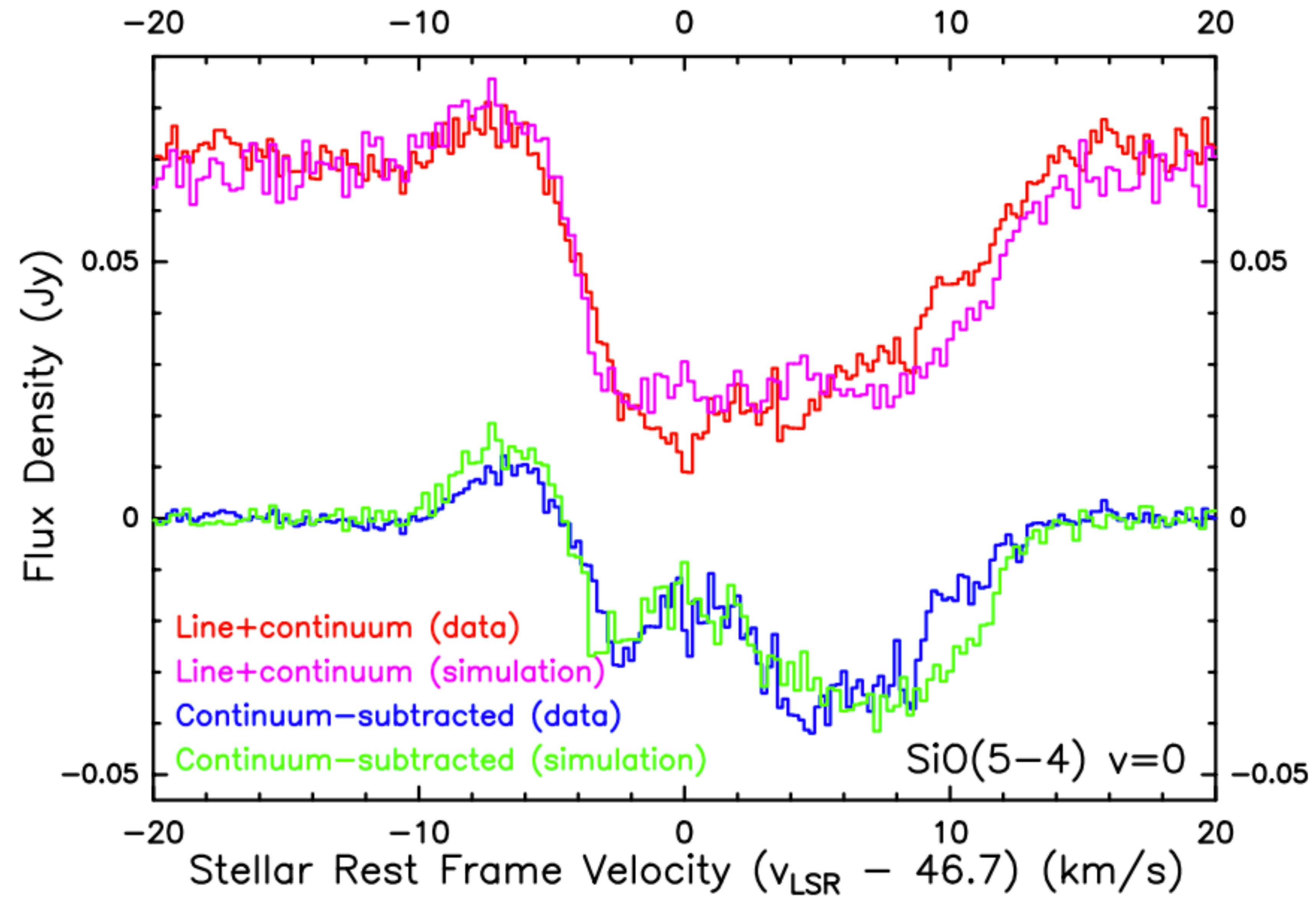


**Fig. B.4.**  $^{28}\text{SiO}$   $v = 0$   $J = 5-4$  spectra extracted from the line of sight towards the centre of Mira's continuum from the full data images (line+continuum; red and magenta at the *top*) and from the continuum-subtracted images (blue and green at the *bottom*). The red and blue spectra correspond to the images from the actual data of Mira's ALMA SV observation, and the magenta and green spectra correspond to the simulated data using CASA task `simobserve`. The imaging procedures for the observed and simulated data are identical.

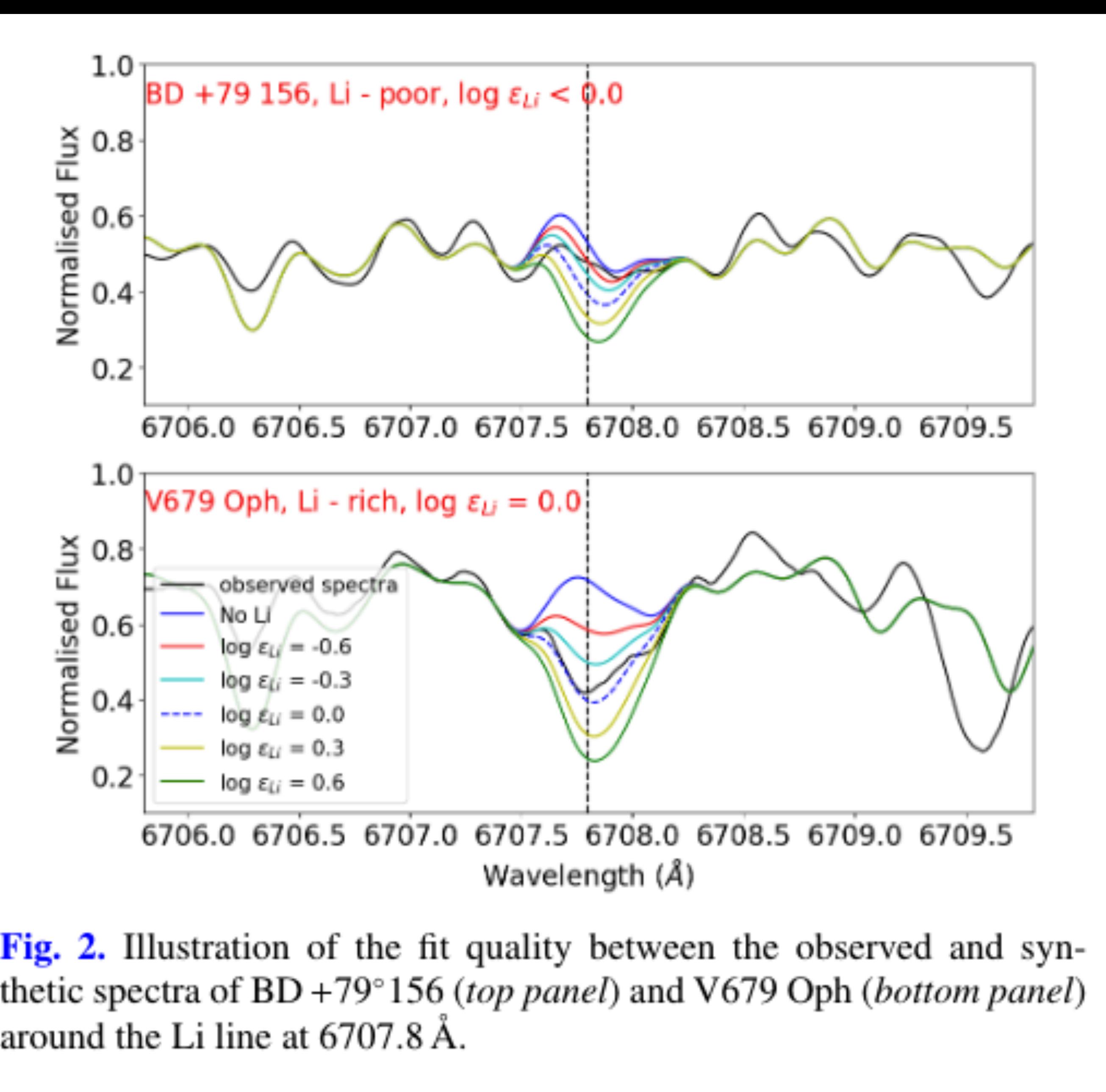
# **S stars and s-process in the Gaia era**

## **(Paper 12)**

# S stars and s-process in the Gaia era

## Shreeya Shetye (Paper 12)

- The first plot were just lines of Tc
- Light-s-process elements (Sr, Y, Zr, Nb)
- Heavy-s-process elements (Ba, Ce, Nd)
- Other heavy elements (Pr, Sm, Eu)
- And Tc was treated separately



# S stars and s-process in the Gaia era

Shreeya Shetye (Paper 12)

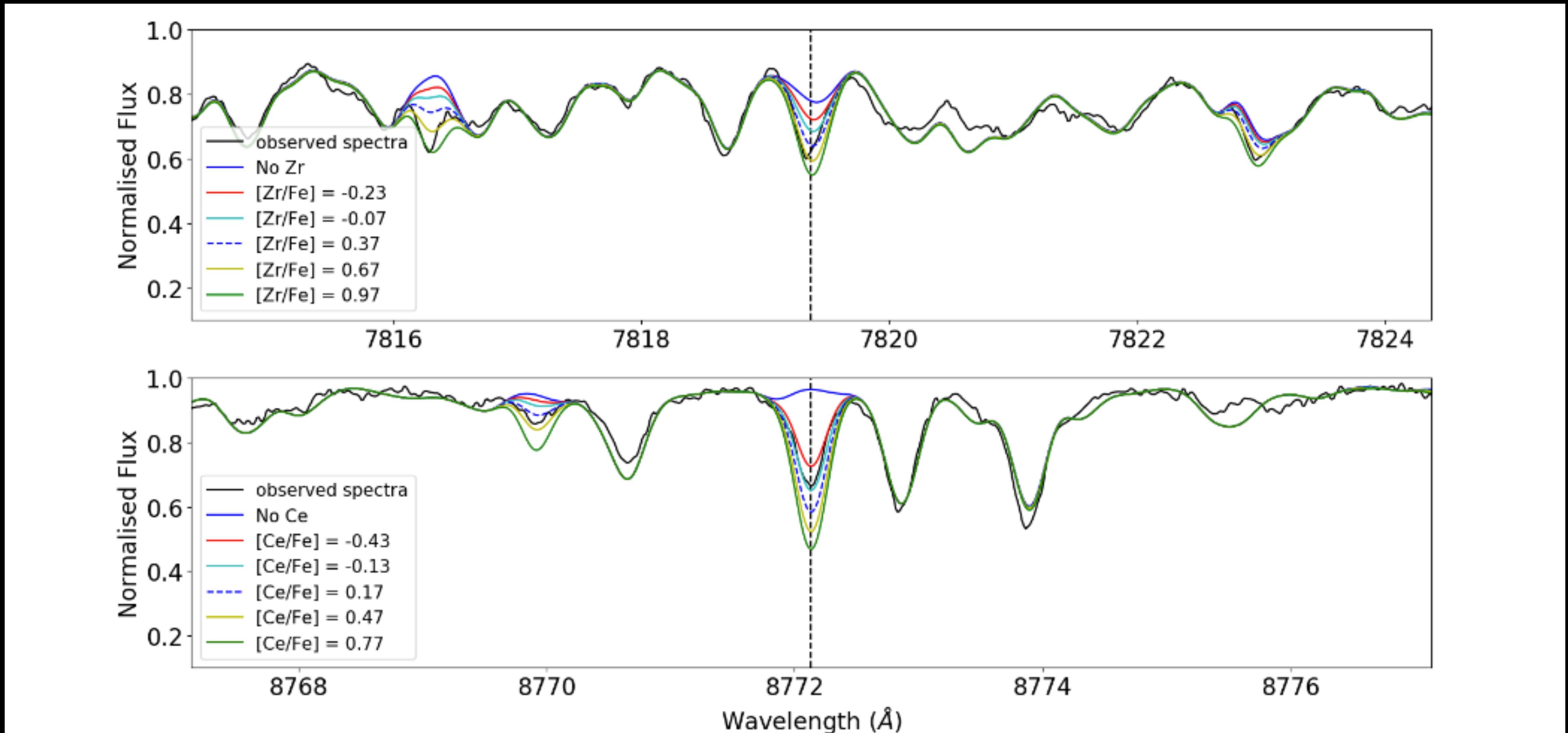


**Fig. 3.** Illustration of the fit between the observed and synthetic spectra for the S star HR Peg. *Top panel*: presents 5  $\text{\AA}$  around the Zr I line at 7819.37  $\text{\AA}$  and *bottom panel*: around the Ce II line at 8772.135  $\text{\AA}$ .

# S stars and s-process in the Gaia era

Shreeya Shetye (Paper 12)

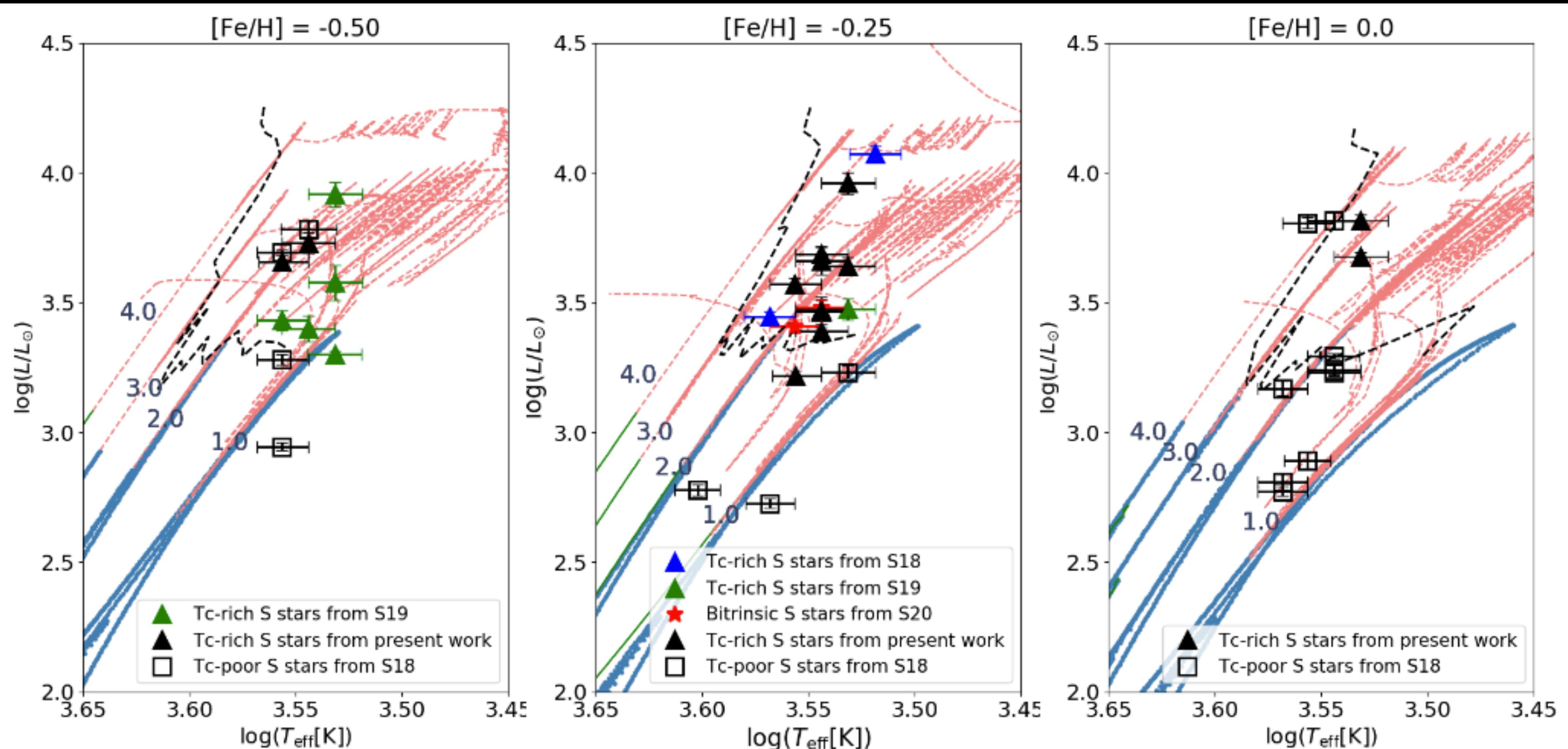


**Fig. 4.** HR diagram of intrinsic (filled triangles) S stars from our large sample and extrinsic (open squares) S stars from S18 along with the STAREVOL evolutionary tracks corresponding to the closest metallicities. The red giant branch is represented in blue, the core He-burning phase in green, whereas the red dashed lines correspond to the AGB tracks. The black dashed line represents the predicted onset of the third dredge-up, i.e., the lowest stellar luminosity following the first occurrence of a TDU episode (down to  $1.5$ ,  $1.3$ ,  $1.0 M_{\odot}$  for  $[\text{Fe}/\text{H}] = 0.0$ ,  $-0.25$ ,  $-0.50$  respectively).

# S stars and s-process in the Gaia era

Shreeya Shetye (Paper 12)

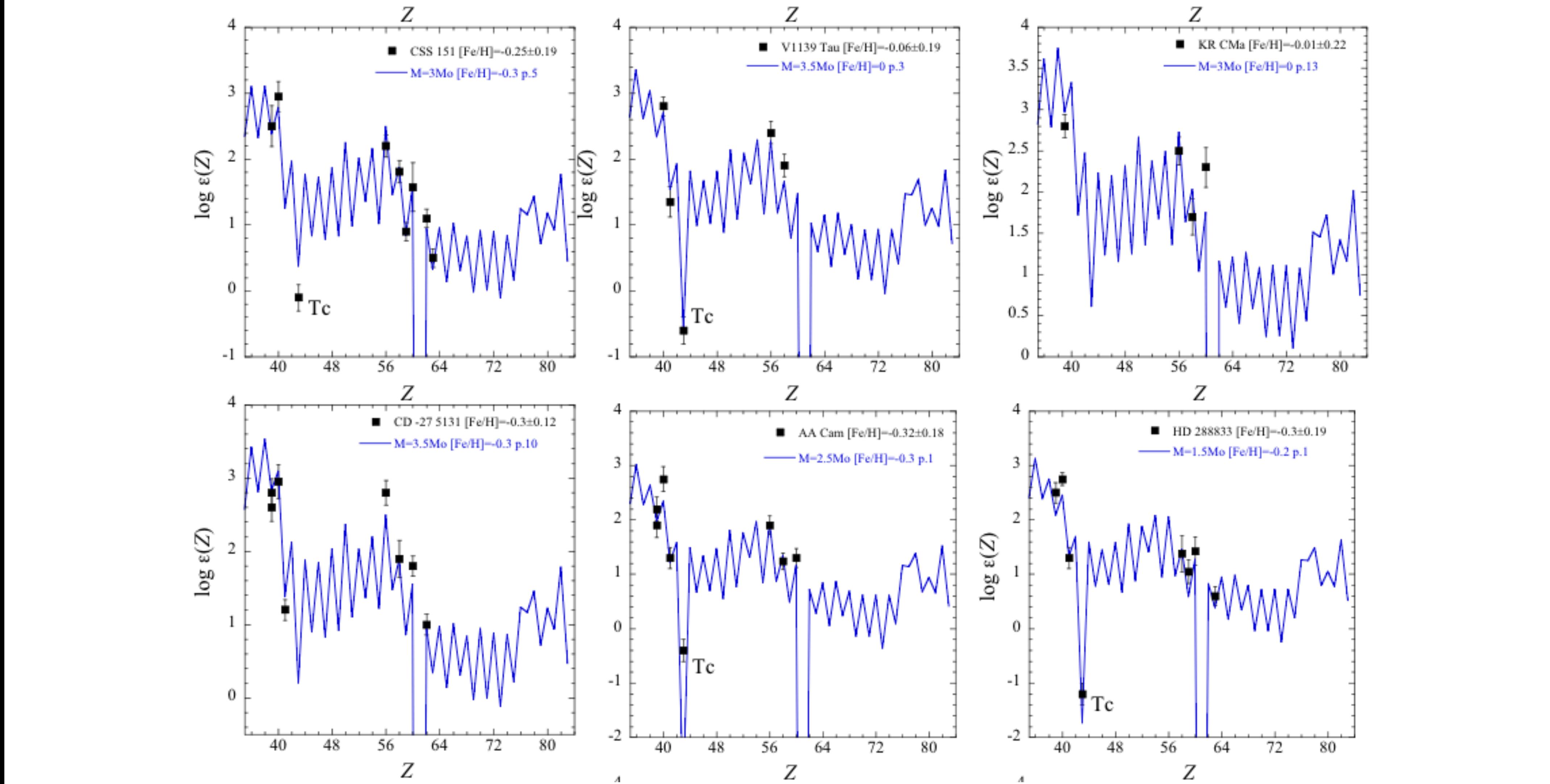


**Fig. 5.** Measured *s*-process element abundances compared with the nucleosynthesis predictions. The blue line represents the nucleosynthesis predictions compatible with the mass and metallicity of the individual stars. The number of pulses  $n$  required to best-match the measured abundances is mentioned in the label of every panel as “ $p.n$ ”.

# S stars and s-process in the Gaia era

## Shreeya Shetye (Paper 12)

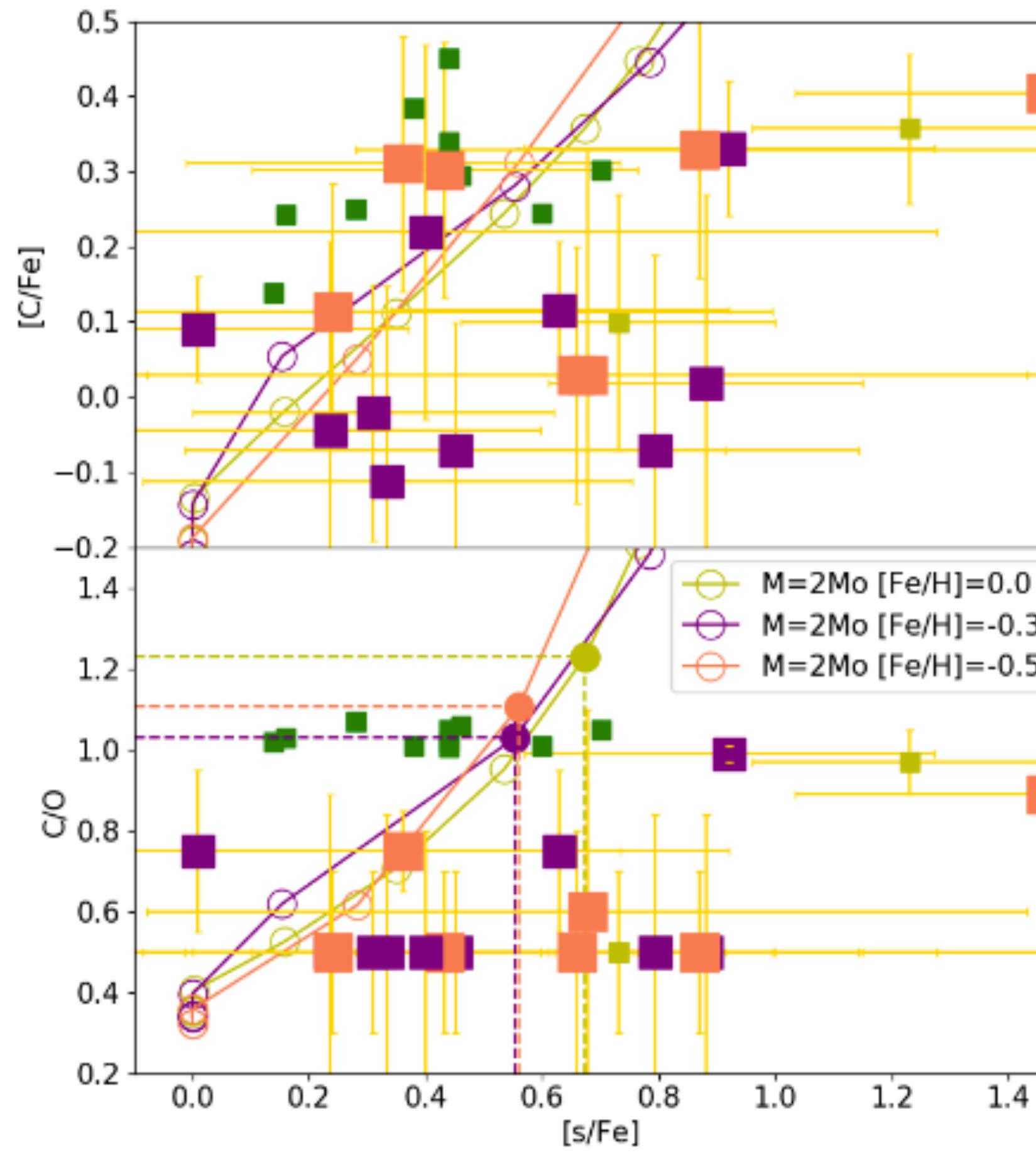


**Fig. 6.** Distribution of the carbon abundance of our sample stars with respect to their  $[s/\text{Fe}]$  index. *Top panel*: measured  $[\text{C}/\text{Fe}]$  abundances as a function of  $[s/\text{Fe}]$  for our large sample of Tc-rich S stars (light green, purple and orange squares) where the size of the symbol increases with decreasing metallicity, considering three metallicity bins:  $[\text{Fe}/\text{H}]$  in  $[0.0; -0.2]$ ; light green,  $[-0.2; -0.4]$ ; purple, below  $-0.4$ ; orange. Tc-rich carbon stars from Abia et al. (2002) are shown as green squares. *Bottom panel*: derived  $\text{C}/\text{O}$  ratio versus  $[s/\text{Fe}]$  for the same stars. Predictions for a  $2 M_{\odot}$  STAREVOL model at metallicity  $[\text{Fe}/\text{H}] = 0.0$  (light green),  $-0.3$  (violet) and  $-0.5$  (orange) are overplotted. The empty circles along the tracks indicate the successive TDUs, while the three filled circles mark the first TDU, which led to  $\text{C}/\text{O} > 1$  in each model.

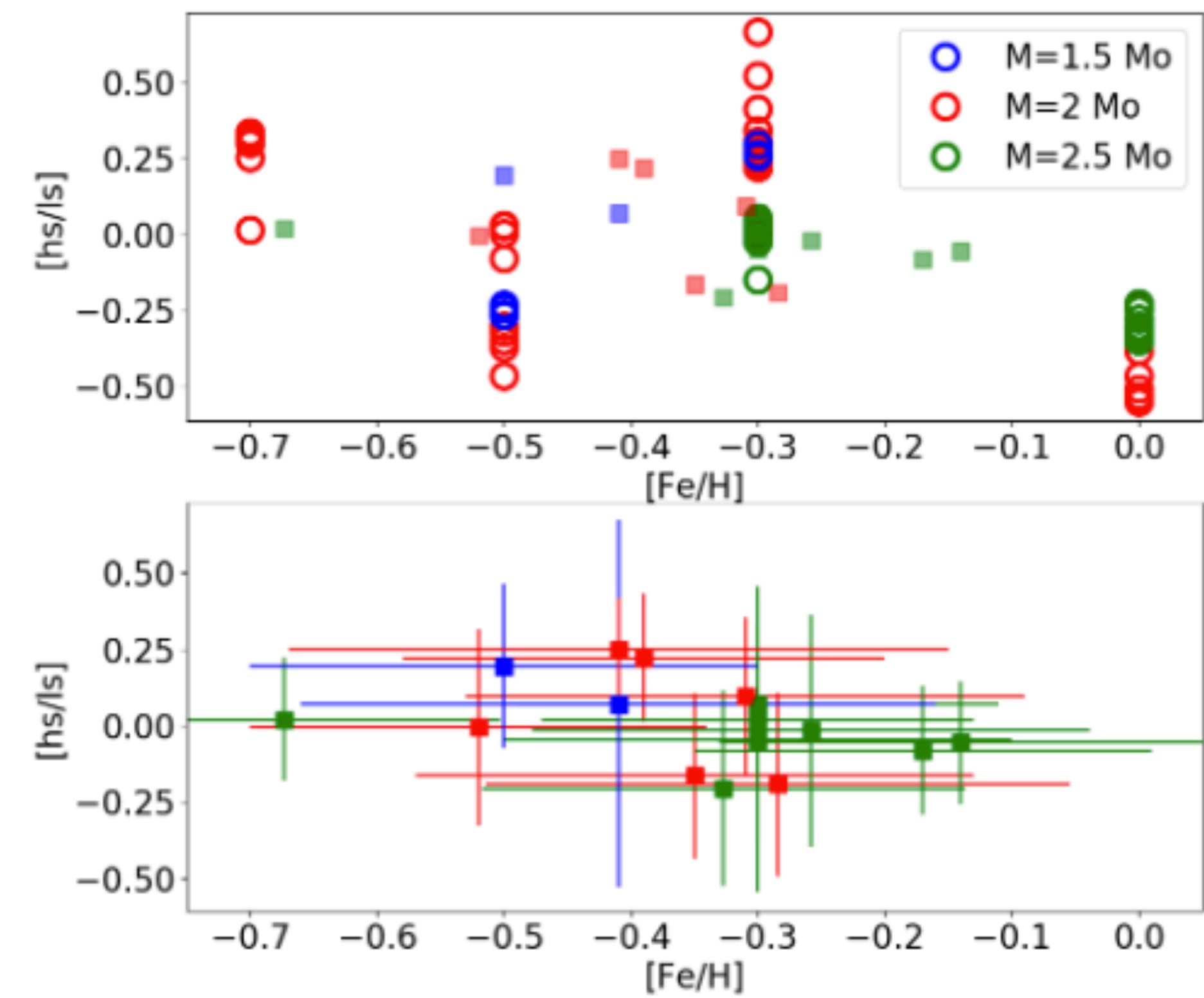


**Fig. 7.** Distribution of  $[\text{hs}/\text{ls}]$  as a function of metallicity for the intrinsic S stars of our study (filled squares). The hs-index has been calculated using Ba and Nd, and the ls-index using Y and Zr. The symbols are color-coded with respect to the initial mass in the bins  $M_{\text{ini}} < 1.5 M_{\odot}$  (blue),  $1.5 \leq M_{\text{ini}} < 2.5 M_{\odot}$  (red), and  $M_{\text{ini}} \geq 2.5 M_{\odot}$  (green). We note that these mass bins are designed to match the  $[\text{hs}/\text{ls}]$  STAREVOL predictions only available for  $M_{\text{ini}} = 1.5, 2, 2.5 M_{\odot}$ . Open circles denote the predictions from pulse to pulse for the different initial masses.

# S stars and s-process in the Gaia era

Shreeya Shetye (Paper 12)

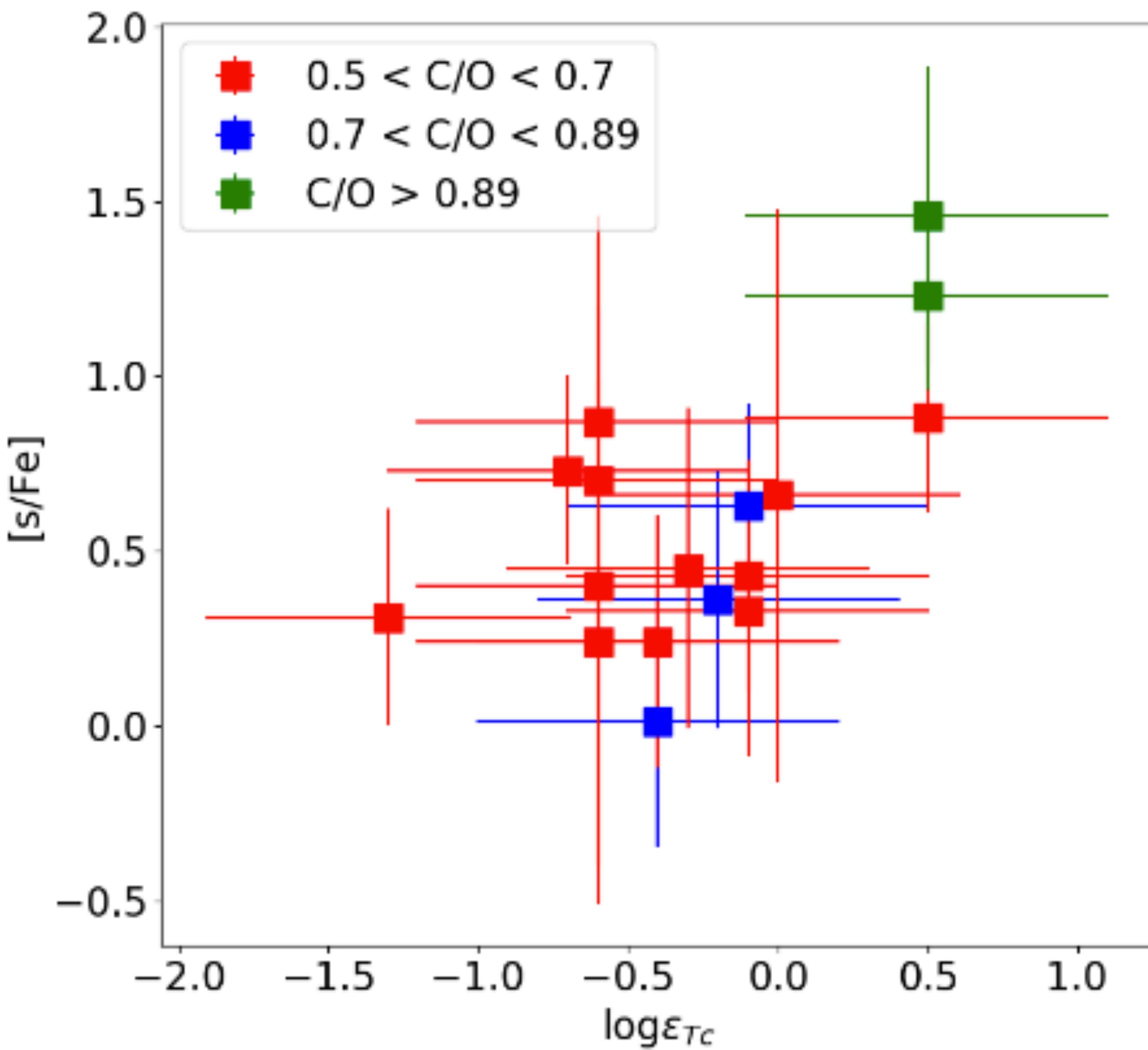


**Fig. 8.** [s/Fe] index versus Tc abundance. The different colors represent different C/O ratio bins as described in the figure.

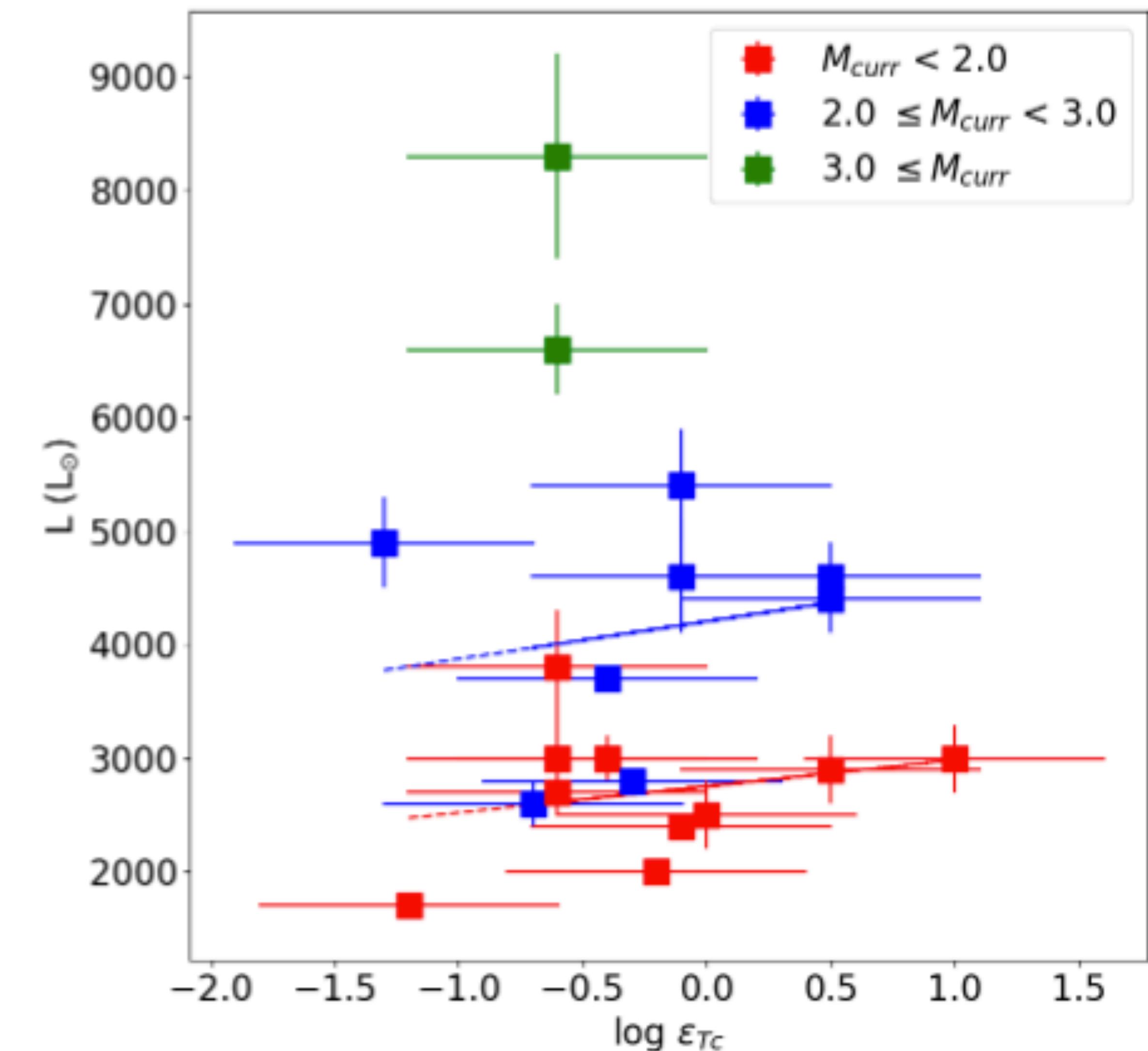
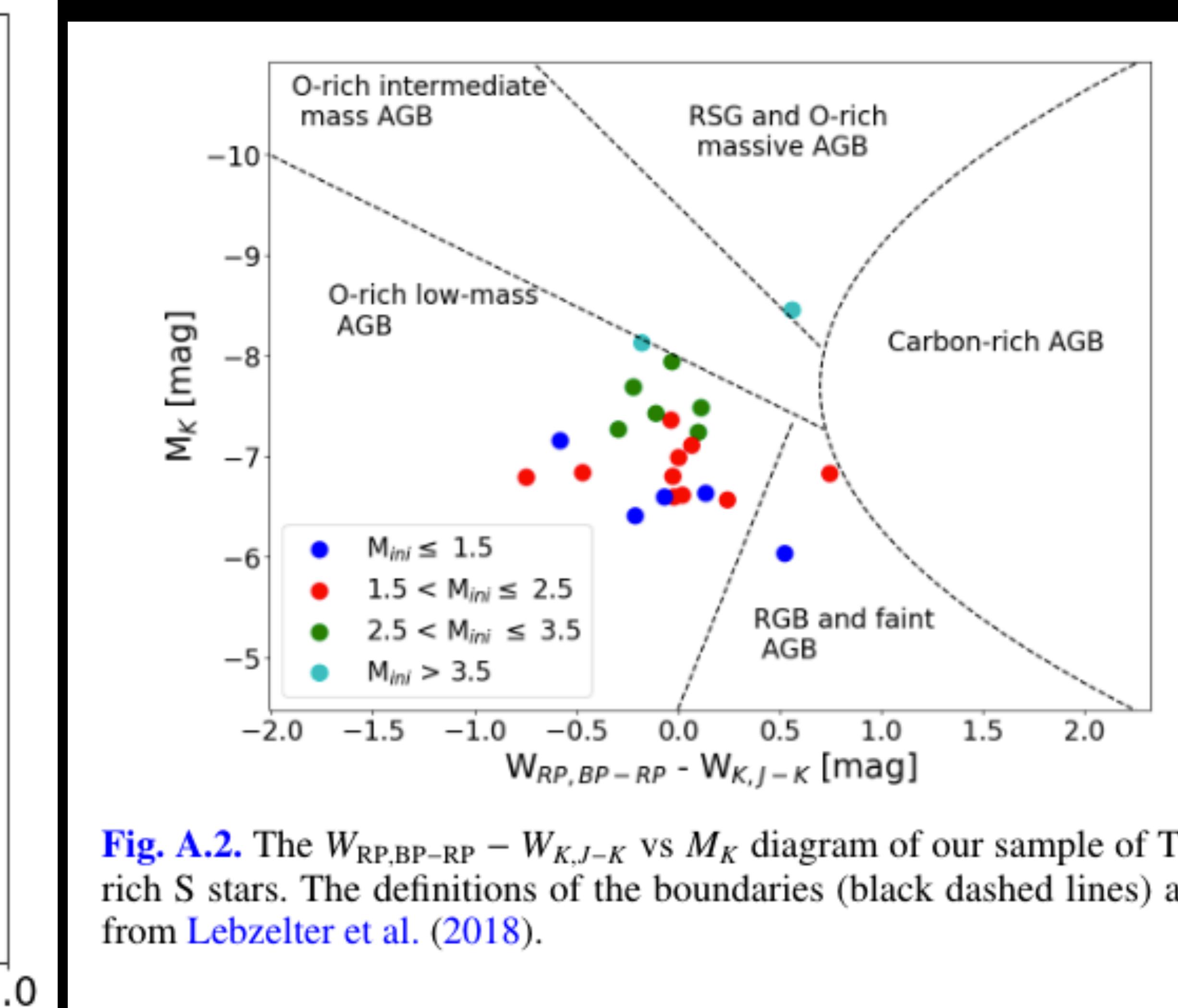
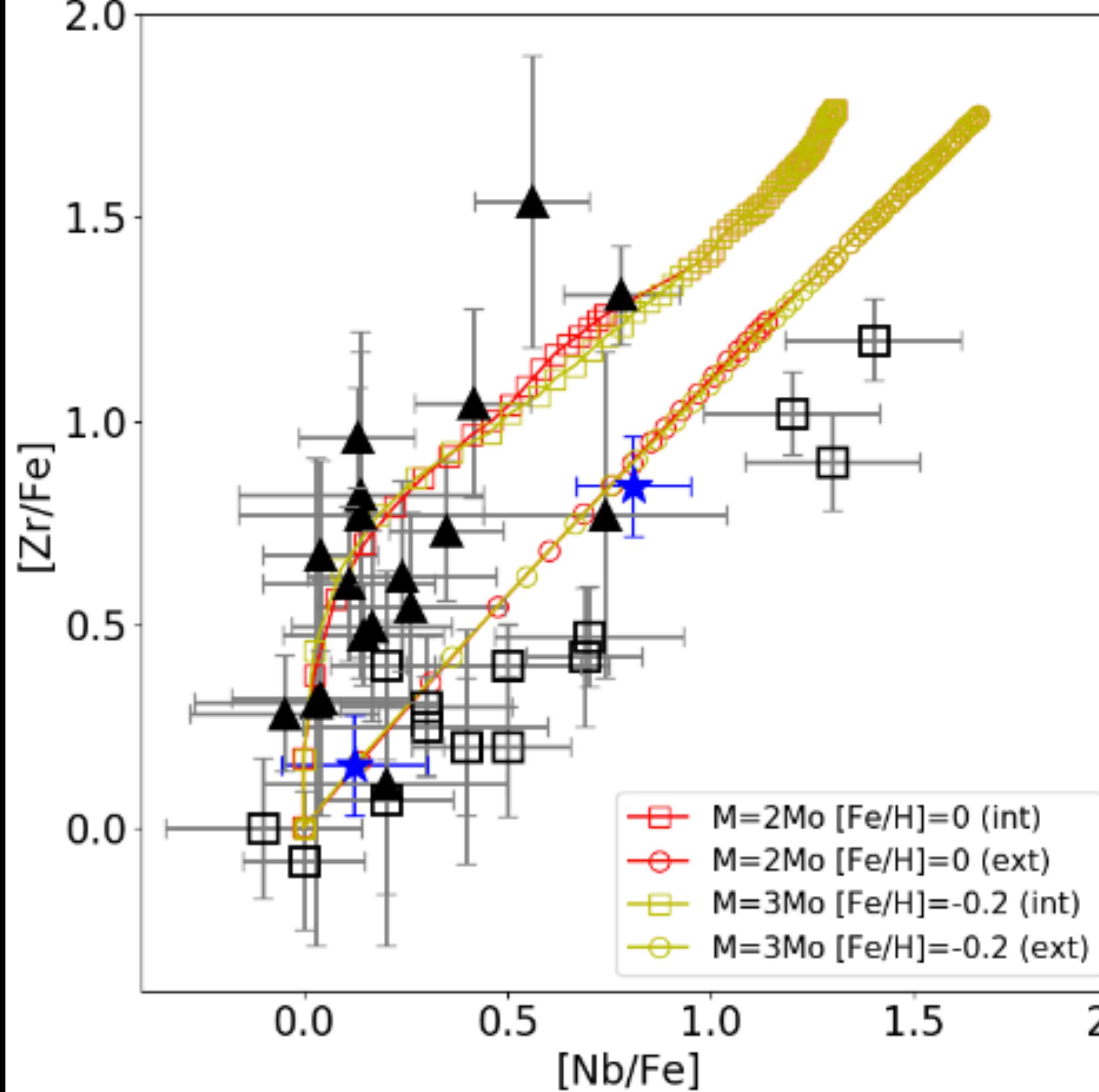


**Fig. 9.** Stellar luminosity as a function of Tc abundance. The symbols are color coded according to their mass bin. The blue and red dashed lines represent the linear least-squares fit for the stars in the corresponding mass bin.

S stars and s-process in the Gaia era  
Shreeya Shetye (Paper 12)



This is a classification map for AGB stars based on mag of Gaia and 2MASS  
(Lebzelter et al. (2018))

WRP=GRP-1.3 (GBP-GRP)  
 $W_{K, J-K} = KS - 0.686 (J-K)$

**Identification of Strontium in the merger of  
two neutron stars**

**(Paper 13)**

# Identification of Strontium in the merger of two neutron stars

Darach Watson (Paper 13)

- Kilonova
- R- process elements
- Strontium the only one found that produces the feature
- P Cygni profile:  
Is a combination of features in a star's spectrum that points to an outflow of material in the form of either an expanding shell of gas or a powerful stellar wind. The P Cygni profile is characterized by strong emission lines with corresponding blueshifted absorption lines

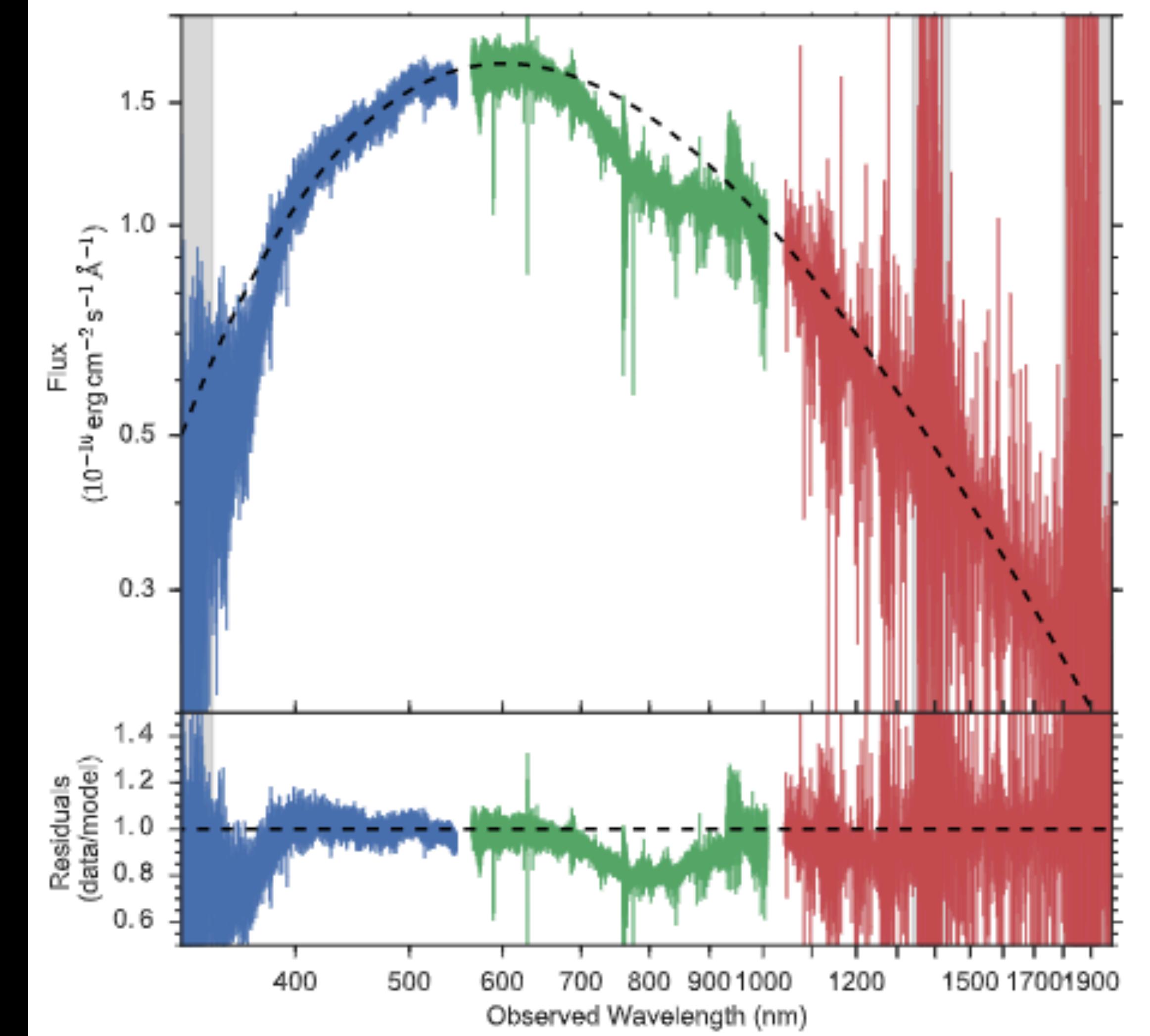


**Figure 1 | Spectrum of the kilonova, AT2017gfo, showing broad absorption features.** The spectrum was observed at 1.5 days after the merger. The dashed line is the blackbody component of a blackbody model with broad absorption lines (see text). The residuals of data minus blackbody are shown in the lower panel with the dashed line indicating the  $1\sigma$  uncertainty on each spectral bin. The data in the sections overplotted with grey bars are affected by telluric features or are poorly-calibrated regions and are not included in the fit.

# Identification of Strontium in the merger of two neutron stars

Darach Watson (Paper 13)

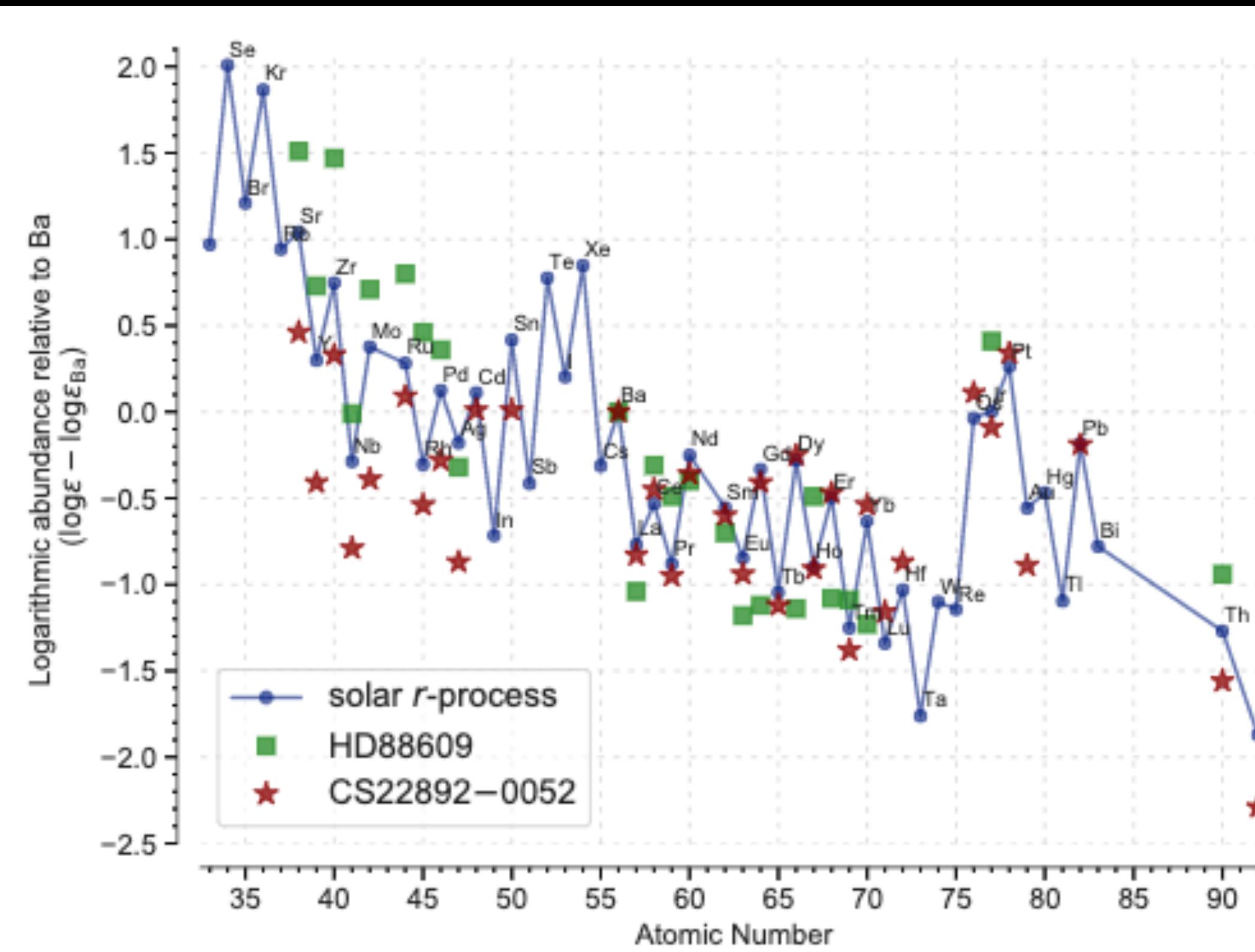


**Figure 2 | The abundances of elements produced by the *r*-process.** Relative *r*-process abundances normalized to the Ba abundance are shown for the sun and two metal-poor stars, one rich in heavy *r*-process elements, CS 22892–052<sup>39,54</sup>, and the other rich in light *r*-process elements, HD 88609<sup>20</sup>. These are the abundances of the elements used in Fig. 3, *inset*.

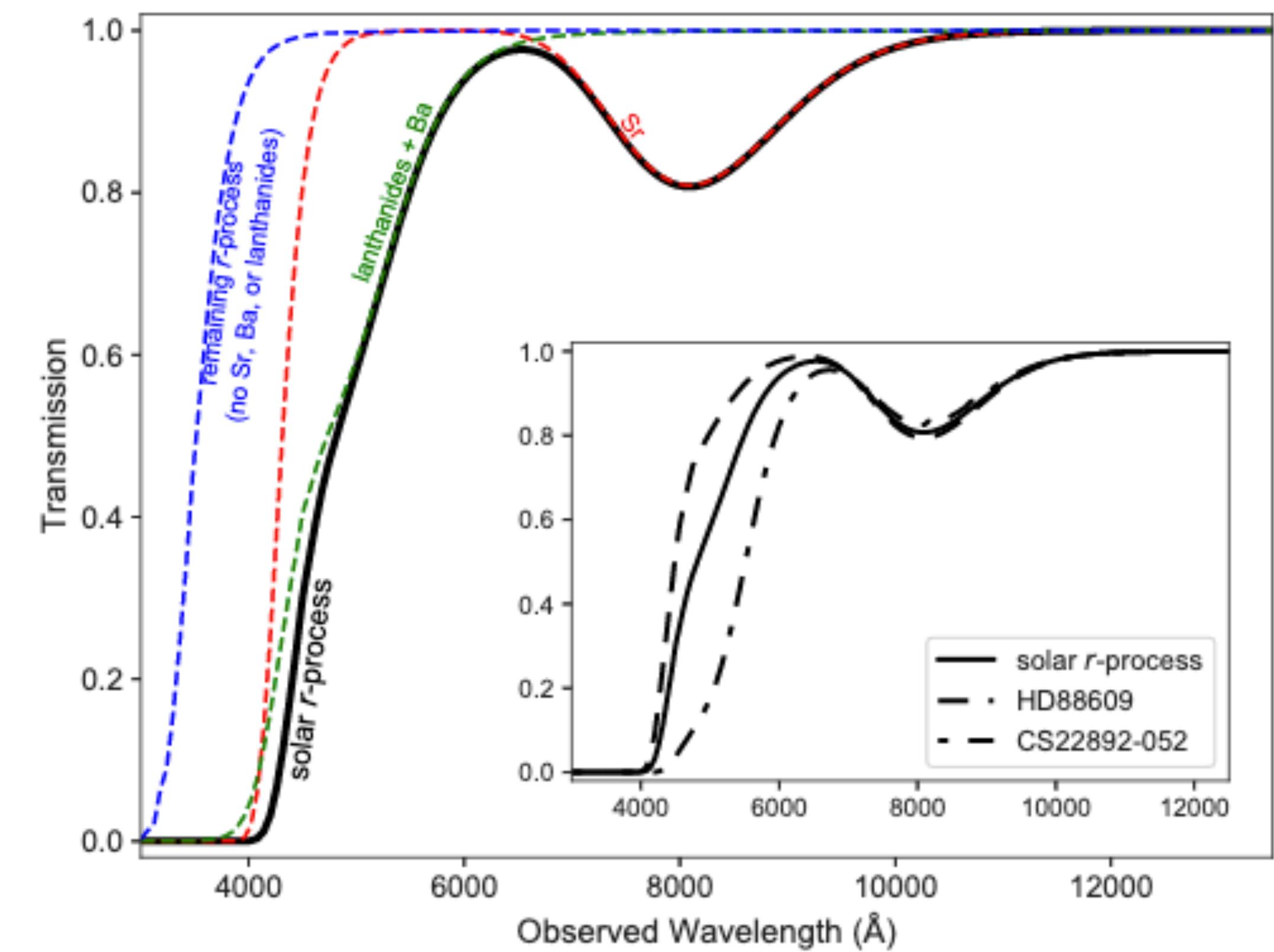
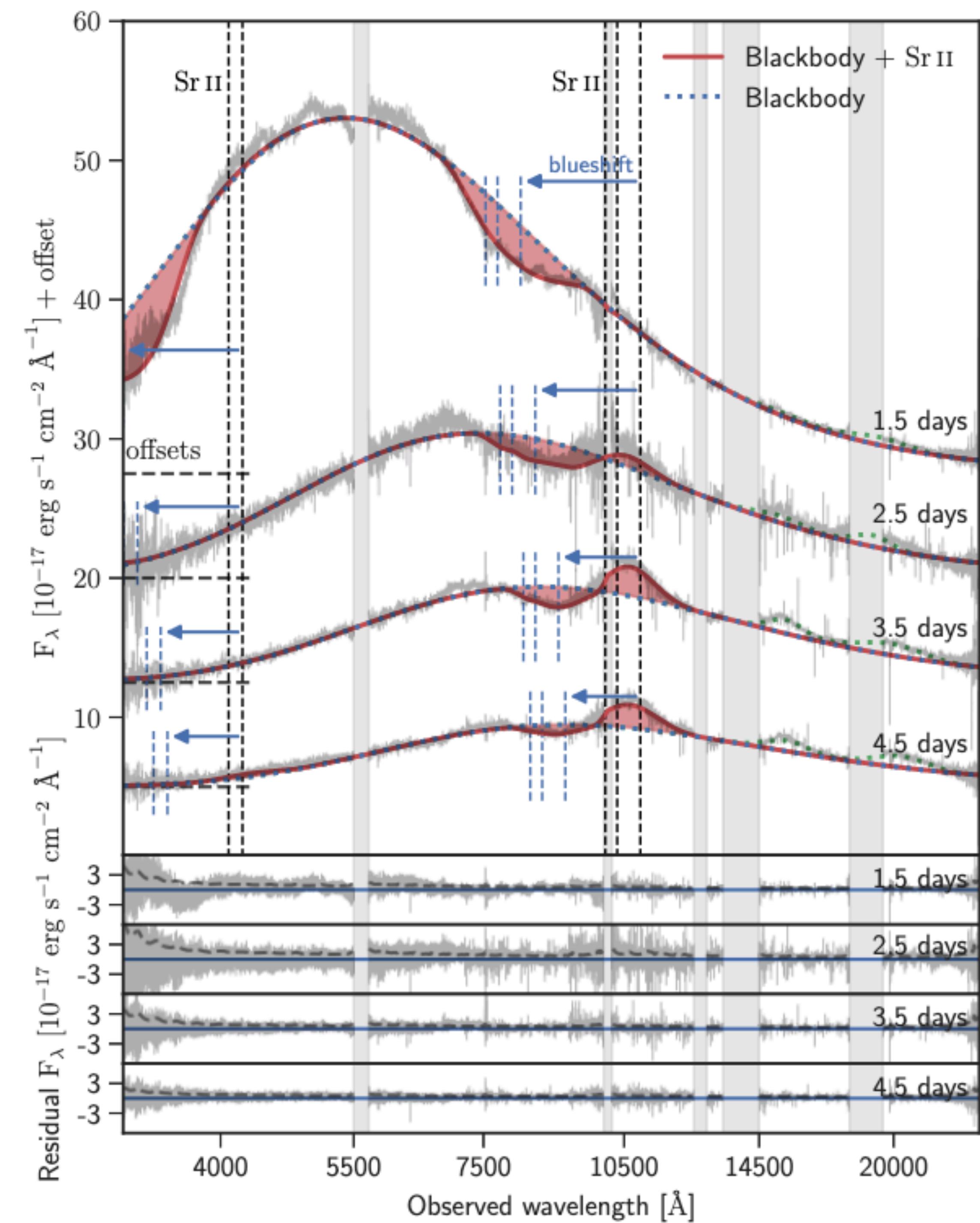


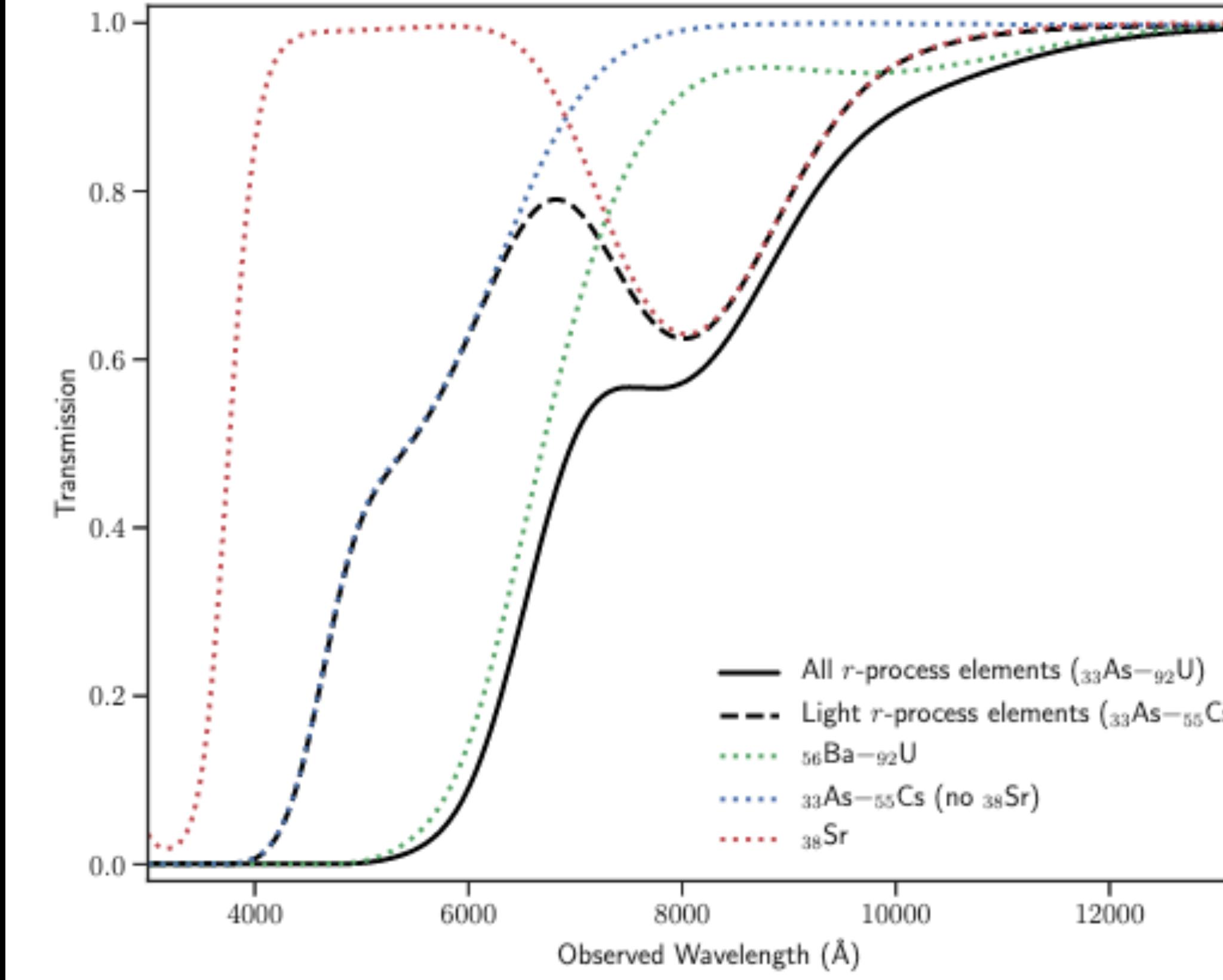
**Figure 3 | Thermal *r*-process element transmission spectrum.** The spectra are based on the lines formed in a gas in local thermal equilibrium with a temperature of 3,700 K and an electron density of  $10^7 \text{ cm}^{-3}$ , broadened by  $0.2c$  and blueshifted by  $0.23c$ . The spectrum produced by a solar *r*-process abundance ratio is plotted as a solid line. Contributions due to Sr (red dashed), Ba and the lanthanides (green dashed), and the remaining *r*-process elements (blue dashed) are shown. *Inset:* spectra resulting from a solar *r*-process abundance ratio (solid line), and from the abundance ratios of the metal-poor stars HD 88609<sup>20</sup> (dashed line) and CS 22892–052<sup>39,54</sup> (dash-dotted line).

# Identification of Strontium in the merger of two neutron stars

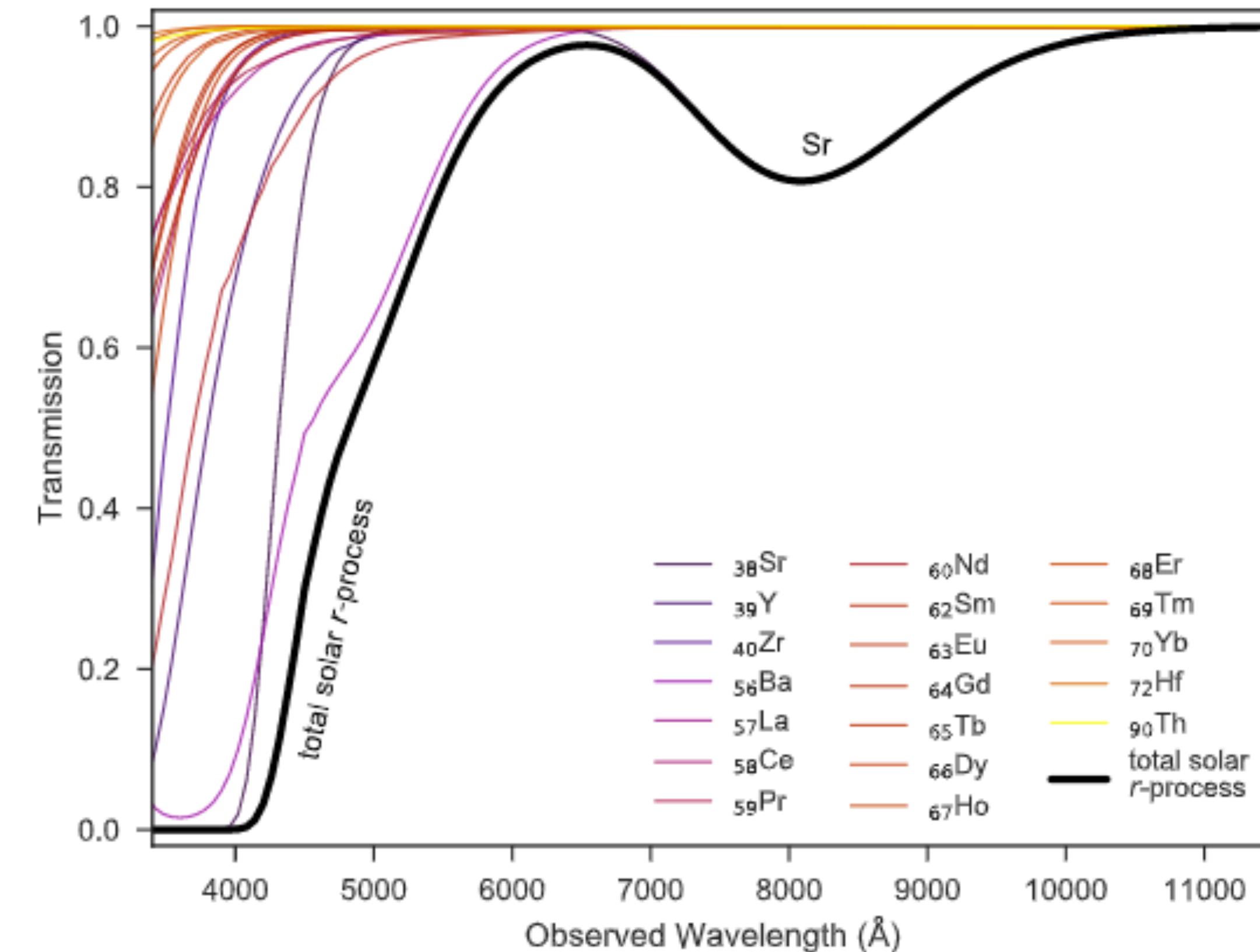
Darach Watson (Paper 13)

**Figure 4 | Spectral series of AT2017gfo 1.5–4.5 days after the merger.** Data are shown in grey and have been smoothed slightly. A model (solid red lines) consisting of a blackbody (blue dotted lines) with P Cygni profiles (red transparent fill) for the Sr lines is shown. The rest (black) and observed (blue) positions of the model's Sr lines are shown, with the blueshift indicated by arrows. Green dotted lines show the Gaussian emission profiles added to ensure the overall continuum is not biased. A vertical offset has been applied to each spectrum for clarity, with zero flux indicated by the dashed horizontal line segment. Bottom panels show the residuals between model and data.

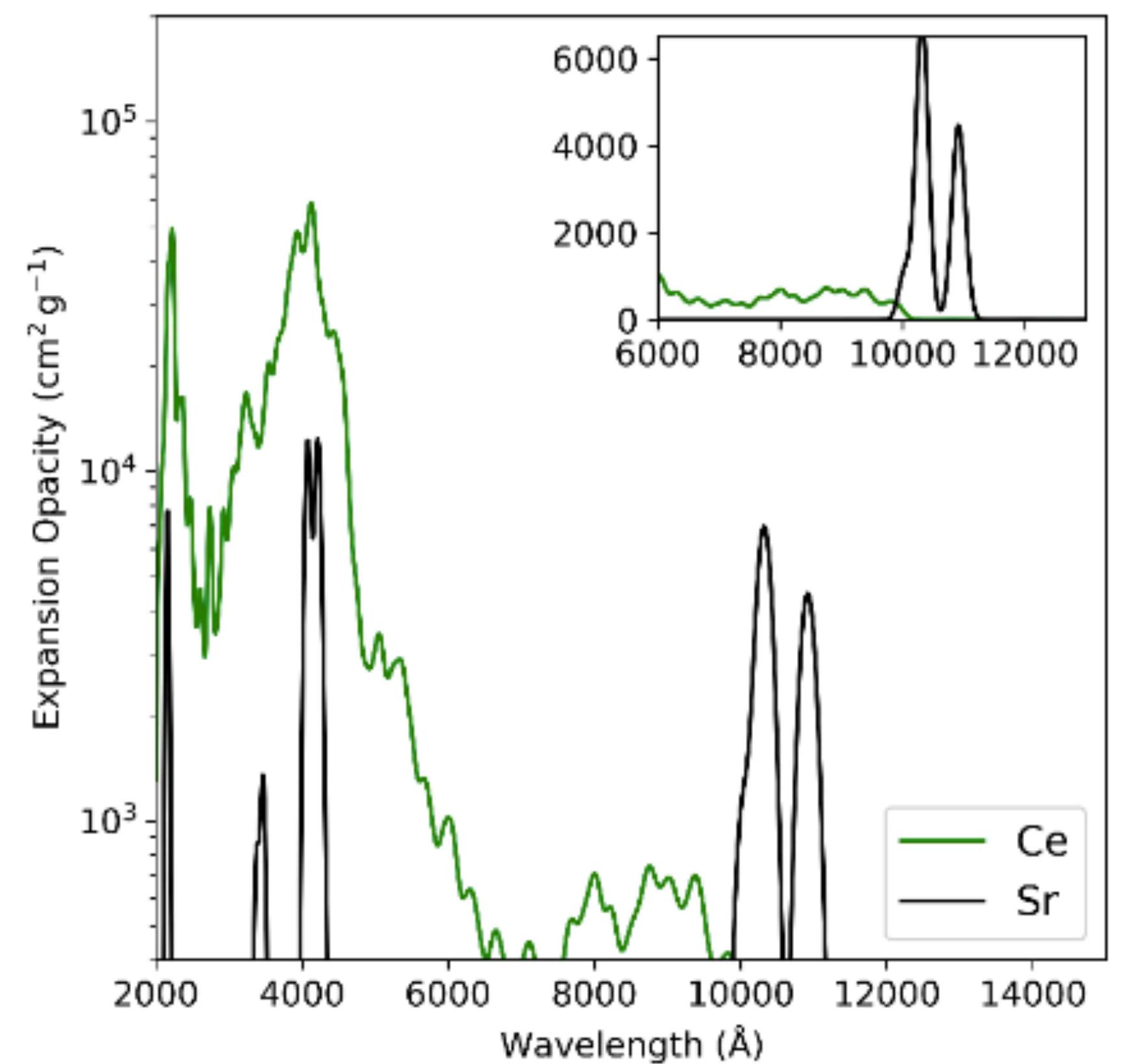




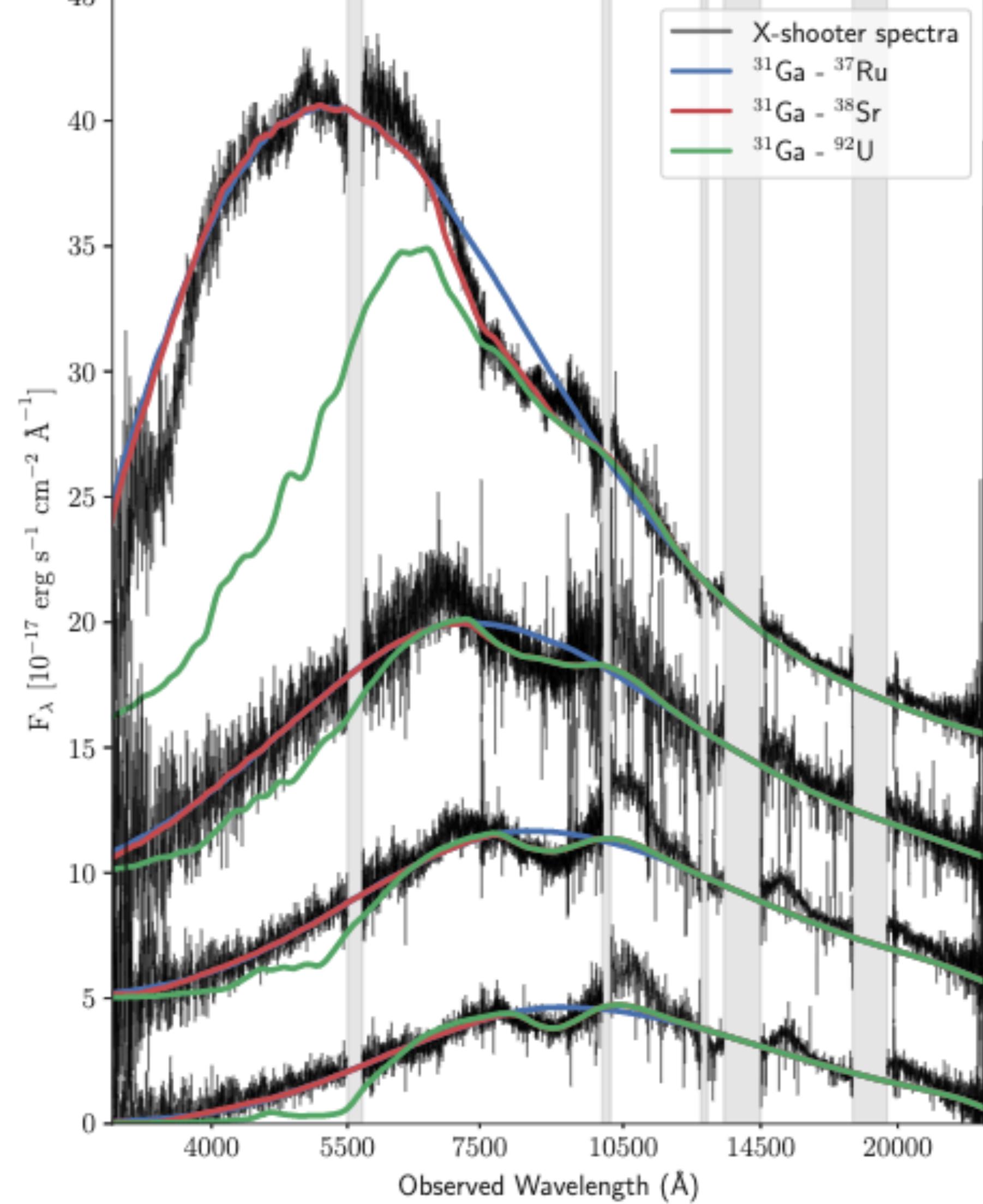
**Extended Data Figure 1 | Synthetic *r*-process element transmission spectra.** The spectra are generated using MOOG, where the relative abundances are based on solar *r*-process abundances. The spectra are blueshifted, broadened and normalized as in Fig. 3. The solid, black line is the total transmission spectrum for an atmosphere containing all the *r*-process elements ( $^{33}\text{As}$ – $^{92}\text{U}$ ). The dashed, black line is the same spectrum, only including the light *r*-process elements ( $^{33}\text{As}$ – $^{55}\text{Cs}$ ). The contributions from different subsets of species are also shown. The green, dotted line shows the heavy *r*-process elements ( $^{56}\text{Ba}$ – $^{92}\text{U}$ ), the blue, dotted lines shows the light *r*-process elements ( $^{33}\text{As}$ – $^{55}\text{Cs}$  excluding Sr), which are both shown individually as thin, black lines and summed in the red, dotted line. This plot shows how Sr stands out in absorption, regardless of the composition of the material. The normalization is arbitrary and different to the LTE equivalent in Fig. 3 for display reasons.



**Extended Data Figure 3 | Thermal transmission spectra for *r*-process elements plotted individually.** The spectra are based on the lines formed in a gas in local thermal equilibrium. The abundances of elements are scaled to the solar *r*-process and the spectra are velocity broadened, blueshifted and normalised as in Fig. 3. The spectrum derived from the total solar *r*-process abundance mix is plotted as a thick black line. The contributions from Sr clearly dominate at  $\sim 8,000\text{ \AA}$ , with no significant contribution from any other element.



**Extended Data Figure 5 | Comparison of the expansion opacities at modest optical depths for Sr and Ce.** This calculation shows the potential of Sr to dominate the opacity at  $\sim 1 \mu\text{m}$  at low optical depths. The opacities are based on local thermal equilibrium calculations for a gas at a temperature of 5,000 K, a mean local density of  $8.4 \times 10^{-17} \text{ g cm}^{-3}$  of Sr or Ce, an electron density of  $7.6 \times 10^8 \text{ cm}^{-3}$ , and a 1% atmospheric radius at 1.5 days after the explosion. Line lists used for Sr and Ce are from the Kurucz and VALD databases respectively.



**Extended Data Figure 6 | Radiative transfer models from the first four epochs using the TARDIS code.** The blue line is the synthetic TARDIS spectrum using relative solar *r*-process abundances and including elements from <sup>31</sup>Ga to <sup>37</sup>Rb, i.e. without Sr. The red line additionally includes <sup>38</sup>Sr. The green line is a model including all elements from <sup>31</sup>Ga to <sup>92</sup>U. These models show that the spectra are well-reproduced with elements around the first *r*-process abundance peak, specifically Sr.

# **A critique of the Spite Plateau, and the Attrition of primordial lithium**

## **(Paper 14)**

# A critique of the Spite Plateau, and the Attrition of primordial lithium

J.E. Norris (Paper 14)

- Spite Plateau: is a baseline in the abundance of lithium found in old stars orbiting the galactic halo.
- 

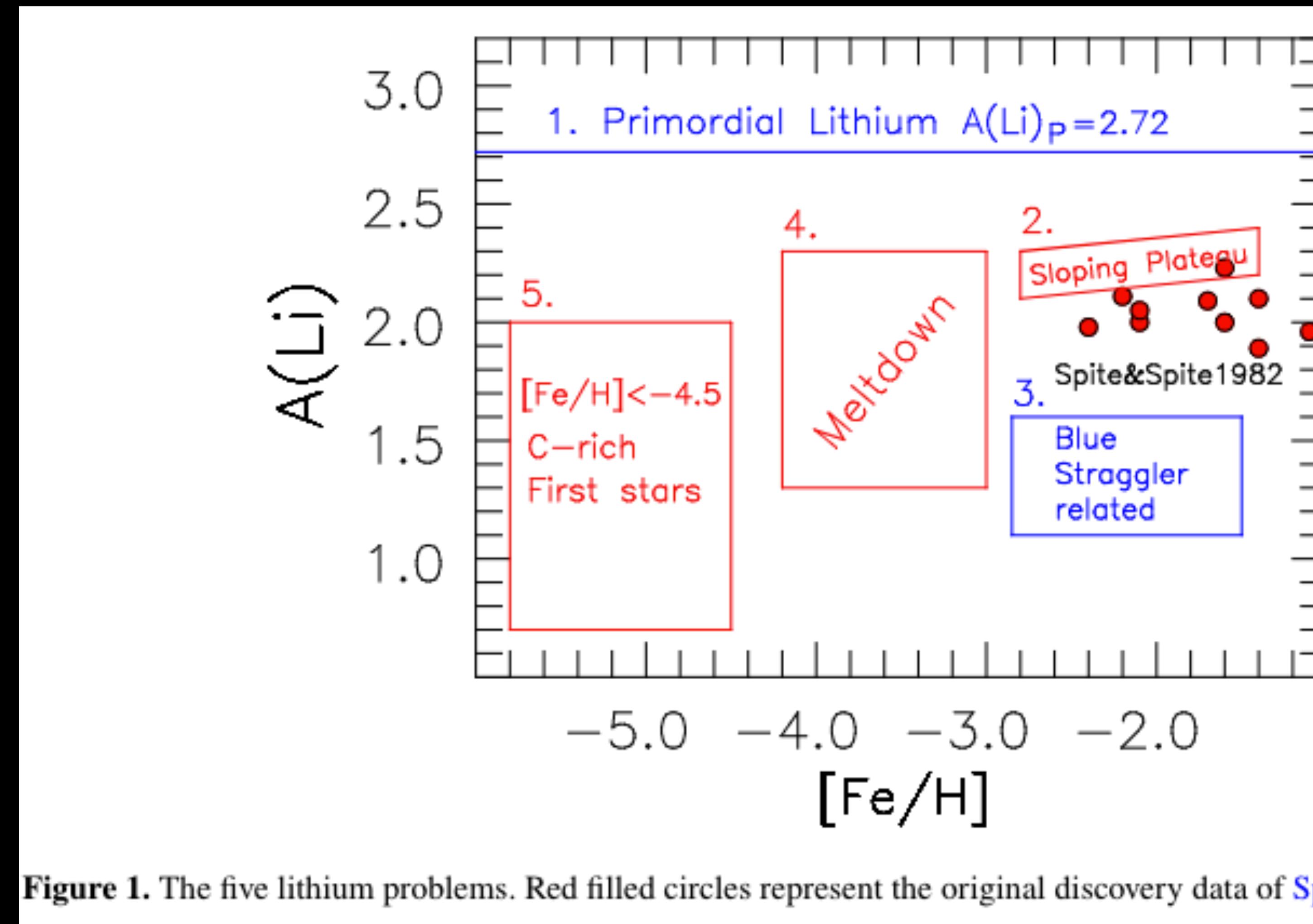


**Figure 1.** The five lithium problems. Red filled circles represent the original discovery data of Spite & Spite (1982).

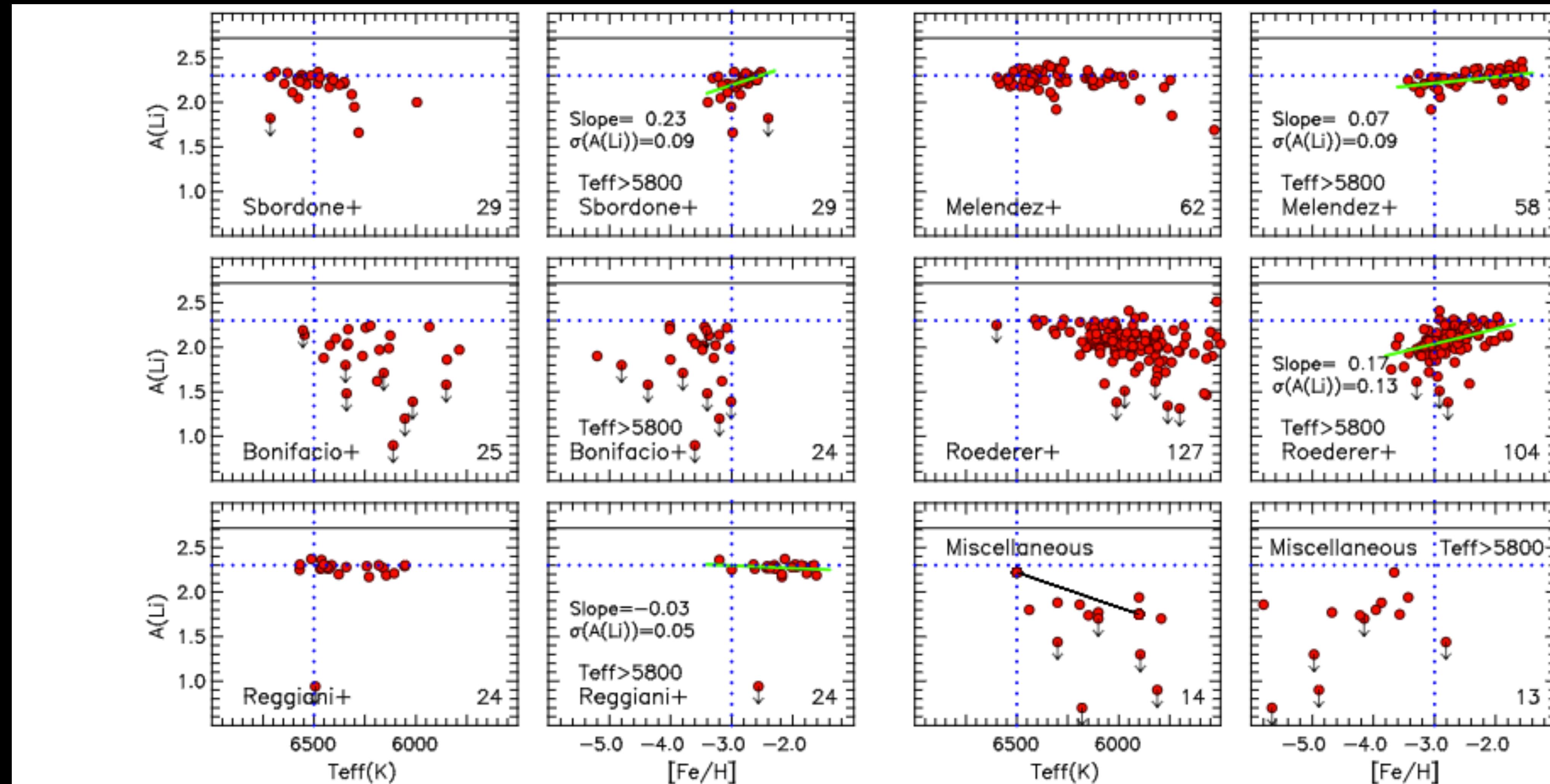


**Figure 2.**  $A(Li)$  vs.  $T_{\text{eff}}$  and  $[\text{Fe}/\text{H}]$  for the 12 “Literature” data samples. The black horizontal lines represent Primordial Lithium ( $A(Li)_P = 2.72$ ). The legends within each panel identify the sample and (at bottom-right) the number of points in the panel. In panels with  $[\text{Fe}/\text{H}]$  abscissae, the sloping line of best fit is shown (where appropriate) for stars in the range  $-3.5 \lesssim [\text{Fe}/\text{H}] \lesssim -1.5$ , for which the slope and RMS scatter are also presented; the adopted  $T_{\text{eff}}$  lower limit is included. The co-joined points represent the EMP double-lined spectroscopic binary CS 22876-032. The dotted blue lines are the same in all panels and included to facilitate comparison between the data sets. See text for discussion.

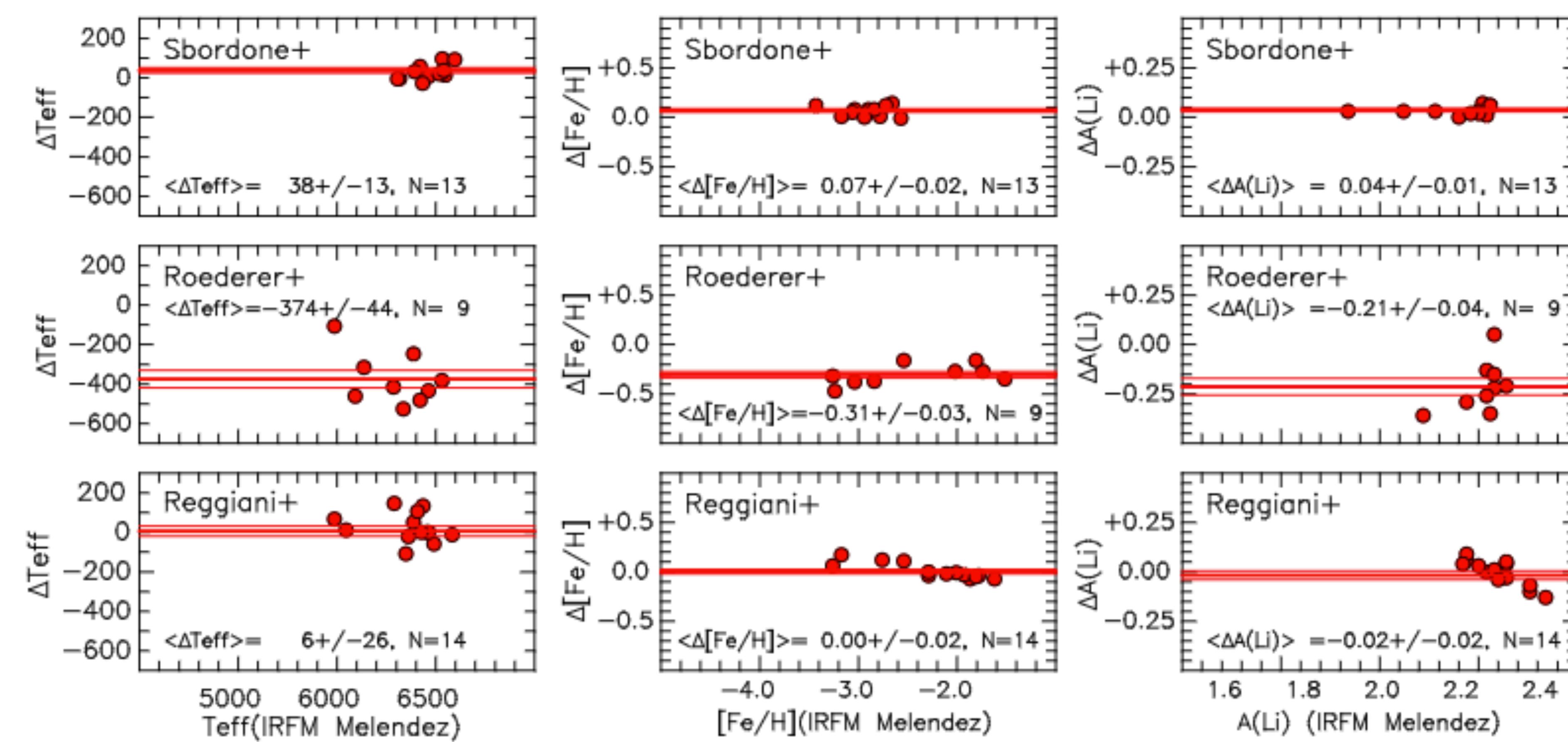


**Figure 3.**  $\Delta T_{\text{eff}}$  vs.  $T_{\text{eff}}(\text{IRFM Melendez})$ ,  $\Delta[\text{Fe}/\text{H}]$  vs.  $[\text{Fe}/\text{H}](\text{IRFM Melendez})$  and  $\Delta A(\text{Li})$  vs.  $A(\text{Li})(\text{IRFM Melendez})$  for nine data subsets. The authors, mean differences with errors, and number of data points appear within each panel.

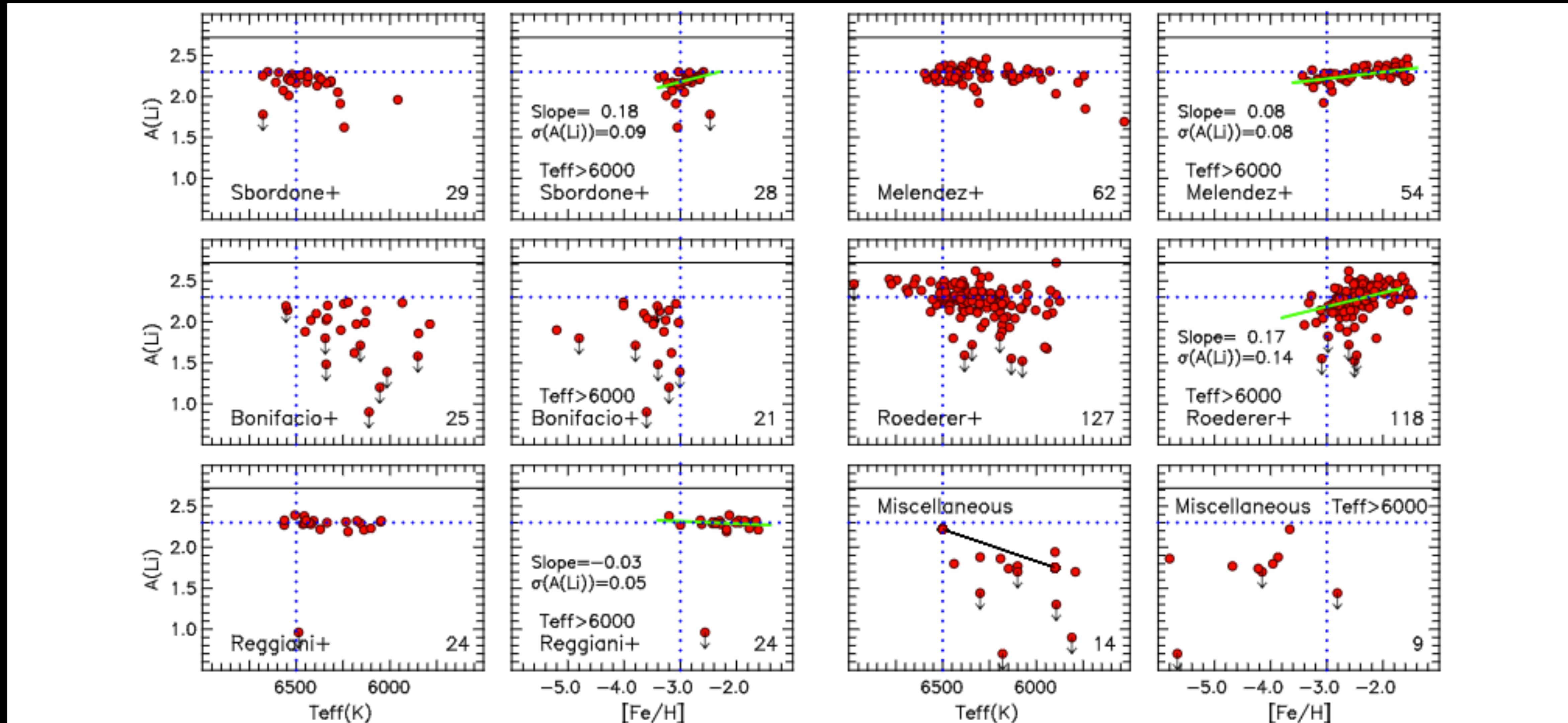


**Figure 4.**  $A(Li)$  vs.  $T_{\text{eff}}$  and  $[\text{Fe}/\text{H}]$  for the 12 data samples, when the “Literature” values have been “Corrected” to the IRFM temperature scale of [Meléndez et al. \(2010\)](#). The format is the same as that of Figure 2. See text for discussion.

# A critique of the Spite Plateau, and the Attrition of primordial lithium

J.E. Norris (Paper 14)

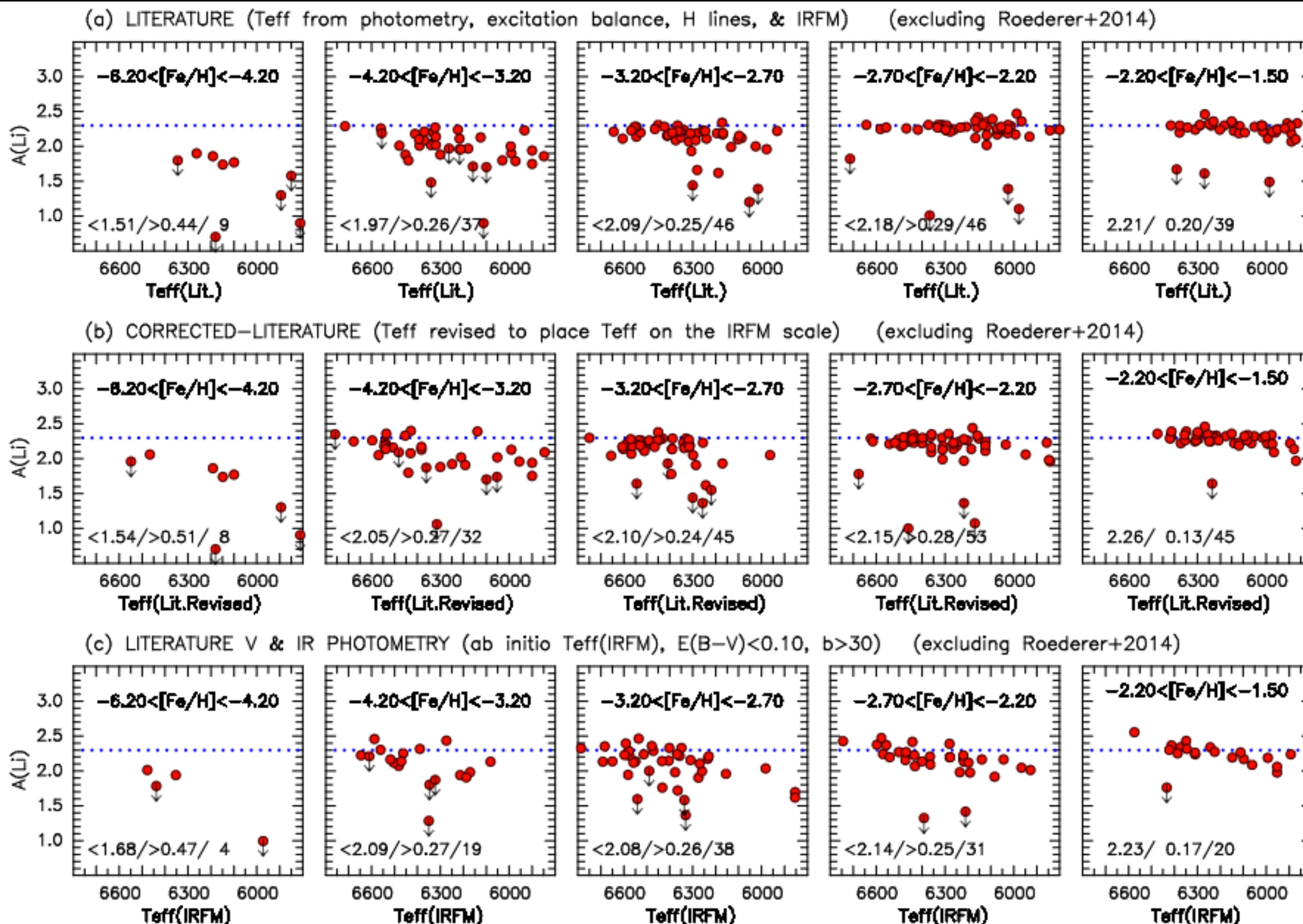


**Figure 6.**  $A(\text{Li})$  vs.  $T_{\text{eff}}$  for (a) the “Literature”, (b) “Corrected-Literature”, and (c) “*ab initio*  $T_{\text{IRFM}}$ ” datasets (excluding the [Roederer et al. 2014](#) sample). In the five panels of each row the range of  $[\text{Fe}/\text{H}]$  is presented towards the top, with  $[\text{Fe}/\text{H}]$  increasing from left to right. At the bottom left of each panel the three numbers represent the mean  $A(\text{Li})$ , its dispersion  $\sigma$ , and number of stars.

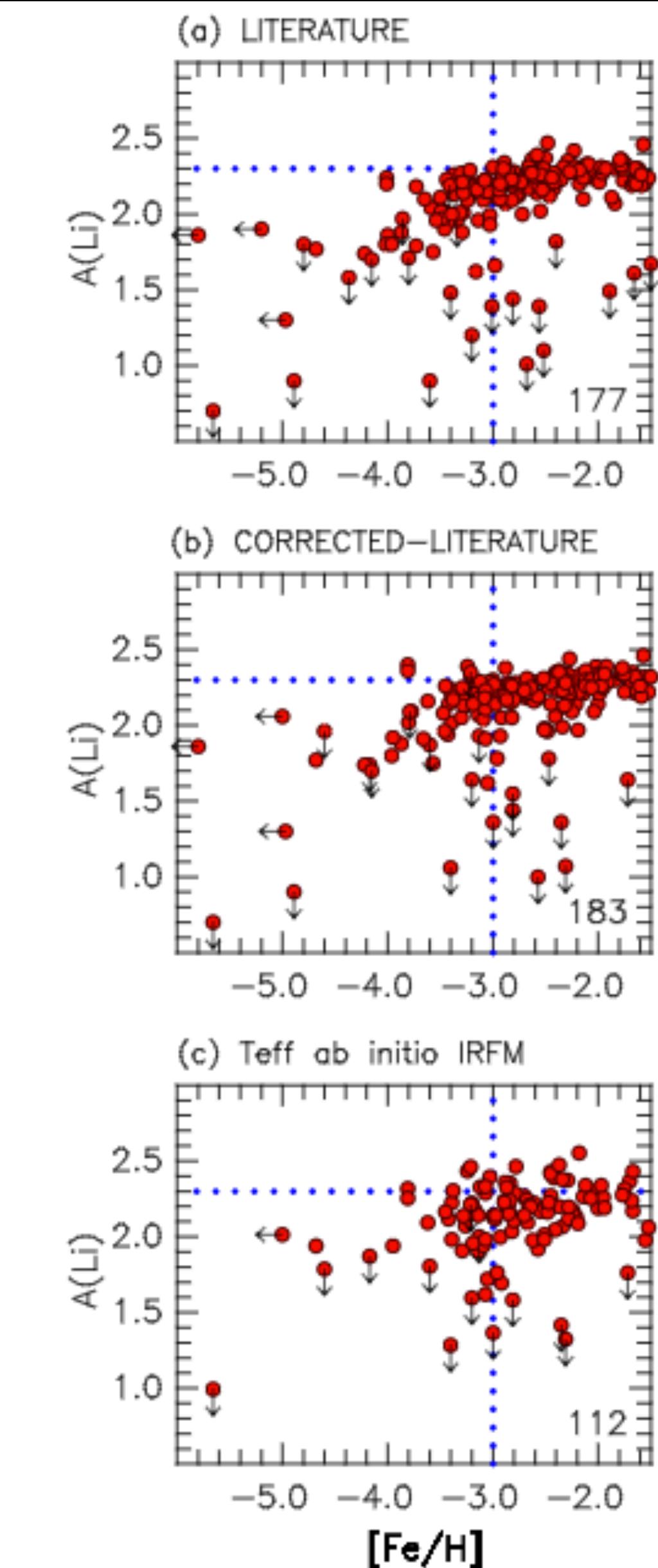


**Figure 7.**  $A(\text{Li})$  vs.  $[\text{Fe}/\text{H}]$  for the (a) “Literature”, (b) “Corrected-Literature”, and (c) “*ab initio*  $T_{\text{IRFM}}$ ” datasets (excluding the Roederer et al. 2014 sample). The number of stars is given at the bottom-right of each panel.

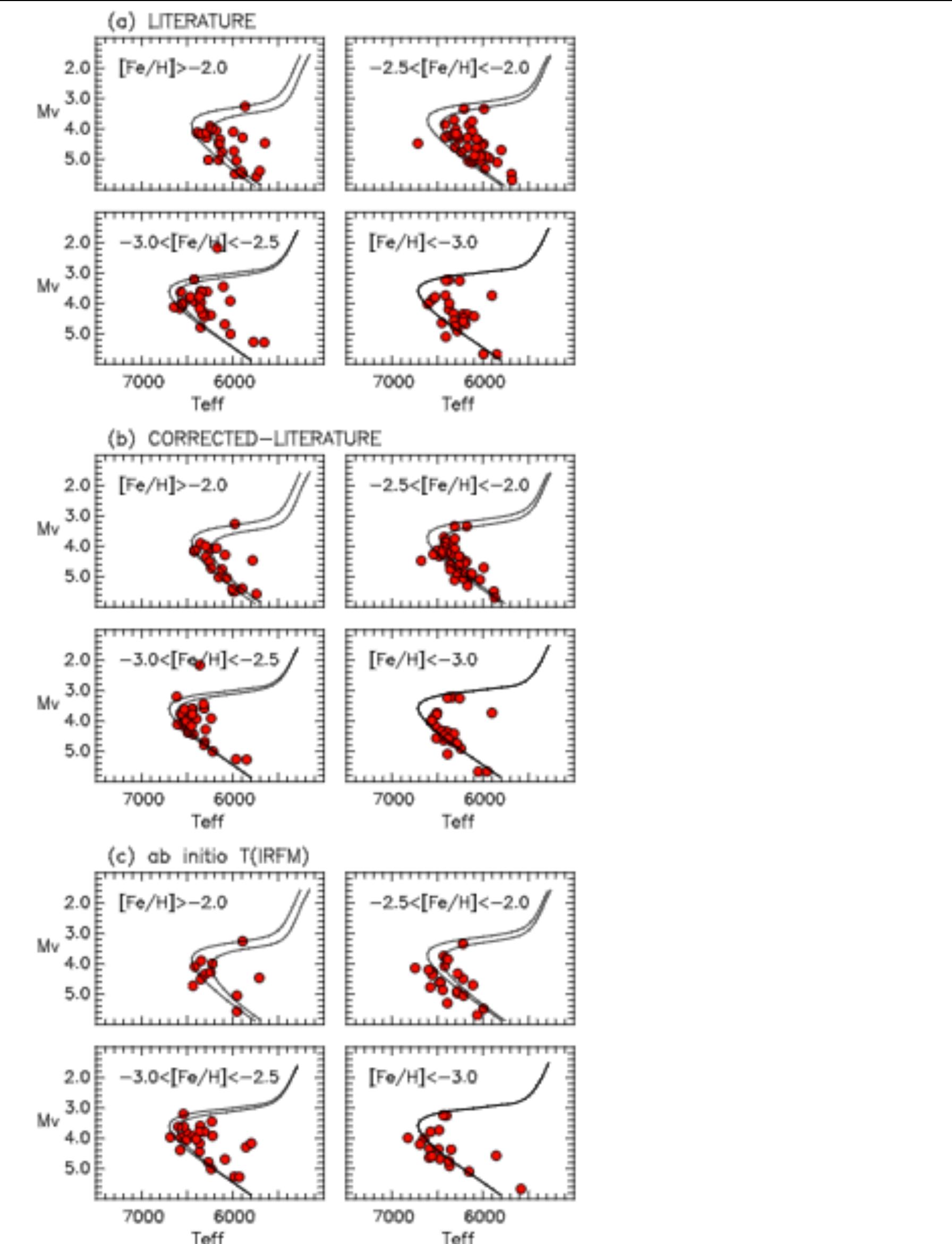


**Figure 9.**  $(M_v, T_{\text{eff}})$  – Colour-Magnitude Diagrams for (a) the “Literature”, (b) “Corrected-Literature”, and (c) “*ab initio*  $T_{\text{IRFM}}$ ” data sets. In each set the four sub-panels pertain to stars within the indicated  $[\text{Fe}/\text{H}]$  limits. Also presented are Yale-Yonsei Isochrones for these  $[\text{Fe}/\text{H}]$  values, helium abundance  $Y = 0.23$ ,  $[\alpha/\text{Fe}] = 0.3$ , and Age = 12 Gyr.

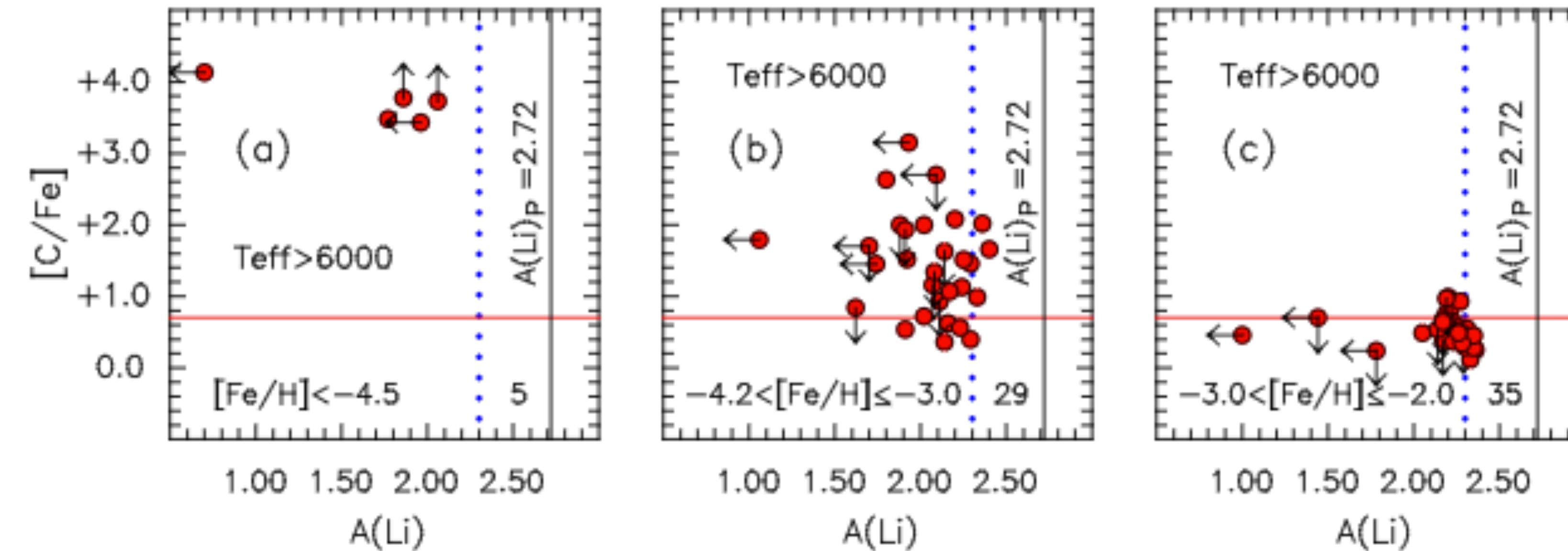


**Figure 10.**  $[\text{C}/\text{Fe}]$  vs.  $A(\text{Li})$  for stars with (a)  $[\text{Fe}/\text{H}] < -4.5$ , (b)  $-4.2 < [\text{Fe}/\text{H}] \leq -3.0$ , and (c)  $-3.0 < [\text{Fe}/\text{H}] \leq -2.0$ , for stars with  $T_{\text{eff}} > 6000$  K. The number of stars is presented at the bottom right. Black vertical lines represent Primordial Lithium ( $A(\text{Li})_P = 2.72$ ), the red line at  $A(\text{Li}) = 0.7$  separates C-weak and C-strong stars, and the blue dotted lines are for reference purposes.

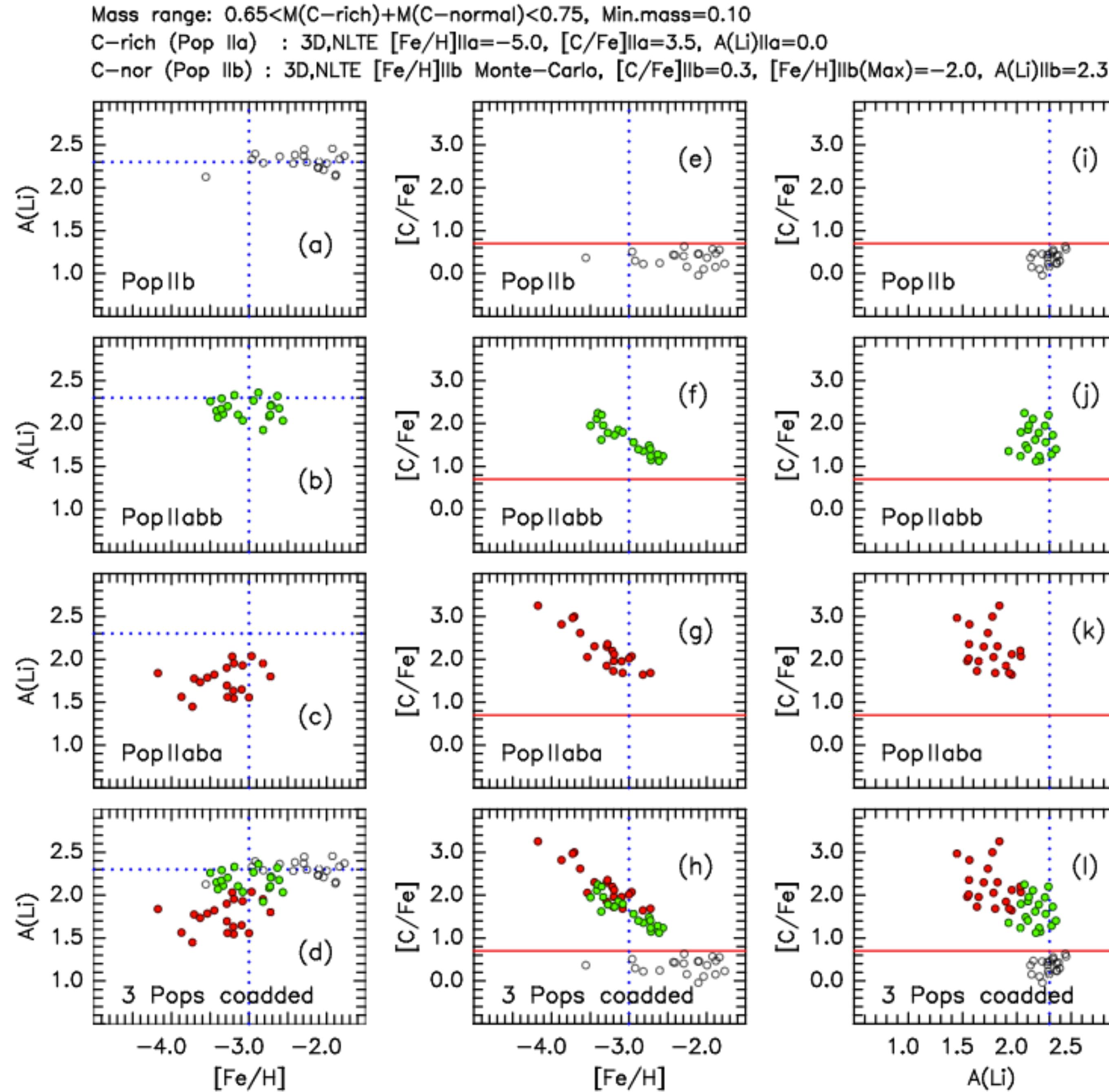


**Figure 11.** (Left)  $A(\text{Li})_{\text{1D,LTE}}$  vs.  $[\text{Fe}/\text{H}]_{\text{1D,LTE}}$ , (Middle)  $[\text{C}/\text{Fe}]_{\text{1D,LTE}}$  vs.  $[\text{Fe}/\text{H}]_{\text{1D,LTE}}$ , and (Right)  $[\text{C}/\text{Fe}]_{\text{1D,LTE}}$  vs.  $A(\text{Li})_{\text{1D,LTE}}$  for the toy-model three Population II subpopulations. From top to bottom the panels present Pop IIb = C-normal halo, Pop IIabb = C-normal dominated component, Pop IIaba = C-rich dominated component, and the co-addition of Pop IIb, Pop IIabb, and Pop IIaba. See text for discussion.

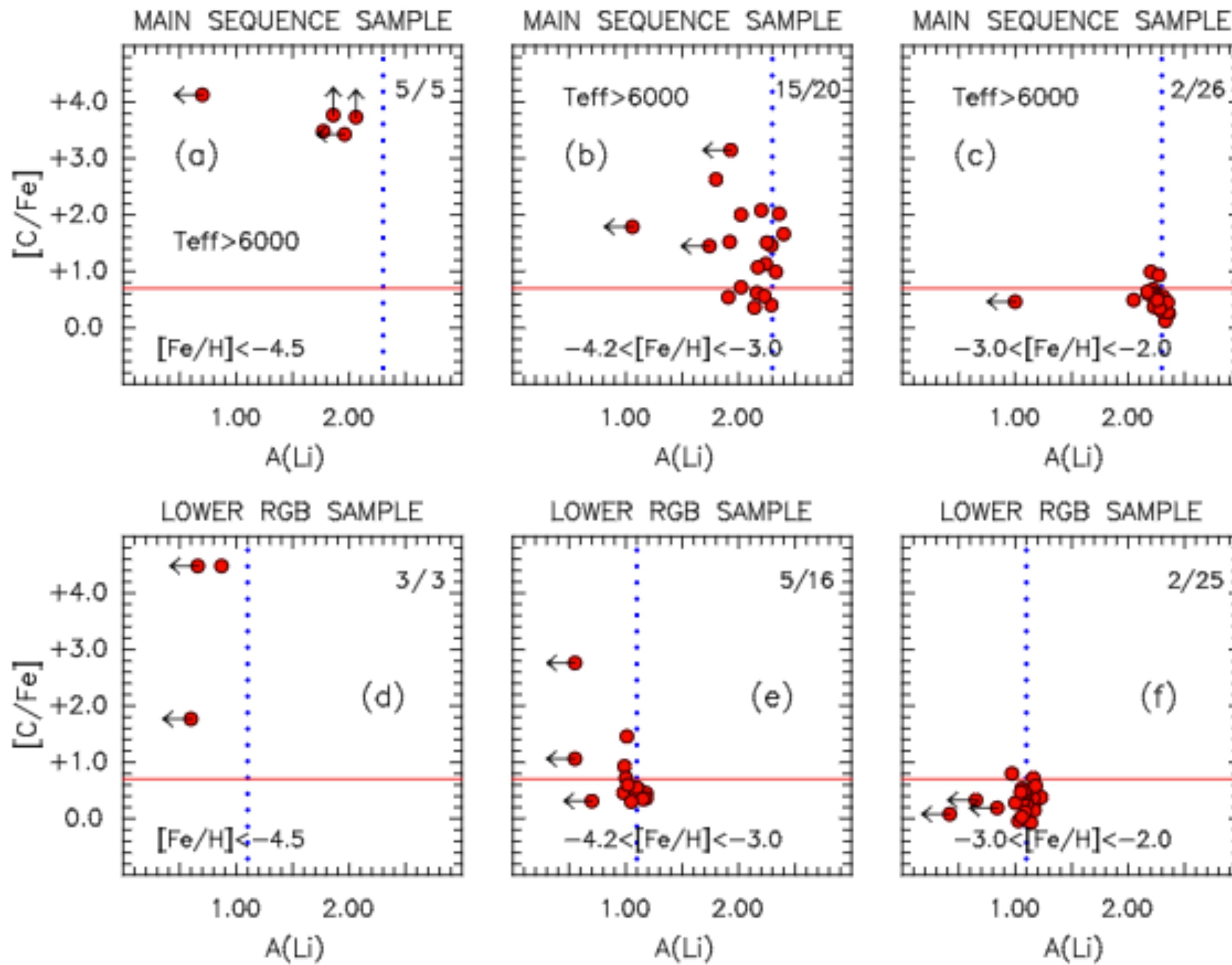


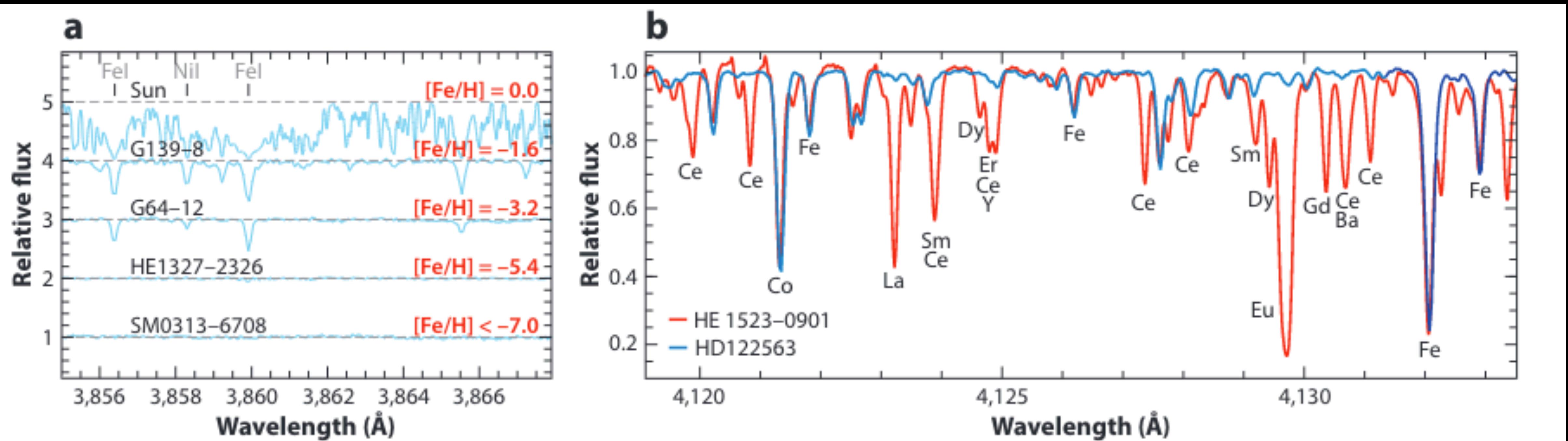
**Figure 12.**  $[C/\text{Fe}]$  vs.  $A(\text{Li})$  for stars with (left)  $[Fe/\text{H}] < -4.5$ , (middle)  $-4.2 < [Fe/\text{H}] \leq -3.0$ , and (right)  $-3.0 < [Fe/\text{H}] \leq -2.0$ . The upper and lower panels present data for main sequence ( $T_{\text{eff}} > 6000$  K) and LRGB stars, respectively. At top right of each panel the two numbers form the ratio of the number of C-rich stars to the total number of stars (excluding the stars with upper limits). The black vertical lines represent Primordial Lithium ( $A(\text{Li})_P = 2.72$ ), the red line at  $A(\text{Li}) = 0.7$  separates C-weak and C-strong stars, and the blue dotted lines are for reference purposes. See text for details.

# **From Nuclei to the Cosmos: Tracing Heavy-Element Production with the oldest stars**

**(Paper 15)**

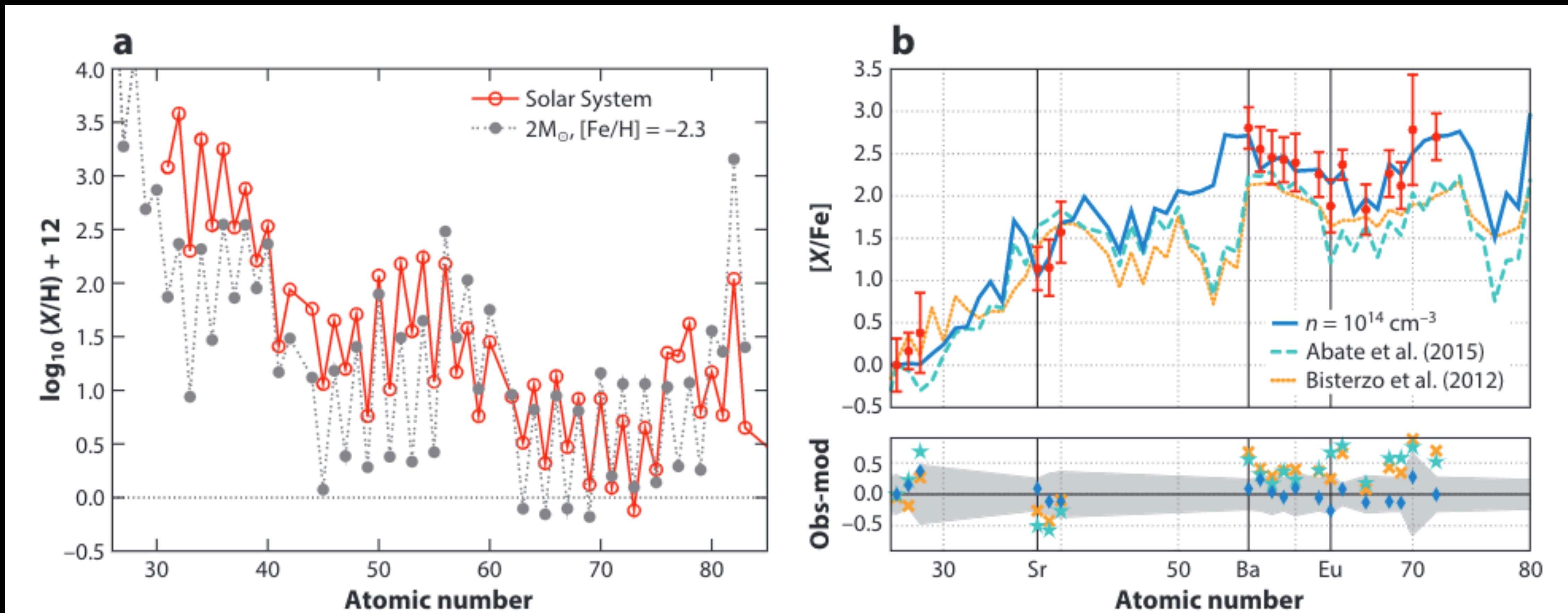
# Tracing Heavy-Element Production with the oldest stars

Anna Frebel (Paper 15)

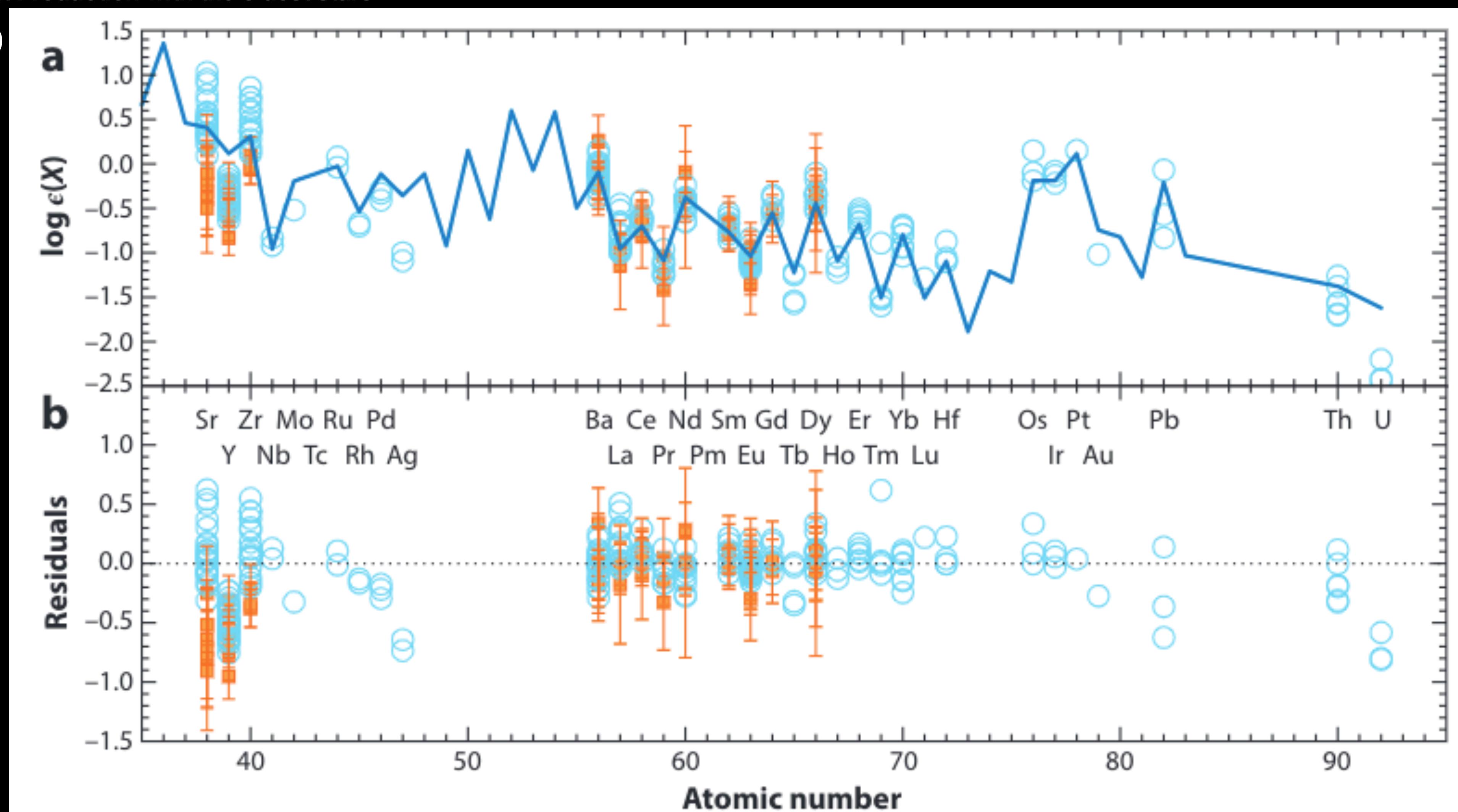


**Figure 2**

(a) Spectral comparison of stars with different metallicities, as shown by decreasing line strengths. In the bottom star, no iron lines are detected (14). Several absorption lines are marked. (b) Spectral comparison around the Eu II line at 412.9 nm of the *r*-process-deficient star HD122563 and the *r*-process-enhanced star HE 1523–0901. Both stars have similar temperatures and metallicities. Panel *b* adapted from Reference 15.

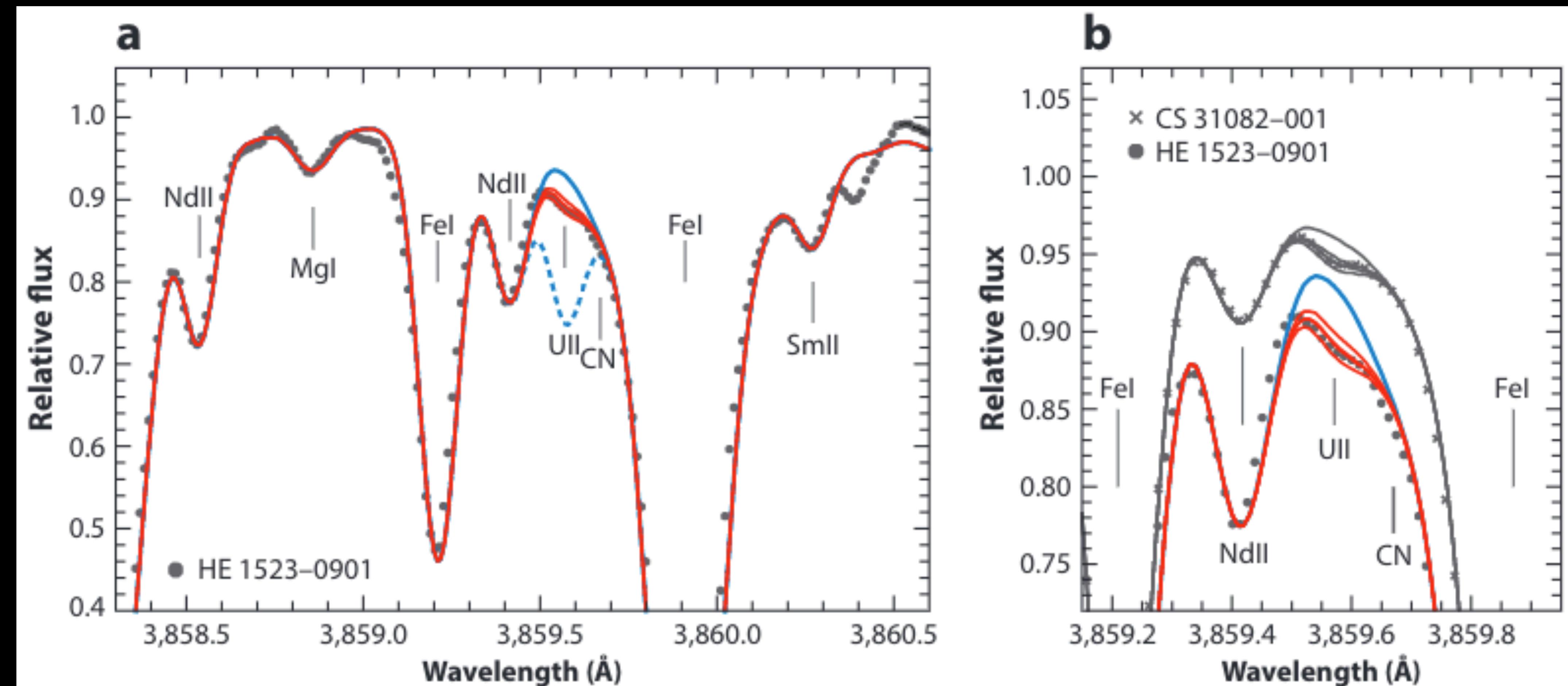
**Figure 3**

(a) The  $s$ -process (absolute) abundance pattern inferred for the Sun compared with that calculated to be produced by a  $2 M_\odot$  evolved star with  $[Fe/H] = -2.3$  (45). At low metallicity, the  $s$ -process operates efficiently enough to produce  $s$ -process abundances equal to or greater than the Solar System values, including large amounts of lead ( $Z = 82$ ). (b) Abundances (red circles) of the star LP 625–44, overlaid with nucleosynthesis models of the  $s$ -process (cyan) (53),  $s$ -process plus an initial  $r$ -process enhancement (orange) (54), and the  $i$ -process (blue) (55). Residuals of models and data are shown at the bottom. The gray area reflects observational uncertainties from the top panel. Panel *a* adapted from image by A. Karakas. Panel *b* adapted from image by M. Hampel.

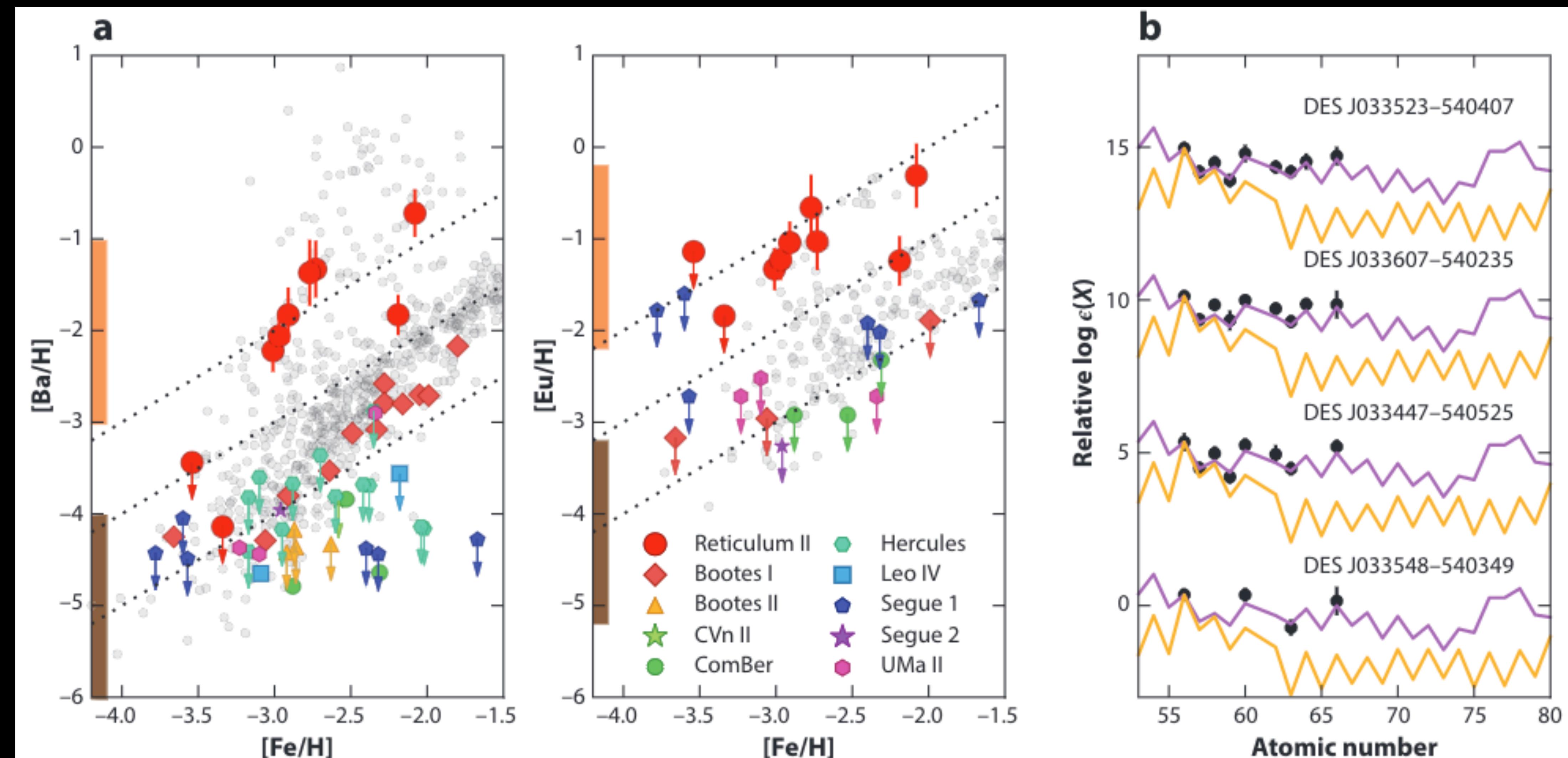


**Figure 5**

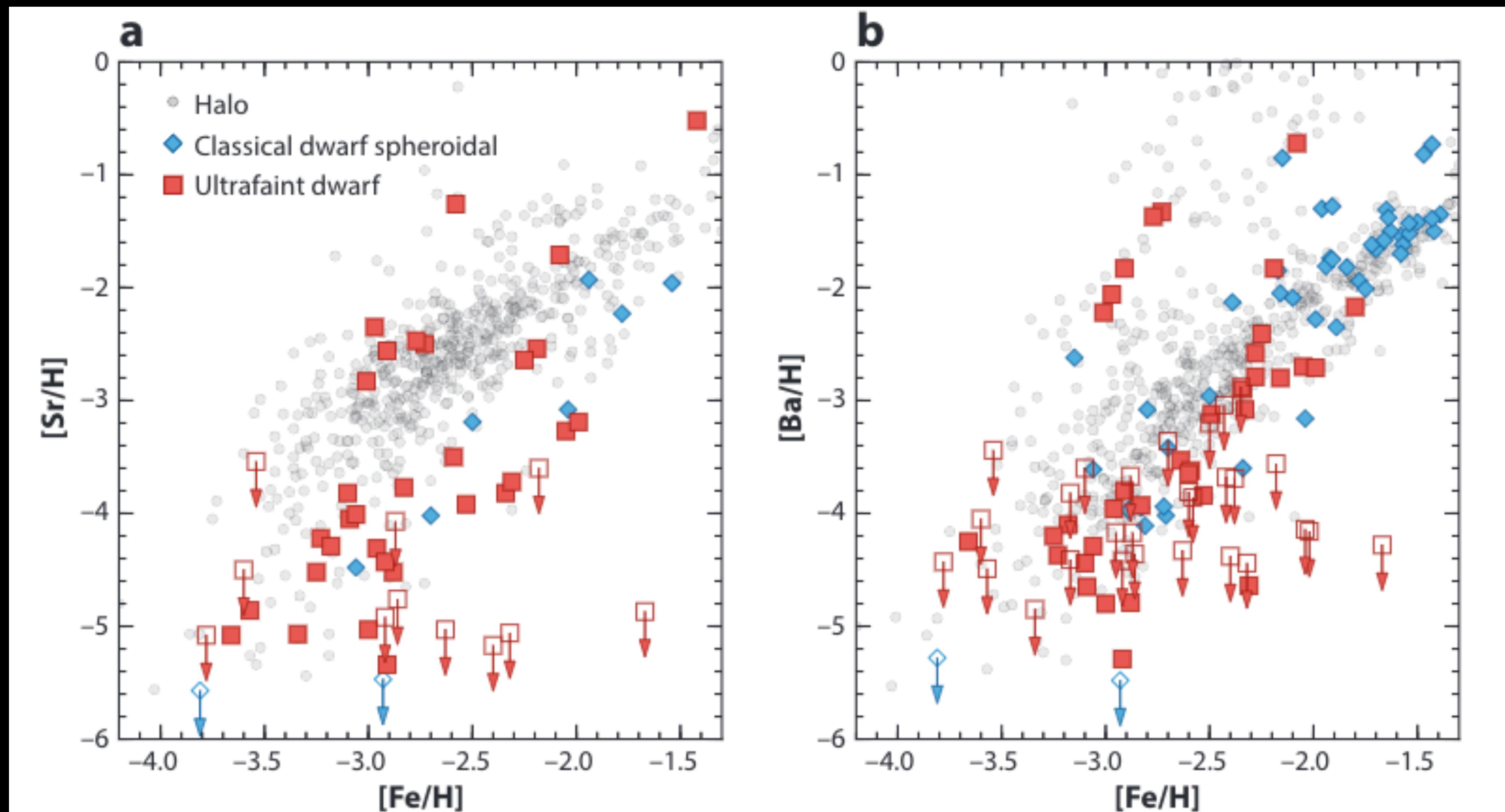
(a) Normalized *r*-process-element abundances of metal-poor halo (open circles) and Reticulum II stars (orange squares), overlaid with the scaled solar *r*-process pattern (line) (61). (b) Differences between the stellar abundances and the solar pattern. Adapted from Reference 142.

**Figure 6**

Spectral region around the U II line at 385.9 nm in (a,b) HE 1523-0901 (*black dots*) and (b) CS 31082-001 (*crosses*). Overplotted are synthetic spectra with different uranium abundances (*red*). The thin blue dotted line in panel *a* represents the line strength if uranium had not decayed, whereas the blue line indicates its absence. Adapted from Reference 129.

**Figure 7**

(a) Barium and europium abundances of stars in Reticulum II (*red points*), in the halo (*gray*), and in ultrafaint dwarf galaxies (*colored points*) as a function of iron abundance. Orange and brown vertical bars indicate yield ranges predicted by a neutron star merger and a core-collapse supernova, respectively. Arrows denote upper limits. (b) Observed abundances overlaid with the scaled solar *r*- and *s*-process patterns, shown in purple and gold, respectively. Adapted from Reference 87.

**Figure 8**

Evolution of the abundances ( $[X/H]$ ) of neutron-capture elements (a) strontium and (b) barium as a function of the iron abundance. Halo stars and stars from classical dwarf spheroidal and ultrafaint dwarf galaxies are shown. Upper limits are indicated with arrows. Figure adapted from image by A. Ji.

**The Comet-Like composition of a protoplanetary  
disk as revealed by complex cyanides**

**(Paper 16)**

# The Comet-Like composition of a protoplanetary disk as revealed by complex cyanides

Karin Oberg (Paper 16)

- Cyanides: complex molecules as HCN, CH<sub>3</sub>, HC<sub>3</sub>N, etc.
- 

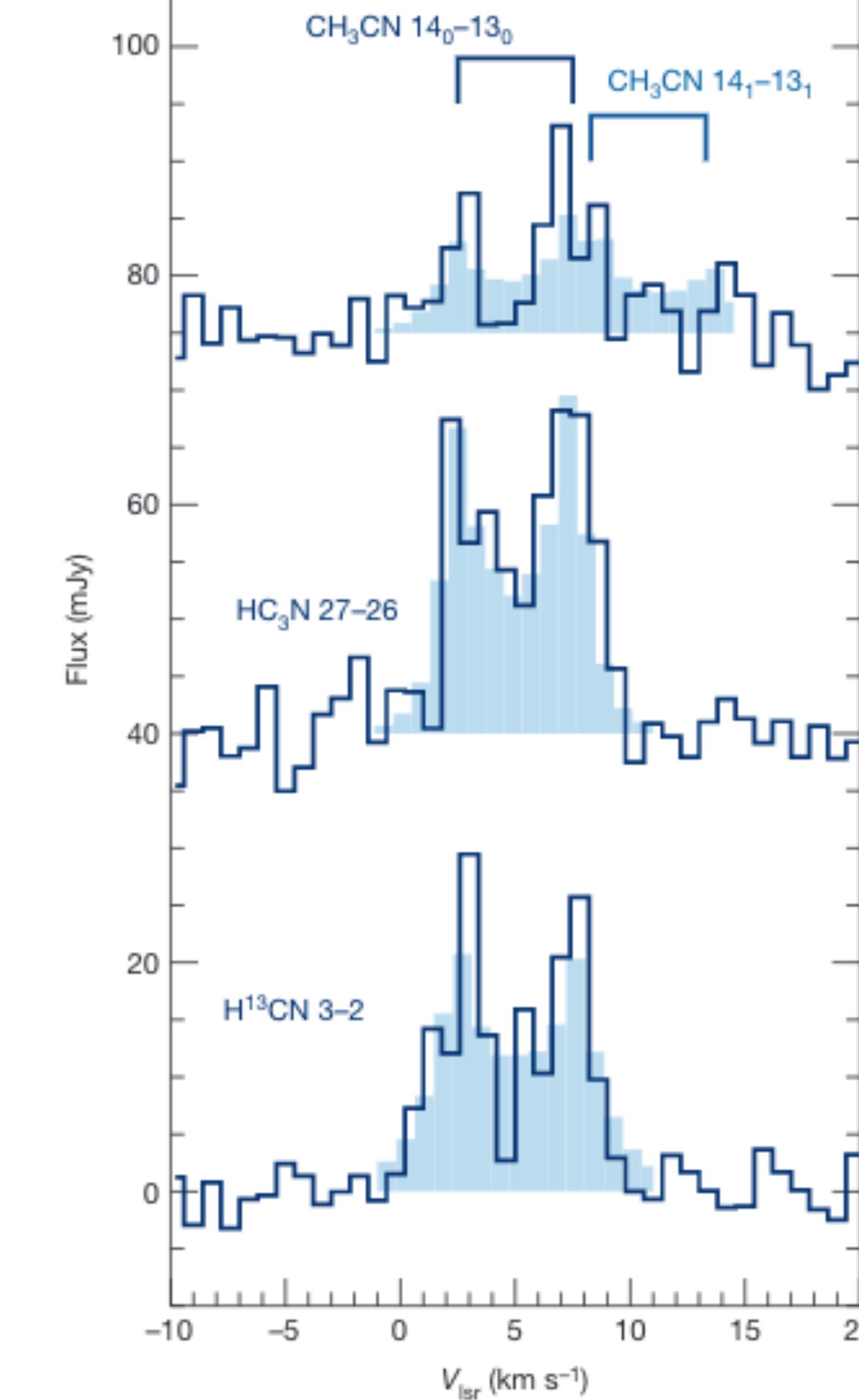


**Figure 2 | Spectra of detected cyanides in the MWC 480 protoplanetary disk.** The observed spectra (contours) of  $\text{H}^{13}\text{CN}$ ,  $\text{HC}_3\text{N}$  and  $\text{CH}_3\text{CN}$  are extracted from ALMA spectral-image data cubes and are shown as functions of the local standard of rest velocity,  $V_{\text{lsr}}$ . The synthetic spectra (light blue shaded histograms) are based on the best-fit disk abundance models in Fig. 3. The  $\text{CH}_3\text{CN}$  spectrum contains two partially overlapping lines identified with the  $14_0-13_0$  and  $14_1-13_1$  transitions. The spectra were extracted from the spectral image cubes using a Keplerian mask to maximize the signal-to-noise ratio.

# The Comet-Like composition of a protoplanetary disk as revealed by complex cyanides

Karin Oberg (Paper 16)

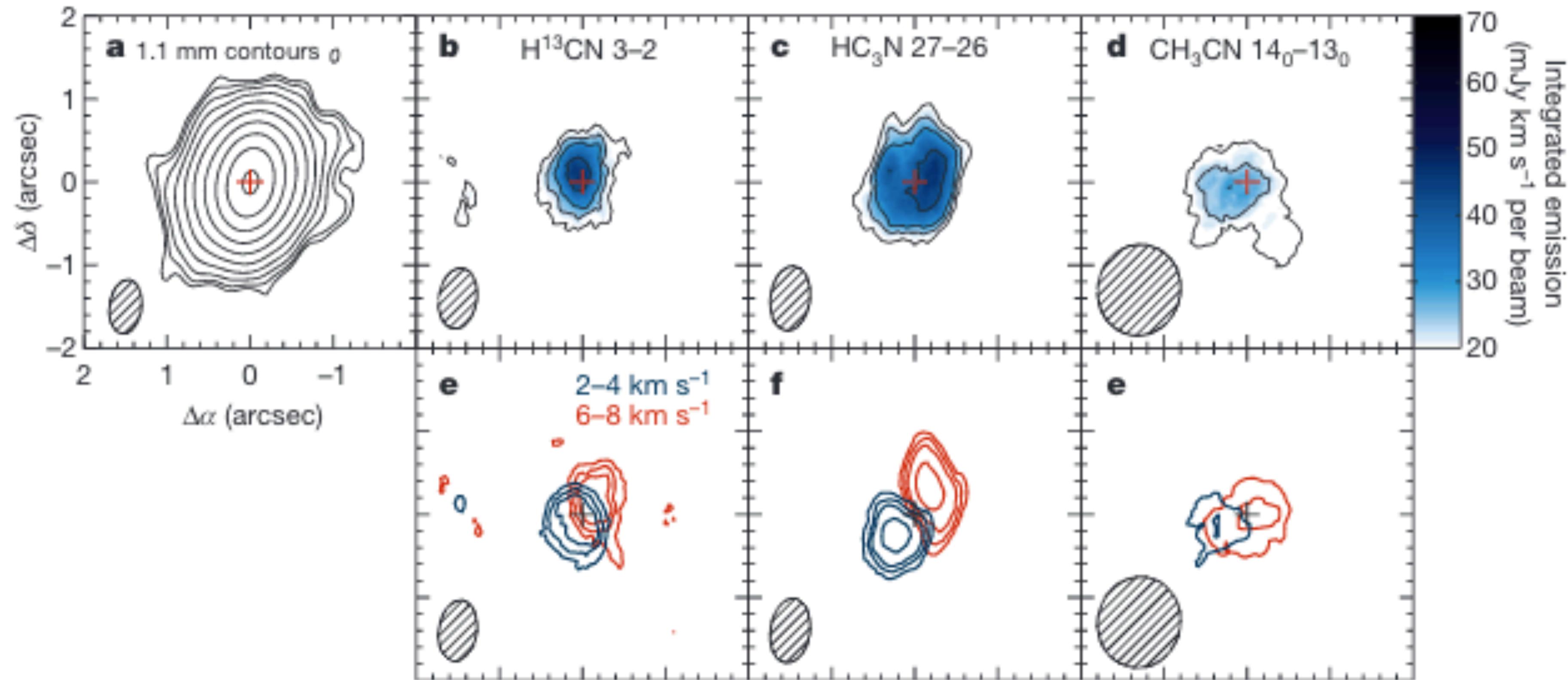


**Figure 1 | ALMA detections of simple and complex cyanides in the MWC 480 protoplanetary disk.** **a**, 1.1 mm emission (black contours are  $3\sigma + \sigma \times 2^{[1,2,\dots]}$ ). **b-d**, Integrated emission of  $\text{H}^{13}\text{CN}$  (**b**),  $\text{HC}_3\text{N}$  (**c**) and  $\text{CH}_3\text{CN}$  (**d**) lines (colour: see colour scale on the right). Black contours are  $[3,4,5,7,10]\sigma$ . **e-g**, As **b-d**, but for 2 km s<sup>-1</sup> velocity bins around the source

mean velocity, displaying the disk rotation. Positions are relative to the continuum phase centre (marked with a cross) at right ascension ( $\alpha$ ) 04 h 58 min 45.94 s and declination ( $\delta$ ) +29° 50' 38.4". The synthesized beam is shown in the bottom left corner of each panel.

# The Comet-Like composition of a protoplanetary disk as revealed by complex cyanides

Karin Oberg (Paper 16)

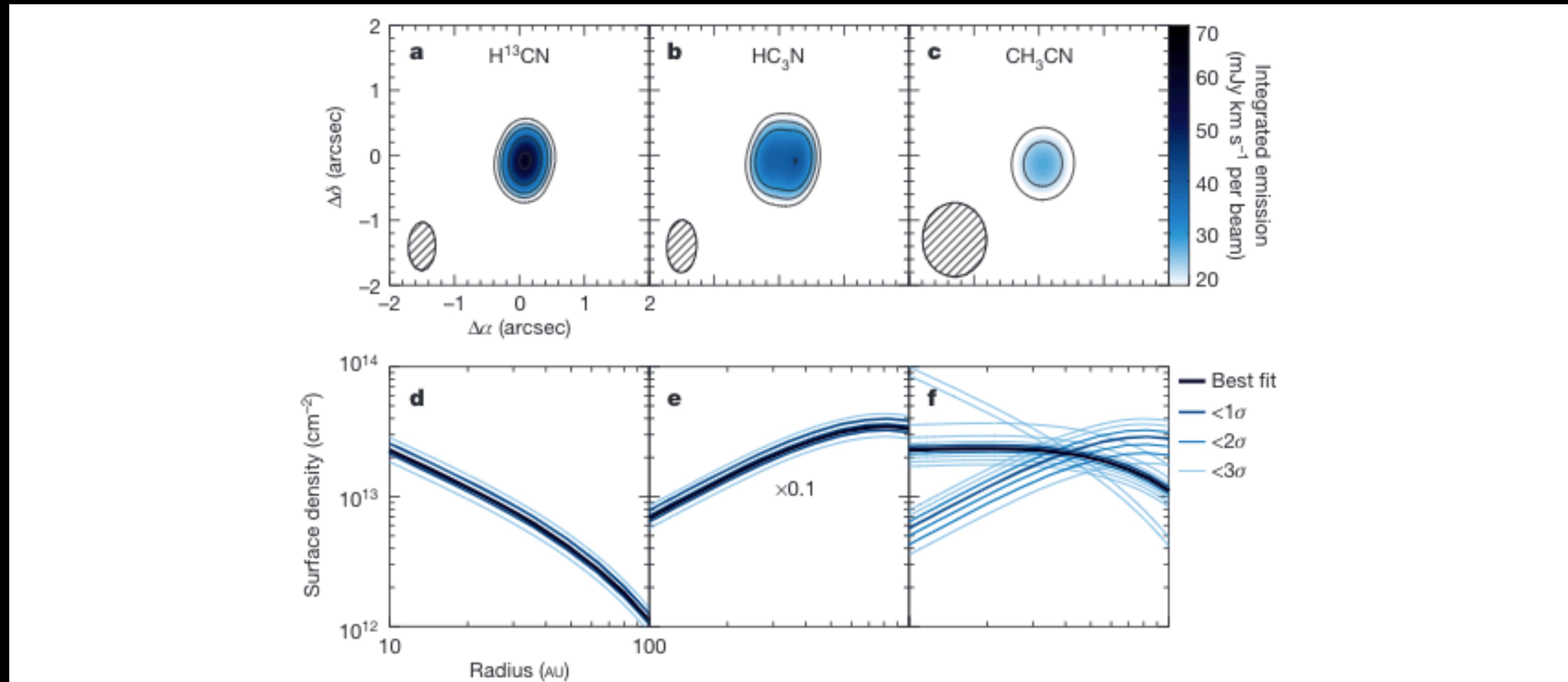
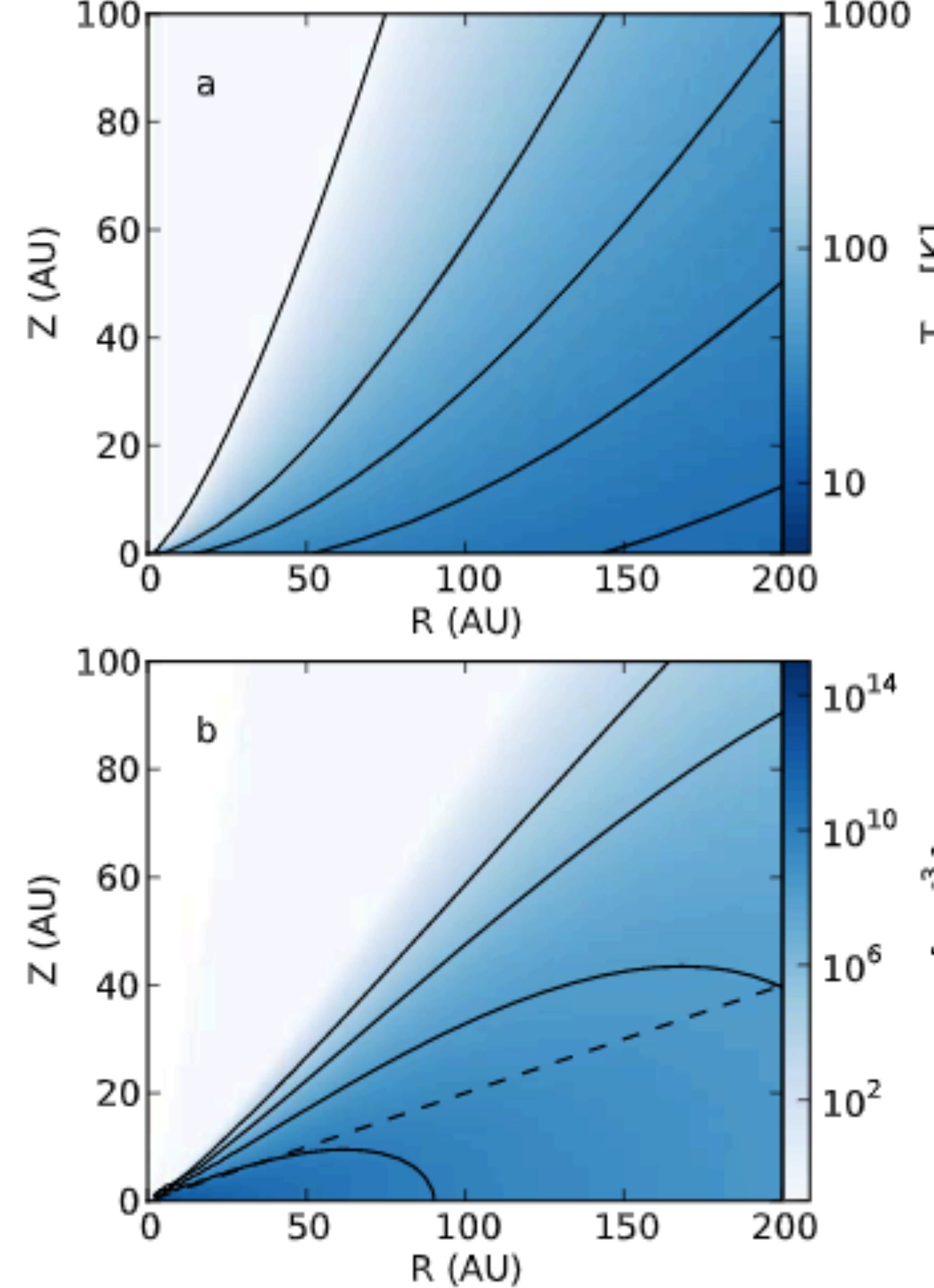
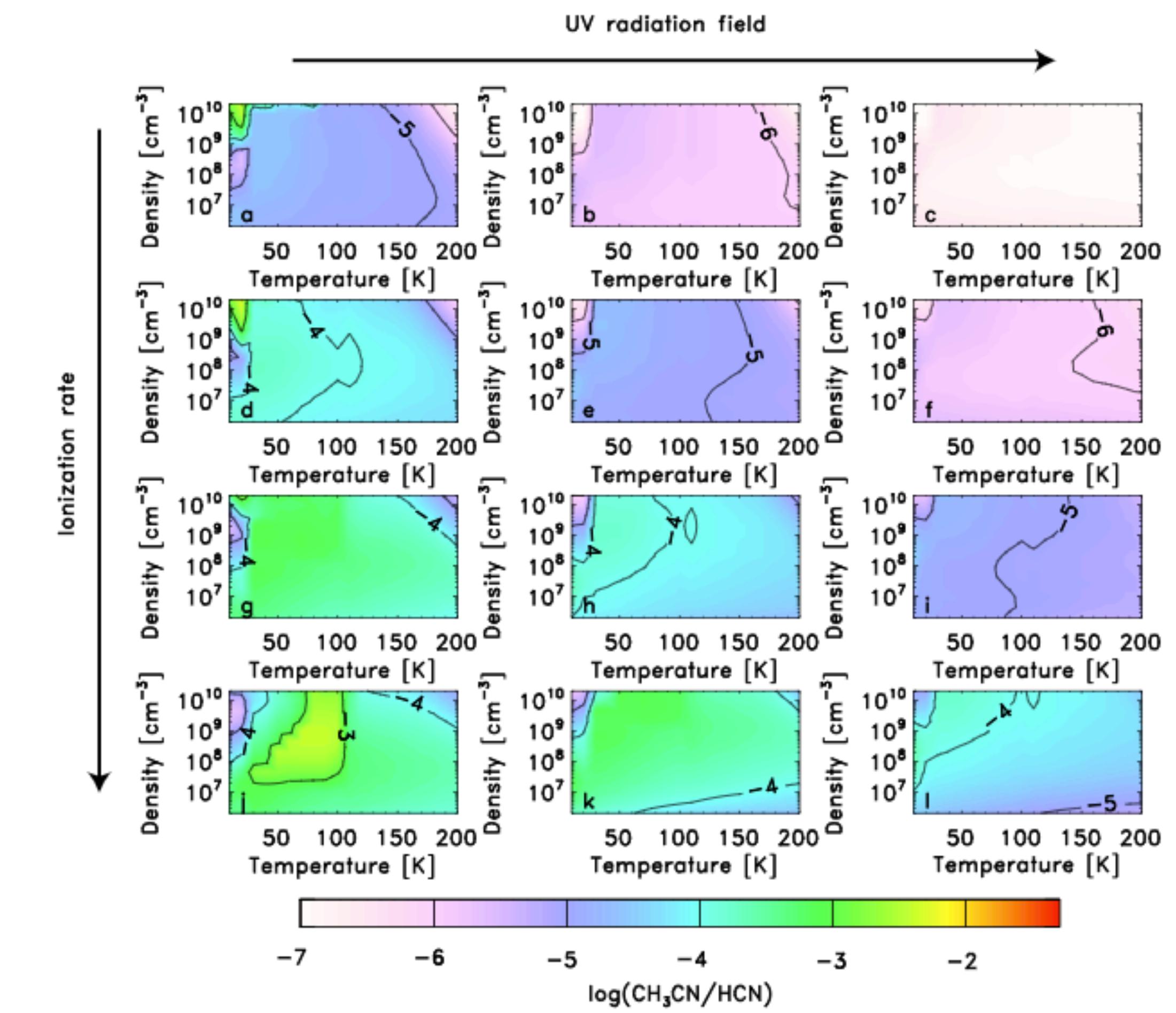


**Figure 3 | Models of cyanide emission and radial distributions in the MWC 480 disk.** **a–c**, Synthetic ALMA observations of the integrated line emission flux without added noise based on the best-fit radial column density profiles of  $\text{H}^{13}\text{CN}$ ,  $\text{HC}_3\text{N}$ , and  $\text{CH}_3\text{CN}$  (colour; see colour scale on the right). Black contours are as in Fig. 1. **d–f**, Best-fit radial column density profiles (thick

dark blue line), shown together with all column density profiles that are consistent with data within 1, 2 and  $3\sigma$  confidence intervals. Increasing deviations from the best fit are shown with successively lighter shades and thinner lines.



**Extended Data Figure 1 | Model of the physical structure of the MWC 480 protoplanetary disk.** **a**, Radial (distance  $R$ ) and vertical (distance  $Z$ ) disk temperature profile (colour: see colour scale on right, contours: the gas temperature  $T_{\text{kin}} = 20, 30, 50, 100$  and  $1,000$  K). **b**, Radial ( $R$ ) and vertical ( $Z$ ) density profile (colour: see colour scale on the right, contours: hydrogen density  $n_H 10^{10}, 10^8, 10^6$  and  $10^4 \text{ cm}^{-3}$ ).  $Z/R = 0.2$  is marked with a dashed line.

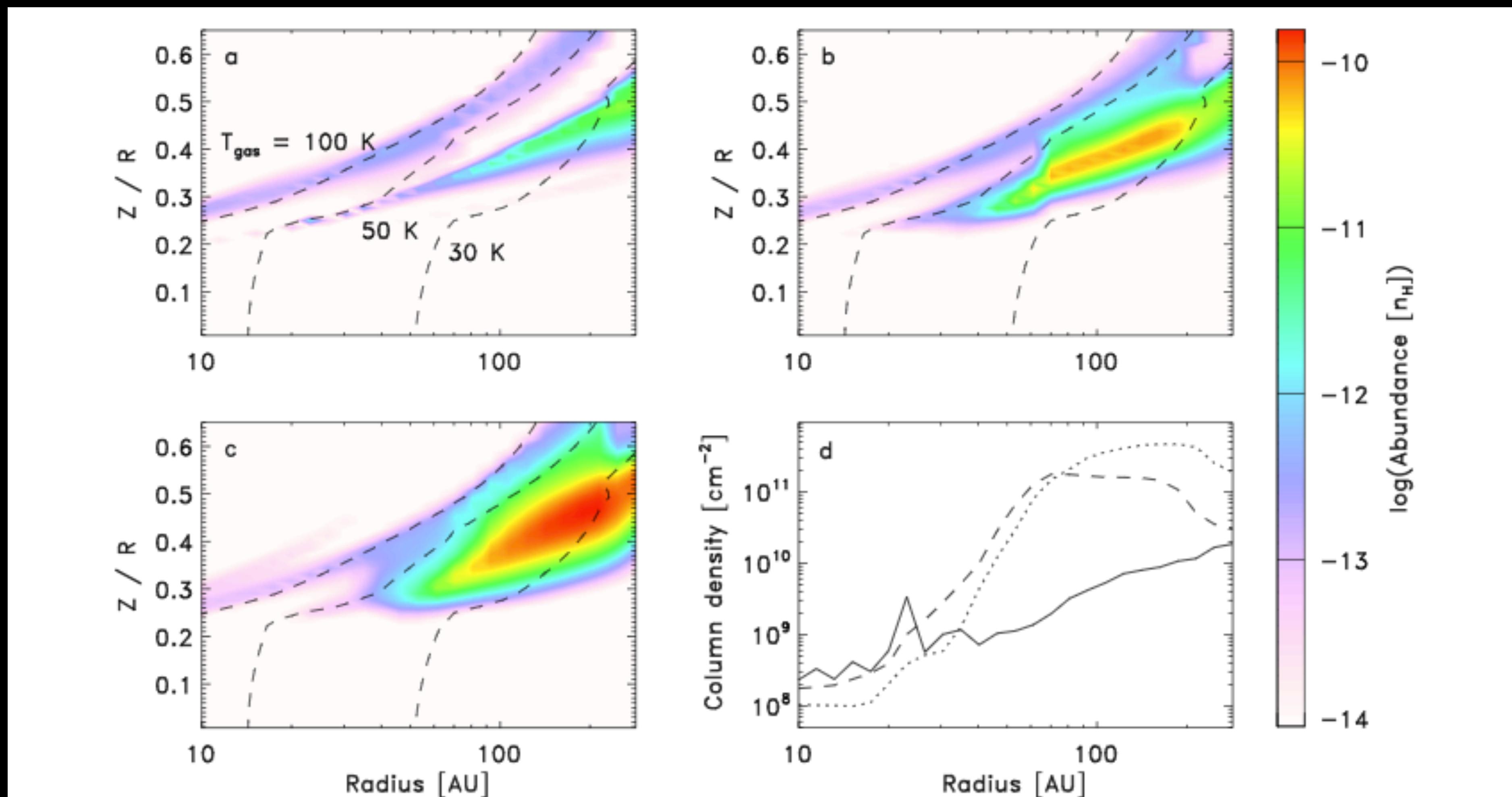


**Extended Data Figure 3 | Models of gaseous  $\text{CH}_3\text{CN}/\text{HCN}$  abundance ratios under different physical conditions.** **a-l**, The  $\text{CH}_3\text{CN}/\text{HCN}$  abundance ratio on a logarithmic scale (colour: see colour scale on the bottom and numbers on contours). The ultraviolet radiation flux increases from left to

right from  $G_0 = 1$  (**a-d, g, j**) to  $G_0 = 10$  (**e-h, k**) to  $G_0 = 100$  (**c, f, i, l**), where  $G_0$  is the scaling factor in multiples of the local interstellar radiation field. The ionization rate of  $\text{H}_2$  increases from top to bottom from  $10^{-17} \text{ s}^{-1}$  (**a-c**) to  $10^{-16} \text{ s}^{-1}$  (**d-f**) to  $10^{-15} \text{ s}^{-1}$  (**g-i**) to  $10^{-14} \text{ s}^{-1}$  (**j-l**).

# The Comet-Like composition of a protoplanetary disk as revealed by complex cyanides

Karin Oberg (Paper 16)



**Extended Data Figure 4 | Models of gaseous  $\text{CH}_3\text{CN}$  in disks with and without turbulent diffusion.** **a,** The abundance of  $\text{CH}_3\text{CN}$  with respect to the hydrogen density  $n_{\text{H}}$  (colour: see colour scale on the right) as a function of disk radius ( $R$ ) and height scaled by the radius ( $Z/R$ ) in a model without turbulence. The dashed lines indicate gas temperatures of [30, 50, 100] K.

**b, c,** As a but in disk models that include turbulence parameterized by  $\alpha_z = 10^{-3}$  (**b**) and  $\alpha_z = 10^{-2}$  (**c**). **d,** The vertically integrated column density of  $\text{CH}_3\text{CN}$  from a–c (solid line:  $\alpha_z = 0$ , dashed line:  $\alpha_z = 10^{-3}$ , dotted line:  $\alpha_z = 10^{-2}$ ).

# **Disk around T Tauri stars with SPHERE (DARTTS-S), Polarimetric Imaging of Eight Prominent T Tour Disks**

**(Paper 17)**

# Disk around T Tauri stars with SPHERE (DARTTS-S)

Henning Avenhaus (Paper 17)

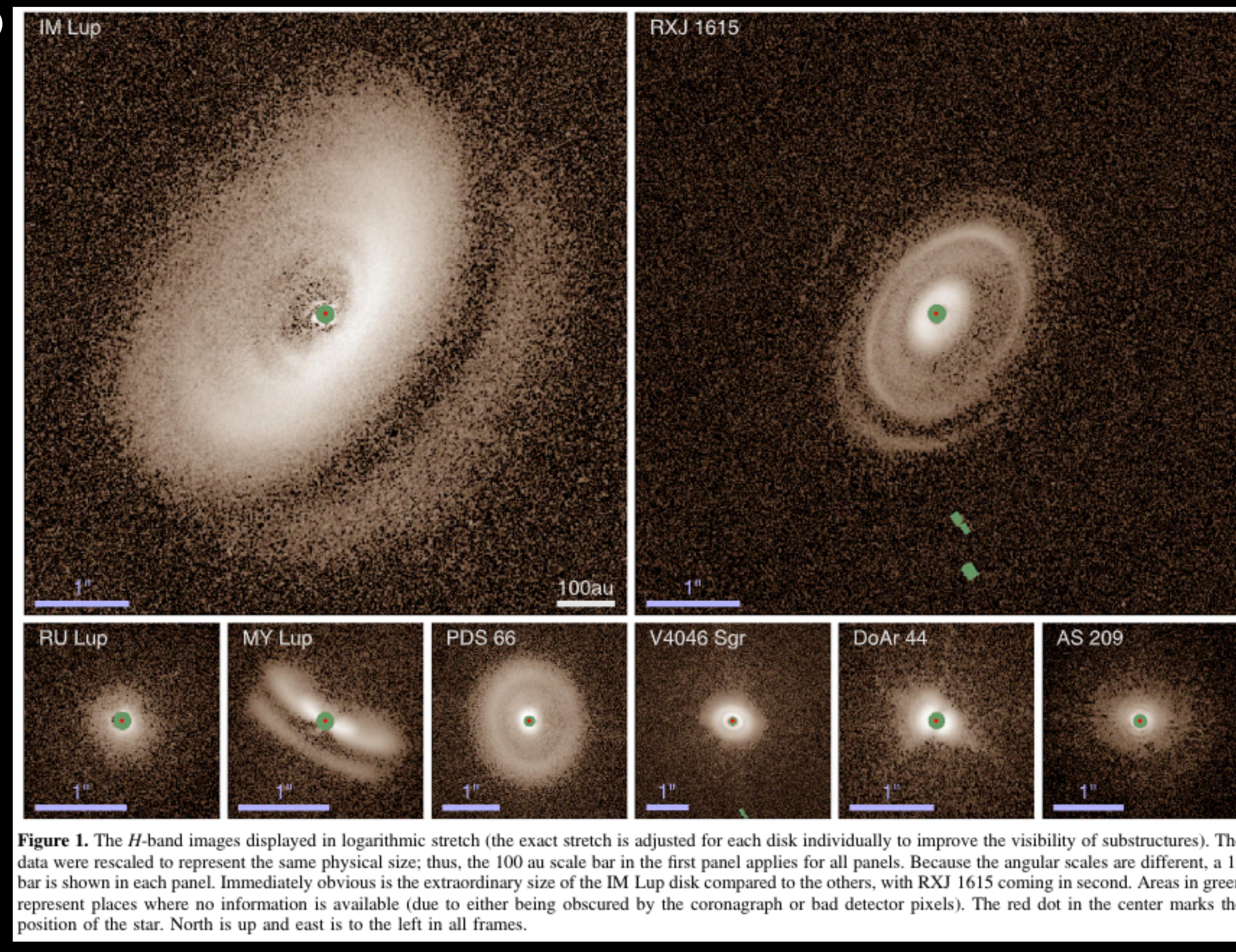
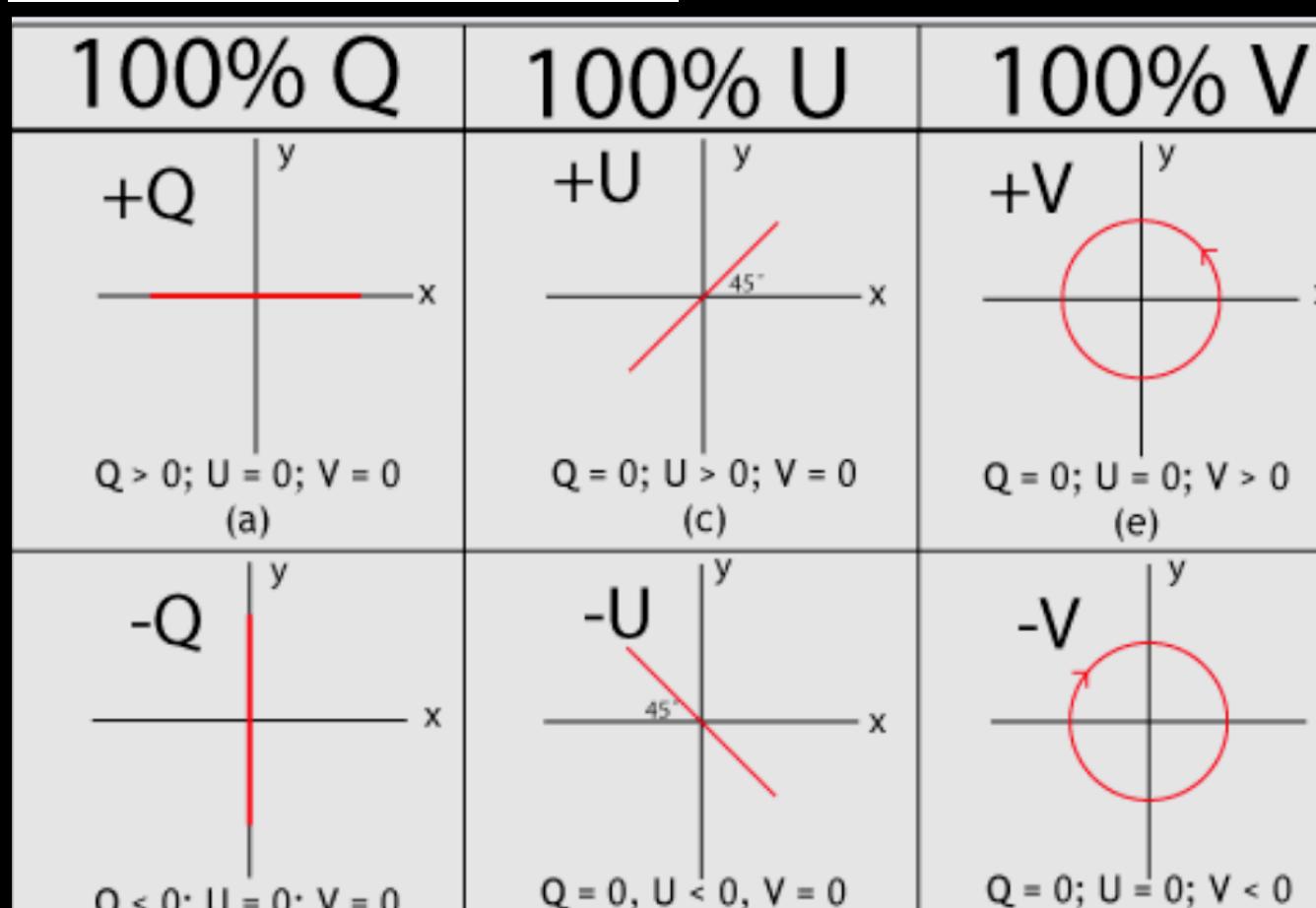
- T Tauri Stars: are a class of variable stars that are less than about ten million years old. They are pre-main-sequence stars in the process of contracting to the main sequence along the Hayashi track
- Stokes parameters: spans the space of unpolarized, partially polarized, and fully polarized light.

$$S_0 = I = E_x^2 + E_y^2$$

$$S_1 = Q = E_x^2 - E_y^2$$

$$S_2 = U = 2E_x E_y \cos \delta$$

$$S_3 = V = 2E_x E_y \sin \delta$$



Disk around T Tauri stars with SPHERE (DARTTS-S)

**Henning Avenhaus (Paper 17)**

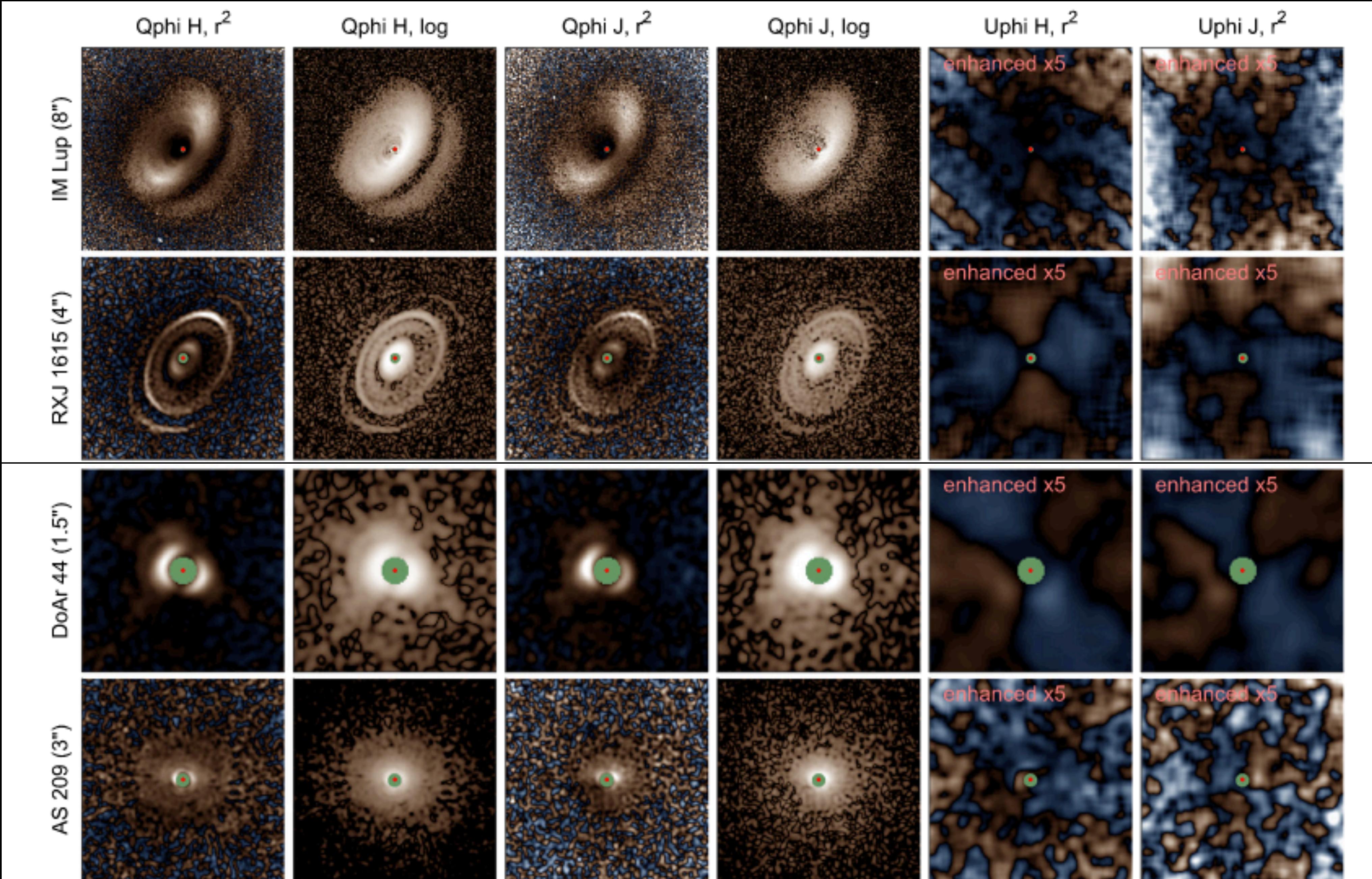


**Figure 2.** All of our observations, corrected for self-cancellation as described in the [Appendix](#) and reconvolved with a 75 mas FWHM Gaussian. The horizontal/vertical FOV is given with the name of the disk. Blue hues correspond to negative values, brown hues to positive values. North is up and east is to the left in all frames.

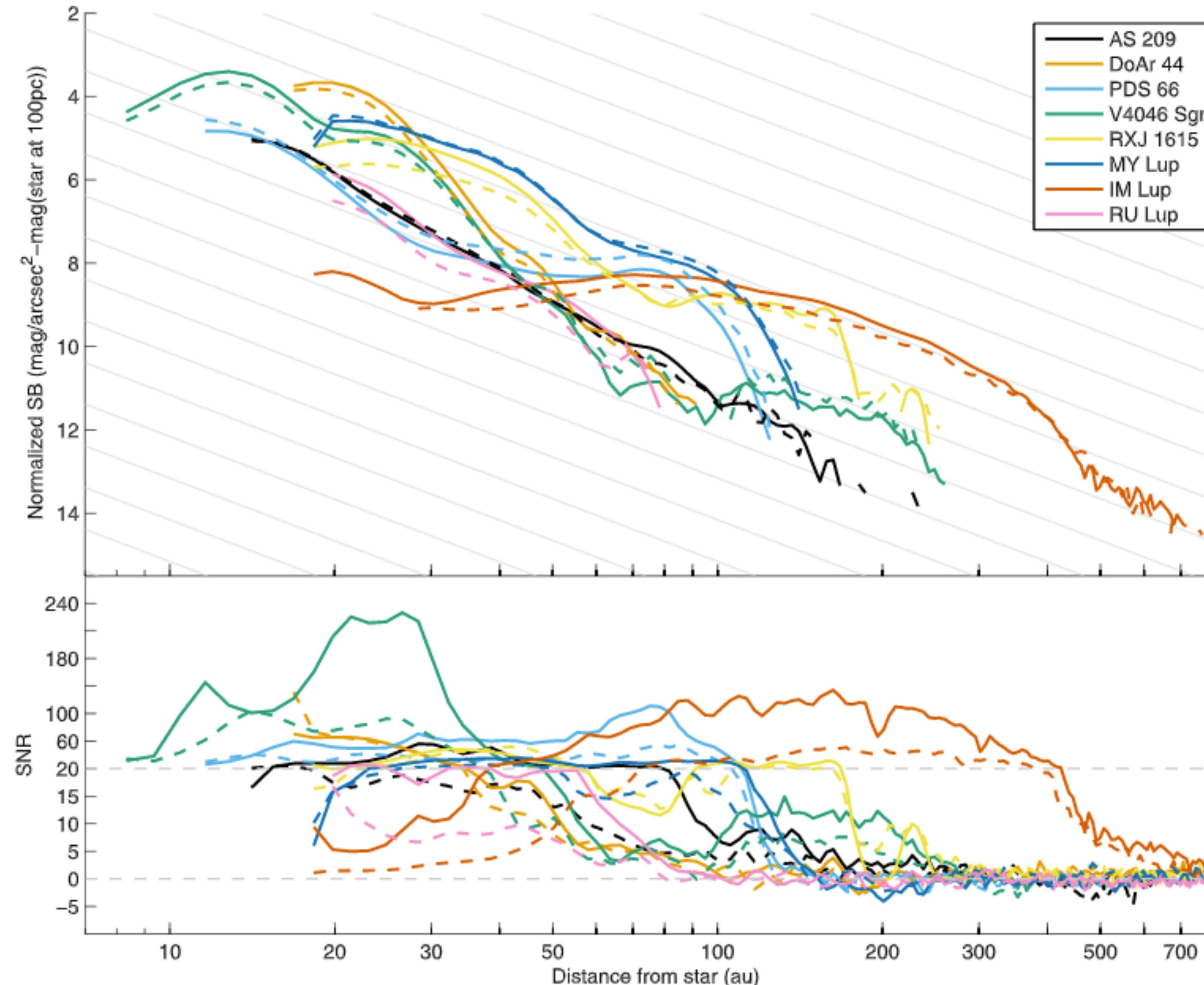


**Figure 3.** Upper panel: azimuthally averaged, normalized surface brightness vs. distance from the host star for our targets, derived from the self-cancel-corrected images reconvolved with a 75 mas Gaussian. Solid lines represent *H*-band and dashed lines *J*-band data. The width of the annuli used for averaging increases with radius proportional to  $r^{1/2}$  (at 50 au, we use a width of 2.5 au). For the sake of readability, error bars are omitted, and data are only shown where the detection is  $>3\sigma$  or the combined detection in the *J* and *H* bands is  $>3\sigma$  and the detection in the individual band is  $>2\sigma$ . The lower panel shows the S/N for all of the data, with noise estimated from the  $U_\phi$  frames. Note the change in scale at S/N = 20. Also note that even for our weakest detection, RU Lup, the S/N peaks at  $>25\sigma$ . The significant negative S/N excursion at  $\approx 500$ –600 au for AS 209 is to be discarded; it stems from time-variable striping of the IRDIS detector. The gray background lines are for guiding the eye and scale as  $r^{-2}$  (similar to the drop-off of stellar light with distance). Note that errors or changes in the distance to the star, especially for those without *Gaia* measurements, would shift the curves along these background lines. Surface brightness plots in observational units, including the surface brightnesses of the  $U_\phi$  frames, can be found in Figure 11.

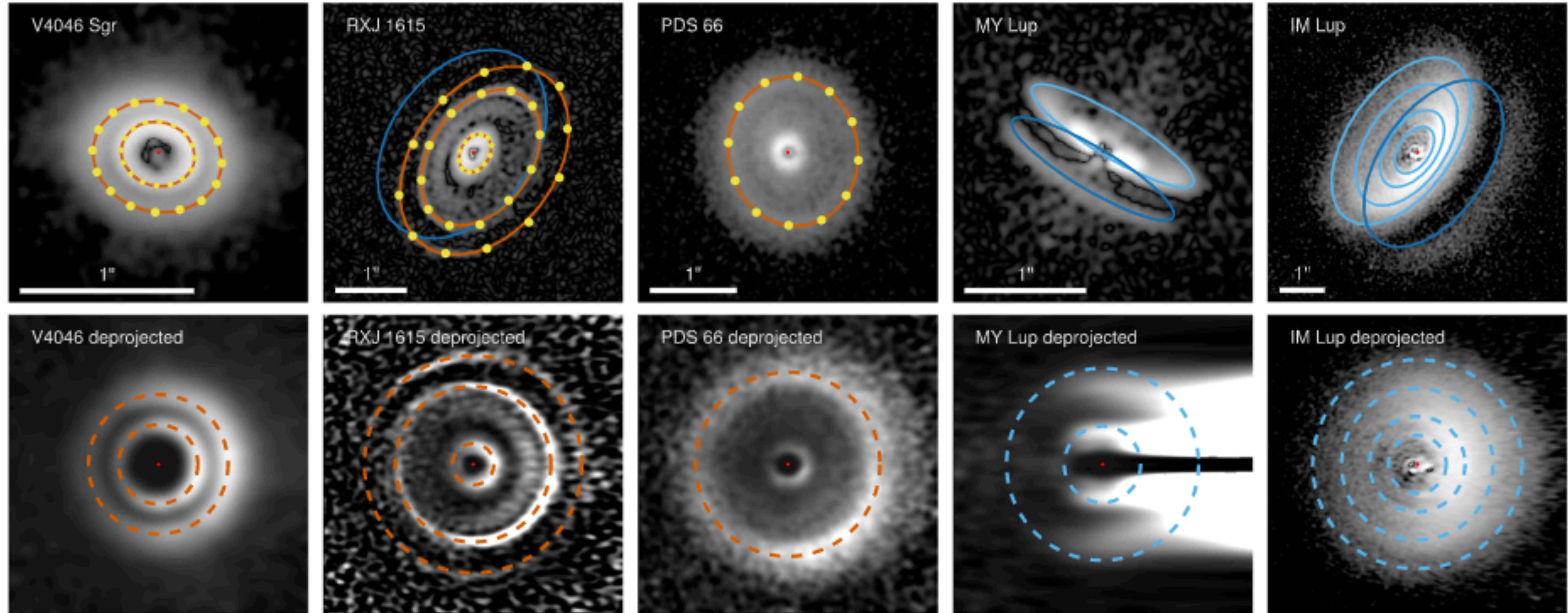


**Figure 4.** Upper row: disks of V4046 Sgr, RXJ 1615, and PDS 66 overlaid with their ring fits. For MY Lup and IM Lup, rings were overlaid by eye, because the automatic fitting procedure failed. Tracking points are yellow, ring fits are red, and rings overlaid by eye are light blue. The rear edge of the disk (mirrored from the outermost ring) is shown in dark blue where applicable (MY Lup, IM Lup, RXJ 1615). Lower row: deprojected images of the disks overlaid with their rings. We use flaring exponents of  $\alpha = 1.605$  (V4046 Sgr),  $1.116$  (RXJ 1615), and  $1.271$  (IM Lup) for deprojection (see Section 4.3). For MY Lup and PDS 66, where only one ring can be tracked, we use  $\alpha = 1.2$ . In the deprojected image of MY Lup, we additionally mark the approximate position of the second ring further in at  $r = 0''.31 / 49$  au. For the deprojections, the semimajor axis is along the vertical, the semiminor axis is along the horizontal, and the near side of the disk is always on the right. For the non-deprojected images, north is up and east is to the left.

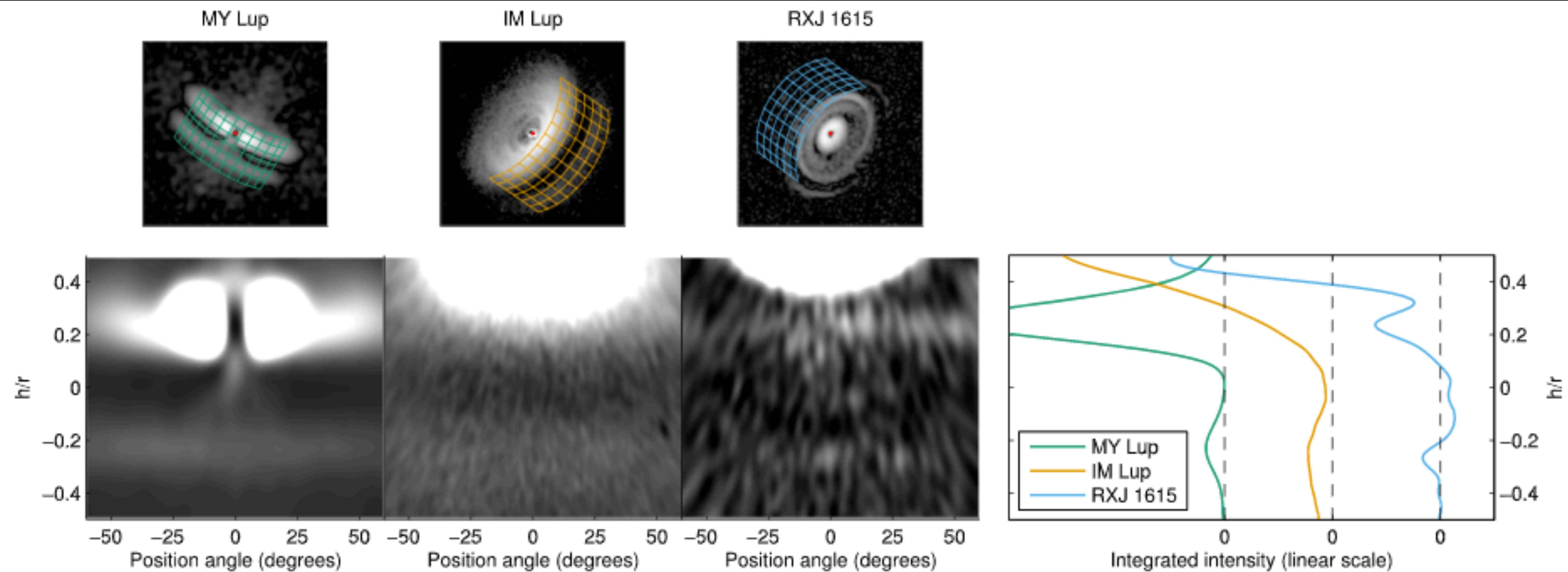


**Figure 6.** Left: deprojection of the disk rims and surface brightness profiles perpendicular to the disk rim of MY Lup, IM Lup, and RXJ 1615, shown in linear scale. The position angle refers to the position angle with regard to the disk minor axis. The meshes in the upper panels give a reference to show how the deprojection was done. Right: integrated intensities along the disk plane between  $-60^\circ$  and  $+60^\circ$ . The scaling of the data for the different disks with respect to each other is arbitrary. As can be seen, the surface brightness goes into the negative for RXJ 1615, a sign that we overcorrected for self-cancellation.

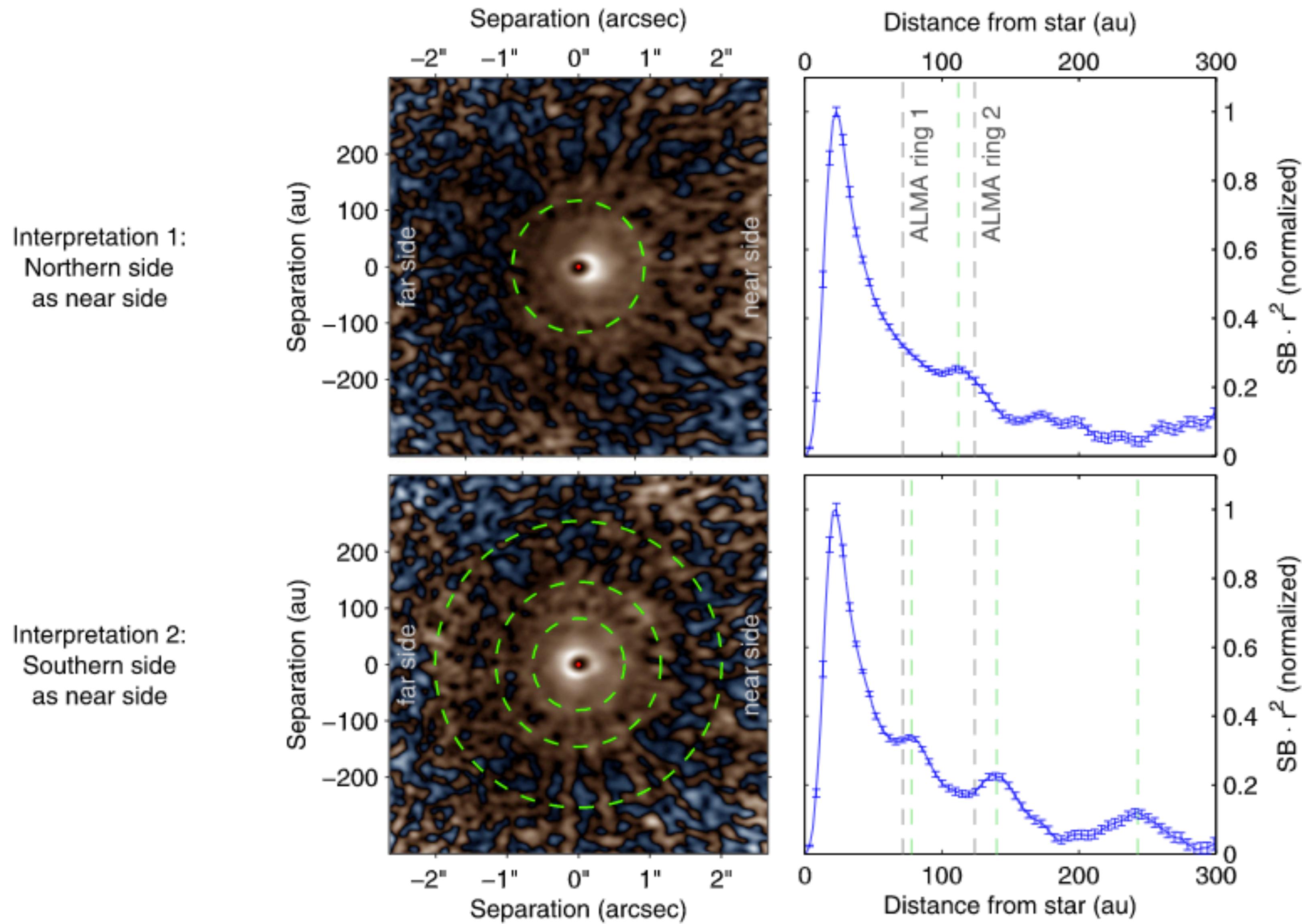


**Figure 8.** Two possible deprojections of AS 209 using  $i = 35.3^\circ$  and P.A. =  $86.0^\circ$ , as determined by Fedele et al. (2017), as well as  $h/r(100 \text{ au}) = 0.1617$  and  $\alpha = 1.219$  (the average values determined for these parameters in Section 4.3). The first (upper) deprojection assumes the northern side to be the near side, while the second assumes the southern side to be the near side (i.e., P.A. =  $86.0^\circ + 180.0^\circ$  in our frame of reference). The frames on the left show the deprojected images displayed in linear stretch after scaling with  $r^2$ , while the plots on the right show azimuthally averaged surface brightness, also scaled with  $r^2$  and normalized to the peak. Rings are detected at around either 112 au (interpretation 1) or 78, 140, and 243 au (interpretation 2) and marked with green dashed lines. The ALMA continuum rings seen by Fedele et al. (2017) at 72 and 124 au are marked with gray dashed lines. The  $1\sigma$  error bars are calculated from the  $U_\phi$  frames, taking into account that the effective beam size changes when deprojecting (see the Appendix for a detailed description of our error derivations). They do not take into account azimuthal variations in the  $Q_\phi$  frame. The dashed lines in the left panel show the position of rings detected in scattered light.

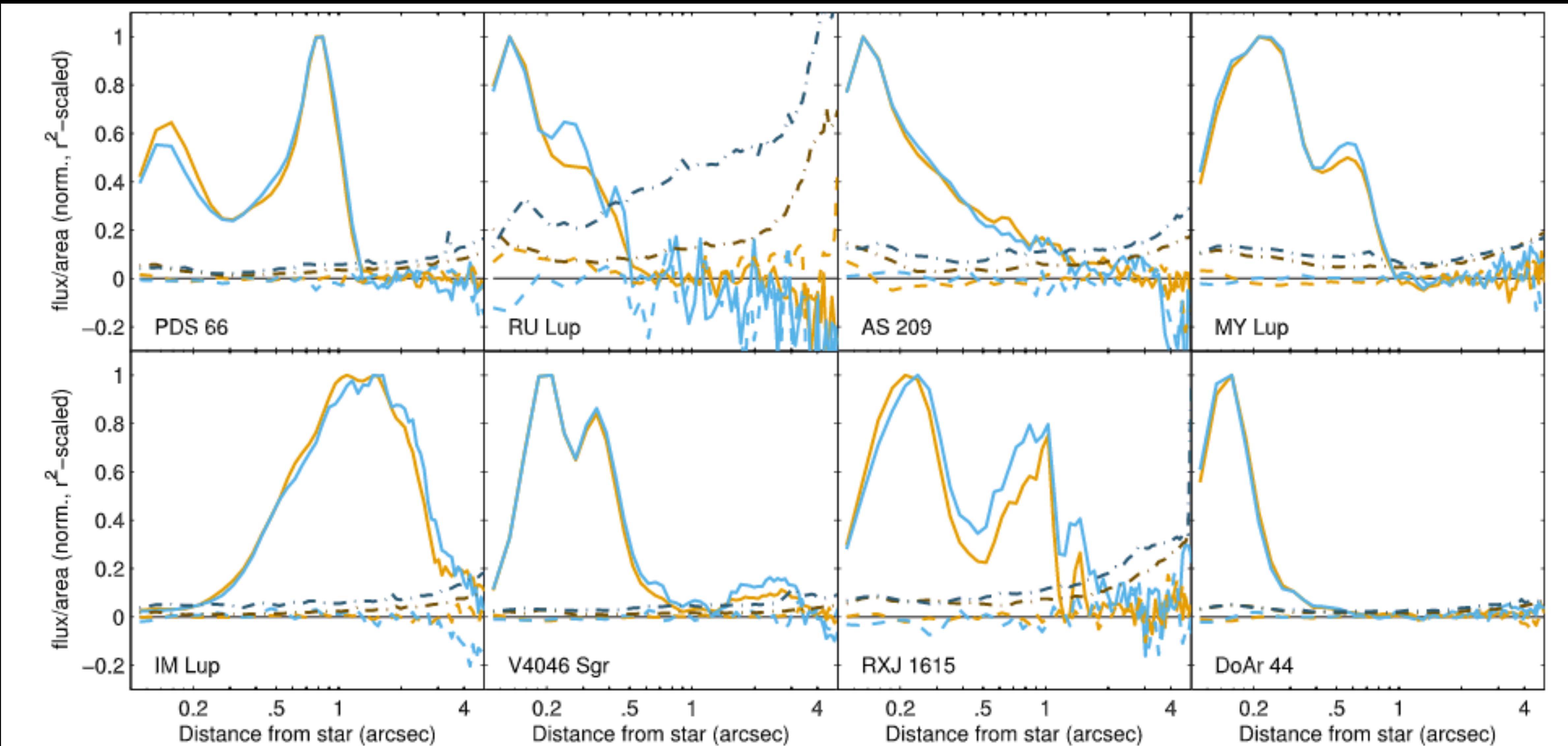


**Figure 11.** Individual normalized  $Q_\phi$  and  $U_\phi$  surface brightness plots vs. distance for all of our targets. Orange lines present  $H$ -band and blue lines  $J$ -band data. Solid lines represent  $Q_\phi$ , and dashed lines represent  $U_\phi$ . Darker dash-dotted lines represent  $3\sigma$  detection limits. The width of the annuli used for averaging increases with radius proportional to  $r^{1/2}$  (similar to Figure 3). Note the logarithmic stretch of the  $x$ -axis. The data have been scaled with  $r^2$  in order to improve readability.

# **Rising from Ashes or Dying Flash? The Mega Outburst of Small Comet 289/Blanpain in 2013**

**Quanzhi Ye 2019**

**(Paper 18)**

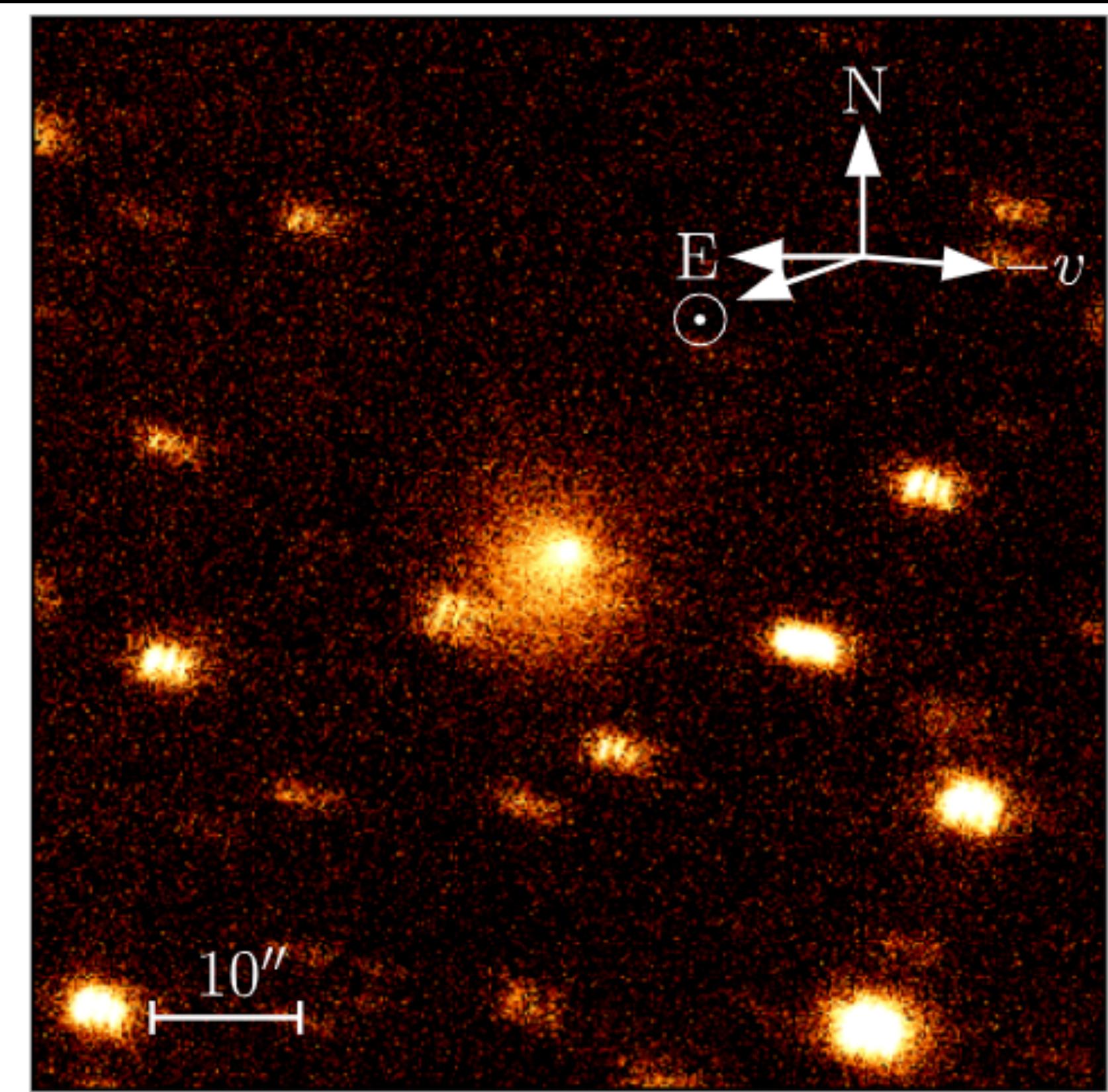


**Figure 1.** Stacked CFHT image of P/Blanpain taken on 2013 July 5 (center). The arrows on the upper-right corner mark the celestial north, celestial east, direction to the Sun ( $\odot$ ), and the minus heliocentric velocity motion ( $-v$ ). Notebook is available here:[https://github.com/Yeqzids/blanpain-2013/blob/master/cfht\\_stack.ipynb](https://github.com/Yeqzids/blanpain-2013/blob/master/cfht_stack.ipynb).

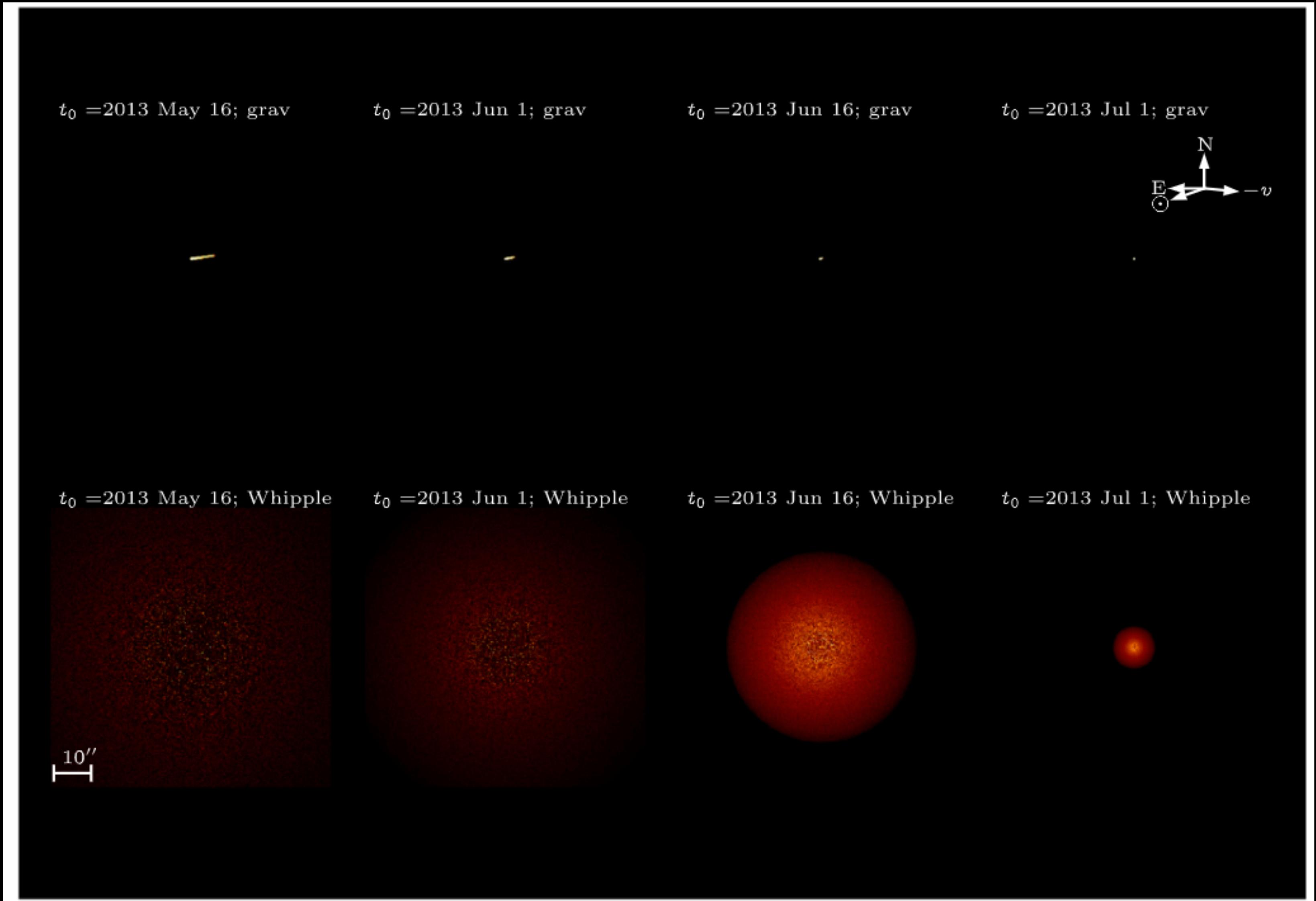


**Figure 2.** Model images of P/Blanpain on 2013 July 5 under different assumptions: ejection dates ( $t_0$ ) of 2013 May 16, June 1, June 16 and July 1, as well as ejections following Whipple model or gravitational escape model. The model most compatible with the observation is the Whipple model with ejection date of 2013 July 1 (lower right). Notebook is available here:[https://github.com/Yeqzids/blanpain-2013/blob/master/coma\\_sim.ipynb](https://github.com/Yeqzids/blanpain-2013/blob/master/coma_sim.ipynb).

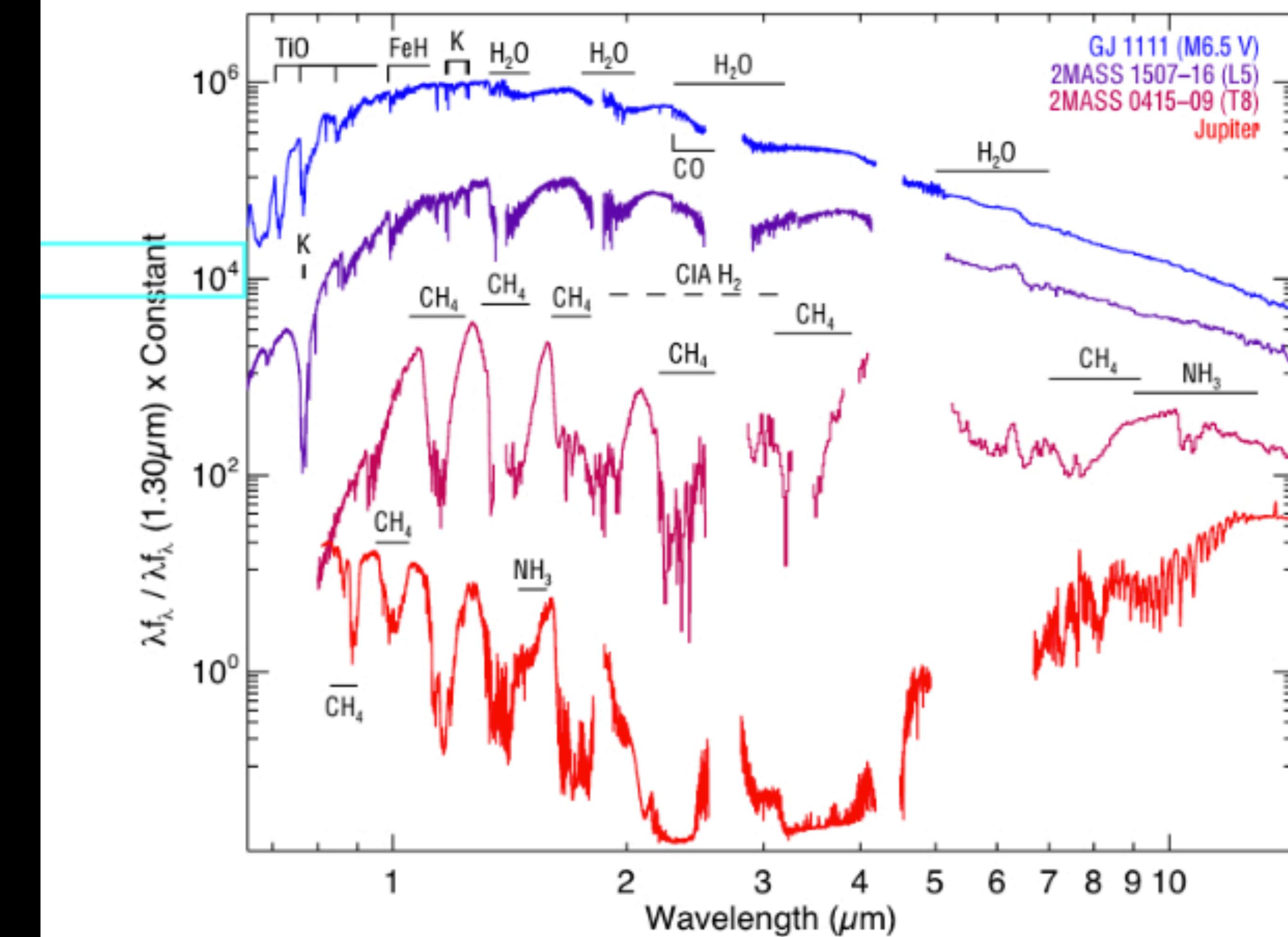
# **The Future of Ultracool Dwarf Science with JWST**

**(Paper 19)**

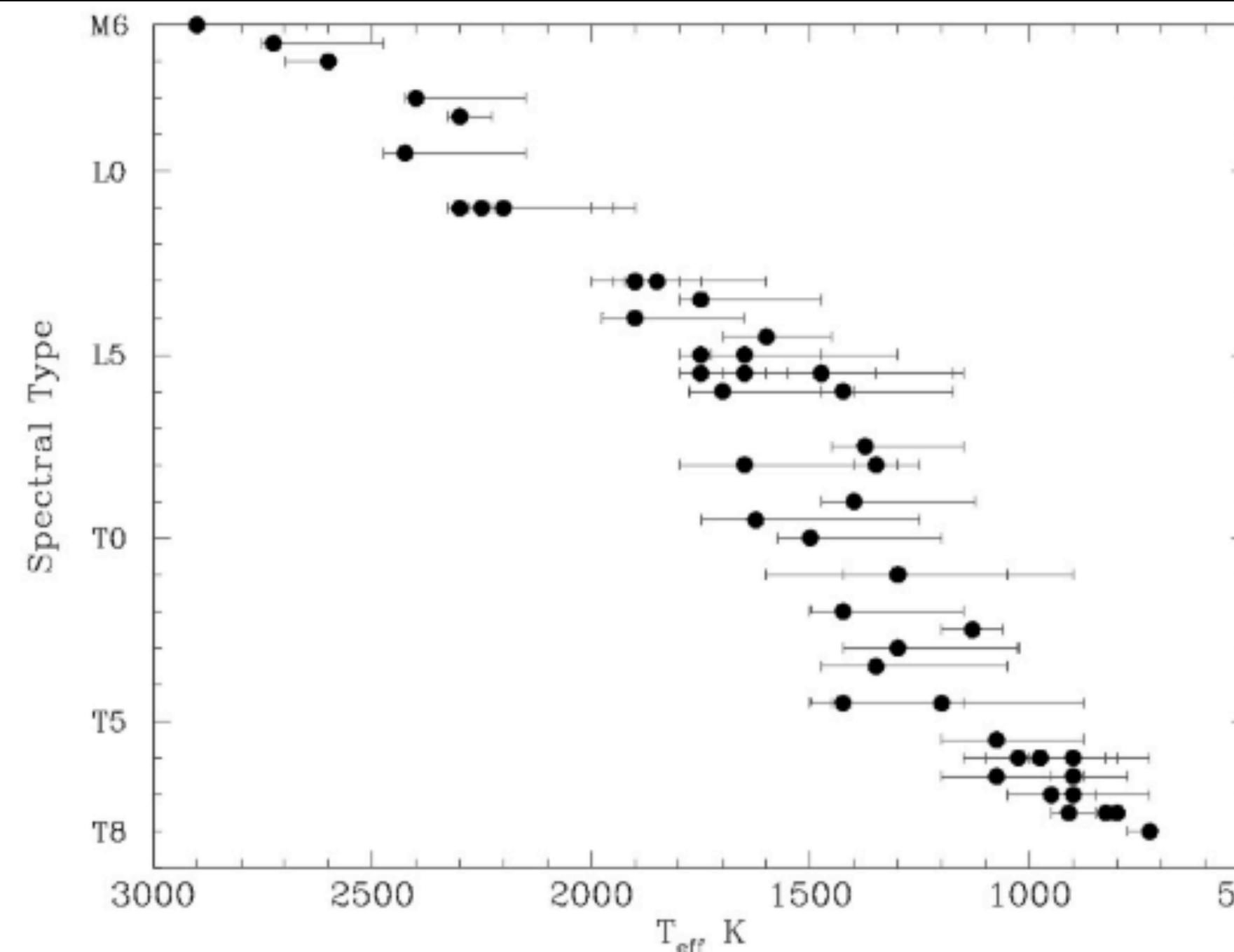
# The Future of Ultracool Dwarf Science with JWST

Mark S. Marley (Paper 19)

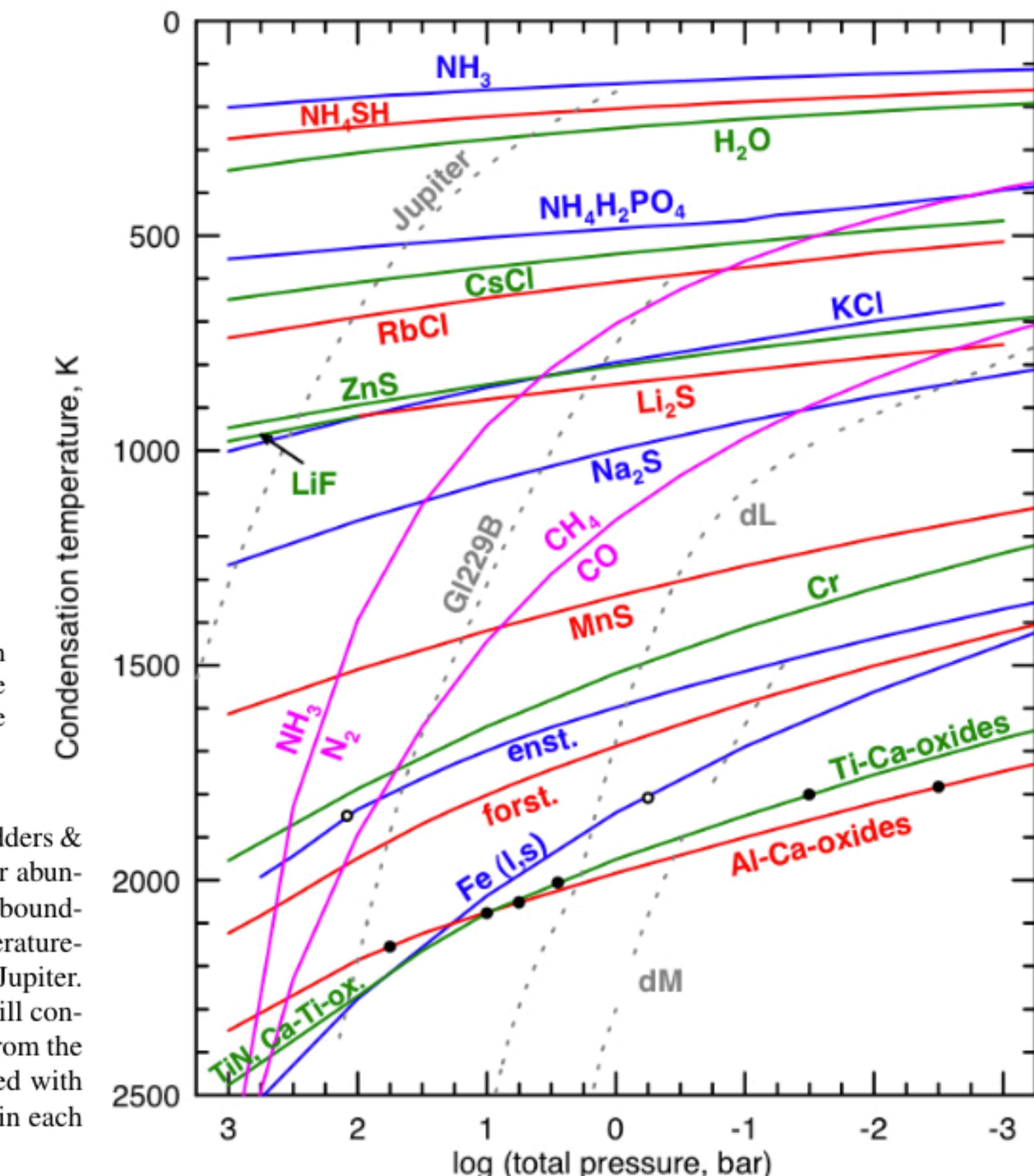
- Ultracool Dwarfs: Stars Type M, L and T respectively
- Take account of precipitation



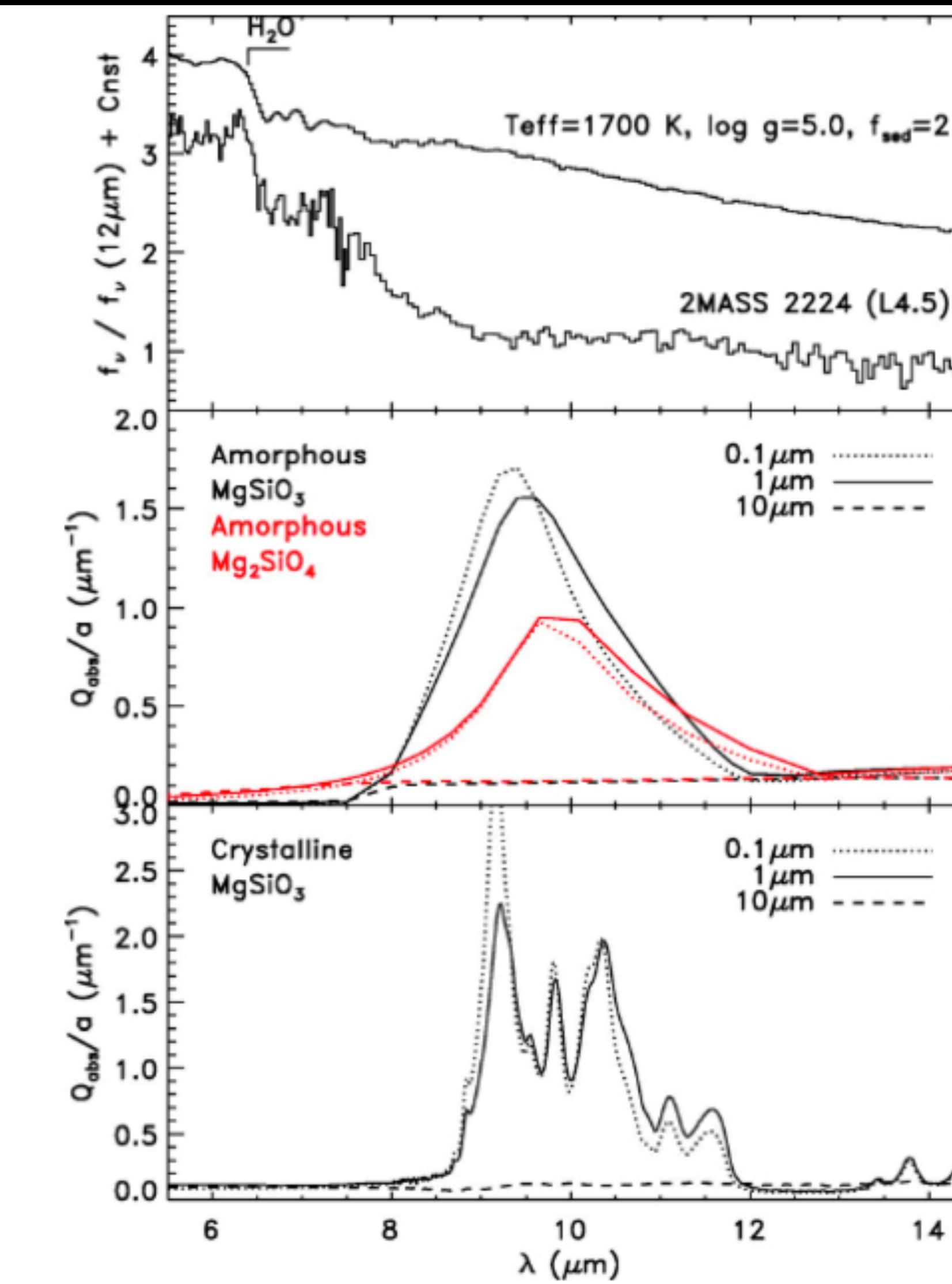
**Fig. 1** The most prominent signatures of the ultra cool dwarf spectral sequence are seen in these 0.65 to 14.5  $\mu\text{m}$  spectra of a mid-M, L, and T dwarfs as well as Jupiter (adapted from Cushing et al. (2006)). The spectra have been normalized to unity at 1.3  $\mu\text{m}$  and multiplied by constants. Major absorption bands are marked. The collision-induced opacity of H<sub>2</sub> is indicated as a dashed line because it shows no distinct spectral features but rather a broad, smooth absorption. Jupiter's flux shortward of  $\sim 4\mu\text{m}$  is predominantly scattered solar light; thermal emission dominates at longer wavelengths (near- and mid-infrared Jovian spectra from Rayner, Cushing & Vacca (in preparation) and Kunde et al. (2004), respectively).



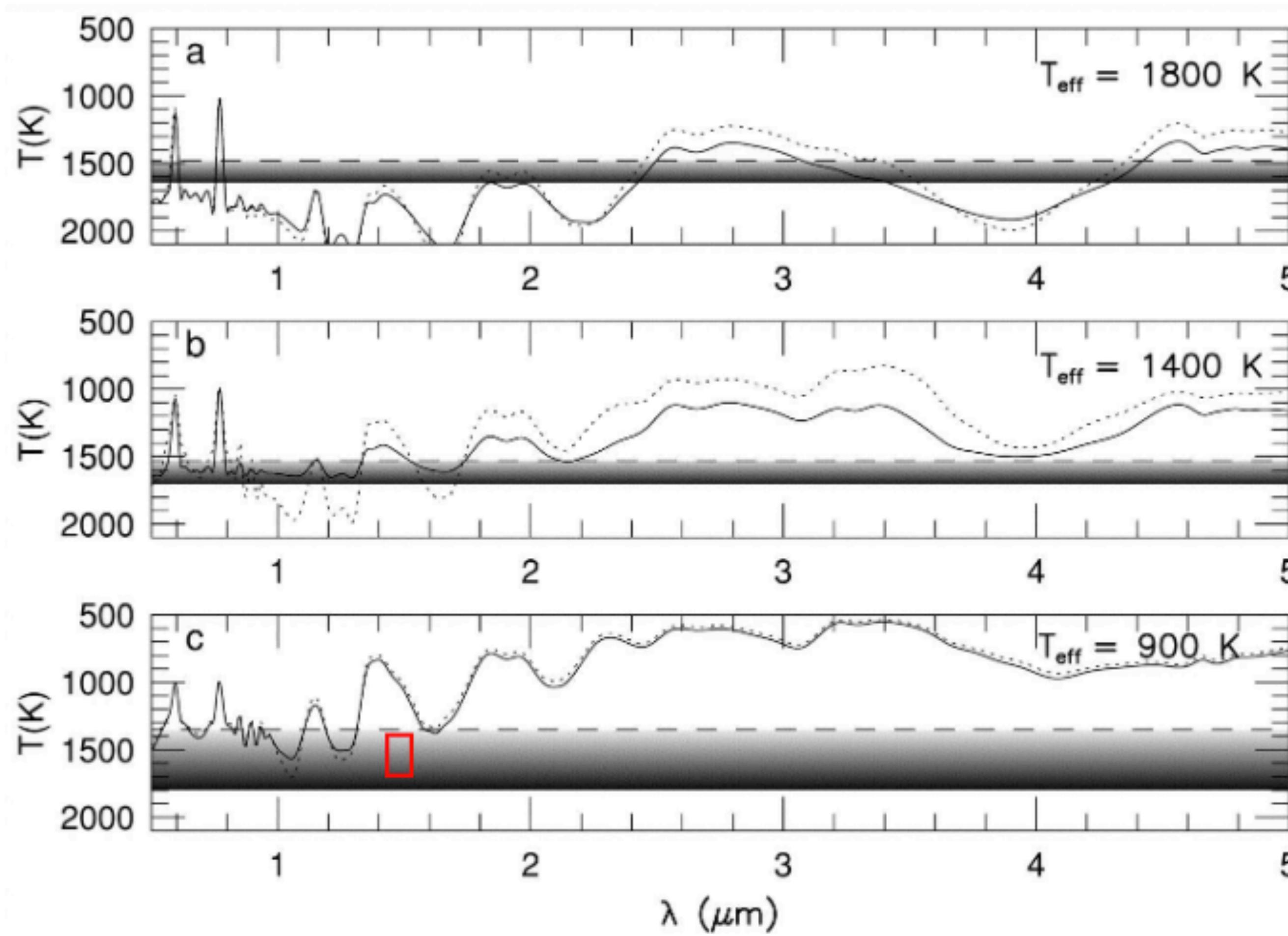
**Fig. 3** Effective temperature as a function of infrared spectral type for ultracool dwarfs with known parallax (data from Golimowski et al. 2004, Vrba et al. 2004, and Luhman et al. 2007). Note the roughly constant effective temperature for dwarfs of spectral types from late L to early T. See Kirkpatrick (2007) for further discussion.



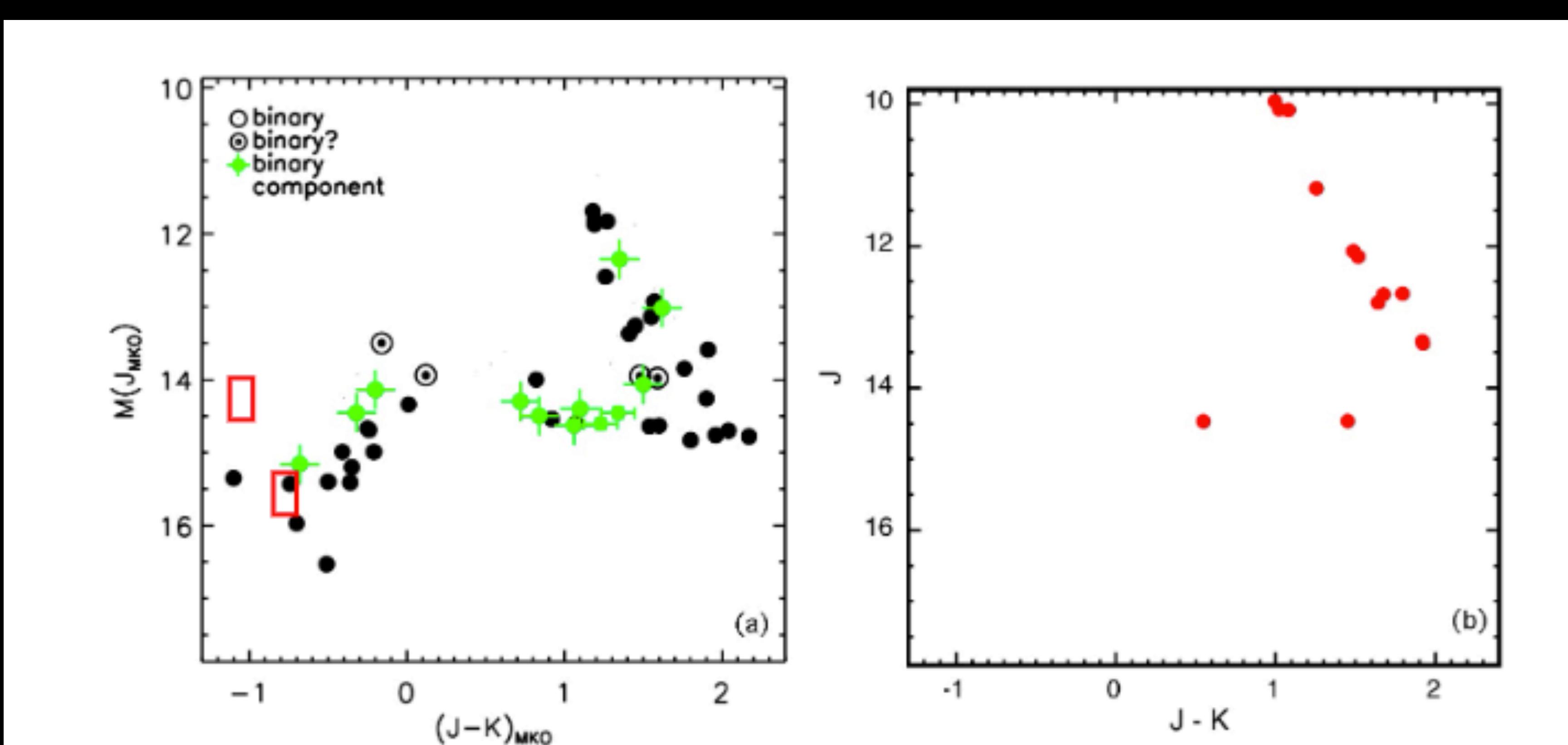
**Fig. 2** Important chemical equilibrium boundaries for substellar objects (modified from Lodders & Fegley 2006). Green, red, and blue lines denote various condensation boundaries for a solar abundance mixture of gasses in a substellar atmosphere. Light purple lines denote equilibrium boundaries between important gaseous species. Grey dashed lines show model atmospheric temperature-pressure profiles for M, L and T dwarfs (the latter specifically for Gl 229 B) as well as for Jupiter. As one moves upwards in the diagram along the model ( $T, P$ ) curves, the labeled species will condense at the intersection with the condensation curves and would be expected to be absent from the gas at lower temperatures further up along the model profiles. This figure can be compared with Figure 1 to understand why spectral features for various compounds are present or absent in each observed spectrum.



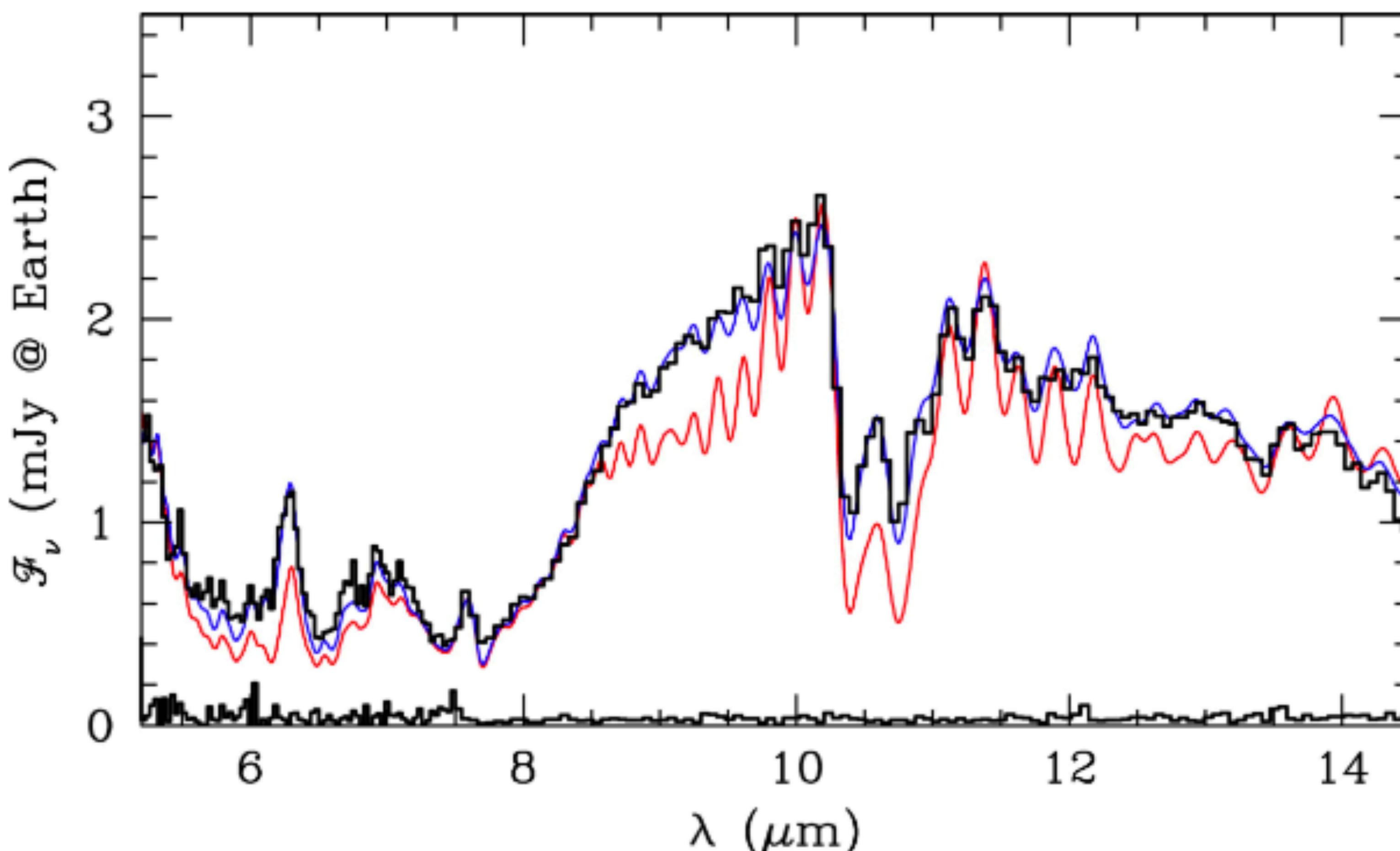
**Fig. 5** Top: *Spitzer* IRS spectrum of 2MASS 2224 (L4.5) and the best fitting model from Cushing et al. (2006). Middle: Optical absorption ( $Q_{\text{abs}}/a$ ) for amorphous enstatite ( $\text{MgSiO}_3$ ) and forsterite ( $\text{Mg}_2\text{SiO}_4$ ) for three different particle sizes, 0.1, 1, and 10 μm. Bottom: Optical absorption for crystalline enstatite, also for three different particle sizes. The deviation of the model (shifted vertically) from the data suggests that additional small, and perhaps crystalline, silicate grains are required to adequately account for the observed spectrum.



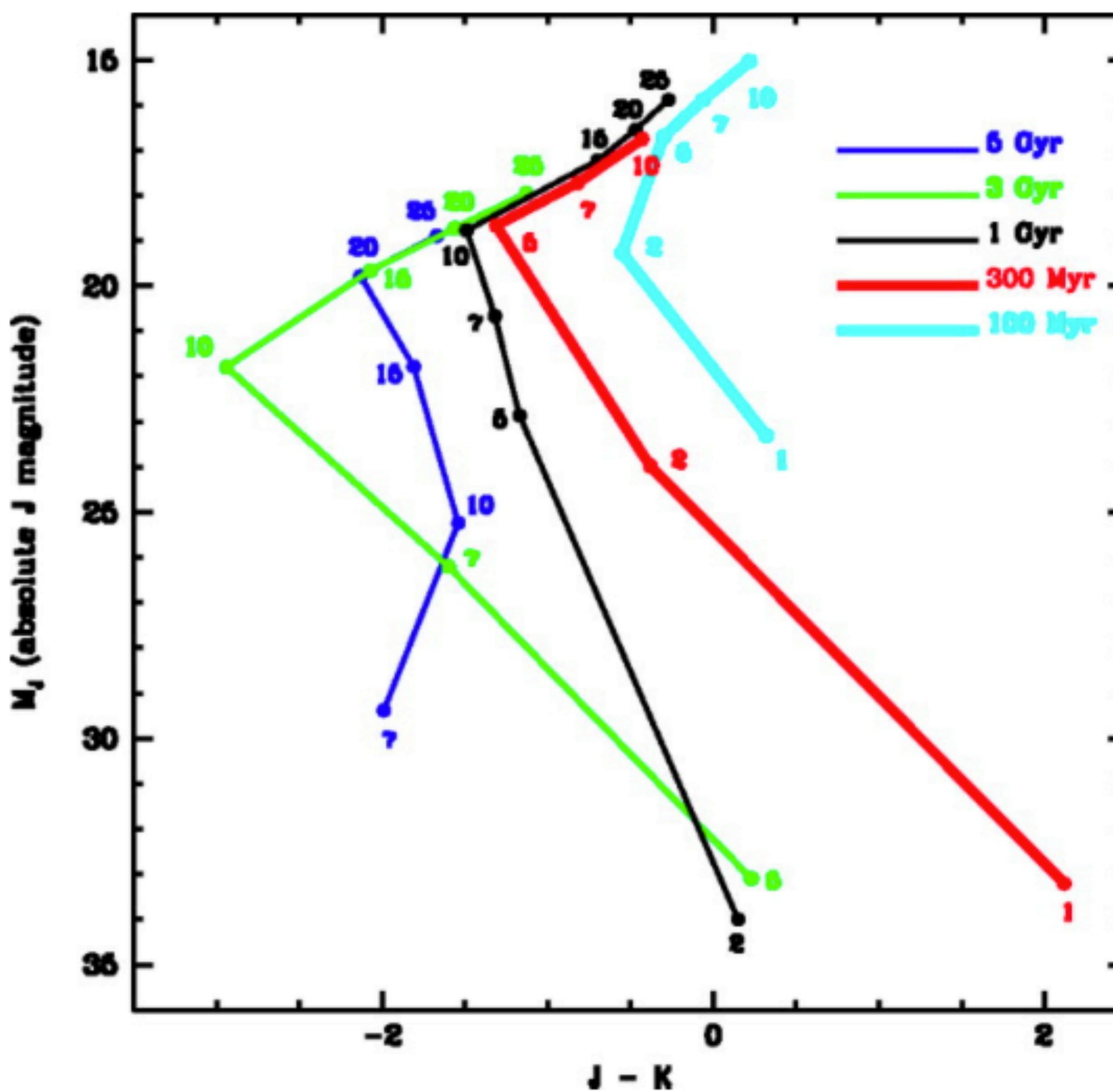
**Fig. 4** Brightness temperature as a function of wavelength for atmosphere models which include (solid) or exclude (dotted) silicate and iron clouds (Ackerman & Marley 2001). Brightness temperature increases downward to suggest increasing depth in the atmosphere from which the wavelength-dependent flux emerges. The solid straight line indicates the base of the silicate cloud while the long dashed line denotes the ‘top’ of the cloud (the level in the atmosphere at which the cloud column extinction reaches 0.1). Shading suggests the decrease in cloud extinction with altitude. Since cloud particle radii exceed 10 μm in these models, the Mie extinction efficiency is not a strong function of wavelength over the range shown. Shown are models characteristic of (a) an early-type L dwarf with  $T_{\text{eff}} = 1800$  K, (b) a late-type L dwarf with  $T_{\text{eff}} = 1400$  K, and (c) a T dwarf with  $T_{\text{eff}} = 900$  K. All of these models are for solar composition and gravity appropriate for a 30 Jupiter-mass brown dwarf. Note that the spectral region just longward of 1 μm is particularly sensitive to the cloud opacity.



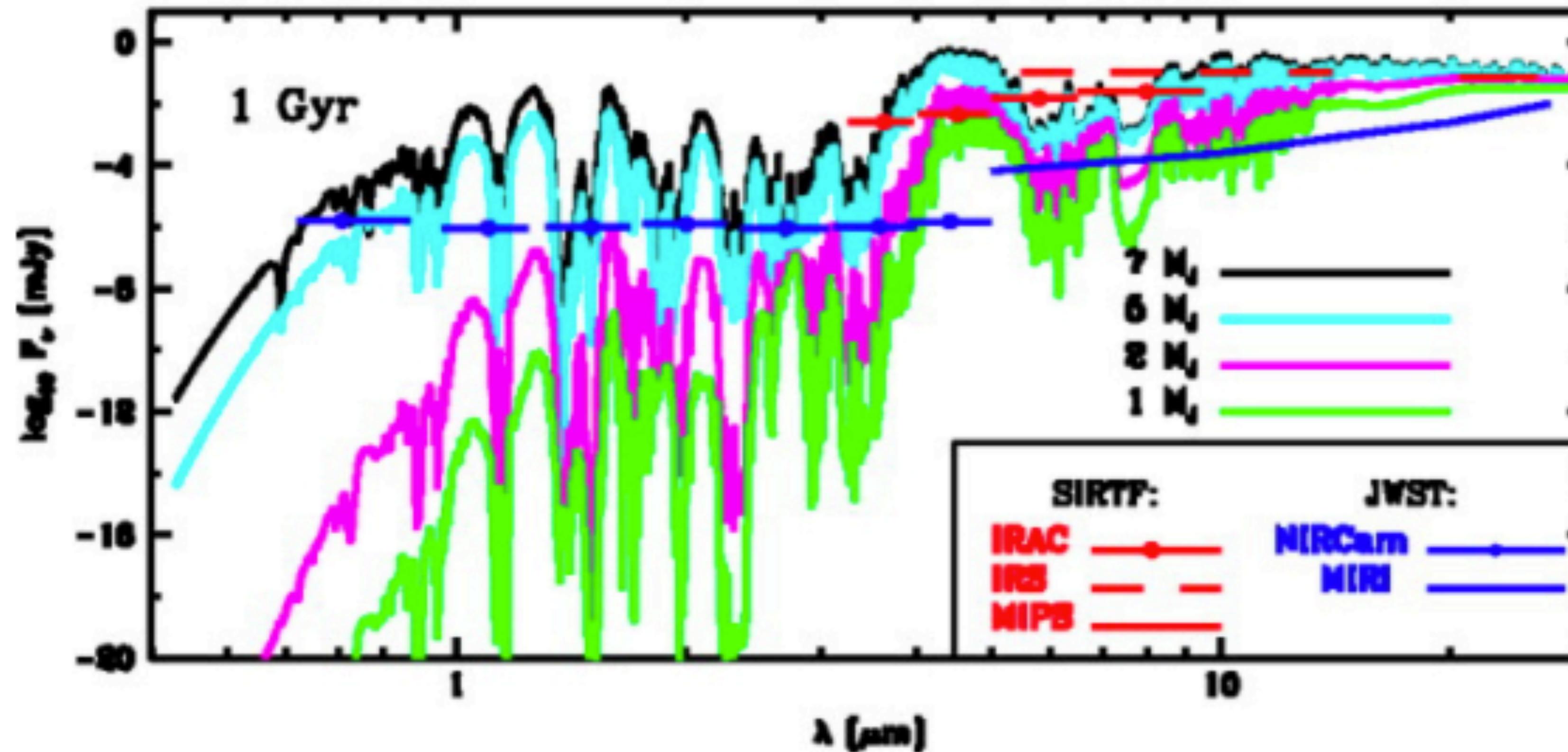
**Fig. 6** Near-infrared color-magnitude diagrams for field and cluster ultracool dwarfs. (a) Black dots show single field L & T dwarfs. Green dots are resolved components of binary systems. Dotted circles are suspected (but unresolved) binaries (figure courtesy M. Liu based on Liu et al. (2006)). (b) Candidate ultracool dwarfs in the Pleiades in the most sensitive current survey (Casewell et al. 2007). Faintest objects in this plot have masses of about  $11 M_{\text{Jup}}$ . Note that at a fixed magnitude the cluster members tend to be redder than the field objects, which is likely a signature of low gravity. JWST will obtain spectra of quality comparable to Figure 1 for the candidate objects shown on this panel which will help calibrate evolutionary models of the brown dwarf cooling sequence. The detection limit for NIRCam on JWST is at about  $J = 22$  for this cluster or  $\sim 1 M_{\text{Jup}}$ . Model predictions for colors of objects with  $J > 15$  are shown in Figure 8.



**Fig. 7** Fits of the IRS spectrum of 2MASS J0415-0935 (Saumon et al. 2007) showing the difference between a model in chemical equilibrium and a model that includes vertical transport that drives the nitrogen and carbon chemistry out of equilibrium. The red thin curve is the best-fitting model in chemical equilibrium, and the blue thin curve is the best-fitting nonequilibrium model. The data and the noise spectrum are shown by the histograms (black). The uncertainty on the flux calibration of the IRS spectrum is  $\pm 5\%$ . The model fluxes, which have not been normalized to the data, are shown at the resolving power of the IRS spectrum.



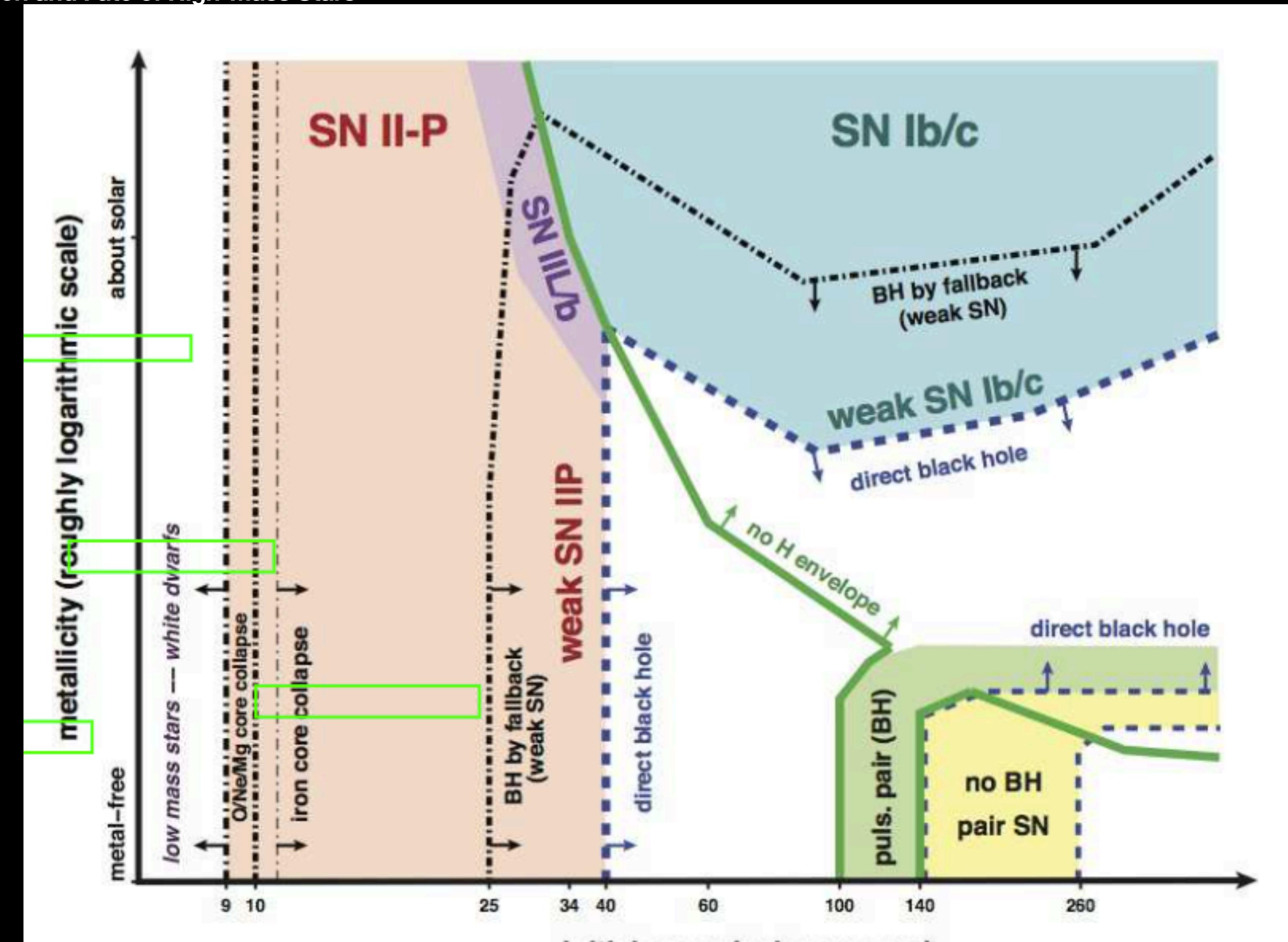
**Fig. 8** Predicted absolute J magnitude ( $M_J$ ) vs.  $J - K$  color for a range of brown dwarf masses and ages. The numbers by the symbols denote the masses of the objects in Jupiter mass units. In the Pleiades the JWST NIRCAM detection limit will be about 1 Jupiter mass. Figure and description from Burrows et al. (2003); see discussion therein for greater detail.



**Fig. 9** Spectra (flux in millijanskys) vs. wavelength (in microns) for a range of brown dwarf masses at an age of 1 Gyr and a distance of 10 pc. Superposed are the approximate point-source sensitivities for instruments on *Spitzer* (red) and *JWST* (blue). The *JWST*/NIRCam sensitivities are  $5\sigma$  and assume an exposure time of  $5 \times 10^4$  sec. The *JWST*/MIRI sensitivity curve from 5.0 to 27  $\mu\text{m}$  is  $10\sigma$  and assumes an exposure time of  $10^4$  sec. Figure and description from Burrows et al. (2003); see discussion therein for greater detail.

# **Mass Loss: Its Effect on the Evolution and Fate of High-Mass Stars**

**(Paper 20)**

**Figure 1:**

Example of the standard expectations for the fates of massive stars as a function of initial mass and metallicity, adapted from Heger et al. (2003) with permission.

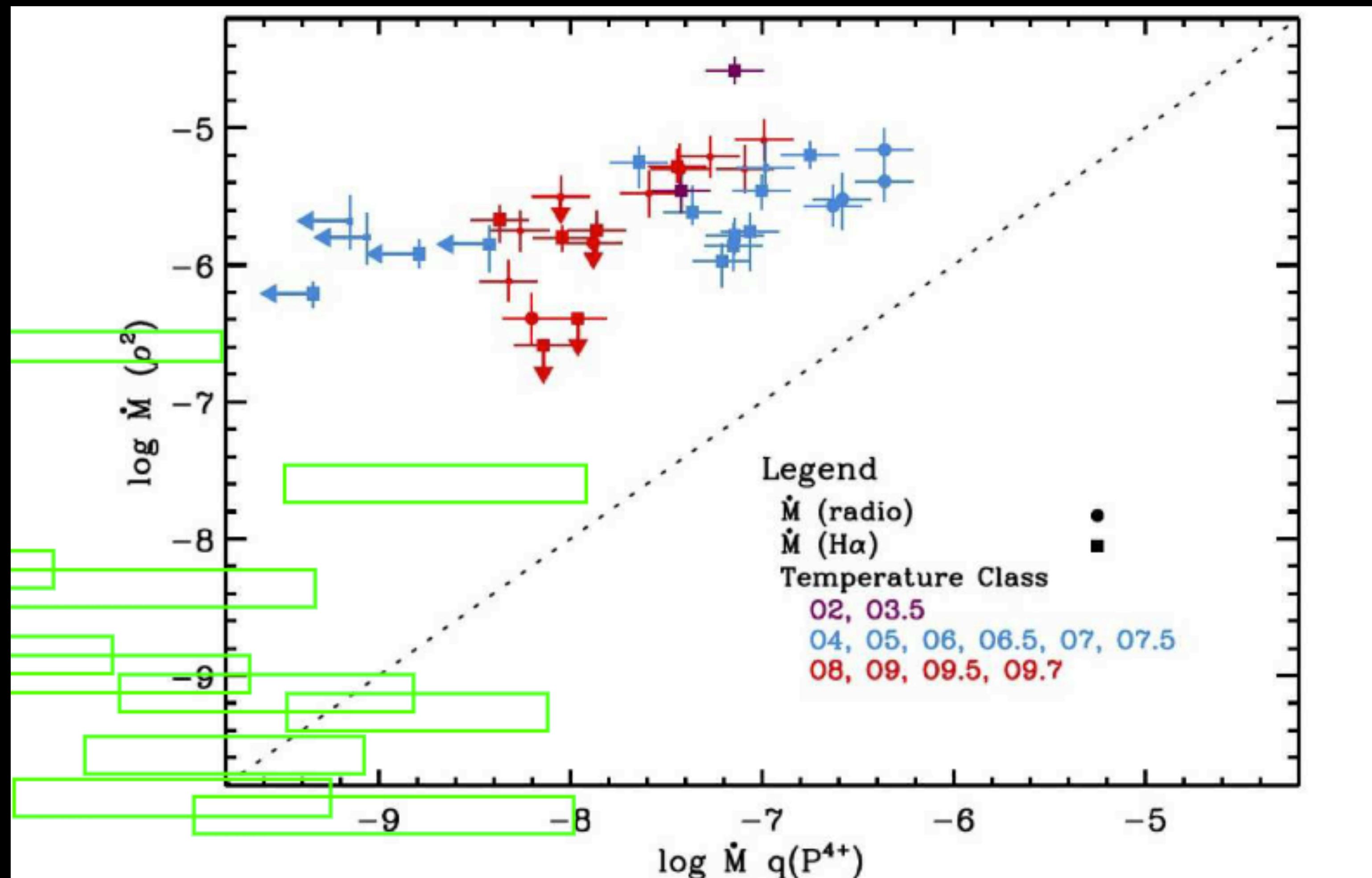
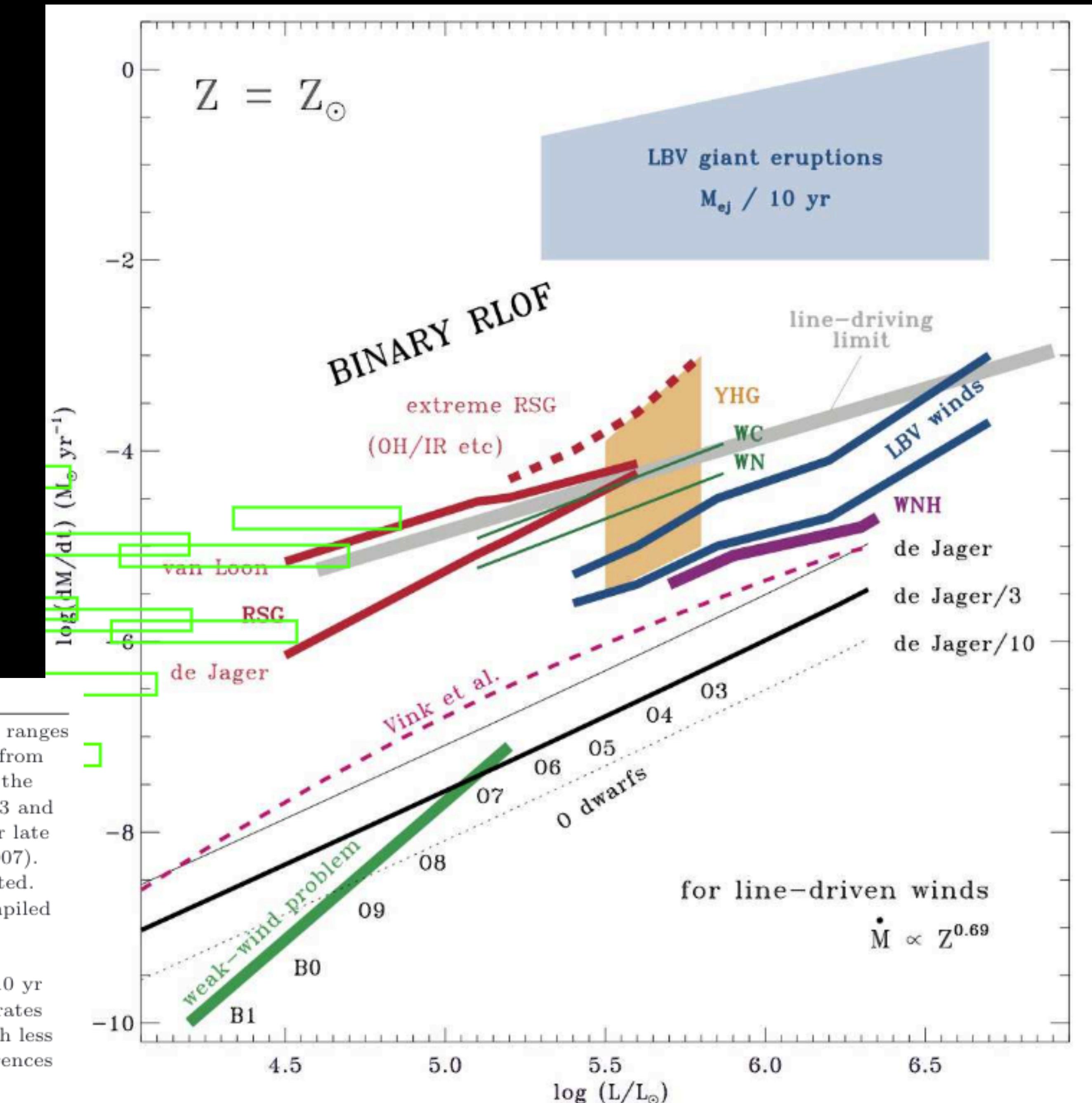


Figure 2:

A comparison of the mass-loss rates derived from diagnostics that are linearly proportional to wind density, like UV P Cyg absoriton, and those which are proportional to  $\rho^2$ , like free-free and H $\alpha$  emission. This is from Fullerton et al. (2006), reproduced with permission. Although there is still discussion about the P v lines used for this study and if they may overestimate the reductions in  $\dot{M}$  that are applied, this nevertheless forced an important discussion in massive star research by highlighting the potential influence of clumping.

# Mass Loss: Its Effect on the Evolution and Fate of High-Mass Stars

Nathan Smith (Paper 20)

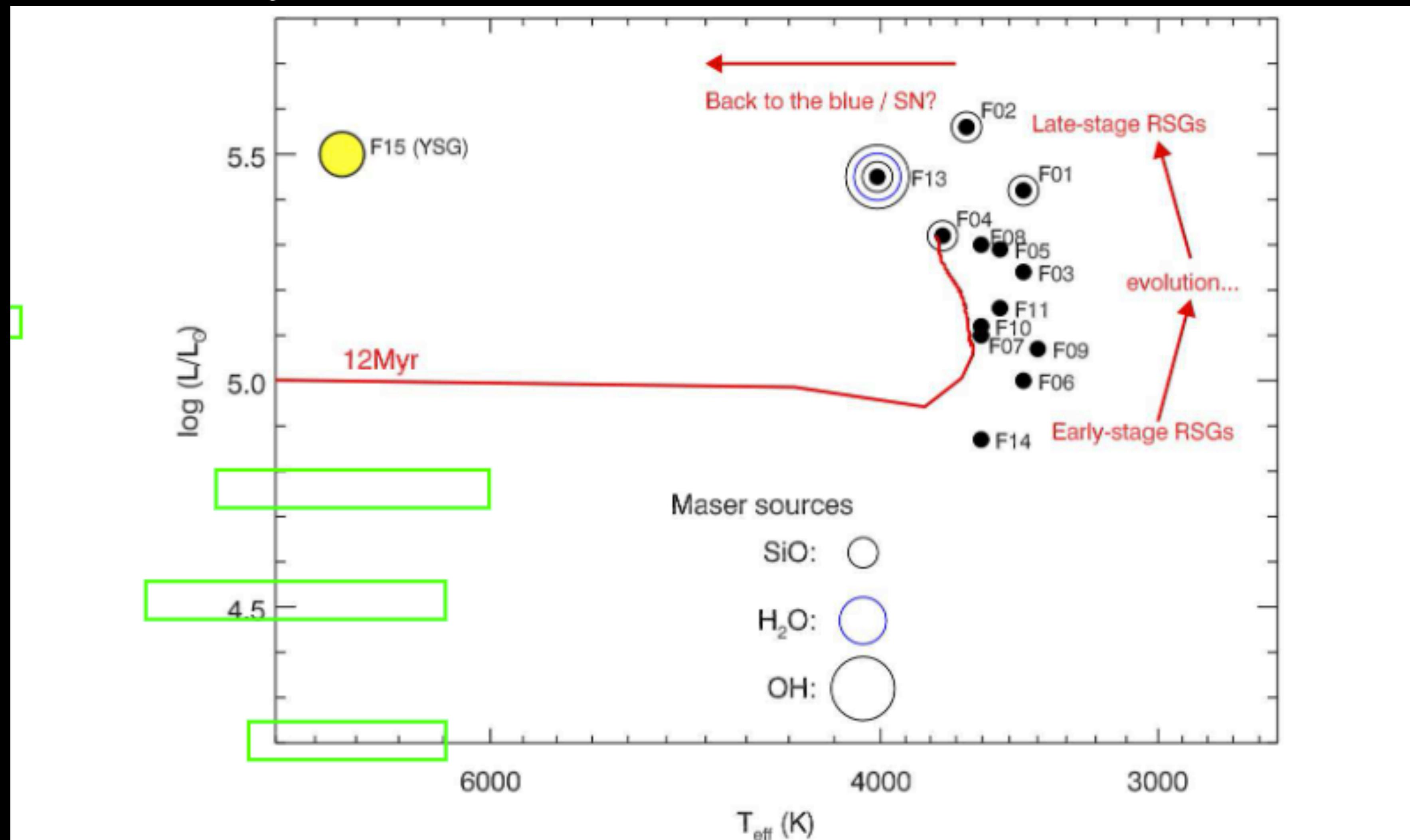


**Figure 3:**

A number of different prescriptions for wind mass loss used in models, as well as typical observed ranges of mass-loss rates for a number of different types of stars. For O-type stars, the theoretical rates from the prescription of Vink et al. (2001) are shown, along with “standard” observational rates using the prescription from de Jager et al. (1988), as well as these same prescriptions divided by factors of 3 and 10 for comparison. The green line labeled “weak-wind problem” refers to lower mass-loss rates for late O-type and early B-type MS stars (see text). Rates for WN and WC stars are from Crowther (2007). RSG mass-loss prescriptions are from de Jager et al. (1988) and van Loon et al. (2005), as indicated. For YHGs, see de Jager (1998). For  $\dot{M}$  corresponding to normal winds of LBVs, values were compiled from a number of studies (Groh et al. 2009, Hillier et al. 2001, Smith et al. 2004, Vink & de Koter 2002). For LBV eruptions, the “rates” shown are calculated from total masses observed in LBV CSM shells (Smith & Owocki 2006) divided by a nominal eruption duration of 10 yr (see Figure 5). For “binary RLOF”, an order-of-magnitude value for the strongest mass-transfer rates expected in brief RLOF phases is noted, although the mass-transfer or mass-loss rate can be much less for slow mass transfer, or possibly more for dynamical common-envelope ejection events; see references in the text, especially the review by Langer (2012).

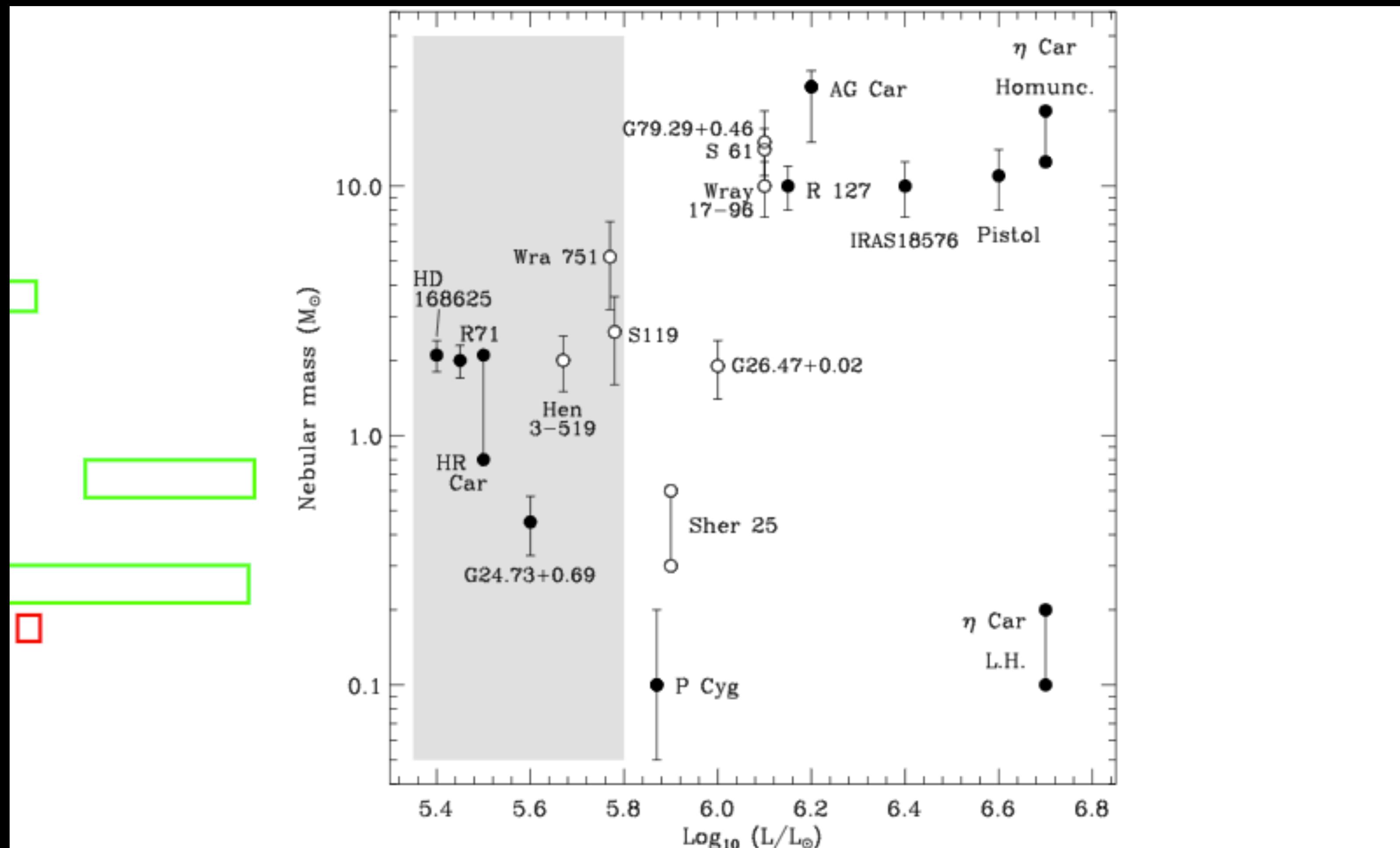
# Mass Loss: Its Effect on the Evolution and Fate of High-Mass Stars

Nathan Smith (Paper 20)



**Figure 4:**

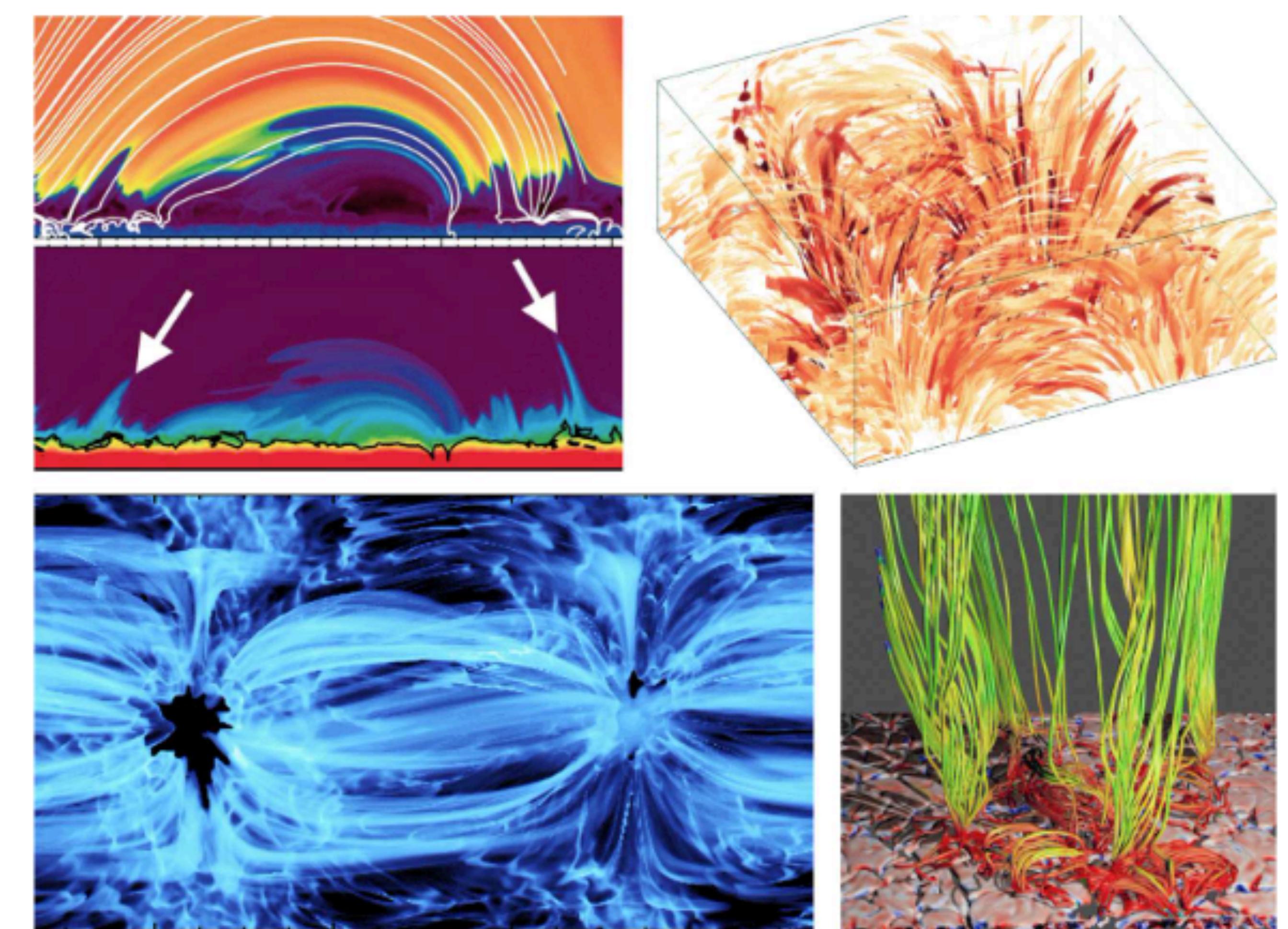
An HR diagram of the cluster RSGC1, with RSGs and a YSG. Sources that are circled include maser emission (as noted) from dense envelopes, indicating especially strong mass loss. Adapted from Davies et al. (2008) with permission.

**Figure 5:**

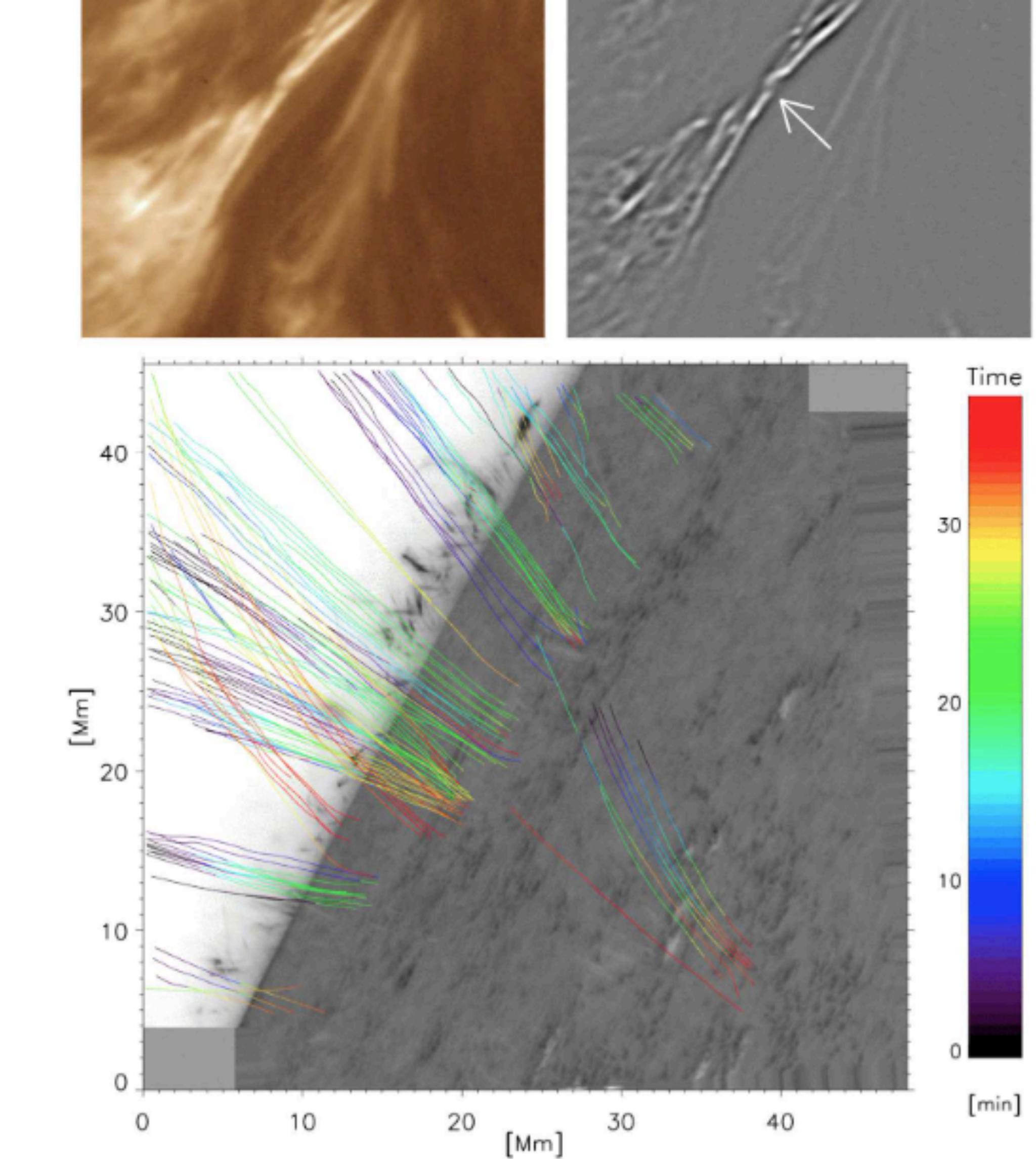
Masses of circumstellar shells around LBVs and LBV-like stars, as a function of luminosity, from Smith & Owocki (2006). The left side of the plot (grey box) corresponds to stars below  $\log(L/L_\odot)=5.8$ , so these LBVs could be post-RSGs and the nebular mass could have been ejected in the RSG phase and swept up into a shell. Objects on the right must have ejected their massive shells in giant LBV eruptions. There may be many lower-mass shells that are hard to detect around the very bright central stars.

# **The Properties of the Solar Corona and Its Connection to the Solar Wind**

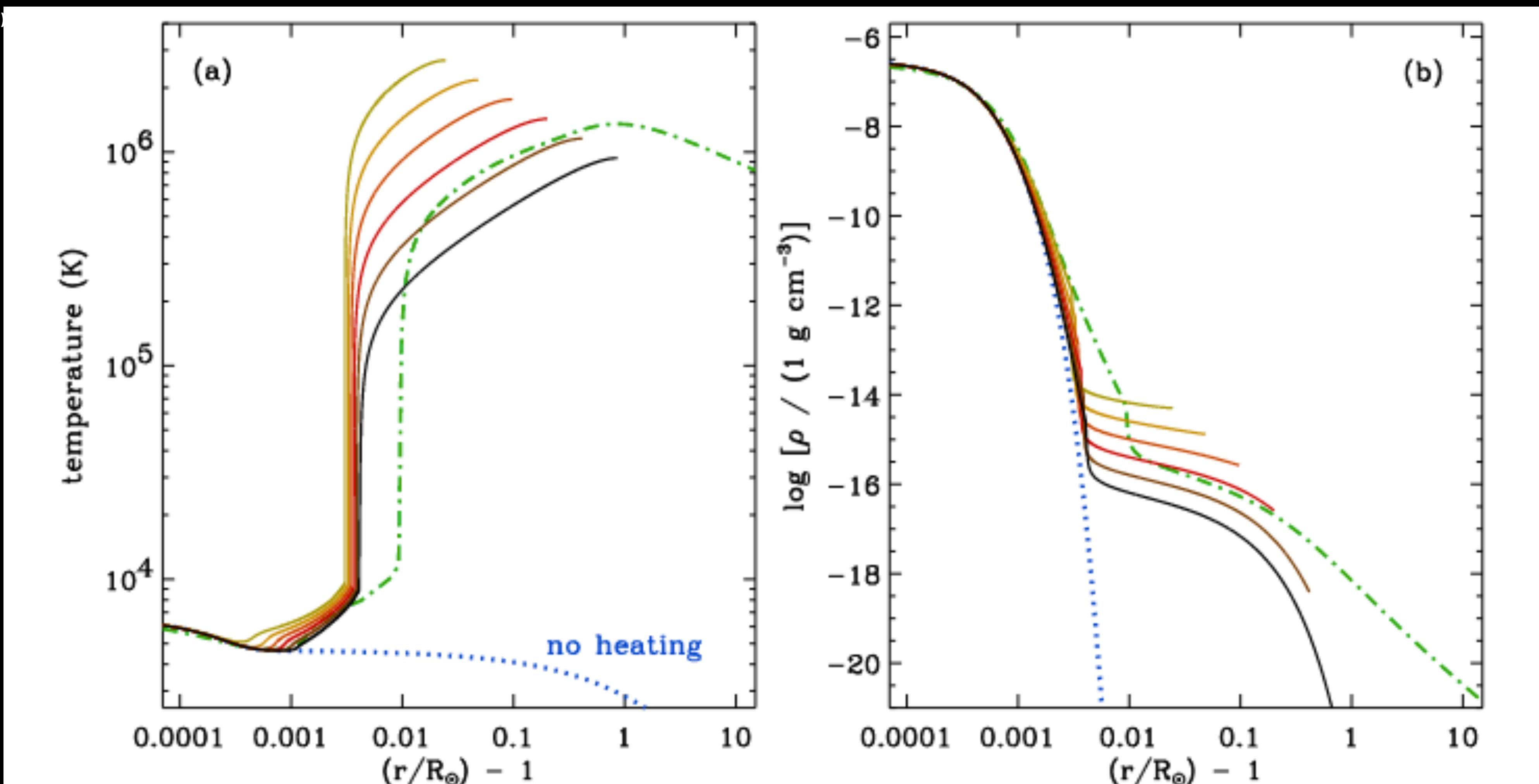
**(Paper 21)**

**Figure 3**

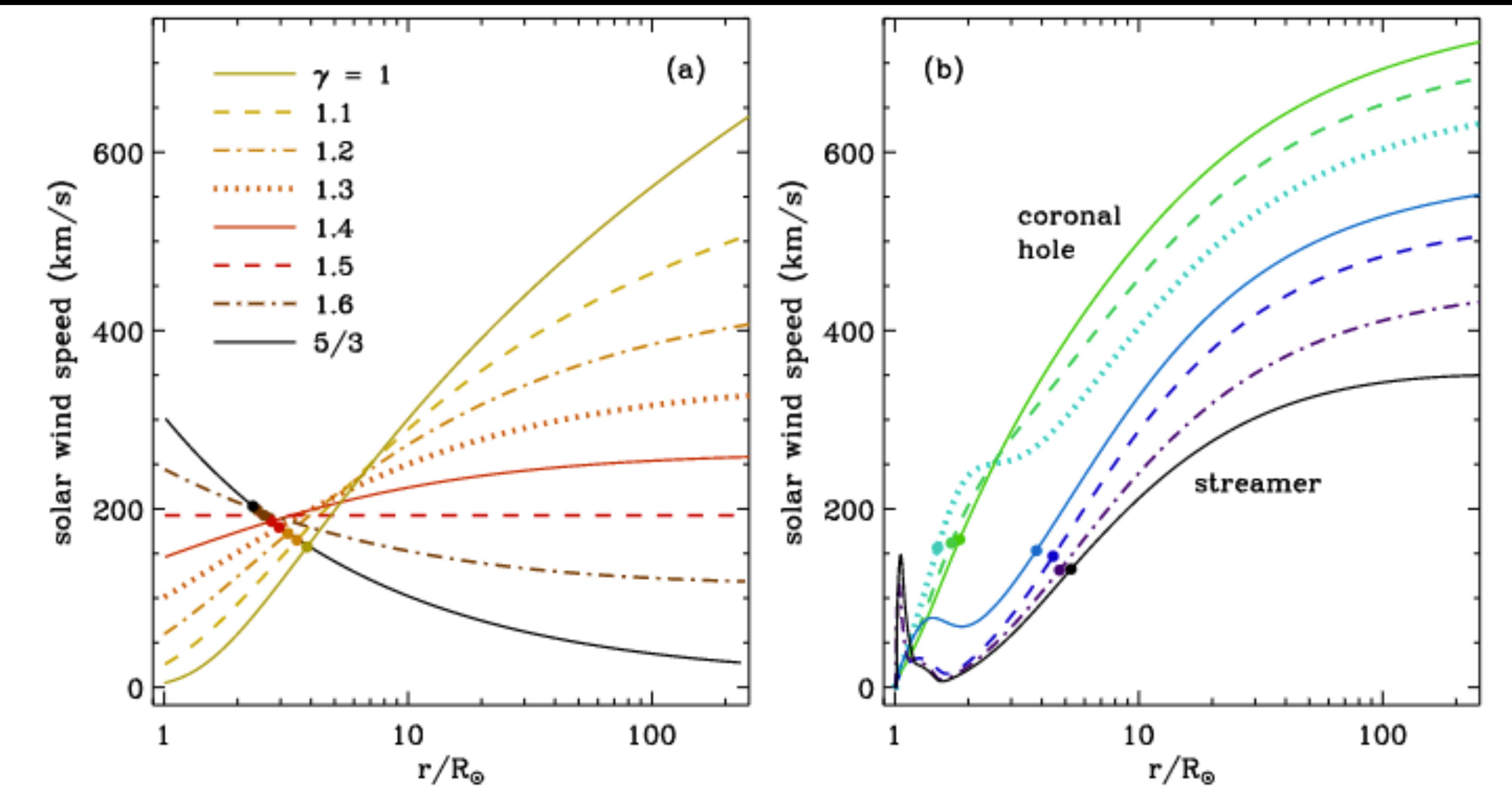
A selection of results from multidimensional MHD coronal models. Clockwise from upper-left, the illustrated quantities are: (1) temperature, with magnetic field lines in white (*top*), and density (*bottom*) from Martínez-Sykora et al. (2017), (2) Joule heating rate from Kanella & Gudiksen (2017), (3) impulsively heated magnetic field lines from Amari et al. (2015), and (4) synthesized emission measure from Rempel (2017). The Amari et al. (2015) image was published on phys.org on 11 June 2015, with credit to Tahar Amari (Centre de Physique Théorique, CNRS-Ecole Polytechnique, France). These simulations are all driven by large-scale surface motions, such that their heating tends to be dominated by DC-type processes.

**Figure 2**

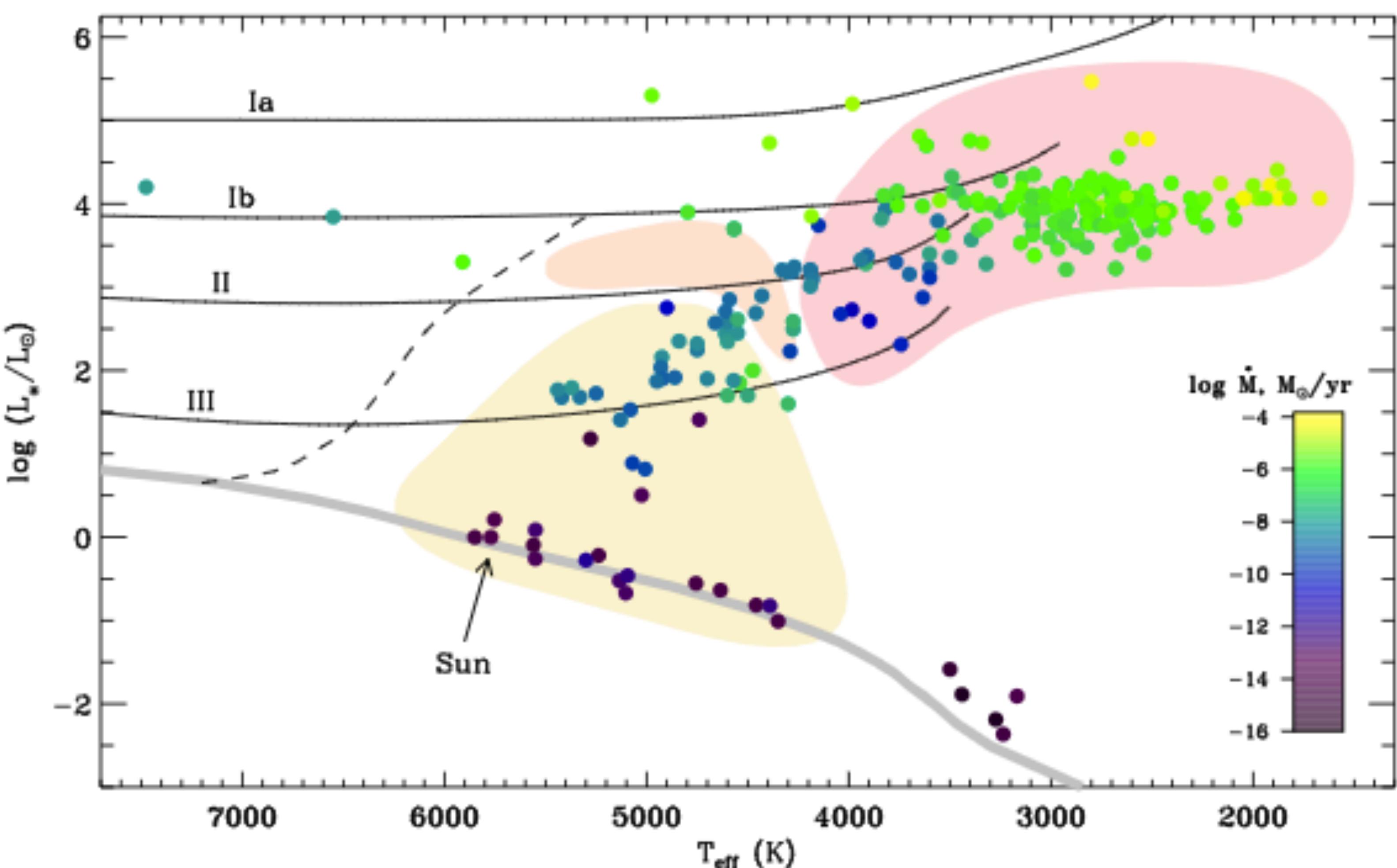
Recent observations find conflicting results about the degree of magnetic tangling of coronal field lines at scales of order  $0.2''$ . *Top left:* Braided active region structure imaged by *Hi-C* at a wavelength of 19.3 nm, on 2012 July 11. *Top right:* Enhanced version of the *Hi-C* image made with an unsharp-masking technique (see Cirtain et al. 2013); an arrow highlights a braided structure. Shortly after this image was acquired, a heating event was observed at this location implying that energy stored in the magnetic field was released. *Bottom:* The paths of coronal-rain plasma parcels, observed by *CRISP* on 2009 May 10, suggest that the field is smooth and unbraided (Antolin & Rouppe van der Voort 2012).

**Figure 4**

Dependence of temperature (a) and mass density (b) on height above the solar surface (i.e., with  $r = R_\odot$  denoting the photosphere, and heights expressed in units of solar radii) for several representative models. Solid curves show closed field-line loops with a range of lengths  $L$  between 30 and 1200 Mm. The green dot-dashed curve shows an open-field coronal hole model from Cranmer et al. (2007). Another open-field model with no coronal heating whatsoever is also shown (i.e., pure radiative equilibrium; blue dotted curve).

**Figure 5**

Illustrations of one-dimensional models of solar wind acceleration. (a) Polytropic solutions in spherical geometry, each computed with  $T = 1.5$  MK at the critical point. (b) Self-consistent models of coronal heating via anisotropic MHD turbulence, for a selection of open field lines from an axisymmetric solar-minimum magnetic geometry (Cranmer et al. 2007). In both panels, solid circles denote the locations of Parker's critical point. Note that 1 AU =  $215 R_\odot$ .

**Figure 6**

Cool-star Hertzsprung-Russell diagram. Symbol colors correspond to observed mass-loss rates (Cranmer & Saar 2011; Wood 2018). Also shown: zero-age main sequence (*thick gray curve*), empirical luminosity classes (*solid black curves*; de Jager & Nieuwenhuijzen 1987), and a boundary between stars with and without subsurface convection (*dashed curve*; Gray & Nagel 1989). Larger regions, from lower-left to upper-right, denote Sun-like stars with hot coronae (*yellow*), warm/hybrid stars with weak or sporadic coronal signatures (*orange*), and cool giants/supergiants without coronae (*red*); see, e.g., Linsky & Haisch (1979); Ayres et al. (2003).

